

Coupling of Leaflet Structure and Collective Fluctuations in Asymmetric Lipid Vesicles

Dissertation

zur Erlangung des akademischen Grades
eines Doktor der Naturwissenschaften

an der Karl-Franzens-Universität Graz

vorgelegt von

Moritz Paul Karl Frewein

am Institut für Physik

Begutachter:

Georg Pabst, Assoz. Prof. Dipl.-Ing. Dr.techn.

Yuri Gerelli, Prof. Ph.D., Università Politecnica delle Marche

Graz, 2022



in cooperation with



In science, there is no problems.
All there is, is questions and challenges.

Preface

This thesis is the product of 3 and a half intense years working on lipid bilayers, mostly with X-ray and neutron scattering. These techniques stand in the center of this work, being challenging tasks both in experiment as well as in data interpretation. All the more rewarding it is to find something significant out of a few wiggles.. Overall in this project we found what we were looking for: Measurable consequences from the asymmetric arrangement of the lipids in a bilayer. This led to two scientific publications and hopefully a third one, which is still in preparation. This thesis summarizes the findings of these three parts of the project and gives an introduction to a large array of experimental techniques used to characterize lipid bilayers.

The time of my PhD study was in many ways a very challenging time. Like many others, it comprised ups and downs, countless hours in the lab and in front of a screen, an introduction to the academic publishing systems and institutional politics, large amounts of coffee and the gain of insight into a complex topic understood only by few. Unlike many others it was partially performed at a user-facility with the possibility to meet people from all over the world, involved a few relocations between Graz and Grenoble, learning a language, two journeys to conferences in the US, many sleepless nights at beamtimes, and a pandemic.

There is many people to thank. It starts of course with Georg, who thought up the project and invited me to join; who runs a formidable lab in Graz, where it is always a pleasure to come back to; who always made sure that there is interested people at my posters; who always knew a way out in difficult situations, and many other things. Next there is Enrico, I am very grateful for all the help with the analysis of scattering data and for many good moments at beamtimes and conferences. Thanks to Lisa for being a great PhD companion. Thanks to Yuri for welcoming me to the ILL and finally for evaluating my thesis. Thanks to Lionel for helping me with access to instruments, for his support in ILL life and for his tricky questions. Thanks to Krishna for his help with biochemistry techniques and his attempts to make some new lipids. Thanks to Haden and Paulina for coming all the way to Grenoble to help me with experiments. Thanks to Milka and Fred for their valuable cooperation and great discussions. Thanks to Giacomo for the time we worked side by side, the experiments we did together and the creation of the door. Thanks to Peter for having the best office, time for french coffee and for proofreading my thesis. Thanks to the Crocoloc for the cozy home and for giving me food when I came home after long experiments. Thanks to many other people for their help and their acquaintance during PhD life. Thanks to the Uni Graz, the ILL and the ESRF for providing funding, instrumentation and beamtime for my studies.

Abstract

Cellular envelopes contain a large number of lipid species that are distributed asymmetrically between the two leaflets of the bilayer. In particular, prototypical mammalian plasma membranes are composed of an outer leaflet enriched in cholinephospholipids, while the majority of aminophospholipids is confined to the inner leaflet. One of the enduring questions of plasma membrane architecture and lipid asymmetry concerns the possibility of interleaflet coupling even in the absence of proteins. This coupling may influence the membrane mechanical properties, the function of trans-membrane proteins as well as a number of physiological processes that require communication between the interior and the exterior of the cell. Among the currently conceived lipid-mediated coupling mechanisms are intrinsic lipid curvature, headgroup electrostatics, dynamic chain interdigitation, or thermal membrane fluctuations.

In the first part of the project we attempt to quantify interdigitation of lipids with differently long chains using small-angle X-ray and neutron scattering (SAXS, SANS). These measurements reveal a linear dependence between the length-mismatch of both chains of the lipid and the localization of the terminal methyl groups, a potential measure for interdigitation.

In the next part we extend the study to asymmetric membranes using asymmetric large unilamellar lipid vesicles (aLUVs), produced via cyclodextrin-mediated lipid exchange. Using selective deuteration of lipid compounds and variation of deuterium content in the solvent, we measure the leaflet-specific thicknesses and lipid packing densities via SAXS and SANS. We find that interdigitating chains can either induce order or disorder into the opposing leaflet, depending on the extent of the overlap of the opposing chains. In weakly interdigitating systems repulsive steric interactions prevail, inducing disorder, in heavily interdigitated systems, the chains can form van der Waals bonds with the neighboring chains, thereby assuming a more ordered state.

In the last part we study the influence of lipid asymmetry on bending fluctuations. Starting with an interdigitated asymmetric system, we gradually increase the complexity of the aLUVs, adding also intrinsic lipid curvature, lipids forming hydrogen bonding networks and head group charges. While for some asymmetric membranes, in particular interdigitated ones, the dynamics of symmetric and asymmetric membranes are similar, other aLUVs experience a large increase in bending rigidity compared to their symmetric counterparts. We hypothesize that the difference in mechanical properties of inner and outer leaflet lipids impedes the bilayer from effectively exhibit collective undulatory motions.

Kurzfassung

Zellmembranen enthalten eine große Anzahl von Lipidspezies, die asymmetrisch auf die beiden Schichten der Membranen verteilt sind. Insbesondere prototypische Plasmamembranen von Säugetieren bestehen aus einer äußeren Schicht, die mit Cholinphospholipiden angereichert ist, während der Großteil der Aminophospholipide auf die innere Schicht beschränkt ist. Eine der wichtigsten Fragen im Zusammenhang mit der Architektur der Plasmamembran und der Lipidasymmetrie ist die Möglichkeit einer Kopplung zwischen den beiden Schichten, selbst ohne membranübergreifende Proteine. Diese Kopplung kann die mechanischen Eigenschaften der Membran, die Funktion von Transmembranproteinen sowie eine Reihe von physiologischen Prozessen beeinflussen, die eine Kommunikation zwischen dem Inneren und dem Äußeren der Zelle erfordern. Zu den derzeit angedachten Kopplungsmechanismen, verursacht durch Lipide, gehören intrinsische Krümmung, Kopfgruppen-Elektrostatik, dynamische Ketteninterdigitation und thermische Membranfluktuationen.

Im ersten Teil des Projekts versuchen wir, die Interdigitation von Lipiden mit unterschiedlich langen Ketten mithilfe von Röntgenkleinwinkel- und Neutronenstreuung (SAXS, SANS) zu quantifizieren. Diese Messungen zeigen eine lineare Abhängigkeit zwischen dem Längenunterschied der beiden Ketten des Lipids und des Aufenthaltsbereichs der terminalen Methylgruppen, einem potenziellen Maß für Interdigitation.

Im nächsten Teil erweitern wir die Studie auf asymmetrische Membranen unter Verwendung asymmetrischer großer unilamellarer Lipidvesikel (aLUVs), die durch Lipidaustausch mit Cyclodextrin hergestellt werden. Durch selektive Deuterierung von Lipidteilen und Variation des Deuteriumgehalts im Lösungsmittel messen wir die spezifischen Dicken und Lipidpackungsdichten der einzelnen Schichten mittels SAXS und SANS. Wir stellen fest, dass interdigitierende Ketten entweder Ordnung oder Unordnung in die gegenüberliegende Schicht induzieren können, je nach dem Ausmaß des Überlapps mit den gegenüberliegenden Ketten. In schwach interdigitierenden Systemen herrschen abstoßende sterische Wechselwirkungen vor, die zu erhöhter Unordnung führen. In stark interdigitierenden Systemen können die Ketten van-der-Waals-Bindungen mit den benachbarten Ketten bilden und dadurch einen geordneteren Zustand annehmen.

Im letzten Teil untersuchen wir den Einfluss der Lipidasymmetrie auf Biegefluktuationen. Ausgehend von einem interdigitierenden asymmetrischen System erhöhen wir schrittweise die Komplexität der aLUVs, indem wir auch intrinsische Krümmung, Lipide mit der Neigung Wasserstoffbrückennetzwerke zu formen und Kopfgruppenladungen hinzufügen. Während bei einigen asymmetrischen Membranen, insbesondere bei interdigitierenden, sich die Dynamik von symmetrischen und asymmetrischen Membranen ähneln, weisen andere aLUVs im Vergleich zu ihren symmetrischen Gegenstücken einen starken Anstieg der Biegesteifigkeit auf. Wir vermuten, dass der Unterschied in den mechanischen Eigenschaften der Lipide aus inneren und äußeren Schichten die Membran daran hindert, effektiv kollektive undulatorische Bewegungen auszuführen.

Contents

Preface	I
Abstract	III
Kurzfassung	IV
Table of Contents	VI
1 Introduction	1
1.1 Lipids and Membranes	1
Heads and Tails	1
The Liquid Crystalline State	2
Trans-Bilayer Asymmetry and Interleaflet Coupling	2
1.2 Previous Work on Vesicles and Asymmetric Membranes	3
Trans-Membrane Structure	3
Production of Asymmetric Membranes	4
Interleaflet Coupling	4
2 Experimental Techniques	6
2.1 Preparation of Lipid Vesicles	6
Asymmetric Vesicles by Cyclodextrin-Mediated Exchange	6
Lipids Used in this Work	7
2.2 Small-angle Scattering	7
Differences of X-ray and Neutron Scattering	9
Instrumentation	9
Data Modelling	11
Joint Analysis of SAXS and SANS	11
2.3 Neutron Spin-echo Spectroscopy	13
The Zilman-Granek Model	15
Reinterpretation of κ	15
Contributions from Vesicle Diffusion	16
2.4 Dynamic Light Scattering	17
2.5 Chromatography Techniques	18
2.6 Nuclear Magnetic Resonance Spectroscopy	18
2.7 Differential Scanning Calorimetry	19
2.8 Determination of Phospholipid Concentration by Organic Digestion to Inorganic Phosphate	20
3 Results and Discussion	23
3.1 Advances in the SDP-Model	23
High-Density Hydration Layer	23
Thickness Polydispersity of Membranes	23
Asymmetric Model	24
3.2 Interdigitation of Chain-Asymmetric Lipids	24
Single Lipid Bilayers	25
Asymmetric Bilayers	26
3.3 Bending Fluctuations in Lipid-only Plasma Membrane Mimics	27
Rigidification of Asymmetric Bilayers	27
Contributions from Intrinsic Curvature and Charge	29
Dynamical Interpretation	30
Concluding Remarks	31
4 Outlook	32
5 Conclusion	33
List of Scientific Publications	34

Bibliography	39
Article: Structure and Interdigitation of Chain-Asymmetric Phosphatidylcholines and Milk Sphingomyelin in the Fluid Phase	40
Article: Interdigitation-induced Order and Disorder in Asymmetric Membranes	66
Supplement: Interdigitation-induced Order and Disorder in Asymmetric Membranes	81
Supplement: SAS analysis of symmetric and asymmetric bilayers measured by NSE	93

1 Introduction

1.1 Lipids and Membranes

Lipids are molecules that belong to the class of surfactants¹ due to their amphiphilic properties. They possess a hydrophilic part, often called head, and one or more hydrophobic² tails. Therefore, their energetically most favorable environments are oil-water interfaces. In aqueous environments they form structures like micelles or bilayers to shield the tails from the solvent (Fig. 1). This process is driven by hydrophobic forces and called self-assembly.

A lipid bilayer is the backbone of the biological membrane, which occurs both as the outer shell of cells, as well as interface to its inner compartments or organelles. It contains hundreds of different lipid species and is a quite impenetrable barrier to most molecules and ions. Water however traverses the membrane rapidly. Embedded in this lipid matrix one finds a complex machinery of other amphiphilic molecules such as proteins or peptides. They perform a wide range of tasks, ranging from transport of ions and small molecules, sensing, signaling, to the maintenance and remodeling of their lipid environment.

This already hints that the membrane is a very dynamic construct. The molecules are strongly confined to the bilayer plane, but can diffuse therein. Due the large variety of molecules and the resulting lateral heterogeneity, the cell membrane was pictorially labeled a "fluid mosaic" in 1972, a concept which is still valid and widely used [1, 2].

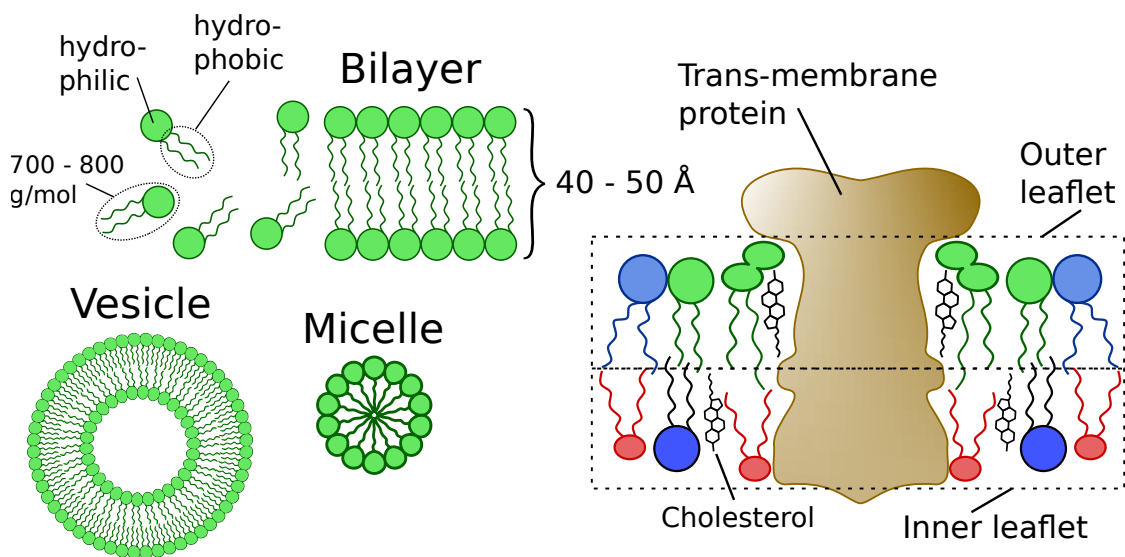


Figure 1: Different aggregates formed by lipids in aqueous environments. Free-floating bilayers always form closed structures, like vesicles, to shield the hydrophobic parts from water. Micelles can form from lipids with large headgroups or only a single chain. The right hand side image demonstrates the asymmetric structure of a membrane and how the bilayer adapts its shape and composition in the vicinity of a membrane protein.

Heads and Tails

The large variety of lipids is both due to differences in the hydrophilic and the hydrophobic part. An important class of lipids – and the only one treated in this thesis – are phospholipids. Their name is due to the prominent negatively charged phosphate group in the head group. Charge or local separation of opposite charges is the reason for the hydrophilicity of the head group, enabling energetically favorable interactions with the partial charges in the water molecules. Linked to the phosphate towards the water phase one can find a wide range of compounds, forming charged or overall neutral, polar head groups.

Towards the oily side a "lipid backbone" connects head and tail groups. This role is often taken by glycerol, a rather rigid moiety with three junctions (labeled sn-1/2/3). While the head group takes the sn-3 position, fatty acids of variable length are usually linked to sn-1 and sn-2. Another common backbone is sphingosine.

¹Surface Active Agents: molecules that lower the interfacial tension between 2 substances

²Hydrophilic: attracted by water. Hydrophobic: repulsed by water. Alternatively also named lipophilic: attracted by fat

It fulfills a similar role, but already contains one hydrocarbon chain, leaving one linkage for the head group and one for a fatty acid.

The main part of fatty acids are hydrocarbon chains, containing between 14 and 24 carbons in natural membrane lipids. These can be linked to each other by single or double bonds, which is labeled saturated or unsaturated, respectively. The tails are confined to the interior of the membrane and interact with the neighboring tails only via van der Waals (vdW) and steric forces. Fully saturated chains can assume ordered states where the attractive vdW forces dominate. Unsaturation however create a kink in the chain, making the membrane looser packed and more fluid. Most membrane lipids contain at least one unsaturated fatty acid chain with up to 4 double bonds. The kink induced by unsaturation also makes the chain buckle, which is why unsaturated chains are generally shorter than saturated ones of the same number of carbons.

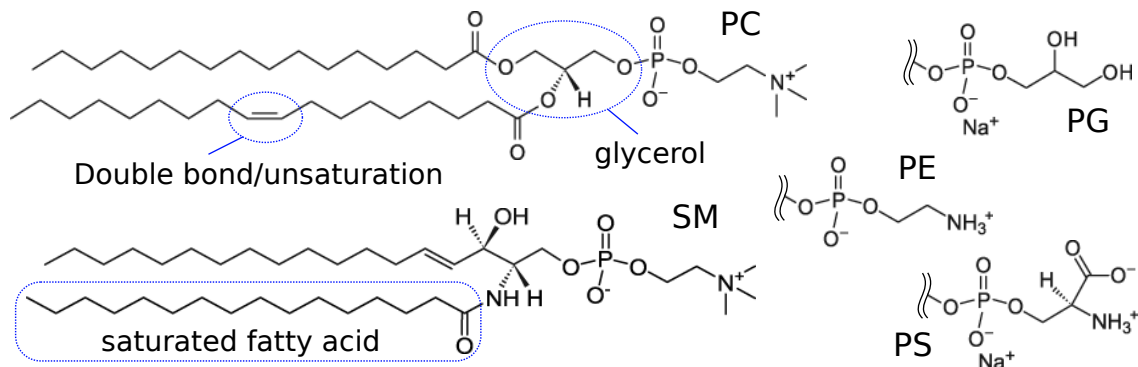


Figure 2: Chemical structures of common phospholipids, which were used in this thesis to mimic natural membranes: 1-palmitoyl-2-oleoyl-glycerol-3-phosphocholine (POPC⁴), palmitoyl sphingomyelin (PSM) and the headgroups phosphoglycerol (PG), phosphoethanolamine (PE), phosphoserine (PS).

The Liquid Crystalline State

The structure of lipids in biological membranes is a liquid crystalline smectic phase. It is however not the only phase lipids can assume. Each lipid has a characteristic temperature T_m below which the chains condense into a hexagonal lattice, which increases the packing density, thickens and stiffens the membrane. This gel phase only occurs at very low temperatures (often below 0 °C) for unsaturated lipids, fully saturated ones can stay in the gel phase up above physiological temperatures. Also a small headgroup, as in the case of phosphoethanolamines, can force the chains to pack tighter and thereby stabilize the gel phase at higher temperatures.

Lipid mixtures can have complicated phase diagrams with regions of coexisting gel and fluid domains. This particularly happens for mixtures of di-saturated and di-unsaturated lipids. Generally, the main transition temperature T_m of a mixture does not exceed T_m of the highest melting component.

Trans-Bilayer Asymmetry and Interleaflet Coupling

Another important feature of natural membranes is that the inner and outer leaflet are different in lipid composition. The outer layer consists mostly of choline-lipids, namely phosphocholine (PC) and sphingomyelin (SM), while the inner leaflet is mainly composed of PC, phosphoethanolamine (PE) and phosphoserine (PS). Furthermore, there is an asymmetry in chain composition. Inner leaflet lipids contain a high number of polyunsaturated chains, while SM in the outer leaflet is largely saturated.

This asymmetric state is evidently not in thermodynamic equilibrium and therefore has to be specifically produced. In nature this is done by a pair of membrane proteins named flippases and floppases⁵, which consume energy to maintain a certain asymmetric lipid composition. Also proteins with the ability to rapidly destroy this asymmetry, scramblases, exist.

A long-lasting question in membrane research is the function of this asymmetry and its consequences on

⁴The first 2 letters designate the fatty acids, the second 2 the head group. D in first position means both chains are equal. An alternative way of naming the chains is by numbers XX:Y, where XX is the number of carbons, Y the number of unsaturations.

⁵Flip-flop is the process of a lipid translocating to the opposite leaflet.

membrane structure and mechanical properties. Function is a question of membrane biology, which provided some answers early on. To name a few of them: A more saturated, tighter packed outer leaflet provides more protection to the cell from outside. Membrane proteins are often asymmetric and require an asymmetric lipid matrix to function. Constraining charged lipids to the inside (notably PS) gives the possibility to transmit signals by flipping them to the outside.

The more biophysical questions of structure and dynamics required more time, as membrane biophysics heavily relies on simplified model systems to study certain aspects of membranes. Producing appropriate asymmetric samples is only possible for a short period, both in experiment as well as in simulation[3]. It was soon clear that an asymmetric membrane is not necessarily the combination of two independent leaflets, introducing the term inter-leaflet or trans-bilayer coupling. Several instances have been observed, where one leaflet would influence the properties of the opposing one, some of which are introduced in the following section.

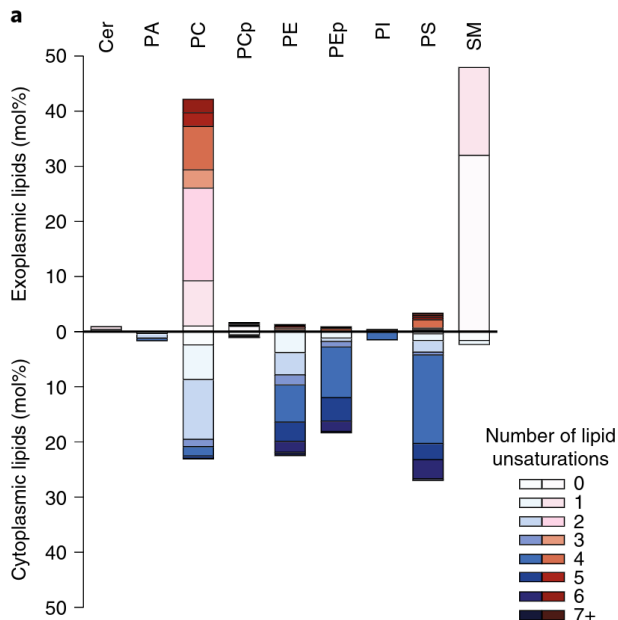


Figure 3: Composition of inner (cytoplasmic) and outer (exoplasmic) leaflet of red blood cells (figure adapted from [4]). Its main components comprise the lipids introduced in Fig. 2. PEP lipids are plasmalogens with the same PE headgroup but a slightly different chain-structure.

1.2 Previous Work on Vesicles and Asymmetric Membranes

The title includes 'work on vesicles', as vesicles (or liposomes) are the model system used in this project. In particular, large unilamellar vesicles (LUVs) are used, which have only a single lipid bilayer and diameters around 100 nm. LUVs can be produced in adequate amounts for small-angle scattering, also with an asymmetric membrane composition, and are sufficiently large so that the membranes can be considered flat. Other model systems include multi-lamellar vesicles, flat bilayers and bilayer stacks, lipid nano-discs and unilamellar vesicles of different size (small < 100 nm, giant > 1000 nm).

Trans-Membrane Structure

While it is possible to observe the lateral structure of membranes via microscopy⁶, the trans-bilayer structure is for now only accessible using X-ray and neutron scattering or molecular dynamics (MD) simulations. Due to the liquid nature of the membrane, the positions and configurations of the lipids fluctuate, which is why membrane structures are usually represented by probability distributions. From simulations they can be

⁶There is a wide range of techniques to study lateral inhomogeneities and molecular interactions between molecules in the membrane including electron microscopy and optical microscopy using fluorescent labels.

retrieved for every single atom, in scattering coarser models are used, where the molecule is parsed in several groups. Fig. 4a shows a model which represents the limit in resolution to which trans-bilayer structures can be determined experimentally. This model was originally designed to describe diffraction data from bilayer stacks[5] and was later adapted to the use for small-angle scattering for symmetric[6] and asymmetric vesicles[7].

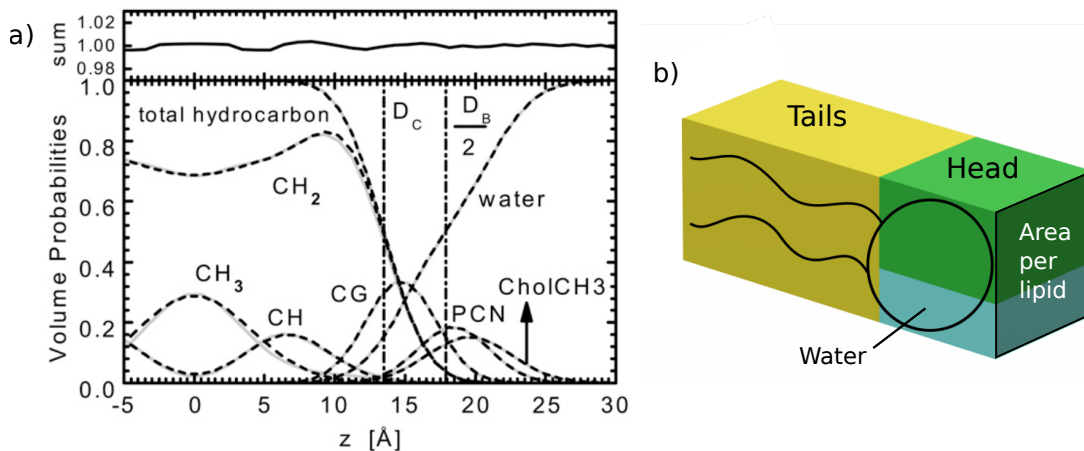


Figure 4: a) Volume probability based model of the bilayer cross-section of DOPC (di18:1-PC). $z = 0$ marks the bilayer center. The lipid is parsed in choline head (CholCH3), phosphate group (PCN), carbonyl-glycerol backbone (CG), saturated carbons (CH_2), unsaturated carbons (CH) and terminal methyl ends (CH_3), which are described by Gaussians and Error-functions. CH_2 , CH and CH_3 are components of the hydrocarbon chains and fill the whole space in the bilayer center. In the headgroup region (CG, PCN, CholCH3) the remaining space is filled with water. D_C is the width of the chain region, D_B the bilayer thickness. Figure adapted from [6]. b) shows a simplified model of the lipid unit cell and demonstrates the connection to the area per lipid.

To build such a model, using volume probability density functions for each part of the lipid, it is necessary to know the volume of each of them. Total lipid volumes are accessible via density measurements. The chain segment and total head group volumes can also be determined quite accurately by measuring the volume of lipids with varying chain length and extrapolating. For the head group segments one has to rely on estimates based on X-ray diffraction and MD-simulation [8].

Finally, the lipid volume also connects the membrane thickness to the the area per lipid A (Fig 4b), which corresponds to the packing density of the membrane. Typical values for A of phospholipids in the fluid phase are around 60 to 70 \AA^2 .

Production of Asymmetric Membranes

Even though lipid asymmetry was discovered in the 1970s [9], research on model membranes continued using symmetric systems. Only recently, several techniques have emerged that are able to produce stable asymmetric membranes[3]. Among these methods, cyclodextrin-mediated exchange is the only one suited to produce asymmetric LUVs (aLUVs) in large enough quantities for X-ray and neutron scattering studies [10]. The protocol relies on the amphiphilic properties of the ring-shaped oligosaccharide cyclodextrin, which solubilizes lipids and inserts them into the outer leaflet of symmetric LUVs. There is several ways to prove that the resulting vesicles are indeed asymmetric, among them small-angle neutron scattering (Sec. 2.2, nuclear magnetic resonance (Sec. 2.6) and differential scanning calorimetry (Sec. 2.7). Vesicles produced this way have been shown to stay asymmetric for several days in the fluid phase and even longer in gel phase[11].

Interleaflet Coupling

Currently conceived lipid-mediated coupling mechanisms consider either intrinsic lipid curvature, headgroup electrostatics, cholesterol flip-flop, dynamic chain interdigitation, thermal membrane fluctuations and differential stress [12, 13]. Several cases of interleaflet coupling have been observed in the past.

Lipid curvature is a consequence of the shape of a lipid. Lipids with a head group that is either larger or smaller than the chain region are cone-shaped and form curved surfaces if arranged in a monolayer. Consequently, the cone-shaped PE-lipids are generally found at the inside of plasma membranes. Asymmetric vesicles with PE inside and PC outside were found to have a coupled phase transition, whereas the other way round they would melt independently from each other [14].

In a study using neutron scattering on asymmetric vesicles, it was found that if lipids in gel and fluid phase are opposed to each other, the gel phase lipids can impose their more ordered structure on the opposing lipids [15].

In MD-simulations, long chain sphingomyelins have been found to penetrate deep into the opposing leaflet and influence the conformational order of the lipids therein [16].

A recent theoretical study [13] also predicts that asymmetry can lead to a drastic increase in bending rigidity in the presence of differential and curvature stress (Fig. 5). And in fact, such stiffening effects have been observed in giant unilamellar vesicles (GUVs) using saturated and unsaturated phosphocholines (PC) opposed to each other [17, 18], but also in unilamellar vesicles containing phosphoethanolamine (PE) and sphingomyelin [19].

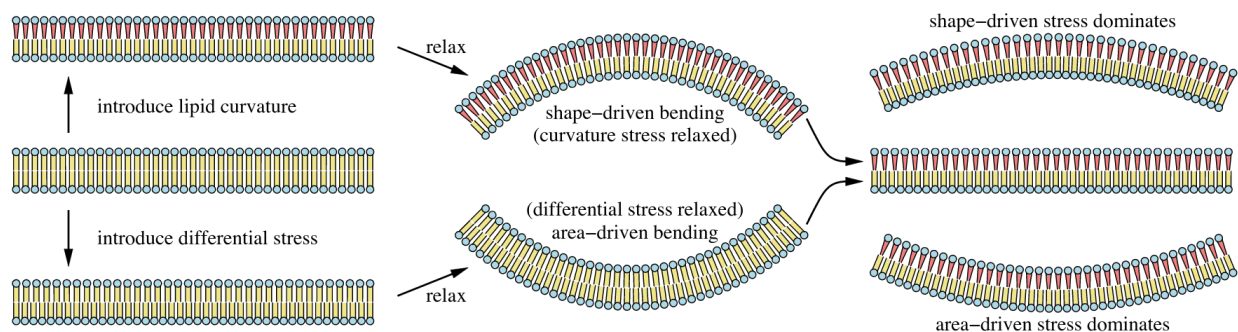


Figure 5: Schematic of the effects of lipid curvature and differential stress on asymmetric bilayers. Lipids with intrinsic curvature naturally tend to assume a curved geometry. In a symmetric bilayer of such lipids, curvatures from both leaflets cancel and the membrane is flat, but stressed. If the opposing leaflet has not intrinsic curvature to resist this drive, a membrane bends. The same can happen in the presence of differential stress, if one of the leaflet contains less lipids than the other. As flip-flop is generally slow, the membrane might relax into a curved state to compensate for the excess area of the depleted leaflet. The stress induced by these membrane properties can lead to an overall higher membrane rigidity [13].

2 Experimental Techniques

2.1 Preparation of Lipid Vesicles

The property of lipids to self-assemble in aqueous environments makes the preparation of vesicles a simple task, various measures are usually taken to ensure sample homogeneity and to avoid undesired aggregation. Dispersed in water most lipids form multilamellar structures. If the desired vesicle diameter is sufficiently small (≤ 100 nm), the undesired layers can be removed via extrusion through a filter with the respective pore-size. To stabilize the unilamellarity over time it is also crucial to include at least a small amount (≥ 5 %) of charged lipids [20].

In this work, the following protocol was applied:

- Lipids are purchased in powder form and stored in a sealed glass container at -20°C or lower. To weigh lipids to a satisfying precision (down to 0.1 mg), it should only be opened at room temperature to avoid water condensation inside the vial. Unsaturated lipids are prone to oxidation and should be stored in an inert gas environment (e.g. N_2 , Ar)
- The weighed lipids are dispersed in organic solvent and vortexed until all aggregates dissolve. Very dilute solutions can be used for increased accuracy, but should be handled at a rapid pace to avoid evaporation of solvent. If aggregates remain after vortexing, heating, sonication or adaption of the solvent mixture can help. We used Chloroform/Methanol 2:1 (vol/vol) for PC, SM and PE; 9:1 for PG and PS.
- After mixing solutions to the desired lipid composition, the solvent is evaporated using a soft beam of inert gas (e.g. N_2 , Ar), forming a film over the bottom of the vial. Thereafter, films should be kept in vacuum (< 100 Pa) for > 6 h to ensure the removal of all organic solvent. Alternatively, a rotary evaporator can be used, especially for large samples (> 50 mg lipid).
- Dry films are hydrated in water or the desired aqueous buffer, which should be pre-heated to a temperature of about 10 °C above T_m of the lipid mixture. The solution is kept at this temperature for 1 h with intermittent vigorous vortexing (e.g. 1 min every 15 min). To further improve the uniformity of the sample, one can perform cycles (3-5) of freezing (freezer/dry ice/liquid nitrogen) and thawing by heating above T_m for 15 min followed by vigorous vortexing.
- The vesicles are extruded 31 times through a 100 nm polycarbonate membrane using a hand-held extruder, while heating well above T_m . The resulting vesicle size is monitored by DLS (see sec. 2.4). If large particles are present or polydispersity is high (> 10 %), the solution can be extruded more times, perhaps it is necessary to change the membrane. Unilamellarity can be confirmed by the absence of Bragg-peaks in SAXS (sec. 2.2).

Asymmetric Vesicles by Cyclodextrin-Mediated Exchange

The protocol to produce asymmetric free-floating membranes via lipid exchange makes use of the amphiphilic properties of methylated cyclodextrin (CD). It is ring-shaped and water soluble, but possesses a hydrophobic cavity in its center. If added to an aqueous lipid suspension, it solubilizes lipids by covering their hydrophobic tails. In the exchange-protocol this is used to transfer lipids from one population (donors) of lipid vesicles to another (acceptors).

In brief, acceptor unilamellar vesicles are produced by the above protocol (sec. 2.1) with the lipids desired in the inner leaflet. Donor vesicles are produced without extrusion, but in a sucrose solution. They are incubated with CD for an elongated time while being heated above T_m , enriching the solution with CD-donor lipid complexes. Acceptor vesicles are added and solubilized lipids exchange with lipids from their outer leaflet (Fig. 6). The heavy, sucrose-filled donor vesicles are finally removed by centrifugation. A full step-by-step description of this protocol can be found elsewhere[10].

The amount of lipid exchanged is determined by the ratio of acceptor and donor vesicles, the duration of the joint incubation of donors and acceptors before separating them and possibly also by temperature. However, in the presence of CD, lipid flip-flop is accelerated, due to defects in the membrane created by interactions with CD. Elongated incubation can therefore lead to higher exchange, but at the cost of lower asymmetry. In this study we did not systematically vary these parameters but used a ratio of 2:1 (mol/mol) donor/acceptor lipids and let them exchange for 15 min at 50 °C. All other parameters were chosen as stated in the cited protocol.

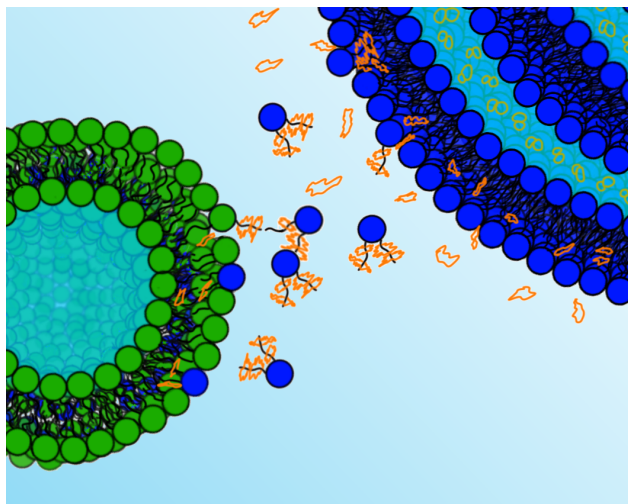


Figure 6: Schematic representation of lipids exchanging from a donor (blue) to an acceptor vesicle (green), mediated by cyclodextrin (orange).

Lipids Used in this Work

Table 1: Lipids used for experiments in this project. m denotes the molecular weight, T_m the main phase transition temperature. d62 denotes the number of hydrogens replaced by deuterium in the acyl chains.

* These lipids are charged and are delivered as sodium salt

† These lipids are natural extracts and therefore a mixture of different species. The most abundant acyl chain composition and the average molecular weight are given.

Abbr.	Full name	Chains	m [g/mol]	T_m [°C]
DPPC	1,2-dipalmitoyl-sn-glycero-3-phosphocholine	di16:0	734	41
DPPCd62	1,2-dipalmitoyl-d62-sn-glycero-3-phosphocholine	di16:0	796	41
DPPG	1,2-dipalmitoyl-sn-glycero-3-phospho-(1'-rac-glycerol)*	di16:0	745	42
DPPGd62	1,2-dipalmitoyl-d62-sn-glycero-3-phospho-(1'-rac-glycerol)*	di16:0	807	42
MSPC	1-myristoyl-2-stearoyl-sn-glycero-3-phosphocholine	14:0/18:0	734	39
SMPC	1-stearoyl-2-myristoyl-sn-glycero-3-phosphocholine	18:0/14:0	734	31
PMPC	1-palmitoyl-2-myristoyl-sn-glycero-3-phosphocholine	16:0/14:0	706	28
POPC	1-palmitoyl-2-oleoyl-glycero-3-phosphocholine	16:0/18:1	760	-4
POPG	1-palmitoyl-2-oleoyl-glycero-3-phospho-(1'-rac-glycerol)*	16:0/18:1	771	≈0
SOPC	1-stearoyl-2-oleoyl-glycero-3-phosphocholine	18:0/18:1	788	6
SOPG	1-stearoyl-2-oleoyl-glycero-3-phospho-(1'-rac-glycerol)*	18:0/18:1	799	≈5
POPE	1-palmitoyl-2-oleoyl-sn-glycero-3-phosphoethanolamine	16:0/18:1	718	26
POPS	1-palmitoyl-2-oleoyl-sn-glycero-3-phospho-L-serine*	16:0/18:1	784	14
MSM	Sphingomyelin (Milk, Bovine)†	23:0	785	35
ESM	Sphingomyelin (Egg, Chicken)†	16:0	785	38

2.2 Small-angle Scattering

X-rays and neutrons are two kinds of radiation, which both penetrate through a wide range of materials, in particular organic matter. Besides absorption, which is exploited in imaging methods, there is also collisions with atoms, through which the particles are scattered away from their incident trajectory. In small-angle scattering (SAS or SAXS/SANS, for X-rays or neutrons) a sample is irradiated with a focused, monochromatic beam and the outgoing radiation is recorded on a 2D-detector (Fig. 7), where it leaves an interference pattern characteristic to the structure of the material. This effect is heavily used in crystallography, where a static lattice leads to peaks in the scattering pattern according to the Bragg law⁷. In soft matter lattices

⁷ $n\lambda = 2d \sin \theta$, with n being the diffraction order and d the spacing of the crystal lattice.

are rare, however, any repeatedly occurring distance in a sample leaves a distinct oscillation in the scattering pattern. This way, quantities such as the radius of monodisperse vesicles or the thickness of lipid bilayers can be measured.

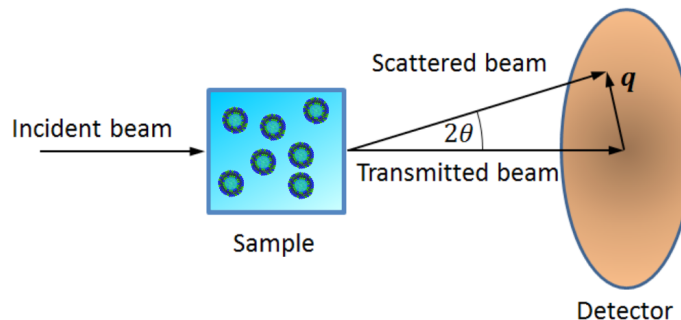


Figure 7: Experimental setup of small-angle X-ray or neutron Scattering.

Scattered particles are detected in dependence of the scattering angle 2θ , however data are usually represented through the magnitude of the scattering vector $q = 4\pi \sin \theta / \lambda$. This quantity represents the momentum exchange between radiation and sample, which is independent on the wavelength λ . At the same time it corresponds to a distance in reciprocal or Fourier space. This means that features at large q -values in a SAS-curve correspond to small objects in the sample and vice-versa, the dimension d of the object roughly following the relation $d \approx 2\pi/q$. Small-angle scattering probes angles of about 0.1 - 10° , which corresponds to length-scales from nano to micrometers.

Every object seen through SAS has a form factor $F(\mathbf{q})$, which corresponds to the amplitude of the wave scattered the object. It is given by the Fourier transform of its scattering length density (SLD) profile $\rho(\mathbf{r})$, a quantity resulting to its structure and composition.

$$F(\mathbf{q}) = \int dV \rho(\mathbf{r}) e^{i\mathbf{q}\mathbf{r}} \quad (1)$$

The SLD $\rho(\mathbf{r}) = b/V$ of a material is calculated from its volume and scattering length b , which is related to the scattering cross-section of an atom for a certain radiation (see next section). For objects in solution the absolute value of ρ however is not decisive, but only the contrast with respect to the solvent $\Delta\rho(\mathbf{r}) = \rho(\mathbf{r}) - \rho_{\text{solvent}}$. Inhomogeneities within the object can also be detected if their SLD is sufficiently different from their surrounding.

If the objects of a monodisperse ensemble are sufficiently far from each other⁸, the intensity $I(\mathbf{q})$ ⁹ measured on the detector is given by the absolute square of the form factor of the object and is scaled by the particle density n . It also contains a flat background originating from incoherent scattering¹⁰. If the objects are isotropical, such as lipid vesicles, the resulting scattering pattern is rotationally symmetric and one can work in one dimension using the magnitude of the scattering vector q .

$$I(q) = n |F_{\text{obj}}(q; \Delta\rho(\mathbf{r}))|^2 + I_{\text{inc}} \quad (2)$$

$F(q)$ has usually the shape of a decaying wave, which can have real and imaginary parts. Upon calculating the absolute square, the phase-information of this wave is lost, as everything is converted to a real value and zero-crossings turn to minima. This complicates the task to retrieve the actual form factor, as there is no unique solution. There is techniques to inverse Fourier-transform the data, the result is however a correlation function¹¹, which again has to be interpreted. It is therefore often necessary to make a mathematical model

⁸Compared to the coherence length of the radiation. Else, a structure factor has to be included, for example for very concentrated samples or multilamellar vesicles.

⁹Here, purely elastic scattering is assumed, meaning that all change in \mathbf{q} is a change in angle. Naturally, also inelastically scattered particles are detected, however their contribution is usually negligible and a purely elastic theory can be applied.

¹⁰In an incoherent scattering process the phase of the wave changes.

¹¹The pair-distance-distribution function. A correlation function contains information about the frequency of an event occurring at a certain distance. In this case the presence of a scattering center at a distance in space.

of the investigated object, using known properties such as shape or composition, and assign parameters to adapt until the form factor of the model matches the data. In this work we used the SDP-model (see sections 1.2, 3.1).

A more detailed description of scattering theory can be found for example in Squires' textbook[21].

Differences of X-ray and Neutron Scattering

X-rays are scattered from the electron cloud, which makes the scattering length b of an element proportional to its number of electrons or atomic number Z ($b_{\text{X-ray}} = Zr_e$, where $r_e = 2.81 \times 10^{-13}$ cm is the classical electron radius). In lipids, phosphorus stands out as the heaviest element, making the distance between the phosphates in inner and outer leaflet the most reliable parameter of a lipid bilayer.

Neutrons, however, interact with nuclei, which not only results in a more complex relation between atomic number and b , but also makes them sensitive to individual isotopes. Particularly important for the research of organic material is the difference between hydrogen (-3.74 fm) and deuterium (6.67 fm). Replacing one isotope with another in parts of the sample gives the possibility to change the contrast between solvent and object or between parts within the object – without effects on its chemical and with only minor effects on its physical properties. Tab. 2 shows an overview of b -values for the atoms contained by lipids.

Table 2: Coherent scattering lengths of some atoms for both X-ray and neutron radiation

Element/Isotope	$b_{\text{X-ray}}$ (fm)	b_{neutron} (fm)
Hydrogen (^1H)	2.82	-3.74
Deuterium (^2D)	2.82	6.67
Carbon (^{12}C)	16.9	6.65
Nitrogen (^{14}N)	19.7	9.36
Oxygen (^{16}O)	22.5	5.80
Phosphorus (^{31}P)	42.3	5.13

Tab. 2 refers only to the coherent b of the shown elements. As mentioned in the description of eq. 2, incoherent scattering enters the picture as a constant background, which influences the signal-to-noise ratio. It is therefore important to mention that the incoherent neutron b of hydrogen exceeds by far that of all other relevant elements. This causes high background scattering for H_2O -rich solvents, which is why SANS-experiments are preferably performed in solvent with high D_2O -content.

Instrumentation

This section describes the functionality of X-ray and neutron scattering instruments in large scale facilities. While it is possible to produce X-rays in laboratory devices like X-ray tubes, neutrons require a nuclear reactor or a spallation source. These facilities, as well as X-ray sources such as synchrotrons or free electron lasers, are often internationally funded institutes, where external users compete for time on the instruments (beamlines) by submitting proposals for experiments. Neutron experiments in this project were mainly performed at the D22 small-angle diffractometer and IN15 spin-echo spectrometer, both at Institut Laue-Langevin (ILL), Grenoble, France. SAXS measurements were conducted at the BM29¹² BioSAXS beamline at the European Synchrotron Radiation Facility (ESRF), Grenoble, France.

A synchrotron is a ring-shaped particle accelerator. To use it for producing X-rays, it exploits the fact that accelerated charges emit radiation. The most prominent part of a synchrotron is the storage ring, which consists of evacuated pipes, in which electrons circle at near light speed. Before entering the ring, the electrons are accelerated in two steps, first in a linear accelerator, where their energy reaches several MeV, then they enter the booster ring, which brings them to GeV and injects them into the storage ring (Fig. 8). The storage ring is not exactly circular, but has straight segments alternating with bending magnets. These literally bend the trajectory of the electrons, upon which they emit synchrotron radiation in tangential direction. X-rays are however of comparably low intensity and badly collimated (they have a large angular distribution). Modern synchrotrons therefore use other insertion devices like wigglers and undulators to produce high intensity, collimated radiation. These are situated at the linear parts of the storage ring and consist of a series of alternating pairs of magnets, which force the electrons to oscillate perpendicular to their trajectory. At each oscillation, they emit a cone of X-rays in forward direction (Fig. 8b). Undulators drive

¹²Traditionally named BM for bending magnet, the radiation from this beamline is not produced by a wiggler.

this principle even further. They produce radiation cones with a very low angle to the forward direction, which causes them to constructively interfere with the radiation produced from neighboring magnet pairs. This leads to even higher intensities.

A nuclear reactor is a specialized container, which is designed to start and maintain a nuclear fission reaction. The most common fissile material is Uranium-235, which fissions upon neutron bombardment. In the process, the ^{235}U nucleus absorbs the neutron, its kinetic energy and the binding energy of the neutron. The resulting excited ^{236}U nucleus breaks into two lighter fission products and releases several free neutrons and gamma rays (Fig. 8c). With the proper arrangement, some of these neutrons trigger more further fission events in the vicinity and therefore produce a chain reaction. Other neutrons escape and can be guided into beamlines for the study of materials. To control the speed of the nuclear reaction and avoid a supercritical chain reaction (where an excess of neutrons increases the rate of nuclear fissions), certain control rods are inserted between the uranium fuel. These contain neutron poisons, which absorb neutrons, and neutron moderators, which slow down neutrons. A more recently established way of producing neutrons for research is the mechanism of spallation. There, heavy elements like tungsten or mercury are bombarded with protons and release neutrons in the collision process.

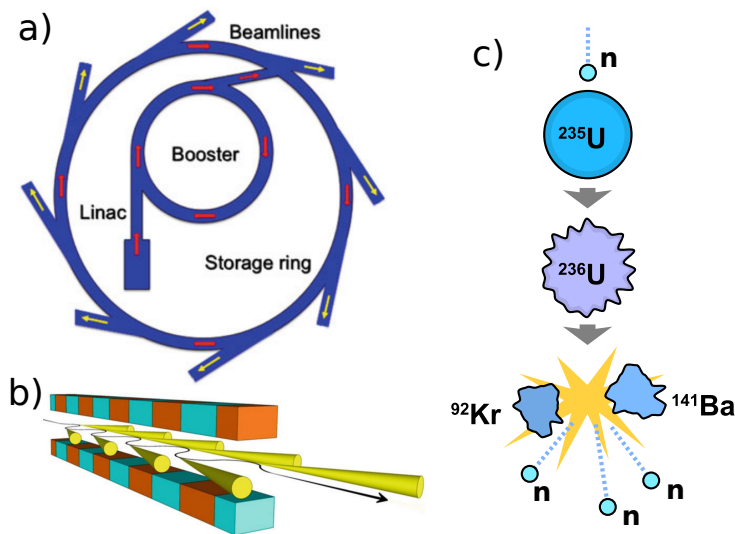


Figure 8: Production of X-rays and neutrons: a) shows the basic arrangement of a synchrotron [22], b) a wiggler and the path of an electron (black line) emitting radiation (yellow) [22], c) nuclear fission induced by neutron bombardment with exemplary fragments created in the fission process.

Beamlines comprise all instrumentation from the radiation source to the detector. SAS beamlines are relatively simple and need to take care of the same functions in case of neutrons and X-rays: guidance of the beam onto the sample, collimation or focussing of the radiation, restriction of the wavelength distribution (monochromator/velocity selector) and detection after the scattering event. The first part is taken care of by mirrors and specialized tubes with reflecting surfaces (neutron guides). Collimation is done by a sequence of pinholes, which restrict the angular distribution of the radiation. This is particularly important for small-angle scattering, as the lower the angles, which are to be detected, the sharper the angular distribution of the incoming radiation has to be. This means however also a loss in beam intensity and has to be compensated with longer measurement times. Wavelength selection is done by crystals or gratings, which separate different wavelengths by the diffraction. For neutrons, due to their finite velocity, also pairs of choppers can be used. These are spinning wheels with pinholes, cutting the beam into pulses. By placing two after each other, only the ones with a certain velocity pass through the second chopper. Detection is done using a 2D-array of pixels sensitive to the respective radiation. In X-rays these are solid state detectors, where X-rays produce an electric signal. Neutrons are somewhat harder to detect, as they interact little with matter. Detectors used at the D22 consist of tubes filled with Helium-3, which has a high propensity to absorb neutrons. In a following nuclear reaction it decays into tritium and a proton. A resulting charge cloud can thereafter be detected and localized by grid of wires. The path between sample and detector is usually kept under vacuum to avoid scattering and absorption by air.

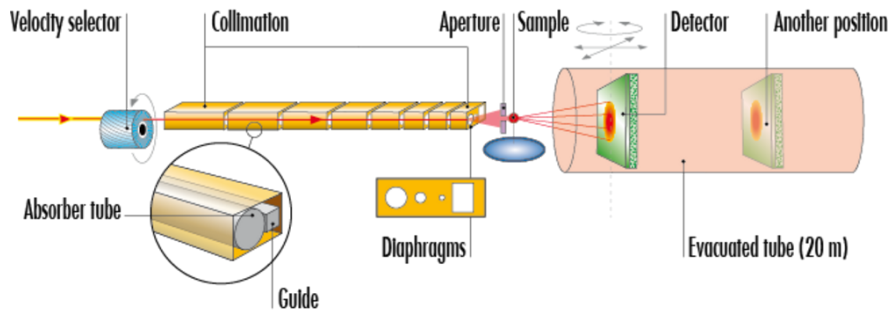


Figure 9: Schematic overview of the D22 beamline at ILL (www.i11.eu/users/instruments/instruments-list/d22, accessed June 22, 2022). The position of the detector can be changed and determines the accessible angular range. In 2021, D22 was equipped with an additional out-of-center detector close to the sample. This gives the possibility to probe high and low angles at once.

Data Modelling

To describe SAS data, first we need to mathematically model the SLD profile of a lipid vesicle. For example, it is possible to think of it as a spherical shell with several layers of different SLDs and a core with water. Each layer needs a thickness and SLD as parameter, then this profile can be Fourier-transformed and fitted to the data [23]. Such models are quick to implement and widely used, however with increasing data quality and the combination of SAXS and SANS, the use of volume probability based models (see sec.1.2) became possible and advantageous.

In 2008 the scattering density profile (SDP) model was introduced. It defines a lipid unit cell with the cross-sectional area A which is then "filled" with the lipid. The chain-region of the bilayer using an error-function and all other parts of the lipid by Gaussians (see Fig. 4). These functions can however not be Fourier-transformed analytically if defined on a sphere [23]. In the past, therefore a flat bilayer was assumed, which sufficiently describes the scattering in the high- q region (0.03 to 0.6 \AA^{-1}). In this approach, the Lorenz-factor q^{-2} has to be included to model the spherical nature of the object. Instead, it is however possible to separately model the sphere and the flat membrane and use the product of both to describe the data (Method of separated form factors [24]). This method is valid if the scattering signals of both membrane and vesicle are sufficiently far apart in q , which is the case for 100 nm vesicles.

The Fourier-transform of the volume probability function of each molecular group i is then normalized by its volume divided by area per lipid V_i/A , which corresponds to its "height" in the unit cell, and its contrast $\Delta\rho$. The error function for the CH_2 groups a priori fills the whole unit cell, reaches from $-D_C$ to D_C and is normalized to 1. $\Delta\rho$ is calculated regarding the solvent w in case of the head group parts $\Delta\rho_i = \rho_i - \rho_w$ and with respect to CH_2 for the chain segments CH and CH_3 , $\Delta\rho_i = \rho_i - \rho_{\text{CH}_2}$. This corresponds to the subtraction of these groups from the CH_2 function. To obtain the total form factor, all of these Fourier transforms are summed.

In case of a symmetric membrane it is sufficient to construct one leaflet this way, as the real part of the Fourier transform is symmetric with respect to the origin and the imaginary part cancels. To include asymmetry, both leaflets have to be modeled and the central error function is separated in two. Also, imaginary parts do not cancel and have to be included [7].

In the course of this thesis, several modifications to these models have been done, which are discussed in section 3.1. The detailed mathematical expressions for the form factors can be found in the attached publications [25, 26].

Joint Analysis of SAXS and SANS

As can be seen in Fig. 10, the distinct features visible in SAXS and SANS are not the same. While for X-rays, the head groups and the terminal CH_3 are highly visible, for SANS this depends very much on the used solvent and lipid deuteration. This encourages to combine these two methods to increase the information output and the constraints to put on complex models like the SDP-model. In fact, this model is very appropriate for this purpose, as the trans-bilayer structure only has to be built once using probability functions and can then be multiplied by the respective SLDs for each contrast. Fig. 11 shows a schematic of how different combinations look to X-rays and neutrons and the corresponding scattering patterns.

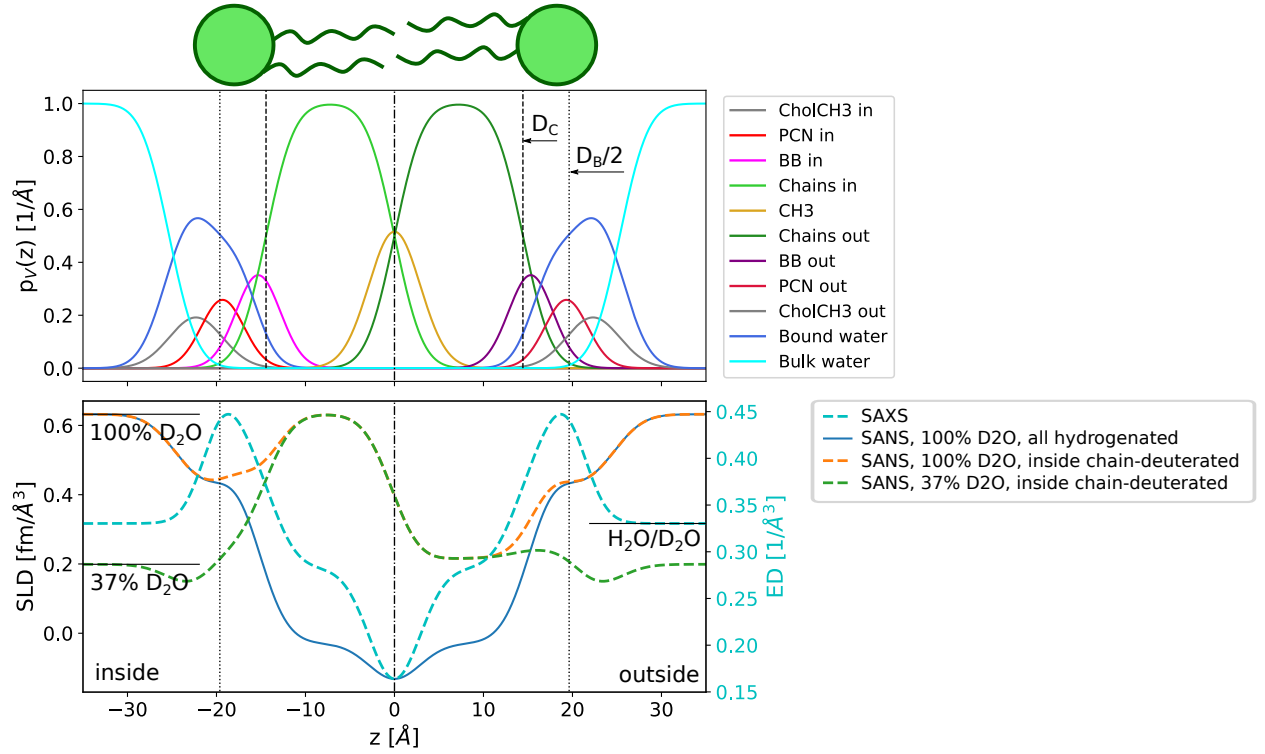


Figure 10: Example for a trans-membrane profile described by the SDP-model and the resulting SLD profiles for X-rays and neutrons different deuteration arrangements. SAXS is insensitive to isotopes, therefore only has one possible electron density (ED) profile. For SANS, 3 possible arrangements are shown: A symmetric, hydrogenated membrane in 100 % D₂O (blue), in which the chain-region has a high contrast with respect to the solvent. An asymmetric membrane with a 90 % chain-deuterated lipids inside and 30 % outside (reasonable distribution achieved by cyclodextrin exchange). In this case, in 100 % D₂O the chain-region of the inner leaflet is matched by the solvent and the measurement is sensitive to the outer leaflet (orange). Vice-versa for 37 % D₂O, here the outer leaflet is invisible for neutrons (green).

Upon coupling several measurements to obtain a single result it is crucial how to weight the data with respect to each other. For fitting a model to a measurement it is common to define a cost function such as χ^2 . It is defined as the sum of the squared disagreement between data d and model m over all data points i , weighted by the experimental uncertainty of the data σ : $\chi^2 = \sum_i \frac{(d_i - m_i)^2}{\sigma_i^2}$. Now, to combine X-ray and neutron measurements it would be unreasonable to simply take the sum of both χ^2 as the total cost function, as SAXS (X) measurements usually yield a significantly higher number of data points and would therefore outweigh the SANS (N) data. To account for this, we weighted the neutron χ^2 by the number of points per measurement n , the covered q -range and the number of neutron measurements N_N :

$$\chi_{total}^2 = \chi_X^2 + \frac{n_X (q_N^{max} - q_N^{min})}{N_N n_N (q_X^{max} - q_X^{min})} \chi_N^2 \quad (3)$$

Another approach, which was conceptualized in this project but not implemented, would be to determine which value of α would make the parameters of interest most meaningful. The idea is to maximize a gradient $\nabla_{\vec{p}} \chi^2(\alpha)$, which measures the impact of a change in the parameters on the simulated scattering curve. Ideally the gradient should be calculated in the area of likely values for \vec{p} , so it would require an iterative approach. One could also restrict it to a change in the most important parameters ($\nabla_{\vec{p}_{priority}} \chi^2(\alpha)$). After determining the ideal value of α , one could start the parameter optimization using any algorithm.

The problem hereby might be the calculation of the gradient numerically, which seems to be a non-trivial issue itself, e.g. the choice of the appropriate step-sizes Δp_i .

Going one step further, one can think about seeing every single data point as a separate measurement

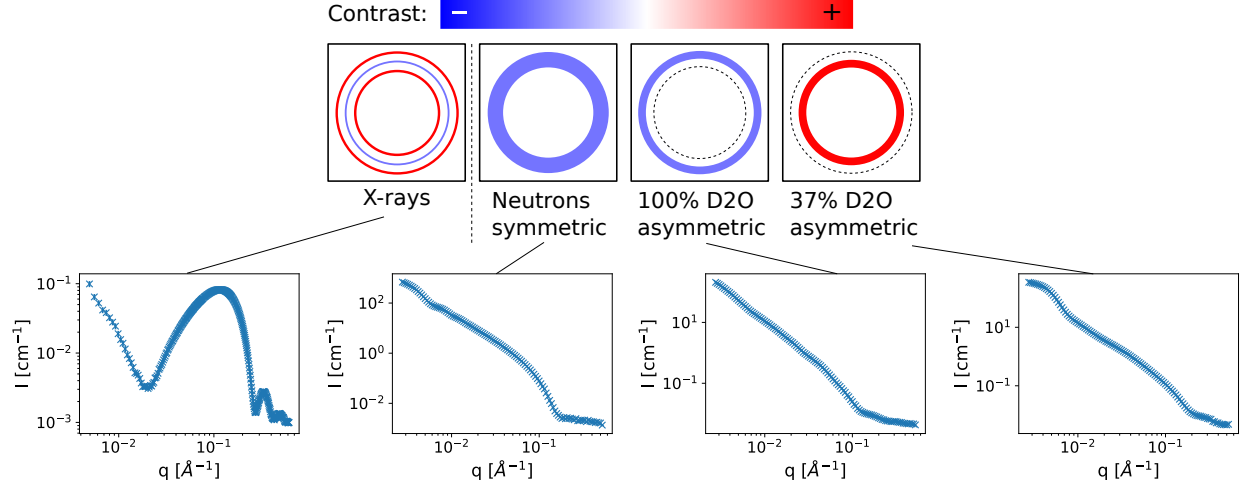


Figure 11: The figure shows schematics for the SLD-profiles drawn in fig. 10 and corresponding data from SAXS and SANS measurements. The oscillation in the low- q region is connected to the overall vesicle shape, the features at high- q to the trans-membrane profile.

Algorithm 1 Possible approach for determining α

Assign start value for α_1

repeat

$\alpha_0 \leftarrow \alpha_1$

$\vec{p}_{opt} \leftarrow \text{minimize } \chi^2(\vec{p}|\alpha_0)$

$\alpha_1 \leftarrow \text{maximize } \nabla_{\vec{p}} \chi^2(\alpha|\vec{p}_{opt})$

until $|\alpha_1 - \alpha_0| < \delta$

Start optimization (e.g. MCMC¹³) using α_1

which should be weighted in an appropriate way. This could be especially important for scattering experiments, as several orders of magnitude are contained in a single scattering curve and the areas where some parameters have any impact might be limited to a small range. In the case of lipid vesicles such an approach is additionally supported by the fact that in the high- q range, where the information about the bilayer characteristics is contained, the signal-to-noise ratio is significantly lower than in the lower q . To give more weight to these regions one could introduce additional parameters to rescale the errors by an appropriate function (which will weight χ^2 by the inverse square-root of this function). Ways to do this could be:

$$\sigma(q_i) \rightarrow e^{\beta(q_{max}-q_i)} \sigma(q_i), \quad (4)$$

which would mean to maintain the "true" error at the highest used q -point and decrease the weight more and more for lower q . One could also implement this by a linear function or a polynomial.

To stress a certain region of the data which is not cut off, one could also weight the data with a Gaussian or similar function, prioritizing the region around a value q_0 (at the cost of yet another parameter σ_q):

$$\sigma(q_i) \rightarrow e^{-\frac{(q_0-q_i)^2}{2\sigma_q^2}} \sigma(q_i), \quad (5)$$

This could be also implemented in the approach described above, making the maximization of $\nabla_{\vec{p}} \chi^2(\vec{\alpha}|\vec{p}_{opt})$ a multidimensional problem ($\vec{\alpha} = \begin{bmatrix} \alpha \\ \vec{\beta} \end{bmatrix}$; $\vec{\beta}$ including all parameters to describe the datapoint-weighting for all datasets).

2.3 Neutron Spin-echo Spectroscopy

Neutron spin-echo spectroscopy (NSE) is an inelastic neutron scattering (INS) technique and was developed in the 1970s at Institute Laue-Langevin (ILL), France, by Ferenc Mezei[27]. INS means that neutrons change

their energy upon scattering on quasi-particles or collective motions in the sample. Among the currently available INS techniques NSE probes the longest time-scales (up to 1000 ns at IN15, ILL), making it sensitive to fluctuations in large-scale soft matter systems such as lipid vesicles. Other characteristics of the technique are the high neutron flux as one can use a broad wavelength bandwidth $\Delta\lambda/\lambda$ (typically 15 %) and the direct access to the intermediate scattering function $S(\mathbf{q}, t)$ instead of the dynamic structure factor $S(\mathbf{q}, \omega)$ ¹⁴, which is accessible by other INS techniques.

The general idea of NSE is that polarized neutrons pass through two magnetic fields in a row, the second one exactly reverting the spin precession effect induced by the first. If a sample, placed between both fields, scatters inelastically, the neutrons will not return to their initial state, thus the energy exchange can be detected via the final neutron polarization. Fig. 12 shows the general setup of an NSE beamline.

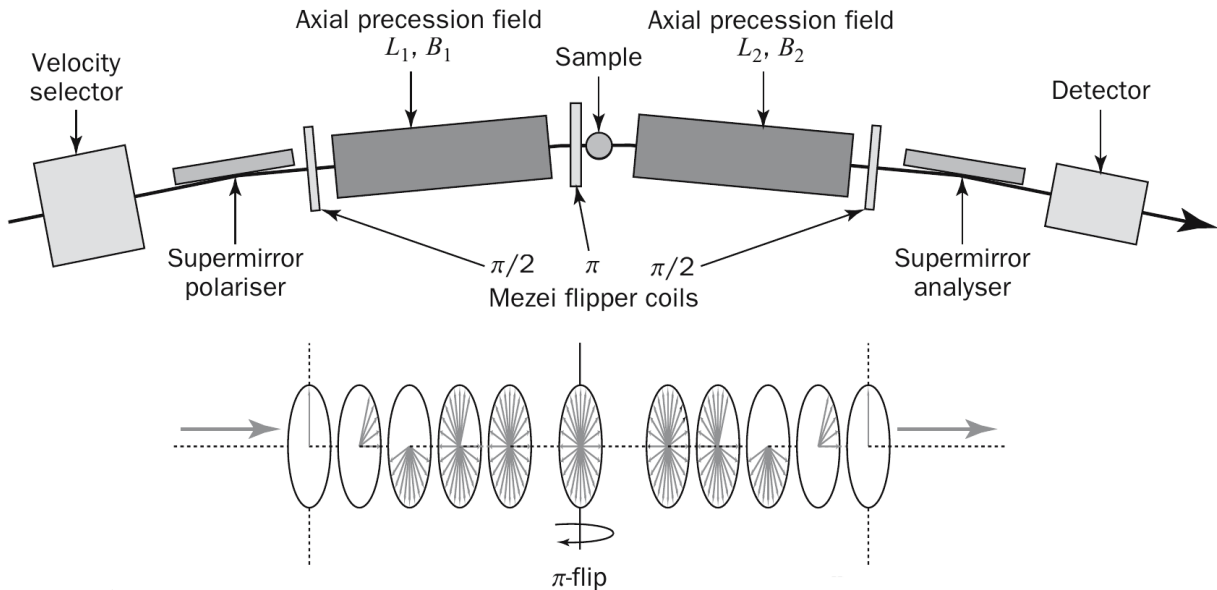


Figure 12: Experimental setup of NSE (figure from [28]). The lower graph shows the evolution of the spin polarizations of neutrons with different velocities between both $\frac{\pi}{2}$ -flippers in the case of elastic scattering.

The experiment is outlined in the following, a more detailed discussion can be found in textbooks e.g. by Mezei[29] or Hippert[28]. First, the desired wavelength band is selected from the incident neutron beam and neutron spins polarized in the direction of the beam. Then they are flipped by 90° ($\frac{\pi}{2}$) before entering the first precession field B_1 . As the Larmor precession frequency is equal for all neutrons, particles with different velocities v will have different polarization angles φ at the end of the coil ($\varphi_1 = \gamma_L B_1 L_1 / v$, γ_L being the Larmor constant and L_1 the path length trough the field). Before entering the sample, spins are flipped by 180° . This allows the second precession field B_2 to point in the same direction as the first (2 neighboring magnetic fields of opposite directions would lead to technical difficulties). The total precession angle after passing through both fields is now given by

$$\varphi_T = \varphi_1 - \varphi_2 = \frac{\gamma_L B_1 L_1}{v_1} - \frac{\gamma_L B_2 L_2}{v_2} \quad (6)$$

In case of elastic scattering ($v_1 = v_2$) and equal magnetic fields ($B_1 L_1 = B_2 L_2$) neutrons are therefore reverted to their initial state ($\varphi_T = 0$), independent of their velocity. After passing through both precession fields, neutron spins are again flipped in forward direction so that one can analyze the polarisation direction using another supermirror. If this analyzer is configured to the same angle as the polarizer (forward direction), all neutrons that scattered elastically on the sample, will arrive at the detector. If neutrons exchange energy, they arrive at the detector at a different precession angle. It can be shown that the angle is connected with a quantity t_f , named the Fourier time. Measuring the intensity in function of t_f and the momentum transfer

¹⁴Here, ω means change in wavelength, giving a direct measure of how much energy was exchanged in the INS process. It can be obtained by measuring the energy of scattered neutrons using time-of-flight techniques or crystals.

\mathbf{q} , one obtains the intermediate scattering function $S(\mathbf{q}, t)$, which is a time correlation function and sensitive to collective fluctuations within the sample in the ns range.

The Zilman-Granek Model

The interpretation of NSE data of membrane bending fluctuations is a somewhat controversial topic and the corresponding theory was re-adjusted several times and is most likely still not complete. In the following we give an overview of the evolution of the model.

To measure bending fluctuations of liposomes, large unilamellar vesicles with standard hydrogenated lipids in 100 % D₂O are generally used¹⁵. This way the membrane looks to neutrons like an almost flat, single-layered sheet. The most common theory to describe this experiment mathematically was developed by Zilman and Granek (ZG)[30]. It starts with the general expression for the intermediate scattering function, which is a correlation function of the time-dependent positions $R(t)$ of all scattering centers i, j :

$$S(\mathbf{q}, t) = \left\langle \sum_{i,j} e^{i\mathbf{q}[\mathbf{R}_i(t) - \mathbf{R}_j(0)]} \right\rangle \quad (7)$$

$R(t)$ is reparametrized using an in-plane, 2-dimensional component $\mathbf{r}(t)$ and a perpendicular component $z(t)$. For small undulations it is assumed that $\mathbf{r}(t)$ is constant over time and the deviations in flatness are described by the function $h(\mathbf{r}, t) = z(t)$. This leads to a correlation function in terms of $[h(\mathbf{r}, t) - h(\mathbf{r}', 0)]$, which is connect to the Helfrich bending Hamiltonian[31], introducing the bending rigidity κ :

$$H = \frac{1}{2} \kappa \int d^2r [\nabla^2 h(\mathbf{r})] \quad (8)$$

In the following, one arrives at a stretched exponential behavior for the orientation-averaged intermediate scattering function:

$$S_{ZG}(q, t) = S(q) e^{-(\Gamma_q t)^{2/3}}, \quad \Gamma_q = 0.025 \gamma \sqrt{\frac{k_B T}{\kappa} \frac{k_B T}{\eta}} q^3 \quad (9)$$

Here, γ is a function of $\frac{\kappa}{k_B T}$ and approaches 1 for $\frac{\kappa}{k_B T} \gg 1$, which is used throughout the literature. η is the solvent viscosity (Before 2010, several groups used a higher value, e.g. $3\eta_{D_2O}$ [32] to be in agreement with other experimental data, this was later revised, see below). Zilman and Granek [33] later expanded their theory, introducing a more general expression for the decay constant and stating that it might be slightly larger than 2/3. The value 2/3 has however been used to fit NSE-data ever since by a several research groups [34, 35, 36, 37, 38, 19].

Reinterpretation of κ

The necessity to rescale the solvent viscosity in order to quantitatively agree with other experiments led Watson and Brown [39] to include the effect of internal dissipation according to the theory by Seifert and Langer [40]. This led to a reinterpretation of the value of κ measured by NSE and is since then labeled the *effective* or *dynamic* bending modulus $\tilde{\kappa}$:

$$\tilde{\kappa} = \kappa + 2h^2 k_m \quad (10)$$

The additional parameters are the position of the monolayer neutral plane measured above the bilayer midplane h and the monolayer compressibility modulus k_m .

k_m (sometimes labeled K_A) is closely connected to the bending rigidity, as bending is just a combination of expansion and compression. Several models predict a connection with the *mechanical* bilayer thickness D in the following shape [41]:

$$\kappa = k_m d^2 / \alpha \quad (11)$$

The constant α is however dependent on the model, 12 if the bilayer is seen as a single uniform sheet, 48 if assuming two independent sheets free to slide past each other and 24 in case of a partially coupled polymer

¹⁵NSE measurements require long measurement times, which is why the highest possible contrast with the smallest possible contribution from incoherent scattering is used.

brush model proposed by Rawicz et al. [42]. They showed the d^2 -dependence using the thickness seen by X-ray scattering and arrived at the value $d = d_{PP} - 1$ nm, d_{PP} being the phosphate-phosphate distance. According to joint SAXS-SANS measurements this value agrees with a high precision with the hydrophobic thickness $2D_C$ [43], which is the usual value used in the NSE-community [34, 44, 37]. Inserting into eq. (10) one arrives at the following relation:

$$\tilde{\kappa} = \left[1 + 2\alpha \left(\frac{h}{2D_C} \right)^2 \right] \kappa \quad (12)$$

For the position of the neutral plane h there is currently no definitive measurement available, also it is also unclear where exactly the neutral plane is positioned. Lee et al. [34] estimated the value $\frac{h}{2D_C}$ to 0.605 by measuring $\tilde{\kappa}$ of DOPC by NSE and inserting $\kappa = 20k_B T$, which was obtained from diffuse X-ray scattering experiments [45]. The Nagao-group later used the value 0.5 (effectively meaning $h = D_C$) and established thereby the frequently used formula

$$\Gamma_q = 0.0069 \sqrt{\frac{k_B T}{\kappa}} \frac{k_B T}{\eta} q^3 \quad (13)$$

These values correspond to a ratio $\tilde{\kappa}/\kappa$ of 7 to 10, explaining also why assuming $3\eta_{D_2O}$ (which comes in squared relative to κ) worked to a good approximation.

Another possibility is to estimate h by the position of the glycerol or sphingosene backbone. Table 3 summarizes the corresponding values for several lipids obtained by SAS analysis on LUVs, which all lie between the values suggested by Nagao and Lee.

Table 3: Measured values of the ratio between backbone position h_{BB} and chain thickness D_C measured by SAXS and SANS. κ are the corresponding values for the bending rigidity evaluated with equations (9) and (10).

Lipid system	$h_{BB}/(2D_C)$	κ [$k_B T$]
DPPC/DPPG 19:1	0.53	12.0 ± 0.4
POPC/POPG 19:1	0.53	8.9 ± 0.3
POPE/POPG 9:1	0.54	8.5 ± 0.3
POPE/POPS 7:3	0.59	7.8 ± 0.5
MSM/DPPG 19:1	0.56	22.4 ± 0.9
ESM/DPPG 19:1	0.60	16.5 ± 0.8

Contributions from Vesicle Diffusion

Using the ZG-model it is possible to accurately describe the stretched exponential decay in the data, however, the resulting values for Γ_q only follow the predicted q^3 dependence for high q and deviate more and more for decreasing q -values (Fig. 13a,b). It is thought that for lower q , the diffusion of the overall vesicle contributes to the decay, for which several models have been proposed [46]. The simple approach $S(q, t) \propto S_{diff}(q, t)S_{ZG}(q, t)$ definitely improves the fit, but scales κ to unreasonably high values (Fig. 13c,d; also [37]). Other models suggest a scaling of the diffusion term with regard to the ZG model, but this introduces another q -dependent parameter, which leads to an overparametrization of the model.

Gupta et al.[47] took a closer look on the Fourier-timescale and suggested that the ZG-model is only valid in a certain range. Outside of it, the $S(q, t)$ does not follow the assumed $t^{2/3}$ -decay due to diffusion and non-Gaussian motions. To verify this, they plot the mean square displacement $\langle \Delta r(t)^2 \rangle$ over Fourier time t , which corresponds within the used Gaussian approximation to the exponent of the intermediate scattering function, normalized by q^2 :

$$\frac{S(q, t)}{S(q)} = \exp \left[-\frac{q^2 \langle \Delta r(t)^2 \rangle}{6} \right] \quad (14)$$

The ZG-model is then used in the region where $\langle \Delta r(t)^2 \rangle$ has a $t^{2/3}$ dependence, thereby excluding contributions from diffusion and other motions not connected to bending fluctuations.

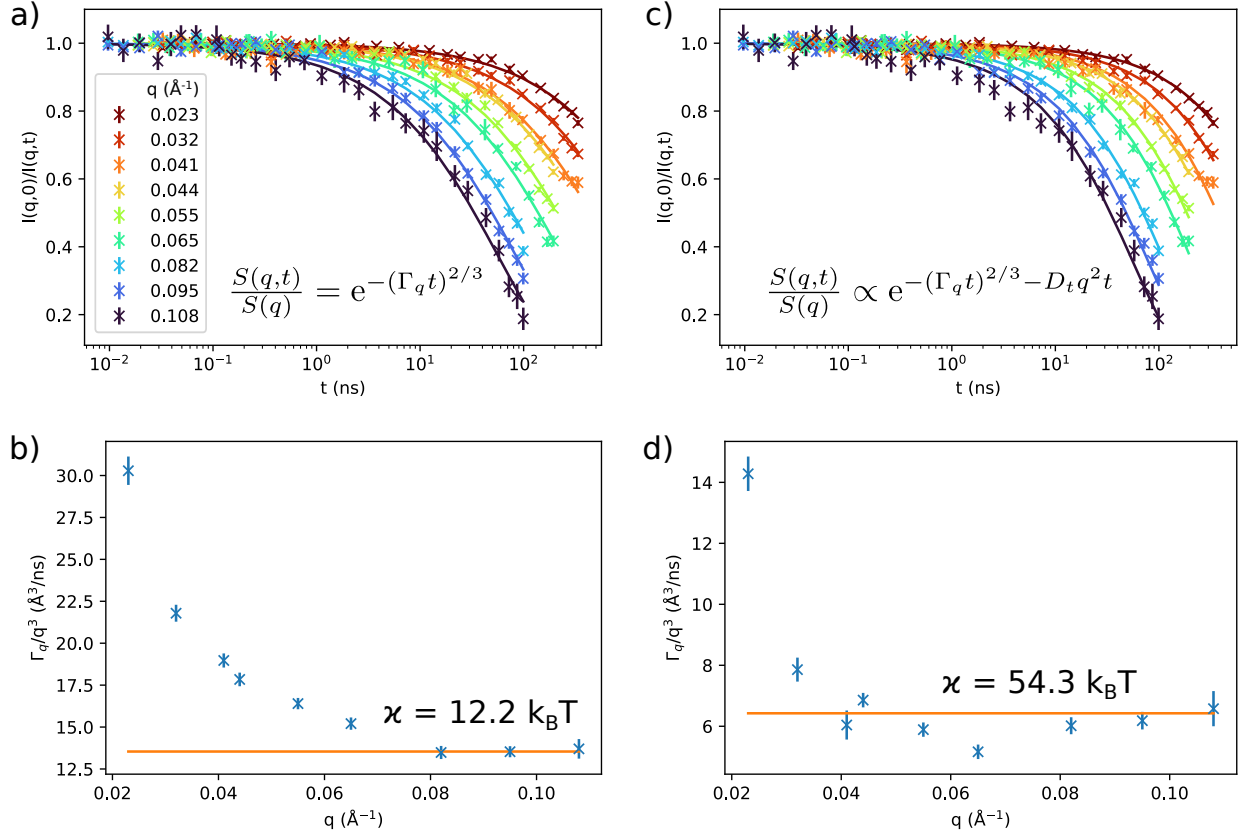


Figure 13: The graphic shows the comparison of 2 models used to evaluate NSE-data of DPPC-vesicles at 50 °C: (I) the pure Zilman-Granek (ZG) model (a,b) and (II) the ZG model with a contribution from diffusion (c,d), using a translational diffusion constant $D_t = 0.66 \text{ \AA}^2/\text{ns}$, measured by dynamic light scattering. The formulas to fit data are given in (a) and (c). Both models are in reasonable agreement with the raw data, however using model (I), the resulting values for the q -dependent decay constant Γ_q (b) do not follow q^3 as predicted by the ZG-theory. Model (II) improves the agreement over a wider q -range (d), but still deviates at low q . The given values for the bending rigidity κ in (b) and (d) correspond to the orange lines.

2.4 Dynamic Light Scattering

Similar to NSE, dynamic light scattering (DLS) is a scattering technique, which probes the dynamics in the sample by measuring a time correlation function. Its principle is however simpler: The sample is irradiated with visible light and the intensity of scattered photons are recorded at a certain angle with a high temporal resolution. From these, seemingly noisy data, the intensity-time correlation function $G_2 = \langle I(0)I(t) \rangle$ is calculated. For particles of the size of lipid vesicles and the used wavelength, the probed dynamics is particle diffusion. Therefore, the model used to describe the correlation function is again

$$G_2 \propto e^{-2Dq^2t} \quad (15)$$

Faster movement of the particles therefore leads to a earlier decay of the function. From the diffusion coefficient D , the hydrodynamic radius can be calculated using the Einstein-Stokes equation:

$$R_h = \frac{k_B T}{6\pi\eta_0 D} \quad (16)$$

Here, η_0 is the viscosity of the solvent. In case of polydisperse particles, a cumulant approach can be used, which introduces a polydispersity index and changes the slope of the correlation function [48]. In this case, the average hydrodynamic radius can be determined. If there is several populations of very differently sized particles present in the sample, the resulting G_2 is an overlay of exponential decays from each population.

In this case, the average radius and polydispersity from each population can be determined. For this work, a Malvern Zetasizer device was used. It is a fully automated device to measure particle sizes, using a wavelength of 632.8 nm and a scattering angle of 90°. Fig. 14 shows an exemplary correlation function and particle size distribution from lipid vesicles. DLS was used in this project to screen the vesicle size after extrusion and in the production of aLUVs to check if all multilamellar vesicles have been removed after the the separation spin.

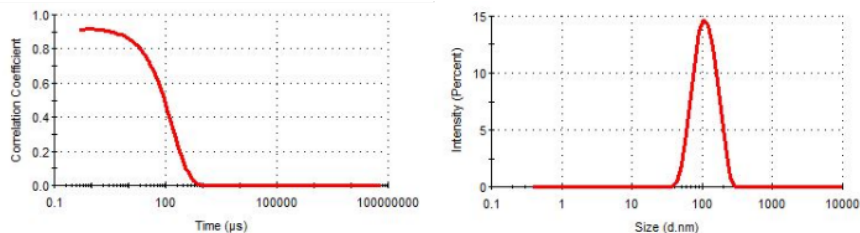


Figure 14: DLS data from extruded lipid vesicles. The left panel shows the correlation function, the right one the resulting particle distribution, automatically evaluated by the software of the Malvern Zetasizer.

2.5 Chromatography Techniques

Chromatography comprises a series of techniques used to analyze chemical compositions and in some cases to separate or purify chemicals. The common principle is that all components of a mixture pass through a carrier medium and either arrive at the other end at different times or, in the case of thin layer chromatography (TLC), accumulate at different positions. We used gas chromatography (GC) and high performance TLC to analyze the composition of asymmetric vesicles after exchange.

With GC it is possible to analyze the chain composition of the lipid sample by producing fatty acid methyl esters (FAMES). This is done by incubating them for 1 h in a 2.5 vol% methanolic H_2SO_4 solution at 95 °C. To retrieve the FAMES, the solution is mixed with hexane and H_2O , upon which they accumulate in the hexane phase. After extraction of the FAMES in hexane, they can be injected into the GC-column. The column is a long tube arranged as a coil in the instrument. Through this coil flows an inert carrier gas, which is heated above 150 °C during the experiment. After injection the sample flows through this column and is detected on the other end after being ionized in a flame. From the retention time in the column, the type of fatty acid can be determined. The detailed protocol for this method is described elsewhere [49].

In TLC, intact lipids can be measured. They are dispersed in organic solvent (e.g. Chloroform/Methanol) and placed on a TLC plate. After evaporation of this solvent, the plate is placed vertically and immersed in a different solvent at the bottom (the mobile phase). This solvent runs up the plate by capillary action, carries the sample with it and drops different compounds at different positions. According to the sample certain chemicals are used to develop plate and visualize the accumulations of compounds under UV light. To quantify the lipid concentrations, the plate is scanned and the accumulations of molecules analyzed digitally.

2.6 Nuclear Magnetic Resonance Spectroscopy

In nuclear magnetic resonance (NMR) spectroscopy is a technique heavily used in chemistry, as it is able to probe the chemical environment of molecules. It uses a strong constant magnetic field, which aligns the nuclear spins in the sample, which start performing a precession movement at a certain resonance frequency along the axis of the field. This alignment is then perturbed by a short pulse of a weaker oscillating field. After the pulse the nuclear spins relax into the original position, emitting electromagnetic in the course. The frequency of this signal is dependent on the chemical environment of the atom. For example, in ^1H -NMR the signal of a H-atom in the acyl chains is different from one in the head group. Data is recorded in dependence of the relative shift in frequency, which the chemical environment imposes on the atom compared to an unshielded atom. This effect is exploited to measure the asymmetry of aLUVs containing choline-lipids. On the tip of these lipids there are 9 chemically identical H-atoms, which give a single signal at a certain frequency. Before the measurement, a paramagnetic salt (Pr^{3+}) is added to the solution, which temporarily binds to the head groups, but does not penetrate the bilayer. This causes a chemical shift of the H-atoms in the cholines of the outer leaflet, while the inner leaflet cholines stay at their original position (Fig. 15). By

the difference in area under the resulting peaks, the amount of choline lipids in inner and outer leaflet can be determined [50].

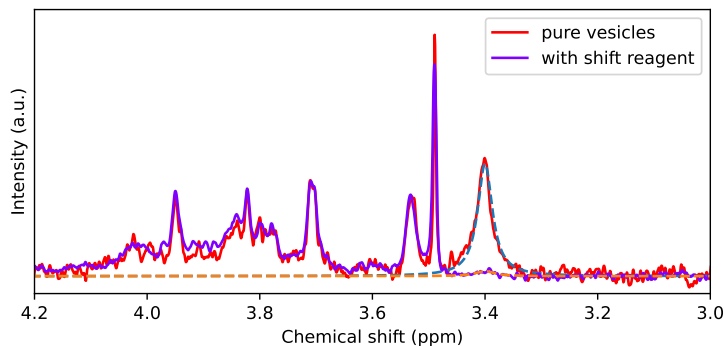


Figure 15: The graph shows a part of the NMR spectrum of asymmetric vesicles before and after adding Pr^{3+} . While the majority of the choline peak is moved from its original position (3.4 ppm), the rest of the spectrum is unaffected. Dotted lines mark Lorentzians used to fit the peaks and to calculate the underlying areas.

2.7 Differential Scanning Calorimetry

Differential scanning calorimetry (DSC) is a technique to probe the phase behavior of a substance. For liquid samples in solution like vesicles, the sample is filled in a container or capillary, which is then heated or cooled simultaneously with another container filled only with the solvent. During the measurement, the energy required to heat (or the heat released in case of cooling) by the sample is recorded and compared with the one of the solvent. If the sample goes through a phase transition, the additional heat required for melting (or released for condensing) creates a peak in the heat rate (Fig. 16). This way, phase transition temperatures can be measured. The method can be also used to measure the asymmetry of aLUVs and to test their stability over time. It is however restricted to lipids with T_m clearly above 0 °C and sufficiently different from the lipids in the other leaflet.

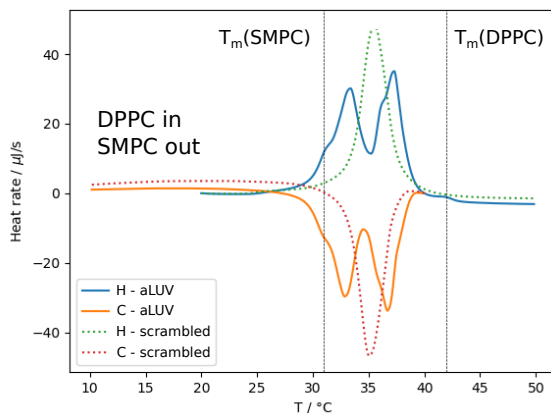


Figure 16: DSC heat (H) and cooling (C) scans of an asymmetric bilayer system and the corresponding scrambled sample. The aLUV shows two distinct phase transitions for the individual leaflets. In the scrambled vesicle the lipids are mixed and have a single transition between the two leaflets. Dotted lines mark the phase transitions of the pure acceptor and donor lipids.

2.8 Determination of Phospholipid Concentration by Organic Digestion to Inorganic Phosphate

The following protocol was used to determine the phospholipid concentration of standard solutions used to accurately measure concentration series in GC. The phosphate assay is based on the hydrolysis of phospholipids into orthophosphate by incubation with concentrated sulfuric acid (H_2O_2), followed by oxidation using hydrogen peroxide and spectrophotometric quantification of inorganic phosphate after reaction with ammonium molybdate and ascorbic acid in a boiling water bath. The foundations of the assay were laid in the early 20th century [51, 52] and have been further developed continuously [53, 54]. A variation of the assay is to use perchloric acid instead of H_2O_2 [55], which is however discouraged due to its explosive hazard [56] as well as possible interference in the reduction process [57]. Possible alternatives include the Stewart assay [58] and $^1\text{H-NMR}$ [59].

Equipment:

- Heating block (200 °C) inside a fumehood
- Boiling water bath
- 7 ml glass vials with caps

Chemicals:

- Ultrapure H_2O
- Hydrochloric acid (HCl) solution [37 % w/w]
- Concentrated Sulfuric acid [$> 95\%$]
- Hydrogen peroxide (H_2O_2) [30%]
- Ammonium Molybdate (IV) tetrahydrate ($(\text{NH}_4)_6\text{Mo}_7\text{O}_{24}\cdot 4\text{H}_2\text{O}$)
- Ascorbic acid ($\text{C}_6\text{H}_8\text{O}_6$)
- Potassium dihydrogen phosphate (KH_2PO_4)

Preparation of Reagents

- 8.9N H_2SO_4 solution (100 ml)
 1. Fill a glass flask with about 25 ml of H_2O and slowly add 25 ml of concentrated H_2SO_4 .
 2. Ensure heat can dissipate from the container.
 3. Dilute with H_2O to a total of 100 ml and mix by gentle shaking.
 4. Store at room temperature in a sealed container.
- 0.05 N HCl solution (1000 ml)
 1. Fill a glass flask with about 250 ml of H_2O and slowly add 4.1 ml of the HCl stock solution.
 2. Dilute with H_2O to a total of 1000 ml and mix by gentle shaking.
 3. Store at room temperature in a screw-cap bottle for up to 1 year.
- 0.1 N HCl solution (500 ml)
 1. Fill a glass flask with about 125 ml of H_2O and slowly add 4.1 ml of the HCl stock solution.
 2. Dilute with H_2O to a total of 500 ml and mix by gentle shaking.
 3. Store at room temperature in a screw-cap bottle for up to 1 year.
- 0.65 mM Phosphate standard solution (50 ml)
 1. Weigh 4.42 mg KH_2PO_4 and transfer to a beaker.
 2. Add 25 ml 0.05 N HCl solution and mix the solution well.
 3. Dilute to 100 ml with 0.05 N HCl solution.

4. Store at 4 °C screw-cap bottle for up to 1 month.
- 10 % w/w Ascorbic acid solution (25 ml)
 1. Cover a falcon tube with aluminum foil or use any opaque container.
 2. Weigh 2.5 g ascorbic acid and transfer to the container.
 3. Add 20 ml H₂O and mix the solution well.
 4. Dilute to 25 ml with H₂O.
 - 2.5 % w/w Ammonium Molybdate (IV) tetrahydrate solution (25 ml)
 1. Cover a falcon tube with aluminum foil or use any opaque container.
 2. Weigh 0.625 g Ammonium Molybdate (IV) tetrahydrate and transfer to the container.
 3. Add 20 ml H₂O and mix the solution well.
 4. Dilute to 25 ml with H₂O.

Procedure

1. Clean the glass vials by incubating with 0.1 N HCl solution for 1 h, then rinse with H₂O.
2. Preparation of standards
Fill glass vials with the quantities of phosphate standard solution (Pi) and 0.05 N HCl solution as indicated in table 4.

Table 4: Phosphate standard concentrations for a standard curve and corresponding lipid mass in the case of POPC (760 g/mol).

No.	Phosphate [μ mol]	Pi [μ l]	0.05 N HCl [μ l]	POPC [μ g]
0	0.0000	0	2000	0
1	0.0325	50	1950	25
2	0.0650	100	1900	49
3	0.1138	175	1825	86
4	0.1625	250	1750	124
5	0.2275	350	1650	173
6	0.3250	500	1500	247
7	0.4875	750	1250	371
8	0.6500	1000	1000	494
9	0.9750	1500	500	741
10	1.3000	2000	0	988

3. Preparation of samples
Estimate the concentration of your samples and determine the amount corresponding to the center of your standard curve. Fill samples into glass vials and fill with 0.05 N HCl solution to a total volume of 2000 μ l. If the samples are dispersed in organic solvent, first evaporate all solvent under a soft N₂ beam.
4. Place all tubes without caps in the heating block and leave at 200 °C for 30 min or until all liquid is evaporated.
5. Add 0.45 ml H₂SO₄ solution to each of the standards and samples. Leave them at 200 °C for another 60 min. Remove the vials from the heater and allow them to cool for 5 min.
6. Add 150 μ l H₂O₂ to each vial and continue heating to 200 °C for 30 min. At this point the samples should be colorless. If any brown color persists, add 50 μ l H₂O₂ and heat for another 15 min.
7. Cool the vials to ambient temperature and prepare 10 % w/w ascorbic acid and 2.5 % w/w ammonium molybdate (IV) tetrahydrate solutions.

8. Add 3.9 ml H₂O to each vial.
9. Add 0.5 ml ascorbic acid solution and 0.5 ml ammonium molybdate (IV) tetrahydrate solution to each vial, close them with lids and vortex vigorously. After this point, the vials should not be exposed to direct light.
10. Heat all vials to 100 °C in boiling water bath for 7 min, then let them cool to room temperature.
11. Spectrometric analysis
Zero the spectrometer using the blank standard (0). Determine the absorbance at 820 nm wavelength of all standards and samples.
12. Generate a calibration curve using a linear regression through the standards and determine the amount of phosphate in the samples.

3 Results and Discussion

3.1 Advances in the SDP-Model

The SDP model proved as a versatile tool to describe high- q SAS-data from both symmetric and asymmetric vesicles. Upon extending the model to lower q , using the separated form factor method, the model did not agree with measurements. Also the minima in SAXS measurements were not always correctly fitted, especially for saturated PC [43]. The following modifications were performed, to address these shortcomings.

High-Density Hydration Layer

In SAXS-data of most lipids we found a minimum around $q = 0.02 \text{ \AA}^{-1}$. This is already outside of the previously studied range, which applied the SDP-model on single lipid liposomes [43]. With the parameters given in the publication, the model predicts this minimum however at a lower q -value (Fig. 17a). To correctly fit this minimum, it was necessary to slightly change the head group volume V_H from the given value (322 \AA^3 compared to previously 331 \AA^3), while leaving the hydrocarbon chain volume unchanged. This decrease in volume leads to an increase in SLD in the head group region, which can however also be interpreted in a different way. In the evaluation of SAS-data of proteins it is common to include a layer of water molecules around the protein, which are more ordered and therefore denser [60]. We included another layer of this kind in the SDP model (Fig. 17b) and found that it can fit the data equally well. In fact it is mathematically almost indistinguishable from changing V_H , leading to a sharp linear correlation between V_H and the volume per water molecule in the hydration shell (Fig. 17c). Curiously, a decrease in water volume around the head group was also found in MD-simulations, which were performed by collaborator Milka Doktorova to complement these measurements. This measurement questions however the density measurement, which yielded the total lipid volume in the first place [61], as that method is equally sensitive to a denser hydration layer would yield a different result for the density instead.

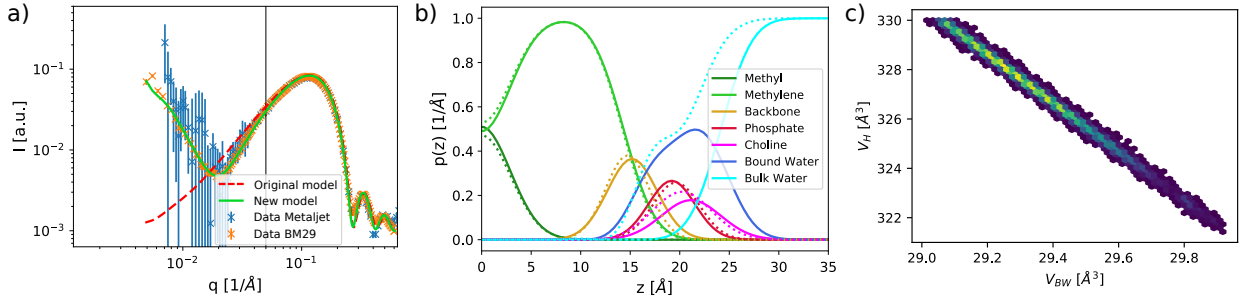


Figure 17: a) Comparison of the present and original SDP-models for SAXS-measurements of DPPC at 50 C. b) shows the volume probability distributions $p(z)$ of the lipid moieties through the bilayer profile, including a higher density hydration shell. c) Parameter correlation between the headgroup volume V_H and the volume per water molecule in the hydration shell V_{BW} , obtained by Markov chain Monte Carlo [62]. Figure adapted from the attached publication [25].

Thickness Polydispersity of Membranes

The second change in the model addresses the lift-off of the minima in SAXS from the incoherent background. These are not covered by the old model, in which the minima reach down to the incoherent background. A way to "smear out" these minima is by including a thickness polydispersity of the membrane, meaning that the total intensity coming from the membrane is a sum of several membranes of varying thicknesses, weighted by a distribution (Fig. 18). This is implemented by varying the chain-thickness D_C of the membrane by a Gaussian distribution \mathcal{N} with mean value \bar{D}_C and standard deviation σ_{Poly} :

$$I \propto \sum_i \mathcal{N}(D_{C,i} | \bar{D}_C, \sigma_{Poly}) |F(q; D_{C,i})|^2 \quad (17)$$

This procedure notably has not the same effect as smearing out the SLD-profile by using error functions or Gaussians instead of abrupt slabs, which solely adds a factor of $\exp(-\sigma^2 q^2)$ and therefore leads to a faster

decay at high q (Fig. 18). The physical origin of this polydispersity is not entirely clear. It could be likewise caused by sample inhomogeneity as well as as thickness fluctuations [63]. This could be systematically studied by temperature series or comparison with thickness fluctuation data from NSE [44].

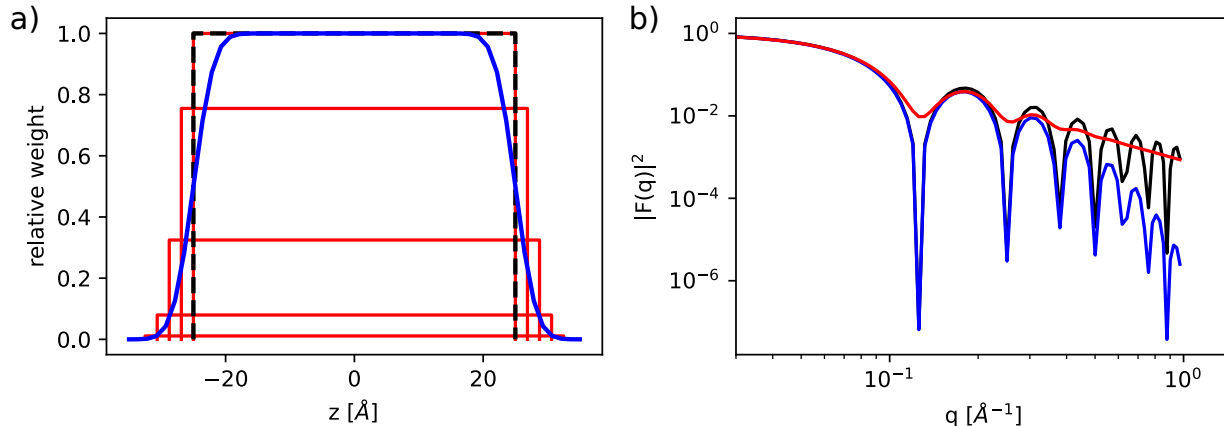


Figure 18: Three different ways to model a slab for SAS-analysis in real space (a) and as scattering form factor (b). In black the original, abrupt slab of 50 Å. In blue it is modeled by error functions with $\sigma = 2.5$ Å, resulting in a faster decay of the form factor. In red the polydisperse ensemble of different slabs, which lead to smeared out minima in the form factor (In (a) only the ones larger than the average slab are shown for clarity, also the smaller ones are included in the calculation of $|F(q)|^2$).

Asymmetric Model

The asymmetric SDP-model has been introduced before [7] and was only slightly modified, notably in the region of the terminal methyl groups. While the old model used slabs created with trigonometric functions, which contained a sharp transition between the leaflets, the new model use error functions, providing a smooth interface at the bilayer midplane. The terminal methyls are modeled using a single Gaussian, which is allowed to move away from the bilayer center. Such a shift can either mean interdigitation or back-bending of chains into one of the leaflets. The full mathematical model as well as concerns about volume balance between the leaflets are detailed in the attached publication [26].

Bilayer asymmetry is another way to model the lift-off of minima in the scattering pattern, which has first been used to detect curvature effects in small unilamellar vesicles [64]. This effect can be observed both in SAXS and SANS, as shown in Fig. 19. The origin is however different. In SAXS, it arises from differences in headgroup structure between inner and outer leaflet, from a differently thick leaflets or from a shift of the methyl distribution out of the center. In SANS, this effect is only detectable if deuterated lipids are used in either of the leaflets. In both cases, the effect is caused by the imaginary term of the form factor, as shown in Fig. 19.

In SAXS, this effect does not cause a change in the overall shape in the scattering pattern. Also, modeling the lift-off in this way can not replace the model features introduced in the former two sections. Indeed, asymmetric lipids frequently show a higher lift-off than symmetric ones, which was used to detect hydrocarbon chain interdigitation in asymmetric bilayers (see sec. 3.2). In SANS, the imaginary part produces a distinct feature, which can be used to measure asymmetry and – if monitored over time – to visualize and quantify lipid flip-flop [49, 26]

3.2 Interdigitation of Chain-Asymmetric Lipids

A large part of phospholipids have two equally or similarly long chains. There is however a fraction with differences in chain length, particularly sphingomyelins can have long saturated acyl chains. Such long chains are thought to penetrate into the opposing leaflet (interdigitation), possibly influencing the structure and enhancing internal friction between the leaflets [16, 65]. If lipids really interdigitate, and are not simply repulsed by the constant movement of the chains in the opposing leaflet, is however debated [66, 67]. In this

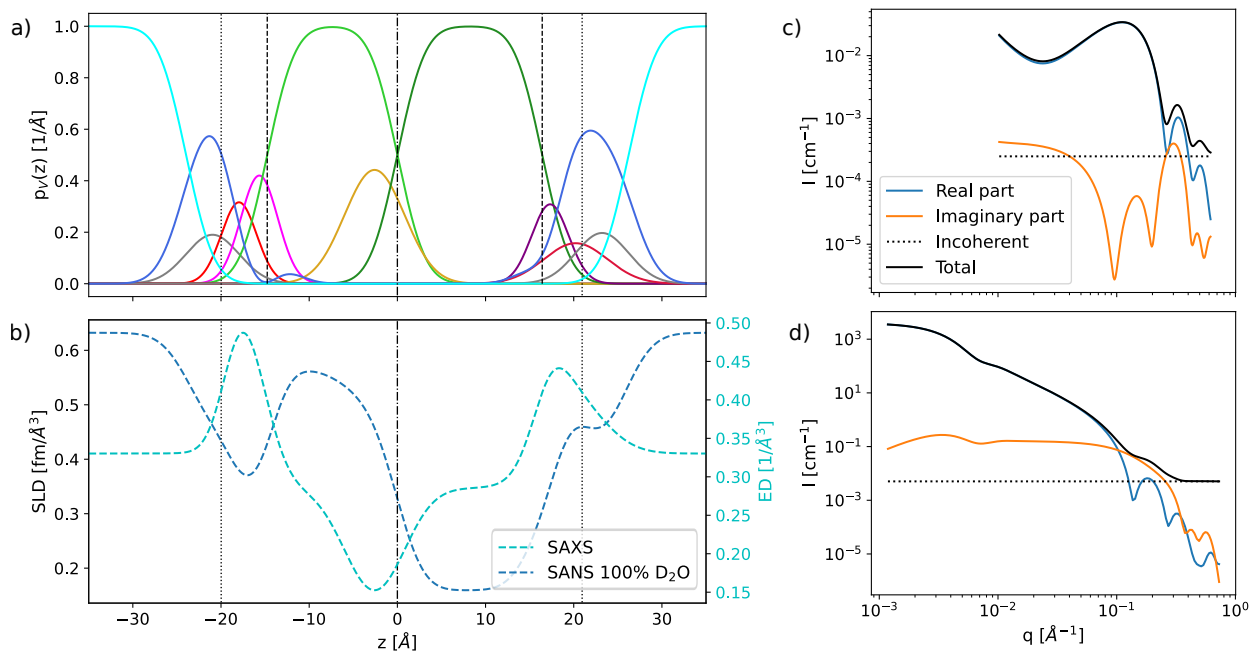


Figure 19: The figure shows the model fit for the asymmetric system DPPCd62ⁱⁿMSM^{out} [26]. Differences between inner and outer leaflet in deuteration and head group structure, as well a shift of the methyl groups towards the inner leaflet (a) lead to an asymmetric SLD profile both for X-rays and neutrons. (c) and (d) respectively show the X-ray and neutron scattering intensities.

part of the project we tried to measure and quantify interdigitation of chain-asymmetric lipids in symmetric and asymmetric bilayers and study the effects on the trans-bilayer structure.

Single Lipid Bilayers

To study interdigitation in single lipid bilayers, we characterized the trans-membrane structures of choline lipids with different chain-compositions by SAS [25]. We start with the reference lipid DPPC (di16:0) and then compare the overall structure and the arrangement of the chains in the bilayer center to PC with more complex chain-structures including differently long chains and unsaturations, and eventually also the natural lipid extract milk sphingomyelin (MSM), which contains a large fraction of very long chains (22:0, 23:0, 24:0). All samples were measured at 50 °C, to ensure that all membranes are in the fluid phase.

It turned out that the chain-asymmetry, although having a large influence on the phase behavior (see melting transition temperature Tab. 1), did not significantly change the structure. This can be best seen from the comparison between DPPC, MSPC (14:0/18:0) and SMPC (18:0/14:0), all of them having 32 saturated carbons in different combinations. Their SANS-curves overlap and in SAXS the only difference can be found in the height of the third oscillation around 0.5 Å⁻¹ (see Fig. 20a). This difference is reflected in the model by the width of the distribution of the terminal methyl groups σ_{CH_3} . While it is unclear if the physical meaning of this is actually interdigitation – as it can also mean that the long chains bend back – it shows that SAXS is sensitive to the chain confirmation at the interface. Plotting σ_{CH_3} over the difference in chain length (calculated from structures of chain-symmetric lipids), we see a clear correlation between these two parameters. Furthermore, the difference between SMPC and MSPC shows that the sn-position of each chain is also important in this regard. The tilt in the glycerol backbone pushes the sn-1 chain further into the bilayer, which causes even nominally symmetric lipids as DPPC have a nonzero hydrocarbon chain overlap. For gel-phases this tilt in the backbone has been estimated in the past to correspond to between 1.2 and 1.5 CH₂ segments [68, 69], in the fluid phase we find that this value is reduced to about 0.5. In principle, it would have been possible for nature to avoid this tilt, by attaching the head group to the sn-2 position and the chains to the identical sn-1 and sn-3 positions. Exactly this would however be a problem for example in the production of chain-asymmetric lipid, as then the two chain positions could no longer be specifically targeted by enzymes etc.

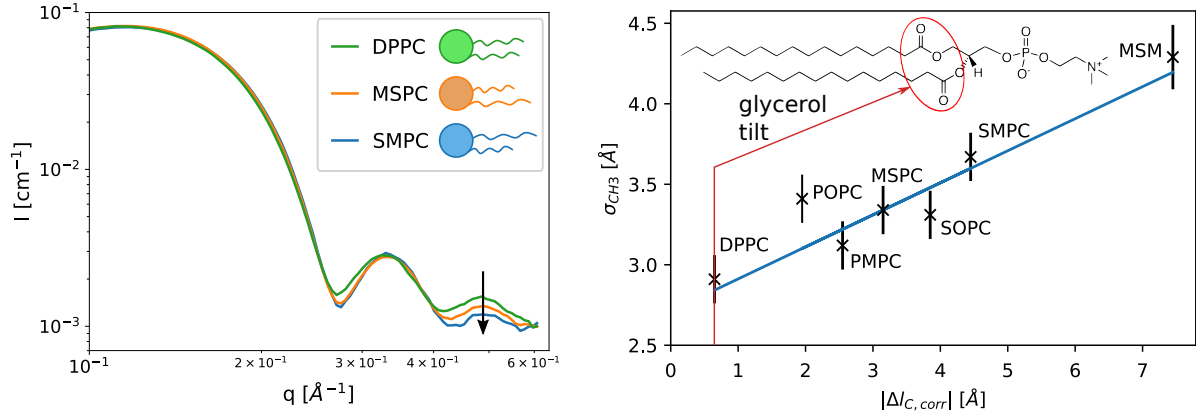


Figure 20: The left image shows the high- q region of SAXS-patterns for 3 different lipids with the same chemical composition, but different structures. The amplitude in the third oscillation decreases with increasing chain-asymmetry. In the right subfigure width of the CH_3 distribution in the SDP-model is plotted for several lipids over the length-difference between their chains, corrected by the tilt in the glycerol backbone. Figure adapted from [25].

Asymmetric Bilayers

Next, we produced asymmetric bilayers using chain-deuterated DPPC-d62 in the inner leaflet and the above mixed-chain lipids in the outer leaflet. The contrast in neutron-SLD between inner and outer chain-regions made it possible to measure the inner and outer chain- and monolayer thicknesses and thus also the packing densities. After determining the leaflet-specific compositions of the asymmetric vesicles via GC and SANS, we also produced symmetric reference vesicles matching the composition of either leaflet. Tab. 5 summarizes the fit-results obtained from combined SAXS/SANS measurements using SANS contrasts at 100 % and 37 % D_2O . Again, this study was conducted at 50 °C, well above T_M of all lipids. Details about the analysis and fits can be found in the attached publication [26].

Table 5: Summary of fit results for bilayer thicknesses D_B , monolayer thicknesses D_M , chain thicknesses D_C , areas per lipid A and shift of the methyl groups z_{CH_3} of asymmetric vesicles (columns A), produced with DPPCd62 as acceptor lipid and mixed-chain PCs or MSM as donors. Properties of inner/outer leaflet reference LUVs are given in the respective columns S. ϵ is the relative experimental uncertainty of the aLUV parameter values.

Donor	ϵ [%]	MSPC		SMPC		PMPC		MSM		POPC		SOPC	
		A	S	A	S	A	S	A	S	A	S	A	S
D_B [Å]	3	37.0	39.6	38.1	39.5	36.1	38.6	40.9	40.0	36.3	38.9	37.3	39.3
D_M^{in} [Å]	6	18.0	19.8	18.5	19.8	18.0	19.3	20.0	19.4	17.8	19.7	18.2	20.0
D_M^{out} [Å]	6	18.9	19.8	19.6	19.7	18.1	19.3	21.0	20.6	18.6	19.2	19.1	19.4
D_C^{in} [Å]	5	13.2	14.5	13.5	14.6	13.2	14.1	14.8	14.3	13.0	14.5	13.4	14.7
D_C^{out} [Å]	5	14.0	14.5	14.5	14.4	13.2	14.0	16.4	16.1	13.8	14.2	14.3	14.5
A^{in} [Å ²]	5	67.4	62.4	65.8	62.1	67.5	63.7	60.9	64.2	68.9	62.8	67.7	62.3
A^{out} [Å ²]	5	65.8	62.2	63.5	62.7	66.5	61.7	63.9	63.2	68.3	65.9	68.5	67.3
z_{CH_3} [Å]	10	-0.96		-0.95		-0.69		-2.59		1.00		-0.35	

A shift in of the terminal methyl groups z_{CH_3} towards the inner leaflet was found for all donor lipids, except POPC, and was most pronounced for MSM, followed by MSPC and SMPC. These results correlate well with the the interdigitation found in symmetric vesicles (Fig. 20) and suggest that the relatively high value for σ_{CH_3} for POPC comes either from backbending of the chains or from the propensity to accomodate

chains from the opposing leaflet. The long 18:0-chain of SOPC however seems to slightly interdigitate with DPPC.

Along with these results we found a change in structure induced by the asymmetric arrangement for all bilayers. For all PC-donors we found that the asymmetric membrane was thinner than the symmetric reference. This thinning was generally more pronounced in the inner leaflet, suggesting that the interdigitating chains induce disorder in the opposing leaflet, therefore increasing the A^{in} and thinning the leaflet. In the case of POPC and SOPC there could be an additional effect coming from the unsaturated chains, making these lipids intrinsically more disordered. In asymmetric vesicles there is therefore a significant difference in the chain-dynamics of both leaflets, which could also reflect in a change in structure.

MSM on the other side induced a thickening of the inner leaflet. In this case we assume that the long chains penetrate deep enough to experience significant van der Waals (vdW) attraction with the neighboring chains, leading to an ordering of the opposing leaflet. This effect demonstrates the delicate interplay between attractive vdW forces and repulsive steric interactions present in the hydrocarbon chain region of a bilayer.

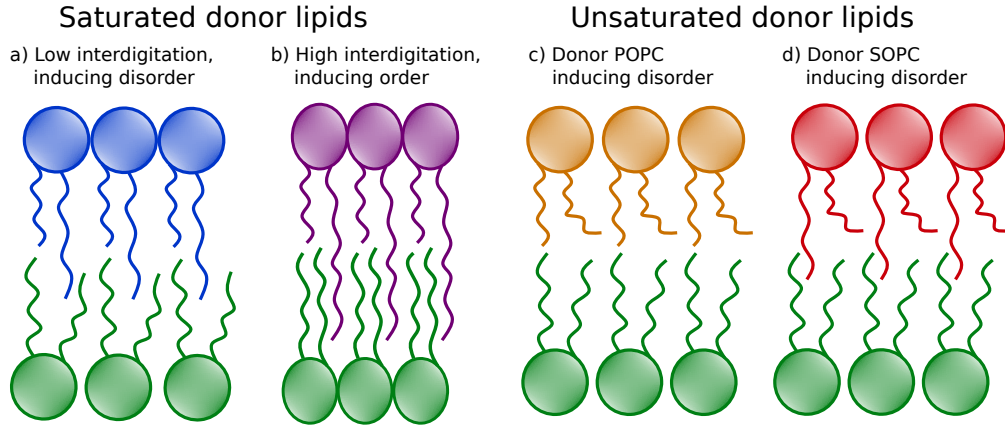


Figure 21: Schematic of possible lipid arrangements of interdigitated systems with saturated lipids of low (a) ($\text{DPPC}^{in}/\text{MSPC}^{out}$, $\text{DPPC}^{in}/\text{SMPC}^{out}$, $\text{DPPC}^{in}/\text{PMPC}^{out}$) and high (b) chainlength-mismatch ($\text{DPPC}^{in}/\text{MSM}^{out}$), as well as $\text{DPPC}^{in}/\text{POPC}^{out}$ (c) and $\text{DPPC}^{in}/\text{SOPC}^{out}$ (d).

3.3 Bending Fluctuations in Lipid-only Plasma Membrane Mimics

The last part of the project is about the influence of membrane asymmetry on collective fluctuations of the bilayer. We keep studying MSM as a potential trigger for interdigitation-induced bilayer coupling, but also introduce the negatively curved lipid POPE and the negatively charged POPS. Both these lipids are found in the inner leaflet of mammalian plasma membranes and are known to form hydrogen bond networks between the headgroups [70]. Using NSE, we measured bending rigidities κ of asymmetric systems of these lipids, gradually increasing complexity and similarity with the lipid composition of the plasma membrane. As references, we used scrambled vesicles, where the asymmetry was artificially destroyed by evaporating the solvent, rehydrating and extruding. We also measured symmetric inner/outer leaflet mimics as in the earlier chapter. The NSE data was analyzed by the method of Gupta (Sec. 2.3, Fig. 22). The values for pure lipids agree with some former measurements [50], however there is several methods to measure κ of bilayers and they do not generally agree. Therefore, absolute values given here are to be taken with care, looking mainly at the relative differences between the samples. We also measured SAXS and SANS with these vesicles, however, as all lipids were hydrogenated, leaflet-specific parameters are not measured. Due to the relatively high T_M of DPPC, ESM and MSM, again we measured all samples at 50 °C.

Rigidification of Asymmetric Bilayers

Fig. 23 summarizes measured values for the bending rigidity κ and the corresponding hydrophobic thicknesses $2D_C$ of the components individual components of the aLUVs, the aLUVs and the corresponding symmetric references. From the individual lipids, it is already visible that there is no clear correlation between $2D_C$ and κ . For PCs it was found that κ is proportional to the square of the mechanical thickness, being $(2D_C)^2$ for unsaturated PCs and the distance between both phosphates for saturated ones [42, 10]. This explains the

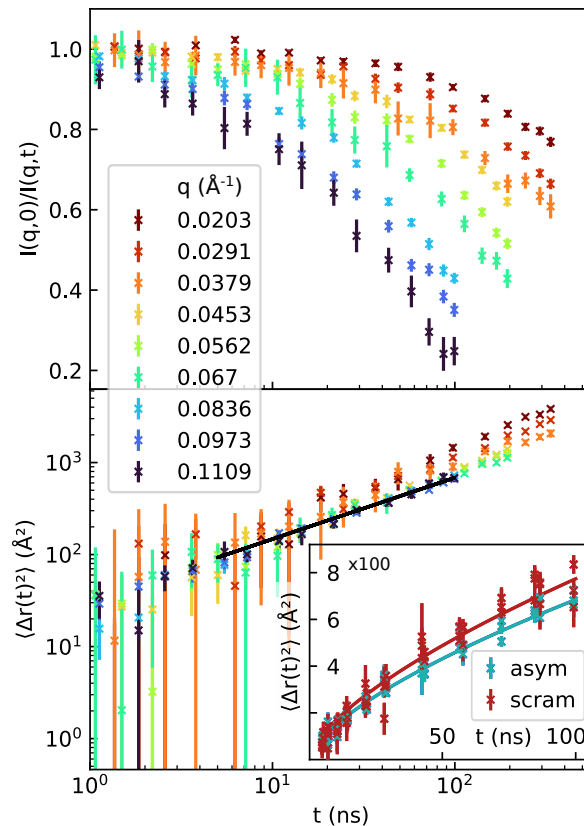


Figure 22: NSE data (upper panel) and the corresponding mean square displacements (lower panel) for asymmetric vesicles $\text{POPE}^{in}/\text{POPC}^{out}$ as a function of scattering vector q and Fourier time t . A solid black line marks the $t^{2/3}$ -slope for the range where the Zilman-Granek model is assumed to be valid [47]. Low- q and high- t data have a steeper slope as they might include be sensitive to particle diffusion and internal dissipation effects. The inset shows only data from the ZG-range for asymmetric and the corresponding symmetric vesicles of POPE/POPC shown in the inset, whose difference in dynamics are already visible in this representation of the data.

higher rigidity of DPPC compared to POPC, lipids with different headgroups do however not follow this trend. Particularly POPE due to its high packing density is thicker than POPC and the mixture POPE/POPS, which have the same chain composition. Their κ are however the same within the experimental uncertainty. MSM and egg sphingomyelin (ESM) are both more rigid than the PCs, which is expected for MSM, due to its long chains and the following more bulky chain region. ESM forms a surprisingly thick membrane with an area lipid A of 55 \AA^2 , even though the prevalent acyl chain is 16:0, making it nominally similar to DPPC (which was also found in [71]). In a recent study [19], however, ESM was also found to form similarly thick bilayers. The reason is unclear, though as it is a natural extract, irregularities could originate in impurities or undesired additional compounds.

The first asymmetric sample was the previously characterized $\text{DPPC}^{in}\text{MSM}^{out}$. From the thickening of the inner leaflet we would also expect a more rigid aLUV than the symmetric vesicle. We did find a slight increase in κ due to asymmetry, the effect is however small, looking at absolute values and experimental uncertainty. Next, we have POPE in the inner leaflet (prepared with 10 % POPG to ensure unilamellarity) and either ESM or MSM in the outer leaflet. $\text{POPE}^{in}\text{ESM}^{out}$ was recently studied at 30 and 45 °C, both in the fluid phase [19], where they found a significant stiffening of the bilayer. In our case, at 50 °C, this asymmetric system is slightly thinner and less rigid than its symmetric counterpart. Also using MSM in the outside, there is no dramatic change in κ , even though the asymmetric samples is somewhat thicker.

However, using 1-palmitoyl-2-oleoyl-glycero-3-phosphocholine (POPC) in the outer leaflet instead of SM leads to a 50 % increase in κ , connected with a significant increase in thickness. Also the 1:1 mixture POPC/MSM

in the outer leaflet brings a similar effect. The next step towards realistic plasma membrane mimics has even more dramatic effects on κ . Complementing POPE with 30 % POPS brings an asymmetry-induced rigidification for either MSM (70 %), POPC (120 %) or the mixture of both (90 %) in the outer leaflet.

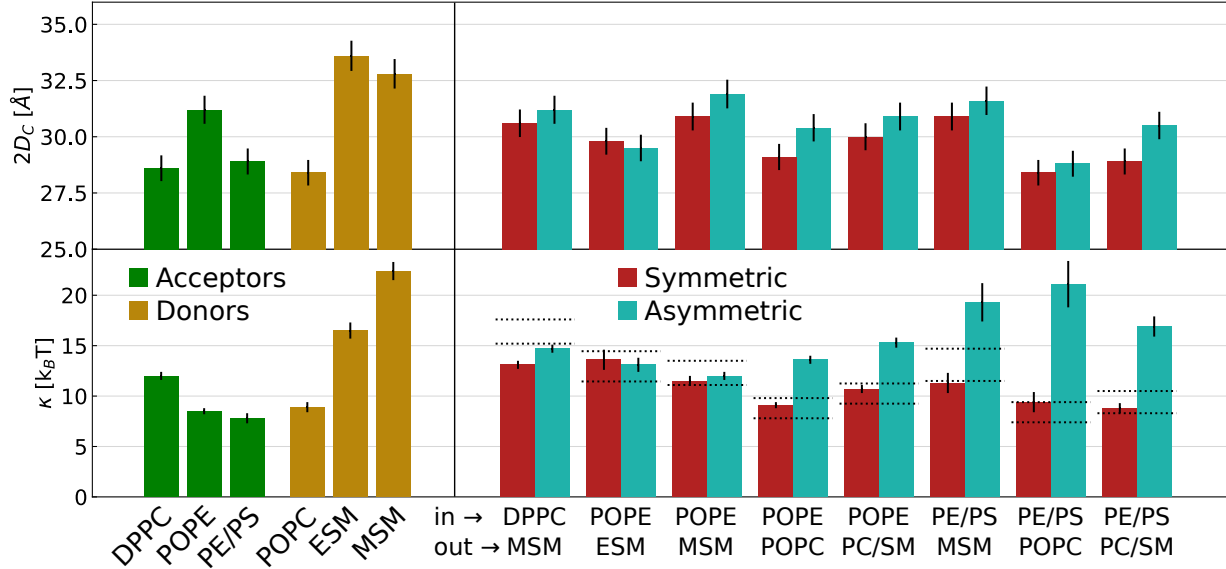


Figure 23: Mechanical/hydrophobic thicknesses D_C and bending rigidities κ measured of the studied lipid systems: the left panels show the values for acceptor and donor lipids, which are located predominantly in the inner and outer leaflet of asymmetric vesicles, respectively. PE/PS designates a 7:3 mixture of POPE and POPS. In the right panels the results are given for asymmetric vesicles and the same after artificially destroying their asymmetry by evaporation of solvent and rehydration. The labels indicate the lipids predominant in inner and outer leaflet, PC/SM being a 1:1 mixture of POPC and MSM. Dotted lines indicate the range of κ expected for symmetric and uncoupled asymmetric vesicles, assuming additivity of κ .

Tab. 3.3 summarizes compositional and structural properties of the aLUVs studied by NSE. Further parameters and model fits of SAS data can be found in the supplementary information.

Table 6: Properties of aLUVs and scrambled vesicles. The compositions χ give the ratio between acceptor and donor lipids for each leaflet and the total bilayer. We estimate the relative uncertainty for D_B about 2-3 %, for χ and A 5 %.

	χ			aLUV		scrambled		$\Delta A/A$ [%]
	χ^{tot}	χ^{in}	χ^{out}	A_{av} [Å ³]	D_B [Å]	A [Å ³]	D_B [Å]	
DPPC ⁱⁿ MSM ^{out}	54:46	83:17	28:72	62.4	40.9	63.8	40.1	-2.2
POPE ⁱⁿ ESM ^{out}	61:39	98:02	28:72	64.0	37.6	61.8	38.2	3.6
POPE ⁱⁿ MSM ^{out}	67:33	82:18	54:46	61.4	40.3	63.8	39.0	-3.8
POPE ⁱⁿ POPC ^{out}	77:23	90:10	65:35	62.0	39.0	64.9	37.4	-4.5
POPE ⁱⁿ PC/Sm ^{out}	52:48	65:35	40:60	62.9	39.6	65.0	38.4	-3.2
PE/PS ⁱⁿ MSM ^{out}	59:41	97:03	25:75	62.8	40.0	64.3	39.1	-2.3
PE/PS ⁱⁿ POPC ^{out}	71:29	97:03	48:52	66.0	39.1	65.8	36.7	0.3
PE/PS ⁱⁿ PC/SM ^{out}	62:38	77:23	49:51	63.4	39.1	66.9	37.1	-5.2

Contributions from Intrinsic Curvature and Charge

While there is some increase in thickness for the samples with increased κ , it is not sufficiently different from the ones that are as stiff as their symmetric counterparts. Next, we investigate the potential influence of intrinsic curvature J_0 on the mechanical properties. We estimate J_0 of each leaflet by summing over the individual components of each leaflet, assuming additive curvatures. Values for J_0 were taken from measurements from hexagonal phases [72, 73] and estimated to be around 0 for POPG, POPS and SM. For

each leaflet we can then calculate the stored elastic energy density in a flat bilayer, which is calculated from its bending rigidity and its intrinsic curvature:

$$E_s = \frac{1}{2}\kappa J_0^2 \quad (18)$$

Tab. 3.3 compares E_s in aLUVs and symmetric references. Values for the monolayer bending rigidity κ_m come from measurements of symmetric references with the composition of inner or outer monolayer and are assumed to be half the bilayer bending rigidity. E_s^{bil} of the whole bilayer is calculated from the sum of both its leaflets.

The differences in E_s between aLUVs and scrambled samples show no correlation to the corresponding changes in κ . The relative changes are also nowhere near the extent κ changes for some of the samples, except for DPPC/MSM, where the absolute change is however also small.

Table 7: Intrinsic curvatures J_0 , monolayer bending rigidities κ_m and resulting stored elastic energy densities E_s for aLUVs and corresponding bilayer values of symmetric references. Values for E_s are given in units of [$1e-5 \text{ k}_B\text{T}/\text{\AA}^2$].

	aLUV				scrambled			ΔE_s	$\Delta E_s/E_s$ [%]
	J_0 [\AA^{-1}]	κ_m [k_BT]	E_s	E_s^{bil}	J_0 [\AA^{-1}]	κ [k_BT]	E_s^{bil}		
DPPC/MSM in	0.004	6.8	5	6	0.003	13.1	4	2	50
out	0.001	9.7	1						
POPE/ESM in	-0.028	4.2	162	174	-0.016	13.6	177	3	2
out	-0.006	7.5	12						
POPE/MSM in	-0.023	5.3	137	205	-0.018	11.4	186	-20	-11
out	-0.014	7.1	68						
POPE/POPC in	-0.025	4.4	141	206	-0.021	9.1	201	-5	-2
out	-0.017	4.5	65						
POPE/Mix in	-0.017	5.0	74	97	-0.013	10.7	90	-7	-7
out	-0.009	5.5	23						
PEPS/MSM in	-0.021	3.9	85	114	-0.014	11.3	107	-7	-6
out	-0.008	9.2	29						
PEPS/POPC in	-0.021	4.2	90	136	-0.017	9.4	141	5	4
out	-0.015	4.2	46						
PEPS/Mix in	-0.014	4.5	46	105	-0.015	8.8	93	-11	-12
out	-0.015	5.0	59						

The influence of charge on membrane rigidity has been explored in a general model by Guttman & Andelman [74]. They predict a rigidification induced by membrane surface charges, which is however weak and of the order of $k_B T$ or lower. It depends however heavily on the lateral distribution of charge and on its freedom to equilibrate throughout the membrane. For the case of asymmetrically distributed charges they do not generally find that the membrane becomes more rigid and even predict a case that favors undulations thus leading to a softening.

On the other hand, it has been shown that shielding the charges of headgroups by ions can decrease the bending rigidity of bilayers [75], suggesting a rigidification by charge. This has however only been tested for symmetric bilayers.

The increase of bending rigidity in the presence of PS can therefore possibly not be explained by charge alone.

Dynamical Interpretation

As the above considerations do not explain the changes in rigidity induced in particular by the asymmetry of POPE and POPC, as well as generally POPS, we propose to look at this data with a more general dynamic view and consider specific lipid interactions. The way NSE probes κ is by neutrons scattering from undulatory motions of the membrane. These collective fluctuations require a certain cooperativity between the lipids and in particular between the two monolayers. In a symmetric bilayer, no matter which lipids are present, fluctuations of lipids happen necessarily in a similar way. However, if the composition is different in inner and outer leaflet, the dynamics of individual lipids might play a large role.

The huge change in rigidity for POPE/POPC could be connected to the lateral fluctuations in lipid area. The area expansion modulus of POPE is almost twice as large than that POPC ($0.0038 K^{-1}$ vs. $0.0022 K^{-1}$ [43, 76]), possibly giving POPE the propensity to perform large thermal fluctuations. This is in contrast to the tight packing of the molecule and the hydrogen bonds it forms with neighboring molecules, acting against these fluctuations like a spring. POPC however has no curvature and a weak potential to expand due to its bulky headgroup and relaxed chains. Its dynamics might therefore be somewhat slower. Due to these different properties the bending modes and connected favorable frequencies and/or amplitudes might impede the ability to oscillate of the overall membrane and thereby increase the overall rigidity.

In the case of MSM this de-coupling of the collective fluctuations is prevented by the long hydrocarbon chains anchored in the opposing leaflet. Again, van der Waals interactions between those chains could force the leaflets to adapt their oscillation modes to each other and lead to a softer membrane. For the 1:1 mixture of POPC and MSM, the influence of POPC seems to simply outweigh this effect. In the case of ESM, the de-coupling has been observed before [19]. It seems to be however decreasing with temperature until it vanishes for $50\text{ }^{\circ}\text{C}$, an indication that entropy can reduce this effect. The increase of κ by the inclusion of POPS can have several origins. First, there is charge which can have an impact on the modes of the inner leaflet. POPS also forms hydrogen bonds in a yet different way from PE and SM [77]. Finally, it is very sensitive to the solvent pH and can change its electrostatic properties according to its environment [78]. PS molecules in the inner and outer leaflet could therefore again behave in a different way. This way, the presence of POPS also causes a de-coupling in aLUVs with interdigitated leaflets or even prevent the long chains from penetrating into the inner leaflet.

Concluding Remarks

The dramatic increase of rigidity in asymmetric membranes is truly remarkable. For a live cell, which disposes of flippases and floppases to create and tune the asymmetry, and of scramblases to destroy it, this is a powerful tool to rapidly change the mechanical properties of the membrane. One has to keep in mind however, that the biological membrane is more complex and contains in particular cholesterol, membrane proteins and is surrounded by ions. Therefore it is not clear that these effects are also present in nature. In principle however, it is thinkable that cells evolved to a state where they can use these kind of properties of natural membranes.

A last point to discuss is the role of sample preparation. We cannot fully exclude that the cyclodextrin mediated exchange protocol induces differential stress in the membrane (see 1.2) and thereby creates the increased membrane rigidity. Exchanging for example one POPE molecule for one POPC will consequently widen the total area of the outer leaflet due to the higher A of POPC. However, during the exchange, in the presence of cyclodextrin, the membrane is highly disturbed and exhibits an elevated flip-flop rate resulting in the amount of donor lipid, which is always present in the inner leaflet. We suggest that this flip-flop should equilibrate the membrane and reduce stress caused by overcrowding of either leaflet. And even if the effect is due to sample preparation, these membranes are stable and could therefore be occurring in nature in a similar way, to use the properties measured by these experiments.

4 Outlook

. Maybe the most intriguing open question has not yet been mentioned in this work. In the course of measuring aLUVs with DPPCd62 in the inner leaflet, we measured one additional SANS contrast at 62% D₂O. This way, both leaflets are presumably visible, one at positive, one at negative contrast (Fig. 24b). This arrangement however is not accurately described by the model. As shown in Fig. 24a, the model predicts an oscillation at high q , which is not present in the data. Furthermore, the intensity I_0 (at $q = 0$) does not conform with the predicted quadratic dependency on the overall bilayer contrast (Fig. 24c). Theoretically, it should be close to the matching point, where the average of inner and outer leaflet contrast result in 0 and therefore I_0 is at a minimum. We find I_0 however significantly higher than predicted. This effect is present for all samples, including DPPCd62ⁱⁿMSM^{out}, where we measured this third contrast using 50% D₂O instead of 62. A possible explanation could be inhomogeneities in composition between the vesicles, resulting from uneven exchange by cyclodextrin. Attempts to model this failed however (data not shown). These data may contain important information about the structure of asymmetric vesicles.

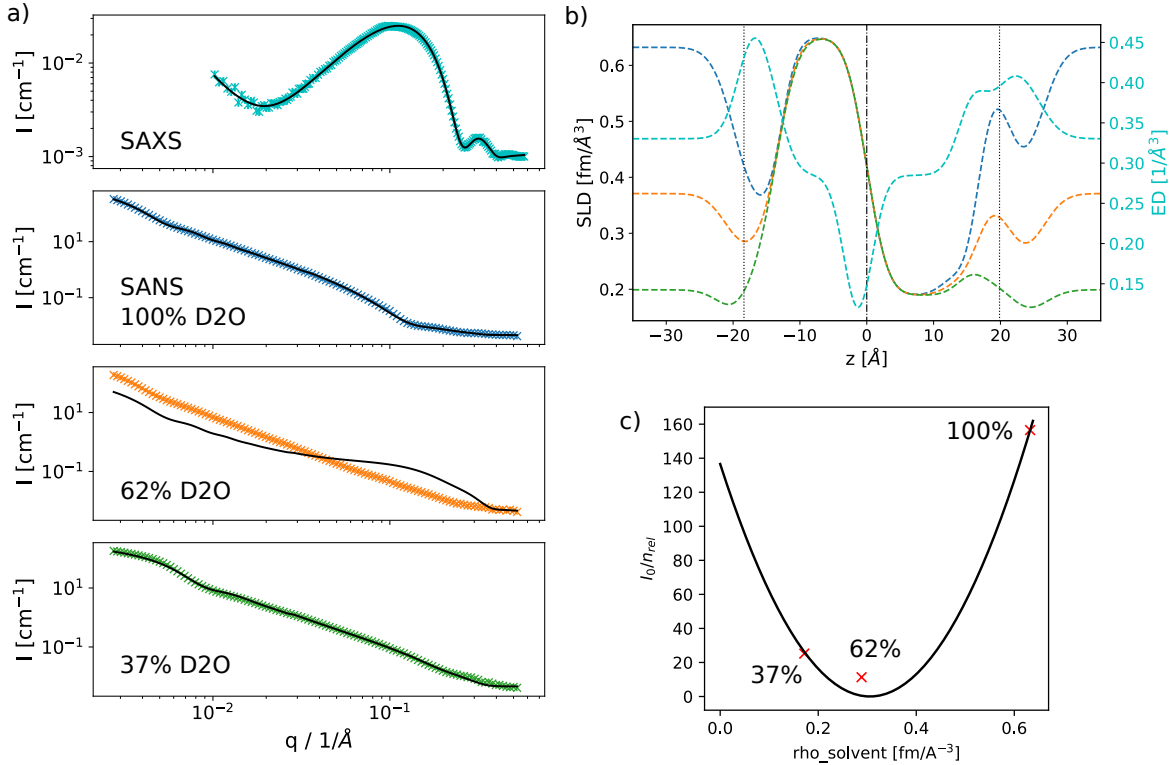


Figure 24: a) SAXS and SANS data of the system DPPCd62ⁱⁿSMPC^{out}, including the third contrast at 62% D₂O. b) shows the corresponding SLD profiles predicted by the SDP model. In c) the intensity values at $q = 0$, normalized by vesicle concentration are plotted for the 3 contrasts, including a possible parabola fitted through the two contrasts that conform with the model.

Other parts, where this project could be continued, would be a systematic study of the thickness polydispersity of and its possible connection to thickness fluctuations.

SAS measurements with one deuterated leaflet could be extended to head group asymmetric membranes to find out more about the leaflet-specific changes in these membranes.

And in the improvement of plasma model membranes, the possibilities are of course countless. The inclusion of salt could be interesting, especially for the vesicles containing POPS. Cholesterol is still completely missing in the picture and might give insight about its partitioning into either leaflet but also on its effect on membrane structure and dynamics. And the complexity in chain composition could be either increased by using natural extracts also for PE, PC and PS or decreased, using synthetic SM.

Work is also required on the theoretical models for NSE data, where more complex theories about diffusion could be included [79] and other contributions such as the tilt modulus might be still missing [80].

5 Conclusion

This study was concerned with the mechanical and structural properties of lipid vesicles. In particular, the effects of interdigitation and trans-bilayer lipid asymmetry were addressed. Small-angle X-ray and neutron scattering proved as adequate tools to quantify interdigitation in symmetric and in asymmetric bilayers and to detect differences in bilayer structure arising from asymmetry.

Interdigitation was studied using choline lipids with differently long chains. We found that these lipids interdigitate in symmetric vesicles with a linear dependence with regard to the chainlength mismatch of the two tails of the lipid. Otherwise, interdigitation has little effect on the bilayer structure of these vesicles. In asymmetric bilayers we found different effects that were induced by the presence of mixed-chain lipids in one leaflet. PC lipids with little interdigitation disturb the order in the membrane and decrease the packing density in the opposing or both leaflets. Long chain sphingomyelin, however, anchors its acyl chains in the opposing leaflet and stabilizes it by van der Waals forces, creating a more ordered opposing leaflet.

Advances were achieved in the modeling of trans-membrane structures for SAS and revealed a hydration layer around the head groups as well as thickness polydispersity in most membranes. SANS also was established as a tool to quantify asymmetry in the presence of isotopically labelled lipids. Close to the neutron contrast matching point of asymmetric vesicles, the model reaches however its limits and is not able to correctly describe the corresponding SANS-data.

Using neutron spin-echo spectroscopy, we found large increases of bending rigidity caused by lipid asymmetry for some systems. This particularly arises from the asymmetry of PE inside and PC outside and is further enhanced if also PS is present in the inner leaflet. Sphingomyelin in the outer leaflet only have an increased stiffness in vesicles including PS. The exact reason for this is not entirely clear, as neither packing stress nor intrinsic lipid curvature show a clear correlation with the rigidity data of the measured samples. It is imaginable that the increase in stiffness arises from specific lipid interactions, which inhibits interleaflet-coordinated undulatory motions. The responsible mechanisms could be lateral thermal fluctuations, hydrogen bonding networks and the influence of surface charge.

List of Scientific Publications

Attached Publications with Author Contributions

- Frewein, M. P. K., Doktorova, M., Heberle, F. A., Scott, H. L., Semeraro, E. F., Porcar, L., & Pabst, G. (2021). *Structure and interdigitation of chain-asymmetric phosphatidylcholines and milk sphingomyelin in the fluid phase*. *Symmetry*, 13(8), 1441.
Conceptualization, M.P.K.F., M.D., F.A.H., E.F.S. and G.P.
Data curation, M.D.
Formal analysis, M.P.K.F., M.D. and F.A.H.
Investigation, M.P.K.F., M.D., H.L.S., E.F.S. and L.P.
Methodology, M.P.K.F. and E.F.S.
Software, M.P.K.F.
Supervision, G.P.
Visualization, M.P.K.F.
Writing - original draft, M.P.K.F. and G.P.
Writing - review and editing, M.P.K.F., M.D., F.A.H., H.L.S., E.F.S., L.P. and G.P.
- Frewein, M. P. K., Piller, P., Semeraro, E. F., Batchu, K. C., Heberle, F. A., Scott, H. L., Gerelli, Y., Porcar, L. & Pabst, G. (2022). *Interdigitation-Induced Order and Disorder in Asymmetric Membranes*. *The Journal of Membrane Biology*, 1-15.
Conceptualization, M.P.K.F., Y.G., L.P. and G.P.
Formal analysis, M.P.K.F., and G.P.
Investigation, M.P.K.F., P.P., E.F.S, K.B., H.L.S., L.P.
Methodology, M.P.K.F. and E.F.S.
Software, M.P.K.F.
Supervision, L.P. and G.P.
Visualization, M.P.K.F.
Writing - original draft, M.P.K.F. and G.P.
Writing - review and editing, M.P.K.F., P.P., E.F.S., K.B., F.A.H., H.L.S., Y.G., L.P. and G.P.

Other Publications

- Semeraro, E. F., Marx, L., Frewein, M. P., & Pabst, G. (2021). *Increasing complexity in small-angle X-ray and neutron scattering experiments: from biological membrane mimics to live cells*. *Soft Matter*, 17(2), 222-232.
- Semeraro, E. F., Marx, L., Mandl, J., Frewein, M. P., Scott, H. L., Prévost, S., ... & Pabst, G. (2021). *Evolution of the analytical scattering model of live Escherichia coli*. *Journal of applied crystallography*, 54(2), 473-485.
- Marx, L., Semeraro, E. F., Mandl, J., Kremser, J., Frewein, M. P., Malanovic, N., ... & Pabst, G. (2021). *Bridging the antimicrobial activity of two lactoferricin derivatives in E. coli and lipid-only membranes*. *Frontiers in medical technology*, 3, 625975.
- Kaltenecker, M., Kremser, J., Frewein, M. P., Zihler, P., Bonthuis, D. J., & Pabst, G. (2021). *Intrinsic lipid curvatures of mammalian plasma membrane outer leaflet lipids and ceramides*. *Biochimica et Biophysica Acta (BBA)-Biomembranes*, 1863(11), 183709.
- Marx, L., Frewein, M. P., Semeraro, E. F., Rechberger, G. N., Lohner, K., Porcar, L., & Pabst, G. (2021). *Antimicrobial peptide activity in asymmetric bacterial membrane mimics*. *Faraday discussions*, 232, 435-447.
- Semeraro, E. F., Marx, L., Mandl, J., Letofsky-Papst, I., Mayrhofer, C., Frewein, M. P., ... & Pabst, G. (2022). *Lactoferricins impair the cytosolic membrane of Escherichia coli within a few seconds and accumulate inside the cell*. *eLife*, 11, e72850.
- Frewein, M. P. K., Piller, P., Semeraro, E. F., Czakkel, O., Gerelli, Y., Porcar, L. & Pabst, G. *Rigidification of Advanced Biomembrane Mimics Induced by Packing Stress and Charge Anisotropy* - Manuscript in preparation

References

- [1] S. J. Singer and Garth L. Nicolson. “The Fluid Mosaic Model of the Structure of Cell Membranes”. In: *Science* 175 (4023 Feb. 1972), pp. 720–731. ISSN: 0036-8075. DOI: 10.1126/science.175.4023.720.
- [2] Garth L. Nicolson. “The Fluid—Mosaic Model of Membrane Structure: Still relevant to understanding the structure, function and dynamics of biological membranes after more than 40years”. In: *Biochimica et Biophysica Acta (BBA) - Biomembranes* 1838 (6 June 2014), pp. 1451–1466. ISSN: 00052736. DOI: 10.1016/j.bbamem.2013.10.019.
- [3] Haden L. Scott et al. “Model Membrane Systems Used to Study Plasma Membrane Lipid Asymmetry”. In: *Symmetry* 13 (8 July 2021), p. 1356. ISSN: 2073-8994. DOI: 10.3390/sym13081356.
- [4] J. H. Lorent et al. “Plasma membranes are asymmetric in lipid unsaturation, packing and protein shape”. In: *Nature Chemical Biology* 16 (6 2020), pp. 644–652. ISSN: 15524469. DOI: 10.1038/s41589-020-0529-6.
- [5] M. C. Wiener and S. H. White. “Structure of a fluid dioleoylphosphatidylcholine bilayer determined by joint refinement of x-ray and neutron diffraction data. III. Complete structure”. In: *Biophysical Journal* 61 (2 1992), pp. 434–447. ISSN: 00063495. DOI: 10.1016/S0006-3495(92)81849-0.
- [6] Norbert Kučerka et al. “Lipid bilayer structure determined by the simultaneous analysis of neutron and X-ray scattering data”. In: *Biophysical Journal* 95 (5 2008), pp. 2356–2367. ISSN: 15420086. DOI: 10.1529/biophysj.108.132662.
- [7] Barbara Eicher et al. “Joint small-angle X-ray and neutron scattering data analysis of asymmetric lipid vesicles”. In: *Journal of Applied Crystallography* 50 (2017), pp. 419–429. ISSN: 16005767. DOI: 10.1107/S1600576717000656.
- [8] John F. Nagle et al. “Revisiting Volumes of Lipid Components in Bilayers”. In: *Journal of Physical Chemistry B* 123 (12 Mar. 2019), pp. 2697–2709. ISSN: 15205207. DOI: 10.1021/acs.jpcc.8b12010.
- [9] Mark S. Bretscher. “Asymmetrical Lipid Bilayer Structure for Biological Membranes”. In: *Nature New Biology* 236 (61 Mar. 1972), pp. 11–12. ISSN: 0090-0028. DOI: 10.1038/newbio236011a0.
- [10] Milka Doktorova et al. “A New Computational Method for Membrane Compressibility: Bilayer Mechanical Thickness Revisited”. In: *Biophysical Journal* 116 (3 Feb. 2019), pp. 487–502. ISSN: 00063495. DOI: 10.1016/j.bpj.2018.12.016.
- [11] Drew Marquardt et al. “¹H NMR Shows Slow Phospholipid Flip-Flop in Gel and Fluid Bilayers”. In: *Langmuir* 33 (15 2017), pp. 3731–3741. ISSN: 15205827. DOI: 10.1021/acs.langmuir.6b04485.
- [12] Jonathan D. Nickels, Jeremy C. Smith, and Xiaolin Cheng. “Lateral organization, bilayer asymmetry, and inter-leaflet coupling of biological membranes”. In: *Chemistry and Physics of Lipids* 192 (2015), pp. 87–99. ISSN: 18732941. DOI: 10.1016/j.chemphyslip.2015.07.012.
- [13] Amirali Hossein and Markus Deserno. “Spontaneous Curvature, Differential Stress, and Bending Modulus of Asymmetric Lipid Membranes”. In: *Biophysical Journal* 118 (3 2020), pp. 624–642. ISSN: 15420086. DOI: 10.1016/j.bpj.2019.11.3398.
- [14] Barbara Eicher et al. “Intrinsic Curvature-Mediated Transbilayer Coupling in Asymmetric Lipid Vesicles”. In: *Biophysical Journal* 114 (1 2018), pp. 146–157. ISSN: 15420086. DOI: 10.1016/j.bpj.2017.11.009.
- [15] Frederick A. Heberle et al. “Subnanometer Structure of an Asymmetric Model Membrane: Interleaflet Coupling Influences Domain Properties”. In: *Langmuir* 32 (20 2016), pp. 5195–5200. ISSN: 15205827. DOI: 10.1021/acs.langmuir.5b04562.
- [16] Tomasz Róg et al. “Interdigitation of long-chain sphingomyelin induces coupling of membrane leaflets in a cholesterol dependent manner”. In: *Biochimica et Biophysica Acta - Biomembranes* 1858 (2 2016), pp. 281–288. ISSN: 18792642. DOI: 10.1016/j.bbamem.2015.12.003.
- [17] K. Karamdad et al. “Studying the effects of asymmetry on the bending rigidity of lipid membranes formed by microfluidics”. In: *Chemical Communications* 52 (30 Apr. 2016), pp. 5277–5280. ISSN: 1359-7345. DOI: 10.1039/C5CC10307J.
- [18] Li Lu et al. “Membrane mechanical properties of synthetic asymmetric phospholipid vesicles”. In: *Soft Matter* 12 (36 2016), pp. 7521–7528. ISSN: 1744-683X. DOI: 10.1039/C6SM01349J.

- [19] Brett W. Rieckard et al. “Transverse lipid organization dictates bending fluctuations in model plasma membranes”. In: *Nanoscale* 12 (3 Jan. 2020), pp. 1438–1447. ISSN: 20403372. DOI: 10.1039/c9nr07977g.
- [20] Haden L. Scott et al. “On the Mechanism of Bilayer Separation by Extrusion, or Why Your LUVs Are Not Really Unilamellar”. In: *Biophysical Journal* 117 (8 2019), pp. 1381–1386. ISSN: 15420086. DOI: 10.1016/j.bpj.2019.09.006.
- [21] G. L. Squires. *Introduction to the Theory of Thermal Neutron Scattering*. Cambridge University Press, Mar. 2012. ISBN: 9781139107808. DOI: 10.1017/CB09781139107808.
- [22] Settimio Mobilio, Federico Boscherini, and Carlo Meneghini, eds. *Synchrotron Radiation*. Springer Berlin Heidelberg, 2015. ISBN: 978-3-642-55314-1. DOI: 10.1007/978-3-642-55315-8.
- [23] Pablo Székely et al. “Solution x-ray scattering form factors of supramolecular self-assembled structures”. In: *Langmuir* 26 (16 Aug. 2010), pp. 13110–13129. ISSN: 07437463. DOI: 10.1021/1a101433t.
- [24] Jeremy Pencer et al. “Method of separated form factors for polydisperse vesicles”. In: *Journal of Applied Crystallography* 39 (3 2006), pp. 293–303. ISSN: 00218898. DOI: 10.1107/S0021889806005255.
- [25] Moritz P. K. Frewein et al. “Structure and Interdigitation of Chain-Asymmetric Phosphatidylcholines and Milk Sphingomyelin in the Fluid Phase”. In: *Symmetry* 13 (8 Aug. 2021), p. 1441. ISSN: 2073-8994. DOI: 10.3390/sym13081441.
- [26] Moritz P. K. Frewein et al. “Interdigitation-Induced Order and Disorder in Asymmetric Membranes”. In: *The Journal of Membrane Biology* (Apr. 2022). ISSN: 0022-2631. DOI: 10.1007/s00232-022-00234-0.
- [27] F. Mezei. “Neutron spin echo: A new concept in polarized thermal neutron techniques”. In: *Zeitschrift für Physik A Hadrons and nuclei* 255 (2 Apr. 1972), pp. 146–160. ISSN: 0939-7922. DOI: 10.1007/BF01394523.
- [28] Françoise Hippert et al. *Neutron and X-ray Spectroscopy*. Ed. by Françoise Hippert et al. Springer Netherlands, 2006. DOI: 10.1007/1-4020-3337-0.
- [29] Ferenc Mezei, Catherine Pappas, and Thomas Gutberlet, eds. *Neutron Spin Echo Spectroscopy*. Vol. 601. Springer Berlin Heidelberg, 2003. DOI: 10.1007/3-540-45823-9.
- [30] A. G. Zilman and R. Granek. “Undulations and Dynamic Structure Factor of Membranes”. In: *Physical Review Letters* 77 (23 Dec. 1996), pp. 4788–4791. ISSN: 0031-9007. DOI: 10.1103/PhysRevLett.77.4788.
- [31] W Helfrich. “Elastic Properties of Lipid Bilayers: Theory and Possible Experiments”. In: *Zeitschrift für Naturforschung C* 28 (11-12 Dec. 1973), pp. 693–703. ISSN: 1865-7125. DOI: 10.1515/znc-1973-11-1209.
- [32] Zheng Yi, Michihiro Nagao, and Dobrin P Bossev. “Bending elasticity of saturated and monounsaturated phospholipid membranes studied by the neutron spin echo technique”. In: *Journal of Physics: Condensed Matter* 21 (15 Apr. 2009), p. 155104. ISSN: 0953-8984. DOI: 10.1088/0953-8984/21/15/155104.
- [33] Anton G. Zilman and Rony Granek. “Membrane dynamics and structure factor”. In: *Chemical Physics* 284 (1-2 Nov. 2002), pp. 195–204. ISSN: 03010104. DOI: 10.1016/S0301-0104(02)00548-7.
- [34] Ji Hwan Lee et al. “Thermal fluctuation and elasticity of lipid vesicles interacting with pore-forming peptides”. In: *Physical Review Letters* 105 (3 July 2010). ISSN: 00319007. DOI: 10.1103/PhysRevLett.105.038101.
- [35] L. R. Arriaga et al. “Dissipative curvature fluctuations in bilayer vesicles: Coexistence of pure-bending and hybrid curvature-compression modes”. In: *European Physical Journal E* 31 (1 2010), pp. 105–113. ISSN: 12928941. DOI: 10.1140/epje/i2010-10551-1.
- [36] Ingo Hoffmann et al. “Softening of phospholipid membranes by the adhesion of silica nanoparticles - As seen by neutron spin-echo (NSE)”. In: *Nanoscale* 6 (12 2014), pp. 6945–6952. ISSN: 20403372. DOI: 10.1039/c4nr00774c.
- [37] Michihiro Nagao et al. “Probing Elastic and Viscous Properties of Phospholipid Bilayers Using Neutron Spin Echo Spectroscopy”. In: *The Journal of Physical Chemistry Letters* 8 (19 Oct. 2017), pp. 4679–4684. ISSN: 1948-7185. DOI: 10.1021/acs.jpcllett.7b01830.

- [38] Elizabeth G. Kelley, Paul D. Butler, and Michihiro Nagao. “Scaling of lipid membrane rigidity with domain area fraction”. In: *Soft Matter* 15 (13 2019), pp. 2762–2767. ISSN: 17446848. DOI: 10.1039/c8sm02362j.
- [39] Max C. Watson and Frank L.H. Brown. “Interpreting membrane scattering experiments at the mesoscale: The contribution of dissipation within the bilayer”. In: *Biophysical Journal* 98 (6 Mar. 2010), p. L9. ISSN: 15420086. DOI: 10.1016/j.bpj.2009.11.026.
- [40] U Seifert and S. A Langer. “Viscous Modes of Fluid Bilayer Membranes”. In: *Europhysics Letters (EPL)* 23 (1 July 1993), pp. 71–76. ISSN: 0295-5075. DOI: 10.1209/0295-5075/23/1/012.
- [41] David Boal. “Biomembranes”. In: Cambridge University Press, 2012. Chap. 7, pp. 243–291. DOI: 10.1017/CB09781139022217.011.
- [42] W. Rawicz et al. “Effect of Chain Length and Unsaturation on Elasticity of Lipid Bilayers”. In: *Biophysical Journal* 79 (1 July 2000), pp. 328–339. ISSN: 00063495. DOI: 10.1016/S0006-3495(00)76295-3.
- [43] Norbert Kučerka, Mu Ping Nieh, and John Katsaras. “Fluid phase lipid areas and bilayer thicknesses of commonly used phosphatidylcholines as a function of temperature”. In: *Biochimica et Biophysica Acta - Biomembranes* 1808 (11 2011), pp. 2761–2771. ISSN: 00052736. DOI: 10.1016/j.bbmem.2011.07.022.
- [44] Andrea C. Woodka et al. “Lipid Bilayers and Membrane Dynamics: Insight into Thickness Fluctuations”. In: *Physical Review Letters* 109 (5 July 2012), p. 058102. ISSN: 0031-9007. DOI: 10.1103/PhysRevLett.109.058102.
- [45] Stephanie Tristram-Nagle and John F. Nagle. “HIV-1 fusion peptide decreases bending energy and promotes curved fusion intermediates”. In: *Biophysical Journal* 93 (6 2007), pp. 2048–2055. ISSN: 00063495. DOI: 10.1529/biophysj.107.109181.
- [46] Sudipta Gupta and Gerald J. Schneider. “Modeling the dynamics of phospholipids in the fluid phase of liposomes”. In: *Soft Matter* 16 (13 2020), pp. 3245–3256. ISSN: 17446848. DOI: 10.1039/c9sm02111f.
- [47] Sudipta Gupta et al. “Dynamics of Phospholipid Membranes beyond Thermal Undulations”. In: *Journal of Physical Chemistry Letters* 9 (11 June 2018), pp. 2956–2960. ISSN: 19487185. DOI: 10.1021/acs.jpcllett.8b01008.
- [48] Jörg Stetefeld, Sean A. McKenna, and Trushar R. Patel. “Dynamic light scattering: a practical guide and applications in biomedical sciences”. In: *Biophysical Reviews* 8 (4 Dec. 2016), pp. 409–427. ISSN: 1867-2450. DOI: 10.1007/s12551-016-0218-6.
- [49] Lisa Marx et al. “Antimicrobial peptide activity in asymmetric bacterial membrane mimics”. In: *Faraday Discussions* 34 (4 2021), pp. 240–241. ISSN: 1359-6640. DOI: 10.1039/D1FD00039J.
- [50] M. Doktorova, D. Harries, and G. Khelashvili. “Determination of bending rigidity and tilt modulus of lipid membranes from real-space fluctuation analysis of molecular dynamics simulations”. In: *Physical Chemistry Chemical Physics* 19 (25 2017), pp. 16806–16818. ISSN: 1463-9076. DOI: 10.1039/C7CP01921A.
- [51] A.E. Taylor and C.W. Miller. “ON THE ESTIMATION OF PHOSPHORUS IN BIOLOGICAL MATERIAL”. In: *Journal of Biological Chemistry* 18 (2 July 1914), pp. 215–224. ISSN: 00219258. DOI: 10.1016/S0021-9258(18)88358-2.
- [52] Cyrus H. Fiske and Yellapragada Subbarow. “THE COLORIMETRIC DETERMINATION OF PHOSPHORUS”. In: *Journal of Biological Chemistry* 66 (2 Dec. 1925), pp. 375–400. ISSN: 00219258. DOI: 10.1016/S0021-9258(18)84756-1.
- [53] Grant R. Bartlett. “Phosphorus Assay in Column Chromatography”. In: *Journal of Biological Chemistry* 234 (3 Mar. 1959), pp. 466–468. ISSN: 00219258. DOI: 10.1016/S0021-9258(18)70226-3.
- [54] P.B. Kingsley and G.W. Feigenson. “The synthesis of a perdeuterated phospholipid: 1,2-dimyristoyl-sn-glycero-3-phosphocholine-d72”. In: *Chemistry and Physics of Lipids* 24 (2 May 1979), pp. 135–147. ISSN: 00093084. DOI: 10.1016/0009-3084(79)90083-5.
- [55] George Rouser, Sidney Fleischer, and Akira Yamamoto. “Two dimensional thin layer chromatographic separation of polar lipids and determination of phospholipids by phosphorus analysis of spots”. In: *Lipids* 5 (5 May 1970), pp. 494–496. ISSN: 0024-4201. DOI: 10.1007/BF02531316.

- [56] Robin L. Anderson and Stephen Davis. “An organic phosphorus assay which avoids the use of hazardous perchloric acid”. In: *Clinica Chimica Acta* 121 (1 May 1982), pp. 111–116. ISSN: 00098981. DOI: 10.1016/0009-8981(82)90216-9.
- [57] Edward A. Nagul et al. *The molybdenum blue reaction for the determination of orthophosphate revisited: Opening the black box*. Aug. 2015. DOI: 10.1016/j.aca.2015.07.030.
- [58] John Charles Marshall Stewart. “Colorimetric determination of phospholipids with ammonium ferri-thiocyanate”. In: *Analytical Biochemistry* 104 (1 May 1980), pp. 10–14. ISSN: 00032697. DOI: 10.1016/0003-2697(80)90269-9.
- [59] Robert Hein, Can B. Uzundal, and Andreas Hennig. “Simple and rapid quantification of phospholipids for supramolecular membrane transport assays”. In: *Organic & Biomolecular Chemistry* 14 (7 Feb. 2016), pp. 2182–2185. ISSN: 1477-0520. DOI: 10.1039/C5OB02480C.
- [60] Giuseppe Zaccai. “Hydration shells with a pinch of salt”. In: *Biopolymers* 99 (4 Apr. 2013), pp. 233–238. ISSN: 00063525. DOI: 10.1002/bip.22154.
- [61] Alexander I. Greenwood, Stephanie Tristram-Nagle, and John F. Nagle. “Partial molecular volumes of lipids and cholesterol”. In: *Chemistry and Physics of Lipids* 143 (1-2 2006), pp. 1–10. ISSN: 00093084. DOI: 10.1016/j.chemphyslip.2006.04.002.
- [62] Moritz P. K. Frewein, Michael Rumetshofer, and Georg Pabst. “Global small-angle scattering data analysis of inverted hexagonal phases”. In: *Journal of Applied Crystallography* 52 (2 Apr. 2019), pp. 403–414. ISSN: 1600-5767. DOI: 10.1107/S1600576719002760.
- [63] Erik Lindahl and Olle Edholm. “Mesoscopic Undulations and Thickness Fluctuations in Lipid Bilayers from Molecular Dynamics Simulations”. In: *Biophysical Journal* 79 (1 July 2000), pp. 426–433. ISSN: 00063495. DOI: 10.1016/S0006-3495(00)76304-1.
- [64] Norbert Kučerka et al. “Curvature effect on the structure of phospholipid bilayers”. In: *Langmuir* 23 (3 2007), pp. 1292–1299. ISSN: 07437463. DOI: 10.1021/la062455t.
- [65] Perttu S. Niemelä, Marja T. Hyvönen, and Ilpo Vattulainen. “Influence of chain length and unsaturation on sphingomyelin bilayers”. In: *Biophysical Journal* 90 (3 2006), pp. 851–863. ISSN: 00063495. DOI: 10.1529/biophysj.105.067371.
- [66] V. Schram and T. E. Thompson. “Interdigitation does not affect translational diffusion of lipids in liquid crystalline bilayers”. In: *Biophysical Journal* 69 (6 1995), pp. 2517–2520. ISSN: 00063495. DOI: 10.1016/S0006-3495(95)80122-0.
- [67] Andreas Horner, Sergey A. Akimov, and Peter Pohl. “Long and Short Lipid Molecules Experience the Same Interleaflet Drag in Lipid Bilayers”. In: *Physical Review Letters* 110 (26 June 2013), p. 268101. ISSN: 0031-9007. DOI: 10.1103/PhysRevLett.110.268101.
- [68] G. Zaccai et al. “Neutron diffraction studies on phosphatidylcholine model membranes”. In: *Journal of Molecular Biology* 134 (4 Nov. 1979), pp. 693–706. ISSN: 00222836. DOI: 10.1016/0022-2836(79)90480-7.
- [69] Derek Marsh. “Analysis of the bilayer phase transition temperatures of phosphatidylcholines with mixed chains”. In: *Biophysical Journal* 61 (4 1992), pp. 1036–1040. ISSN: 00063495. DOI: 10.1016/S0006-3495(92)81911-2.
- [70] Michael A. Gardam, Joseph J. Itovitch, and John R. Silvius. “Partitioning of exchangeable fluorescent phospholipids and sphingolipids between different lipid bilayer environments”. In: *Biochemistry* 28 (2 Jan. 1989), pp. 884–893. ISSN: 0006-2960. DOI: 10.1021/bi00428a072.
- [71] Zoran Arsov et al. “Phase behavior of palmitoyl and egg sphingomyelin”. In: *Chemistry and Physics of Lipids* 213 (July 2018), pp. 102–110. ISSN: 18732941. DOI: 10.1016/j.chemphyslip.2018.03.003.
- [72] Benjamin Kollmitzer et al. “Monolayer spontaneous curvature of raft-forming membrane lipids”. In: *Soft Matter* 9 (45 2013), pp. 10877–10884. ISSN: 17446848. DOI: 10.1039/c3sm51829a.
- [73] Michael Kaltenecker et al. “Intrinsic lipid curvatures of mammalian plasma membrane outer leaflet lipids and ceramides”. In: *Biochimica et Biophysica Acta - Biomembranes* 1863 (11 Nov. 2021). ISSN: 18792642. DOI: 10.1016/j.bbmem.2021.183709.
- [74] Glen D. Guttman and David Andelman. “Electrostatic interactions in two-component membranes”. In: *Journal de Physique II* 3 (9 Sept. 1993), pp. 1411–1425. ISSN: 1155-4312. DOI: 10.1051/jp2:1993210.

- [75] Bing-Sui Lu et al. “Modulation of Elasticity and Interactions in Charged Lipid Multibilayers: Monovalent Salt Solutions”. In: *Langmuir* 32 (50 Dec. 2016), pp. 13546–13555. ISSN: 0743-7463. DOI: 10.1021/acs.langmuir.6b03614.
- [76] Norbert Kučerka et al. “Molecular structures of fluid phosphatidylethanolamine bilayers obtained from simulation-to-experiment comparisons and experimental scattering density profiles”. In: *Journal of Physical Chemistry B* 119 (5 2015), pp. 1947–1956. ISSN: 15205215. DOI: 10.1021/jp511159q.
- [77] Simon J. Slater et al. “Contribution of Hydrogen Bonding to Lipid-Lipid Interactions in Membranes and the Role of Lipid Order: Effects of Cholesterol, Increased Phospholipid Unsaturation, and Ethanol”. In: *Biochemistry* 32 (14 Apr. 1993), pp. 3714–3721. ISSN: 15204995. DOI: 10.1021/bi00065a025.
- [78] Gregor Cevc, Anthony Watts, and Derek Marsh. “Titration of the phase transition of phosphatidylserine bilayer membranes. Effects of pH, surface electrostatics, ion binding, and head-group hydration”. In: *Biochemistry* 20 (17 Aug. 1981), pp. 4955–4965. ISSN: 0006-2960. DOI: 10.1021/bi00520a023.
- [79] Scott T. Milner and S. A. Safran. “Dynamical fluctuations of droplet microemulsions and vesicles”. In: *Physical Review A* 36 (9 Nov. 1987), pp. 4371–4379. ISSN: 0556-2791. DOI: 10.1103/PhysRevA.36.4371.
- [80] John F. Nagle. “Experimentally determined tilt and bending moduli of single-component lipid bilayers”. In: *Chemistry and Physics of Lipids* 205 (June 2017), pp. 18–24. ISSN: 00093084. DOI: 10.1016/j.chemphyslip.2017.04.006.

Article

Structure and Interdigitation of Chain-Asymmetric Phosphatidylcholines and Milk Sphingomyelin in the Fluid Phase

Moritz P. K. Frewein ^{1,2,3,4} , Milka Doktorova ⁵ , Frederick A. Heberle ⁶ , Haden L. Scott ^{7,8} ,
Enrico F. Semeraro ^{1,3,4} , Lionel Porcar ²  and Georg Pabst ^{1,3,4,*} 

- ¹ Institute of Molecular Biosciences, University of Graz, NAWI Graz, 8010 Graz, Austria; moritz.frewein@uni-graz.at or frewein@ill.fr (M.P.K.F.); enrico.semeraro@uni-graz.at (E.F.S.)
- ² Institut Laue-Langevin, 38043 Grenoble, France; porcar@ill.fr
- ³ BioTechMed Graz, 8010 Graz, Austria
- ⁴ Field of Excellence BioHealth, University of Graz, 8010 Graz, Austria
- ⁵ Department of Molecular Physiology and Biological Physics, University of Virginia School of Medicine, Charlottesville, VA 22903, USA; md4xm@virginia.edu
- ⁶ Department of Chemistry, University of Tennessee Knoxville, Knoxville, TN 37996, USA; fheberle@utk.edu
- ⁷ Center for Environmental Biotechnology, University of Tennessee, Knoxville, TN 37996, USA; hscott3@vols.utk.edu
- ⁸ Shull Wollan Center, Oak Ridge National Laboratory, Oak Ridge, TN 37831, USA
- * Correspondence: georg.pabst@uni-graz.at; Tel.: +43-316-380-4989



Citation: Frewein, M.P.K.; Doktorova, M.; Heberle, F.A.; Scott, H.L.; Semeraro, E.F.; Porcar, L.; Pabst, G. Structure and Interdigitation of Chain-Asymmetric Phosphatidylcholines and Milk Sphingomyelin in the Fluid Phase. *Symmetry* **2021**, *13*, 1441. <https://doi.org/10.3390/sym13081441>

Academic Editor: Takashiro Akitsu

Received: 30 June 2021

Accepted: 29 July 2021

Published: 5 August 2021

Publisher's Note: MDPI stays neutral with regard to jurisdictional claims in published maps and institutional affiliations.



Copyright: © 2021 by the authors. Licensee MDPI, Basel, Switzerland. This article is an open access article distributed under the terms and conditions of the Creative Commons Attribution (CC BY) license (<https://creativecommons.org/licenses/by/4.0/>).

Abstract: We addressed the frequent occurrence of mixed-chain lipids in biological membranes and their impact on membrane structure by studying several chain-asymmetric phosphatidylcholines and the highly asymmetric milk sphingomyelin. Specifically, we report trans-membrane structures of the corresponding fluid lamellar phases using small-angle X-ray and neutron scattering, which were jointly analyzed in terms of a membrane composition-specific model, including a headgroup hydration shell. Focusing on terminal methyl groups at the bilayer center, we found a linear relation between hydrocarbon chain length mismatch and the methyl-overlap for phosphatidylcholines, and a non-negligible impact of the glycerol backbone-tilting, letting the *sn1*-chain penetrate deeper into the opposing leaflet by half a CH₂ group. That is, penetration-depth differences due to the ester-linked hydrocarbons at the glycerol backbone, previously reported for gel phase structures, also extend to the more relevant physiological fluid phase, but are significantly reduced. Moreover, milk sphingomyelin was found to follow the same linear relationship suggesting a similar tilt of the sphingosine backbone. Complementary performed molecular dynamics simulations revealed that there is always a part of the lipid tails bending back, even if there is a high interdigitation with the opposing chains. The extent of this back-bending was similar to that in chain symmetric bilayers. For both cases of adaptation to chain length mismatch, chain-asymmetry has a large impact on hydrocarbon chain ordering, inducing disorder in the longer of the two hydrocarbons.

Keywords: mixed-chain lipids; neutron scattering; X-ray scattering; MD simulations

1. Introduction

As the main structural constituents of biological membranes, glycerophospholipids and sphingolipids occur in a large variety of species, differing in their hydrophilic heads, hydrophobic tails and backbone structure. A considerable fraction of the most abundant double-chained membrane lipids exhibit distinct compositional differences of their hydrocarbons [1,2]. Particularly, combinations of a saturated and an unsaturated chain are very common for glycerophospholipids and are therefore widely used in membrane mimics. Some of these, and in particular monounsaturated phosphatidylcholines (PCs) such as palmitoyl oleoyl PC (POPC) or stearoyl oleoyl PC (SOPC) are therefore, well characterized

in their fluid phase structures [3]. In contrast, saturated phospholipids with mixed chain lengths are much less abundant and hence less frequently studied. Large chain length asymmetries including long, saturated chains are, however, frequent in sphingolipids, such as, e.g., sphingomyelin. Sphingomyelin contains a sphingosine backbone of 18 carbons and an acyl chain, which can largely vary in length. Its chain asymmetry and heterogeneity have been shown to impede the formation of liquid-ordered domains in mixtures with cholesterol [4], which might be due to hydrocarbon packing stresses caused either by a penetration of the longer hydrocarbon chain into the opposing leaflet (interdigitation) or by bending the chain back into its host leaflet. Further hydrocarbon chain interdigitation has been also implied in the transleaflet coupling of asymmetric lipid bilayers [5–7].

In order to explore the effects of a hydrocarbon chain interdigitation versus chain backward bending, we focused on the chemically well-defined stearyl myristoyl PC (SMPC), myristoyl stearyl PC (MSPC) and palmitoyl myristoyl PC (PMPC). These lipids melt close to physiological temperatures, but their melting temperature (T_m) strongly depends on the degree of chain length asymmetry [8]. Interestingly, thermotropic data for SMPC, MSPC and dipalmitoyl PC (DPPC) suggest that the T_m is highest for equal chain lengths, which occurs however not for DPPC, but for a hypothetical lipid with an *sn*2-chain that is about 1.5 carbon units longer than the *sn*1 chain. This is usually attributed to the ester bonds that link the acyl chains to the glycerol backbone, which causes an effective tilting of the glycerol backbone with respect to the bilayer central plane [9,10]; see supplementary Figure A1 for lipid structure. On the other hand, this suggests that the hydrocarbons of the DPPC in the lamellar gel phase are slightly interdigitated. This has indeed recently been confirmed by experiments [11]. In addition to indications of the non-equal location of terminal methyl groups in liquid-ordered domains from NMR experiments [12], studies of such effects in the physiologically more relevant lamellar fluid phase are currently missing, but needed to address the aforementioned issues of hydrocarbon-mediated transleaflet coupling.

We therefore studied the fluid lamellar phases of SMPC, MSPC and PMPC using small-angle X-ray and neutron scattering (SAXS/SANS) experiments, exploiting their different contrasts to enhance structural fidelity [13]. In particular, we jointly analyzed scattering data in terms of compositional modeling, applying a slightly modified version of the well-known scattering density profile (SDP) model [14]. The advanced SDP model in combination with the separated form factor technique [15] allowed us to also include scattering intensities at very low scattering vectors and led us to introduce a hydration layer in the lipid's headgroup region. The new model was validated against DPPC and confirmed previously reported structural parameters. We consecutively focused on the fluid structures of SMPC, MSPC and PMPC and also included monounsaturated POPC, SOPC and milk sphingomyelin (MSM), which is a natural lipid extract with high chain length asymmetry.

For the fluid phase lipids, we found a large decrease in the lipids' backbone tilt compared to the gel phase, corresponding to a length difference of about 0.5 carbon units between *sn*-2 and *sn*-1 chains. Moreover, hydrocarbon chain overlap linearly depends on the chain length mismatch for all studied lipids. All-atom molecular dynamics (MD) simulations further helped to disentangle interdigitated from backward-bending hydrocarbons. Interestingly, we found that close to the lipids' backbone, the bending back of hydrocarbons into their host leaflet occurs more frequently than interdigitation from the opposing leaflet. This suggests that the effects of backward-bent hydrocarbons on lateral pressures dominate those of interdigitated hydrocarbons.

2. Results and Discussion

2.1. Introducing a Headgroup Hydration Shell in the Scattering Model for Lipid Bilayers

The SDP model simultaneously accounts for small-angle neutron and the X-ray data (SANS/SAXS) of lipid bilayers thus enabling a unique combination of the different contrasts offered by the two techniques (see, e.g., [13]). The very backbone of the SDP model

is a parsing of the trans-bilayer structure into quasimolecular fragments, based on geometrical considerations [16] and MD simulations [14]. This leads to a representation of the membrane structure in terms of Gaussian-type volume probability distributions (Figure A1). The SDP technique has been highly successful in reporting the high-resolution membrane structures of numerous glycerol- and sphingolipids [3,17–21], including also polyunsaturated phosphatidylcholines [22].

We first implemented the SDP model for a spherical-shell bilayer (i.e., a vesicle) using the separated form factor method [15], which extended the analysis to previously unconsidered low scattering vectors q (see Section 4.3 and Appendix A) and performed a test on the benchmark-lipid DPPC. Using published parameters [3], the model fits very well to the SANS data herein, but not to the low- q region in SAXS (Figure 1a,b). In particular, the SAXS intensity minimum at $q \sim 0.02 \text{ \AA}^{-1}$ is completely missed by the fit, while a good agreement is obtained for $q > 0.1 \text{ \AA}^{-1}$, i.e., the q -range reported previously [3]. We also measured an independently prepared sample of DPPC using a SAXSpoint laboratory camera. Although these data are intrinsically more noisy, particularly at a low q , they clearly agree with synchrotron data and demonstrate that the mismatch of the previous data modeling is a salient feature. Fits to this region have, however, been attained by other models, which unlike SDP, do not depend on the specific composition of the lipid bilayer [23,24]. This indicates that the solution might be an additional degree of freedom in the scattering length density (SLD) profile. Indeed, we found that increasing the contrast in the headgroup region, e.g., by decreasing the headgroup volume, drastically improves the agreement to low- q SAXS-data, while having no significant impact on the neutron form factor (data not shown). Note that a similar approach was reported in [25]. An alternative and physically realistic way to do this is to account for the layer of bound water molecules (Figure 1c,d). In this model, we assumed that the water molecules surrounding the polar headgroup take up a more ordered structure than in the bulk, leading to a higher density in this region. Hydration shells of this kind are extensively used for SAXS data analysis of protein solutions [26,27] and have also been predicted for lipid membranes [16]. We implemented hydration water using an error function that adds one layer of more dense water to the water accessible groups of the lipid bilayer as detailed in Section 4.3 and Appendix A. Our fit estimates the water density in this shell to be 3% higher than in the bulk, which agrees with previous reports on hydration shells for proteins or nucleic acids [26,27]. This increased water density between the headgroups can also be found in all-atom MD simulations (Figures 1e,f and A5), where the volume of water molecules near the lipid headgroups decreased by up to 10% compared to the bulk value.

In achieving the fits shown in Figure 1a,b, we also tested for overfitting or parameter correlations. The SDP model relies on a rather high number of adjustable parameters (i.e., 12 to describe the membrane structure) compared to simpler models using slabs [28] or Gaussian distributions [29]. The high number of adjustable parameters is mostly due to the limited available information about the volumes and structures of the individual moieties in the lipid, which are hardly experimentally accessible and can only be estimated from scattering studies and simulations [30]. Previous studies applying the SDP model led to no obvious temperature or composition-dependent trends for several parameters, especially for those describing the headgroup (σ_{CG} , σ_{PCN} , D_{H1}) and the volume fractions ($R_{CG} = V_{CG}/V_H$, $R_{PCN} = V_{PCN}/V_H$, $r = V_{CH3}/V_{CH2}$, $r_{12} = V_{CH}/V_{CH2}$) [3,20]; see Tables A2 and A3 for a list of all SDP parameters.

Parameter correlations were analyzed using a Markov chain Monte Carlo (MCMC) approach as described in Section 4.3 (see also [31]). MCMC provides the probability density profiles of the used model parameters and, if plotted in two dimensions, correlations between them (Figure 2). Plateaus of high probability as seen in, e.g., (Figure 2c), suggest strong correlations, meaning that the quality of the fit will only change minimally if one moves along iso-probability regions. Small differences in the experimental noise can therefore lead to large changes in these parameters, making the estimates of the most likely value (or global minimum) less reliable. In our case, we observed strong correlations

between headgroup parameters, such as the positions of carbonyl-glycerol and phosphate groups (Figure 2a). Furthermore, the volume fractions (R_{CG} , R_{PCN} , r) are very flexible parameters insofar that they correlate with the standard deviations of their respective Gaussians (σ_{CG} , σ_{PCN} , σ_{CH3}). Figure 2b shows for example the correlation between r and σ_{CH3} . In the following, σ_{CH3} will be one of our parameters of interest. Therefore, we decided to fix the volume of the CH3 group, along with those of the other moieties to the values recently published in [30] (see Tables A2 and A3), to maximize the comparability between different lipids. This also reduces the number of adjustable parameters for the trans-bilayer structure by three (four in the case of mono-unsaturated lipids) compared to previous studies. We also fixed $\sigma_{CholCH_3} = 3 \text{ \AA}$, as has been done before [3], and $\sigma_{CH_2} = 2.5 \text{ \AA}$.

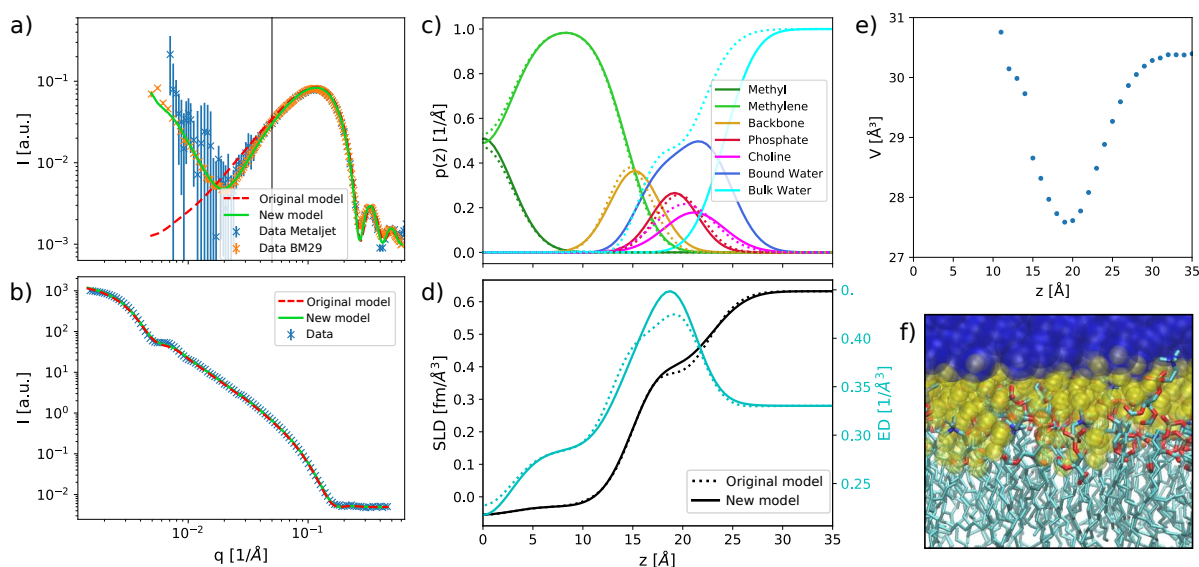


Figure 1. Comparison of the present and original SDP-models [3] for DPPC at 50 °C. The two models mainly show differences in the low- q region of SAXS (a), whereas they overlap in the case of SANS in 100% D₂O (b). The vertical black line in (a) marks the lower limit of the accessible range in the original study. (c) shows volume probability distributions $p(z)$ of the lipid moieties through the bilayer profile. The resulting neutron SLD (black) and electron density profiles (cyan) are drawn in (d). Dashed lines correspond to the original, solid lines to the new model. MD-simulations confirm the presence of higher-density water around the headgroup region, where the volume-per-water molecule is decreased by up to 10% (e). This effect is schematically illustrated in a simulation snapshot of a DPPC bilayer (f) where bulk water is shown in blue (with $z > 25 \text{ \AA}$) and hydration water in yellow (with $z < 25 \text{ \AA}$). Lipids are drawn in a licorice representation with carbons in cyan, nitrogen in blue, phosphate in tan and oxygen in red.

Figure 2c also shows how the introduction of the hydration shell is in fact an alternative to varying the volume of the headgroup V_H . The volume per bound water molecule V_{BW} is linearly correlated with V_H , if we keep the headgroup structure constant. Varying either of them is thus a valid approach to increase the headgroup SLD. We chose to include the hydration shell in order to conform to published values for the volumes [30]. Additionally, if we keep the headgroup volume constant ($V_H = 328 \text{ \AA}^3$), V_{BW} correlates with the width of the headgroup and thus the number of bound water molecules (shown by the correlation between the distance phosphate to choline d_{Chol} and V_{BW} in Figure 2d). The distribution shows the highest probability density between $V_{BW} = 29.0\text{--}29.5 \text{ \AA}^3$ for V_{BW} , which also leads to a physically realistic range of distances d_{Chol} . We chose $V_{BW} = 29.3 \text{ \AA}^3$, which is at the peak of the distribution.

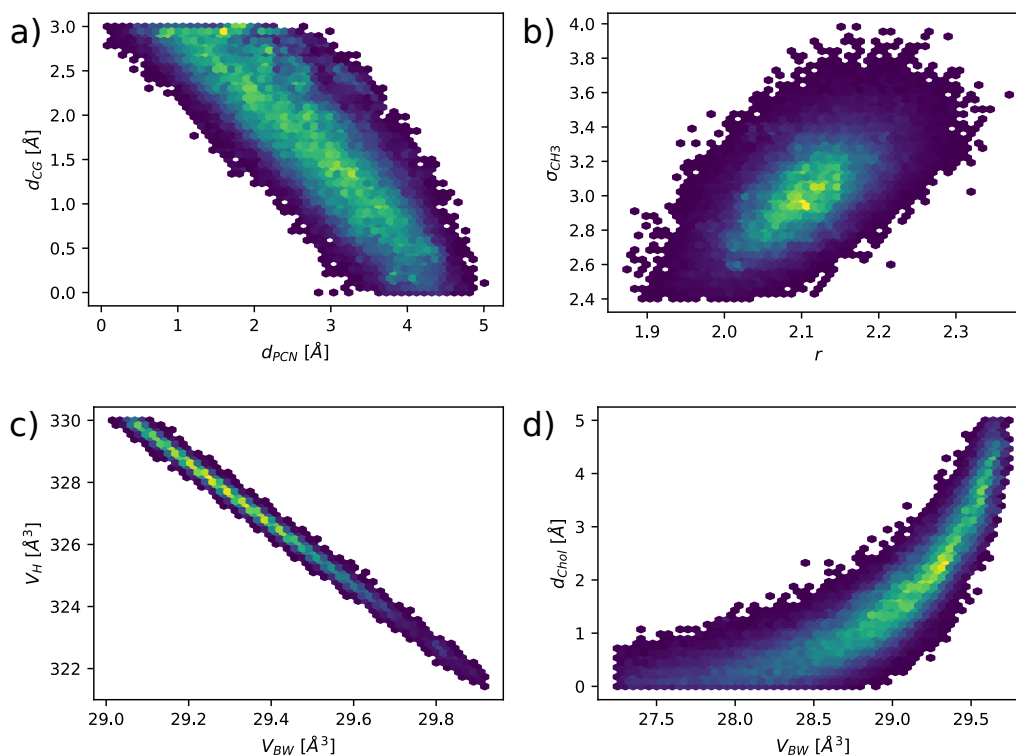


Figure 2. Exemplary parameter correlations in the joint SAXS/SANS-analysis of DPPC vesicles, visualized by MCMC sample histograms. Colored spots correspond to Monte Carlo samples: the brighter the color, the more the samples are contained in the point, thus corresponding to higher probability: (a) shows the correlation between the positions of the carbonyl-glycerol and the phosphate group; (b) between terminal methyl relative volume r and distribution width σ_{CH_3} ; (c) between volume per bound water molecule V_{BW} and headgroup volume V_H (with constant headgroup structure); and (d) between V_{BW} and the position of the choline- CH_3 group (with constant V_H).

Despite the improved fit of SAXS data at $q < 0.1 \text{ \AA}^{-1}$, we observed only minor changes in membrane structural parameters (Table A2). This can be expected due to the excellent agreement of the previous SDP model for $q > 0.1 \text{ \AA}^{-1}$, i.e., for scattering vectors probing distances in the order of the membrane thickness and below. The newly introduced hydration shell gives us an estimate of the number of bound water molecules per lipid. Note that this is not an explicit fitting parameter, but is defined by the integral over the water volume probability density function within the Luzzati thickness, as has been in detail described in [32]. The number of bound water molecules we obtained varied between 9.6 and 12.8 for saturated PCs and MSM, and was about 16 for the more loosely-packed monounsaturated PCs. These numbers agree roughly with previously published values [32,33]. However, there is a wide spread in measured values, mostly due to varying definitions of n_w . Furthermore, in our case we attribute a large uncertainty to these values, as it is strongly influenced by the choice of other parameters as discussed above.

2.2. Membrane Structure and Interleaflet Hydrocarbon Partitioning

In the next step, we applied our modified SDP analysis to various chain-asymmetric PCs as well as the highly asymmetric milk-sphingomyelin extract (average acyl chain length: C22:0). Fits and all parameters are reported in the appendix, in Figures A2 and A3 and Tables A2 and A3. High-resolution structural data for POPC and SOPC were detailed previously [3]. Again, we find no substantial modifications to reported structural details upon the application of our model. To the best of our knowledge, structural details for MSPC, SMPC, PMPC and MSM have not been reported previously, however. Notably,

we found that the area per lipid, A , of all four lipids is very similar and that A of MSPC, SMPC and PMPC agrees within experimental uncertainty with the A of DPPC. This demonstrates that chain-asymmetry has no major influence on the general packing of these lipids within the bilayer in the biologically most relevant lamellar fluid phase far above the melting transition. Substituting the *sn2*-hydrocarbon with an oleoyl chain significantly increases A , in agreement with [3]. The thickness of the bilayer, D_B , and the thickness of the hydrocarbon chain region, $2D_C$, in turn, varies between MSPC, SMPC, PMPC and MSM according to the total number of methylenes. Interestingly, $D_B = 40.3 \text{ \AA}$ for DPPC, MSPC, and SMPC, suggesting that the overall membrane thickness depends for saturated hydrocarbons only on the average number of carbons per chain and is not even influenced by the extreme acyl chain asymmetries of MSPC and SMPC. Note also that the slightly different $2D_C$ values for these three lipids are equal within experimental resolution.

Several fluid phase structures of sphingomyelins have been recently published [21,34], namely palmitoyl-sphingomyelin (PSM), stearyl-sphingomyelin (SSM) and egg yolk-sphingomyelin (ESM). In both studies, the structure of PSM was measured at $45 \text{ }^\circ\text{C}$; the reported areas per lipid differ, however, possibly due to the different experimental approaches (X-ray surface diffraction on stacks of bilayers vs. SAXS/SANS on vesicles). For ESM, a natural lipid mixture such as MSM, but with PSM as its main constituent and the same structure as for PSM was measured [34], suggesting that hydrocarbon chain heterogeneity does not induce a significant disorder in the chain region. For SSM, however, the reported $A = 62.5 \text{ \AA}^2$ is considerably higher than the one for PSM [21]. Our result for MSM is again higher ($A = 64.8 \text{ \AA}^2$), using a similar methodology as reported in [21]. The lateral packing density of sphingomyelin might therefore be directly related to the (average) length of its acyl-chain: PSM/ESM (16:0) < SSM (18:0) < MSM (22:0). Bilayer thickness and terminal methyl overlap are higher for MSM than for the other published lipids, which is expected, again due to its longer acyl chains.

In the following we focus on the hydrocarbon chain interdigitation, which can be expected to be significant given the chain asymmetries of the presently studied lipids. Interleaflet interdigitation may, however, also arise from the specific backbone structure of glycerophospholipids, where the ester bonded hydrocarbon at *sn2* protrudes less into the bilayer core even at nominally equal chain length [10]. Here, we use the width of the terminal methyl group, σ_{CH3} , as a measure for hydrocarbon chain interdigitation. σ_{CH3} varied significantly for the different lipids studied (Table 1). In order to derive a possible correlation between chain asymmetry and σ_{CH3} , we define the chain length mismatch $\Delta l_C := l_C(sn1) - l_C(sn2)$. Furthermore, we estimated Δl_C by assuming l_C to be equal to the half-hydrophobic thickness D_C of the corresponding chain-symmetric lipid bilayers (see Table A5). Figure 3 presents the resulting dependence of σ_{CH3} on Δl_C . We observed a nearly linear increase in hydrocarbon overlap with increasing chain length mismatch.

Table 1. Results from joint SAXS/SANS data analysis/from MD simulations: Area per lipid A , Luzati thickness D_B , hydrophobic thickness $2D_C$, standard deviation of the terminal methyl Gaussian σ_{CH3} , relative methyl overlap γ (dimensionless). The column ϵ gives an error estimate relative to the values in the table.

	ϵ (%)	DPPC	MSPC	SMPC	PMPC	POPC	SOPC	MSM
A [\AA^2]	2	63.1	62.2	62.0	62.9	67.5	68.8	64.8
D_B [\AA]	5	40.3	40.3	40.3	38.4	38.4	39.4	42.1
$2D_C$ [\AA]	3	28.6	29.1	29.2	27.0	28.4	29.2	32.8
σ_{CH3} [\AA]	5	2.91	3.34	3.67	3.12	3.41	3.31	4.29
n_W	10	9.7	11.3	12.8	12.1	16.6	15.1	9.6
γ	7	0.43	0.55	0.65	0.54	0.60	0.55	0.71

SMPC and MSPC possess a priori the same absolute value of chain length mismatch. In this case, it is, however, important to take the well-known tilting of the glycerol back-

bone [9] into account, which effectively lengthens the *sn1* and shortens the *sn2* chain. We therefore introduce a correction d_{tilt} on the chain length-mismatch (Equation (1)):

$$\Delta l_{C,corr} := l_C(sn1) - l_C(sn2) + d_{tilt} \quad (1)$$

We estimate its value by assuming a linear relation between the corrected, absolute chain length mismatch $|\Delta l_{C,corr}|$ and σ_{CH_3} . In order to evaluate the most likely value for d_{tilt} , we use an iterative approach, alternately optimizing:

$$\sigma_{CH_3} = k|\Delta l_{C,corr}| + \sigma_{CH_3}^{sym} \quad (2)$$

and Equation (1). Here, k is the slope and $\sigma_{CH_3}^{sym}$ is the terminal methyl width of a hypothetical lipid of equally long chains; for details, see the pseudocode Algorithm A1.

The result is shown in the upper panel of Figure 3, with the value $d_{tilt} = 0.48 \text{ \AA}$. In terms of chain length dependence on the number of carbons (Table A5), this corresponds to about half the length of a CH_2 -segment. The parameters of the linear fit result in $k = 0.20$ and $\sigma_{CH_3}^{sym} = 2.75 \text{ \AA}$. The chain overlap thus rises only slowly with the chain length mismatch (20% of its length), which fits into a bilayer picture of fluid hydrocarbon chains, not directly pointing towards the center, but significantly diverted and/or bent. Note that our analysis indicates that even DPPC has some inherent hydrocarbon interdigitation.

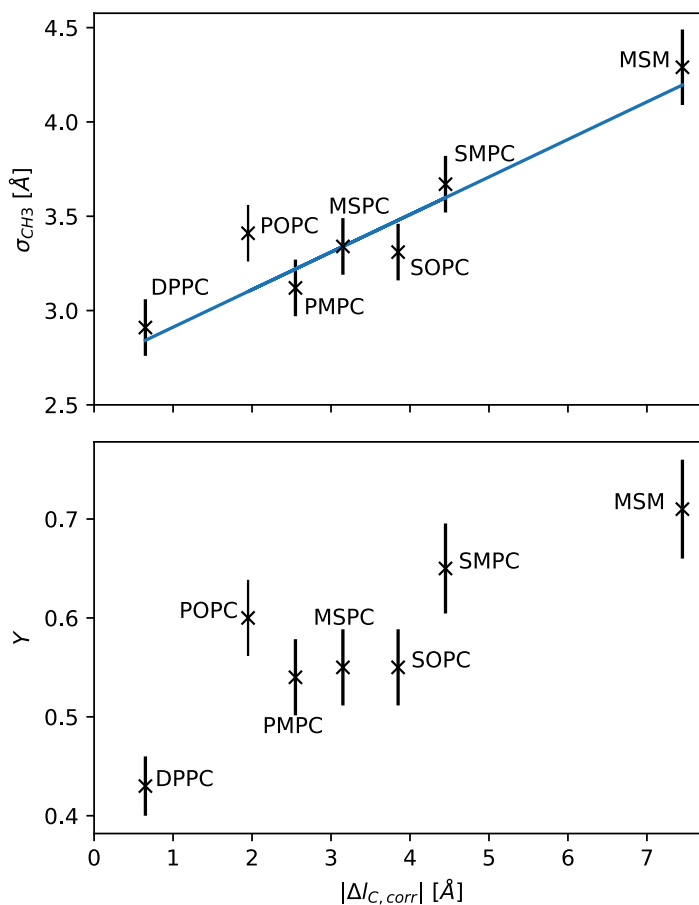


Figure 3. Standard deviations σ_{CH_3} of the Gaussian volume distributions of the terminal methyl groups (**upper plot**) and the relative interdigitation parameters (**lower plot**), plotted over the corrected chain length mismatch $|\Delta l_{C,corr}|$ of the respective lipids. The upper plot contains a linear regression according to Equation (A1). σ_{CH_3} over uncorrected values $|\Delta l_C|$ are shown in Appendix D Figure A4.

2.3. Quantifying Hydrocarbon Chain Overlap Relative to the Hydrophobic Thickness

The standard deviation of the Gaussian accounting for the terminal methyl groups σ_{CH_3} gives a measure for hydrocarbon chain interdigitation or, more precisely, the terminal methyl dislocation. However, in some cases, it might be helpful to describe this quantity relative to the thickness of the hydrocarbon layer to estimate its effect on chain disordering. We therefore introduce the dimensionless parameter Y and connect it to the SDP model, by defining the state $Y = 0$ (no chain overlap) when the volume probability density of the CH_3 -groups reaches one at the bilayer center. This is the case for $\sigma_{CH_3}^0 = 2V_{CH_3}/(\sqrt{2\pi}A)$. Furthermore, we define the state $Y = 1$ by $3\sigma_{CH_3} = D_C$, representing a smeared-out state, where the CH_3 volume is distributed over the whole hydrocarbon region (fully interdigitated). This leads to the definition:

$$Y := \frac{\sigma_{CH_3} - \sigma_{CH_3}^0}{D_C/3 - \sigma_{CH_3}^0}. \quad (3)$$

The extreme states ($Y = 0, 1$) are most likely purely theoretical. $\sigma_{CH_3}^0$ is around 1.4 \AA for the studied lipids, while results from Section 2.2 suggest that $\sigma_{CH_3} \geq 2.75 \text{ \AA}$ for PC-lipids. Moreover, the σ -values of other molecular groups also lie far above this value, suggesting that overall fluctuations of the molecules will not permit localization to such an extent. On the other hand, for Y approaching 1, the probability distribution of the CH_3 group might no longer follow a Gaussian shape. In intermediate cases, as for systems used in this study, Y could mark a major characteristic of a bilayer. Here, our results suggest that the relative dislocation of the chain termini also monotonously increases with hydrocarbon chain mismatch (Figure 3), and can reach up to $\sim 70\%$ of hydrocarbon chain thickness. POPC, interestingly, does not fit into this picture, having within experimental uncertainty a relative chain overlap similar to that of SOPC or SMPC. This is most likely a signature of the unsaturated hydrocarbon, which increases due to its kink at the *cis* double bond the width of the distribution of the terminal CH_3 .

2.4. Chain Interdigitation and Back-Bending in Simulated Systems

From our experiments, we were not able to distinguish between lipids in the inner and outer leaflets. Hence, broadening of the CH_3 -Gaussian could be either caused by interdigitation or by the back-bending of the longer hydrocarbon chain. In order to clarify this issue, we performed MD-simulations on DPPC, MSPC, SMPC, PMPC and dimyristoyl PC (DMPC) to gain access to details in the behavior of the hydrocarbon chains at the bilayer center. Simulation snapshots and the overall volume probability distributions of terminal methyl groups of DPPC, MSPC, SMPC, PMPC are shown in Figure 4. In all cases, the CH_3 distributions are centered in the middle of the bilayer, although their widths are broader than our experimental values (Table A2). However, the trend over the chain length mismatch agrees with our experimental observation. The snapshots additionally show a significant number of chains penetrating deeply into the opposing leaflet for MSPC, PMPC and SMPC. Overlaid are the volume probability distributions of the terminal methyls, which result from fluctuations of both the individual chains and whole lipid molecules (protrusions).

A closer look into the shape of the CH_3 distribution functions reveals that they actually decay slower than Gaussians (Figure A6). Separating the distribution into contributions from *sn1* and *sn2*-chains, from inner and outer leaflet (Figure 5) leads to further insight. In particular, one can see that the deviation from a bell-shaped function is connected to the shape of the distributions of the individual chains, which are slightly asymmetric with a tailing to the back towards their headgroups. This tailing is equally present for DPPC and thus not a consequence of chain asymmetry. However, while for DPPC all methyl groups clearly have the peaks of their distributions in their own leaflet, the distributions of the shorter chains from inner and outer leaflets are well separated for MSPC, PMPC and SMPC, while the long chains overlap much more. In the case of MSPC and PMPC,

the long chain distribution functions from opposing leaflets almost perfectly overlap in the center of the lipid bilayer and only deviate in the tailing toward the headgroup region. This suggests that there is a balance between hydrocarbon interdigitation and back-bending in the center of the membrane, while contributions from backward bent chains dominate over interdigitated hydrocarbons when moving closer to the glycerol backbone. This asymmetric part accounts for 8% of the total area of the distribution (Figure A6). This can be alternatively visualized by plotting the fraction of lipids with their methyl termini located above a certain distance from the center of the bilayer (Figure A7). In the case of SMPC, the long chains penetrate deeper, with the maxima of their distributions in the opposing leaflet.

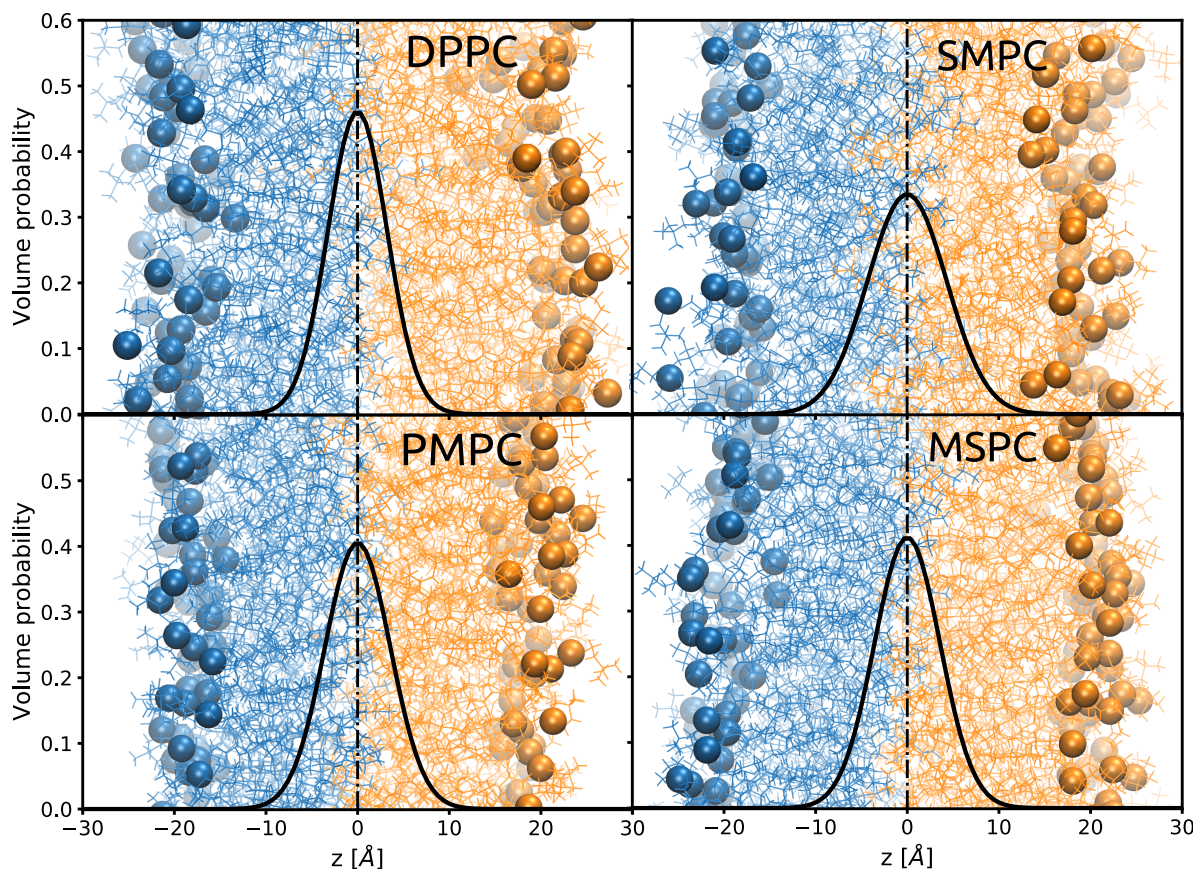


Figure 4. Snapshots of MD simulations for saturated phosphatidylcholines. Spheres mark the positions of phosphorus. The overlaid graphs represent the volume probability distributions of the CH₃ groups, summed over all lipids in the bilayer.

An interesting consequence of the prevalence of contributions from back-bent hydrocarbons further away from the bilayer center becomes clear considering that packing defects typically have larger effects on the lateral pressure profile, if they occur closer to the glycerol backbone [35]. That is, even if we do find similar lipid areas for DPPC, SMPC, MSPC, and PMPC, their stored elastic energies may differ significantly and will be dominated by the back-bent hydrocarbons, not by the interdigitating ones.

Another effect of the hydrocarbon chain mismatch can be seen in the orientational order parameter S_{CH} of the hydrocarbons, which was also derived from MD simulations (Figure 6). This dimensionless number represents the average orientation of the respective C–H bonds relative to the bilayer normal [36] and approaches 1 for perfectly ordered chains. Hydrocarbons are labelled by the number n_C , starting with 1 at the ester bond. In the case of chain-symmetric lipids, the strength of the attractive van der Waals interactions between the hydrocarbon chains increases with chain length, leading to a higher ordered state,

as can be seen in the example of DMPC (14 carbons/chain) and DPPC (16 carbons/chain). If there is a chain length mismatch, however, the longer chain lacks its direct neighbor at its tip, decreasing its order. In fact, order parameters of the longer chains in MSPC, SMPC and PMPC are close to the ones of DMPC for low n_C and well below those of DPPC. Again, we see a difference between MSPC and SMPC: due to the glycerol-tilt, the 18:0 chain in MSPC has a lower effective length difference to its 14:0 chain and is therefore more ordered than in SMPC. On the other hand, the behavior of the short myristoyl-chain is almost identical for all lipids, as they all have a long neighboring chain to optimize van der Waals' interactions. Solely the *sn1*-chain in DMPC, again being longer than its *sn2* due to the glycerol-tilt, has slightly lower order parameters.

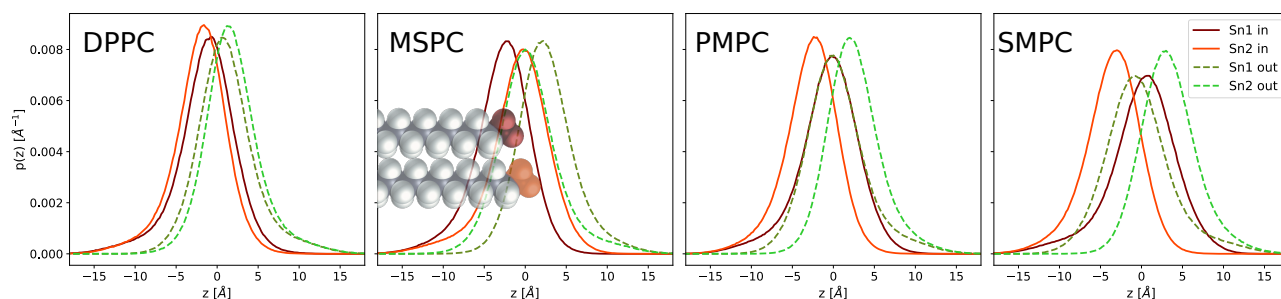


Figure 5. Number probability distributions $p(z)$ from MD simulations of the terminal methyl groups, separately plotted for lipids from the inner (left) and outer (right) leaflet, as well as for *sn1*- and *sn2*-chains.

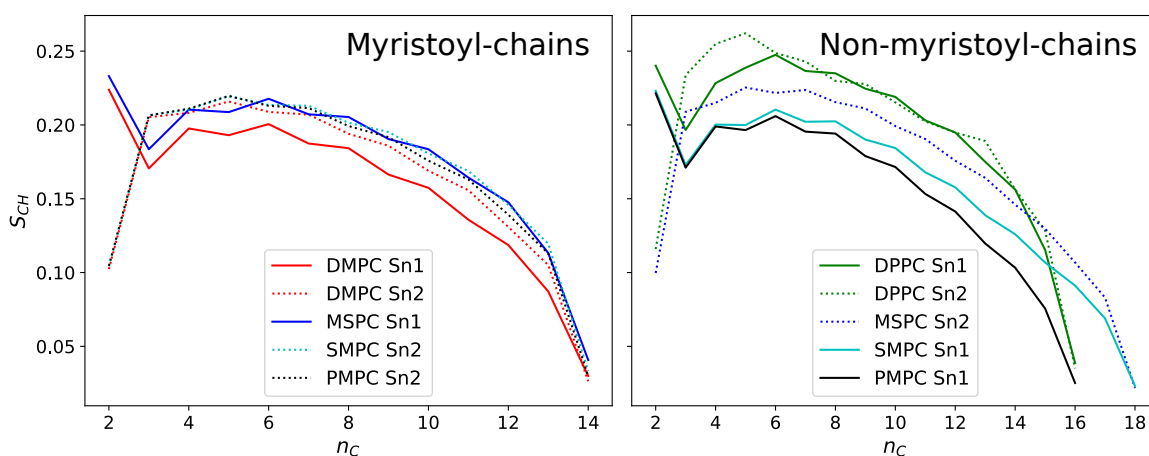


Figure 6. Orientational order parameters S_{CH} from MD-simulations for individual lipids and chains.

3. Conclusions

We report trans-bilayer structural profiles of free-floating large unilamellar vesicles containing several chain-asymmetric PCs as well as milk sphingomyelin. Additionally, we introduced a shell of hydration water into the well-established SDP model, which allowed us to model low- q SAXS-data conserving previously reported lipid headgroup volumes. For fully saturated PCs, we observed no significant effects on the overall bilayer structure resulting from the chain asymmetry, except for the overlap of their terminal methyl groups in the membrane center. This overlap displays a linear dependence on the length difference between both acyl chains, if one considers the tilt of the glycerol backbone. We found that the tilt elongates the *sn1*-chain by 0.48 \AA , which is about one third of the value previously reported for gel phases [8]. For PCs with a saturated and an unsaturated chain, we find a poorer agreement with the linear relation between chain length difference and hydrocarbon overlap, which might be a consequence of the kink induced at the double bond. MSM in

turn is well described by the model and shows, as expected, the highest hydrocarbon chain overlap of all studied lipids. It has, however, a lower packing density than fully saturated PCs, which agrees with other recent studies, suggesting that long acyl chains lead to a lower packing density in the case of sphingomyelins.

Using MD simulations, we found that every chain, which does not have an equally long or longer direct neighbor, is significantly more disordered—not only at its tip, but over the whole chain length. Moreover, close investigation of the positions of the methyl groups revealed that chains are not symmetrically distributed around a mean position, but have a higher fraction of chains bending back towards their own headgroup. Since membrane elasticity is more affected by packing defects close to the lipids' backbone, this suggests a dominating role of back-bent over interdigitated hydrocarbons in any membrane-mediated effect related to lateral pressure changes in this region of the bilayer.

4. Materials and Methods

4.1. Lipids, Chemicals and Sample Preparation

All lipids were purchased in the form of powder from Avanti Polar Lipids (Alabaster, AL, USA) and used without further purification. Chloroform and methanol (pro analysis grade) were obtained from Merck KGaA, Darmstadt, Germany. Lipid films were prepared by dissolving weighted amounts in organic solvent chloroform/methanol (2:1, vol/vol) followed by evaporation under a soft N₂ stream and overnight storage in a vacuum chamber. The dry films were hydrated with ultrapure H₂O, D₂O or a mixture of both, and equilibrated for one hour at 50 °C followed by 5 freeze-and-thaw cycles using liquid N₂ and intermittent vortex-mixing. Large unilamellar vesicles (LUVs) were obtained by 51 extrusions with a hand held mini extruder (Avanti Polar Lipids, Alabaster, AL, USA) using a 100 nm pore diameter polycarbonate filter. Vesicle size and polydispersity was determined via dynamic light scattering using a Zetasizer NANO ZS90 (Malvern Panalytical, Malvern, UK).

4.2. Scattering Experiments

SANS measurements were performed at D22, Institute Laue-Langevin, Grenoble, France [37]. We measured three configurations at sample-to-detector distances of 1.6, 5.6 and 17.8 m with corresponding collimations of 2.8, 5.6 and 17.8 m and a wavelength of 6 Å ($\Delta\lambda/\lambda = 10\%$). Data were recorded on a ³H multidetector of 128 linear sensitive Reuter-Stokes[®] detector tubes, with a pixel size of 0.8 × 0.8 cm. Samples were filled in Hellma 120-QS cuvettes of 1 mm pathway and measured at 50 °C. Lipid concentrations were 5 mg/mL in 100% D₂O, 10 mg/ml in 75% D₂O and 15 mg/ml in 50% D₂O. Data were reduced using GRASP (www.ill.eu/users/support-labs-infrastructure/software-scientific-tools/grasp/ accessed on 25 June 2019), performing flat field, solid angle, dead time and transmission correction, normalizing by incident flux and subtracting contributions from empty cell and solvent.

SAXS data were recorded at BM29, ESRF, Grenoble, France (Experiment MX-2282), equipped with a Pilatus3 2M detector, using a photon energy of 15 keV at a sample-to-detector distance of 2.867 m [38]. Samples were measured at a concentration of 10 mg/mL, at 50 °C and exposed 20 times for 2 s in a flow-through quartz capillary of a 1 mm light path length. Data reduction and normalization were performed by the automated ExiSAXS system; for the subtraction of the solvent and capillary contributions SAXSutilities 2 (www.saxsutilities.eu accessed on 29 October 2020) was used. Additionally, DPPC LUVs were measured using a SAXSpoint camera (Anton Paar, Graz, Austria) connected to a MetalJet X-ray generator (Excillum, Kista, Sweden) with a liquid, Ga-rich alloy, jet anode. Data were recorded using an Eiger R 1 M detector system (Dectris, Baden-Daettwil, Switzerland) and reduced via the software SAXSanalysis (Anton Paar).

4.3. SDP-Modeling of Lipid Bilayers

Small-angle scattering (SAS) data were analyzed in terms of a probability-density-based approach, also known as the scattering density profile (SDP) model, which is frequently used in small-angle scattering and reflectometry, e.g., [14,39–41]. We used the same parsing scheme as Kučerka et al. [3] for saturated phosphatidylcholines, describing the volume probability distributions of individual moieties of the lipid molecules by Gaussian distributions (terminal methyls, carbonyl-glycerol backbone, phosphate group, choline-CH₃ group) and error-functions (hydrocarbon chains without terminal methyls), see Figure 1 and Appendix A. From these functions, the neutron or X-ray scattering length density profiles can easily be calculated. The model in its current form has been applied to describe SAXS data from LUVs in the range of scattering vectors, q from 0.1 to 0.6 Å⁻¹; lower- q data were excluded from the SDP analysis. This motivated us to introduce a few adjustments, permitting us to extend the q range by one order of magnitude.

Upon combining the SDP-model, which describes a flat bilayer, with an appropriate model to describe the overall vesicle shape—according to the separated form factor model [15], we found that the calculated intensities did not fit experimental SAXS data in the low- q region (Figure 1). The position of the first minimum connected to the membrane structure (see Figure 1a, $q \sim 0.02$ Å⁻¹) suggests that the electron density in the head group region is higher than initially thought. One way to account for this is by introducing a layer of higher density water around the headgroup. This was inspired by previous considerations about lipid bilayers [39] as well as the established necessity to include a hydration layer in protein and nucleic acid models [26]. Hydration water was included into the model using another error-function adjacent to the ones describing the hydrocarbon chains, with the same smearing parameter σ_{CH2} and reaching up to the position of the choline-CH₃ group in addition of σ_{Chol} . This ensures that the hydration layer always surrounds the headgroup by roughly one water molecule. We used a width of $d_{shell} = 3.1$ Å around the lipid head group and set the upper limit for the volume per molecule to the bulk water value of 30.28 Å³ (see Appendix B Table A4).

The second modification addresses the mismatch of the model with the depth of bilayer-related minima of the X-ray data. We were able to account for this by including a Gaussian polydispersity on the membrane thickness. It is implemented by varying only the width of the hydrocarbon chain region, while keeping all other parameters unchanged. One could attempt to extend the model to a more flexible headgroup for states of different unit cell area, however, as described in the result section. However, one would risk that area-compressed states could end up with an over-filled unit cell. Furthermore, headgroup parameters from scattering data are generally ill-defined and highly correlated; therefore we remained with a static headgroup. A possible physical explanation for this effect is the influence of peristaltic modes, which were found for this q -region in MD-simulations [42]. These fluctuations, however, do not exert the same amplitudes for all wavelengths. This might also explain why our implementation, despite the large improvement in fit quality, still did not perfectly match the form factor minima.

We further note that the various volume probability functions in our model do not necessarily overlap perfectly for all configurations of positions and standard deviations, potentially leading to an overfilling of the unit cell, which the model would automatically compensate for with “negative water”. To have our optimization algorithm automatically avoid these regions, we introduced a penalty on the cost function minimized in the procedure. To do this, we calculated the number of negative water molecules n_{-H_2O} in each iteration and modified the cost function $\chi^2 \rightarrow \chi^2 + n_{-H_2O}^2 / \sigma_{-H_2O}^2$. The strength of the penalty can be tuned by adjusting $\sigma_{-H_2O}^2$.

In order to “equalize” contributions of SAXS and SANS data to fitting results, we apply a semi-empirical method to weight the cost functions (χ_i^2) of all datasets, according to the examined q -ranges as well as the number of data points recorded, using:

$$\chi^2 = \chi_X^2 + \alpha \chi_N^2, \quad (4)$$

where χ_X^2 and χ_N^2 are the cost functions for X-ray and neutron scattering data, respectively. We determine the scaling coefficient α from the ratio of densities of points in the q -space:

$$\alpha = \frac{n_X / (q_X^{\max} - q_X^{\min})}{N_N n_N / (q_N^{\max} - q_N^{\min})} \quad (5)$$

$n_{X/N}$ being the number of points per X-ray/neutron measurement. If there is more than one neutron contrast, we divide in addition by the number of neutron measurements N_N , provided that all neutron measurements have the same density of points.

Using this approach, we examined the impact of contrast variation by changing the H₂O/D₂O ratio in the solvent. In the case of MSPC, SMPC and PMPC, where we measured 3 contrasts using 100%, 75% and 50% D₂O, we found only negligible differences in the resulting parameters when fitting either all 3 or only 100% D₂O. This is due to the dominant contrast emerging from the protiated hydrocarbon chains. Lipid headgroups are roughly contrast matched at 50% D₂O. However, their contribution is already small at 100% D₂O. Hence, there is only little gain in information from including the 50% and 75% D₂O measurements. For the analysis of POPC, SOPC and MSM, we therefore only used one SANS-contrast.

Parameter optimization was performed using the Trust Region Reflective algorithm from the SciPy 1.6.2 package [43]. To analyze parameter correlations within the model, we used the No-U-Turn Sampler within the PyMC3 package [44,45].

4.4. Molecular Dynamics Simulations

At the time of bilayer construction, the three lipids, MSPC, PMPC and SMPC, were not available in the CHARMM-GUI web server [46–50]. We therefore first used CHARMM-GUI to construct the bilayers of pure distearoyl PC (DSPC) or pure DPPC lipids. Each bilayer had 100 lipids per leaflet (200 lipids total) and was hydrated with 45 water molecules per lipid (without any salt ions). PMPC was then built from the DPPC bilayer by removing the last carbon on the *sn1* chain (C216 in CHARMM36 notation) together with its 3 hydrogens (H16R, H16S, H16T) and the 2 hydrogens bonded to the last-but-one carbon on that same chain (H15R and H15S). Carbon C215 was then changed to hydrogen (H14T) by modifying its atom name, type and charge accordingly to complete the terminal methyl group of the myristoyl chain of the newly created PMPC lipid.

The MSPC and SMPC bilayers were similarly generated from the DSPC bilayer by removing the last 3 carbons and their hydrogens on the *sn1* or *sn2* chains, respectively, then modifying the 15th carbon by removing its hydrogens and changing its name, type and charge to complete the terminal methyl group of the myristoyl chain of the newly created lipids. Additionally, a pure DMPC bilayer was constructed with CHARMM-GUI. The bilayer had 100 lipids per leaflet and was hydrated with 45 water molecules per lipid.

All simulations were run with the NAMD software [51] and the CHARMM36 force field for lipids [52,53]. Each of the bilayer systems, excluding DMPC, was energy minimized for 1200 steps, then simulated for a total of 1 ns with an integration time-step of 1 fs before the production run which employed a time-step of 2 fs. DMPC was equilibrated following CHARMM-GUI's 6-step equilibration protocol. All simulations were run at a constant temperature of 50 °C (323K) and a pressure of 1 atm maintained by NAMD's Langevin thermostat and Nose–Hoover Langevin piston, respectively. Long-range interactions were modeled with a 10–12 Å Lennard-Jones potential using NAMD's vdwForceSwitching option. All hydrogen bonds were constrained with the rigidbonds parameter set to all and electrostatic interactions were modeled using the particle mesh Ewald (PME) method with a grid spacing of 1 Å. The four simulations were run for a total of 1 μs (MSPC), 0.969 μs (PMPC), 1.03 μs (SMPC) and 0.8 μs (DMPC). The first 50 ns were discarded and the rest were used to calculate the number density profile of each system with the density plugin in VMD [54]. The calculation was done at a resolution (slab thickness) of 0.2 Å on trajectory frames spaced 100 ps apart. For comparison, a system of a DPPC bilayer simulated under

the same conditions was taken from [55] and its number density profile was calculated following the same procedure.

The volumes of water molecules from the simulations were calculated with the Voro++ software library (<http://math.lbl.gov/voro++/> accessed on 15 July 2021). Briefly, the indices and coordinates of all atoms in a trajectory frame were used as input to Voro++ which partitioned the space into a discrete number of 3-dimensional Voronoi cells by taking into account the periodic images of the simulation box. The resulting volumes of the water atoms were then extracted, properly grouped to obtain the volumes of the individual water molecules, and binned according to their z positions in MATLAB. The results from all frames were averaged to produce the final plot of water volume as a function of z.

Author Contributions: Conceptualization, M.P.K.F., M.D., F.A.H., E.F.S. and G.P.; data curation, M.D.; formal analysis, M.P.K.F., M.D. and F.A.H.; investigation, M.P.K.F., M.D., H.L.S., E.F.S. and L.P.; methodology, M.P.K.F. and E.F.S.; software, M.P.K.F.; supervision, G.P.; visualization, M.P.K.F.; writing—original draft, M.P.K.F. and G.P.; writing—review and editing, M.P.K.F., M.D., F.A.H., H.L.S., E.F.S., L.P. and G.P. All authors have read and agreed to the published version of the manuscript.

Funding: This research was supported by the ILL graduate school, Ph.D. No. 181-19. M.D. is supported by the National Institute of General Medical Sciences of the NIH under Award Number F32GM134704. F.A.H. is supported by National Science Foundation grant MCB-1817929 and NIH/National Institute of General Medical Sciences grant R01GM138887. Open access funding was provided by the University of Graz.

Data Availability Statement: SANS data is available from ref. [37]. All other data can be obtained from the authors upon reasonable request.

Acknowledgments: We thank Petra Pernot for technical assistance at BM29, ESRF.

Conflicts of Interest: The authors declare no conflict of interest.

Abbreviations

The following abbreviations are used in this manuscript:

SAXS	Small-angle X-ray scattering
SANS	Small-angle neutron scattering
SLD	Scattering length density
SDP	Scattering density profile
MD	Molecular dynamics
MCMC	Markov chain Monte Carlo
LUV	Large unilamellar vesicle
DPPE	1,2-dipalmitoyl-sn-glycero-3-phosphocholine
MSPC	1-myristoyl-2-stearoyl-sn-glycero-3-phosphocholine
SMPC	1-stearoyl-2-myristoyl-sn-glycero-3-phosphocholine
PMPC	1-palmitoyl-2-myristoyl-sn-glycero-3-phosphocholine
MSM	Milk sphingomyelin

Appendix A. Full SAS-Model

The signal in small-angle scattering is described by the absolute square of the form factor, meaning the Fourier-transform of the scattering length density profile (SDP). As the overall vesicle shape and the trans-bilayer structure contribute on different length scales, we can describe them separately and approximate the bilayer as an infinite flat sheet [15]. As we are using error-functions and Gaussians to describe the SDP, the required Fourier transforms are given in the following. Note that the formulas omit the imaginary part of the form factor, which is antisymmetric around the origin and therefore vanishes for a symmetric trans-bilayer profile.

Algorithm A1 Iterative fitting of the chain length mismatch correction to a linear function
Parameters behind ; in function definitions designate fixed inputs in the optimizations
Data inputs are $\Delta l_C, \sigma_{CH3}$

```

function Flin( $k, \sigma_{CH3}^{sym}; |\Delta l_{C,corr}|$ )
    return  $k|\Delta l_{C,corr}| + \sigma_{CH3}^{sym}$ 

function Fcorr( $d_{tilt}; \Delta l_C, k, \sigma_{CH3}^{sym}$ )
     $|\Delta l_{C,corr}| \leftarrow |\Delta l_C + d_{tilt}|$ 
    return  $k|\Delta l_{C,corr}| + \sigma_{CH3}^{sym}$ 

initialize:  $k, \sigma_{CH3}^{sym}, d_{tilt}, |\Delta l_{C,corr}|$ 

while  $|Flin - Fcorr| > \epsilon$  do
     $k, \sigma_{CH3}^{sym} \leftarrow \text{optimize } Flin - \sigma_{CH3} = 0$ 
     $d_{tilt} \leftarrow \text{optimize } Fcorr - \sigma_{CH3} = 0$ 

end while

```

The real part of the Fourier-transform for a slab, described by two mirrored error-functions centered around μ , with a width of d , a smearing parameter of σ and its area normalized to 1, is given by

$$\Re \left\{ \frac{1}{2d} \int_{-\infty}^{\infty} \left[\operatorname{erf} \left(\frac{x - \mu + d/2}{\sqrt{2}\sigma} \right) - \operatorname{erf} \left(\frac{x - \mu - d/2}{\sqrt{2}\sigma} \right) \right] e^{iqx} dx \right\} = \frac{\sin(qd/2)}{qd/2} e^{-\frac{\sigma^2 q^2}{2}} \cos(\mu q) \quad (\text{A1})$$

For the Gaussian distribution centered at μ and standard deviation σ we use the following:

$$\Re \left\{ \int_{-\infty}^{\infty} \frac{1}{\sqrt{2\pi}\sigma} e^{-\frac{(x-\mu)^2}{2\sigma^2}} e^{iqx} dx \right\} = e^{-\frac{q^2\sigma^2}{2}} \cos(q\mu) \quad (\text{A2})$$

Table A1. Molecular groups described by individual functions * Sphingosine backbone in the case of MSM.

Abbr.	Content	Function
CH3	Terminal methyl group	Gaussian
CH2	Methylene chains	Error function
CG	Carbonyl-glycerol backbone *	Gaussian
PCN	Phosphate + CN	Gaussian
Chol	Choline-CH3 group	Gaussian
BW	Hydration layer	Error function

We added up scattering contributions of the parts in Table A1 by using the normalized functions (A1) and (A2), weighted by the factors $\frac{V_k}{A}$, A denoting the area per lipid and V_k the volume of the respective moiety. The functions for CH2 and BW are treated differently: they are normalized to fill the whole unit cell area, followed by the subtraction of the groups they contain. We applied polydispersity on the chain-width D_C by summing

over a series of form factors with different $D_{C,i}$, weighted by a Gaussian distribution $\mathcal{N}(x|\bar{D}_C, \sigma_{poly})$ with a mean \bar{D}_C and standard deviation σ_{poly} . The average chain-width is calculated by $\bar{D}_C = \frac{n_{CH2}V_{CH2}+2V_{CH3}}{A}$. Contrasts of the individual moieties k are defined by $\Delta\rho_k = \frac{b_k}{V_k} - \rho_{solvent}$, b and ρ denoting scattering length and scattering length density for either radiation (X-rays or neutrons). A graphical representation of all distances between moieties and thicknesses is given in Figure A1:

$$I(q) \propto F_{sphere}(r_{mean}, \sigma_R) \sum_i \mathcal{N}(D_{C,i}|\bar{D}_C, \sigma_{Poly}) \left[\begin{aligned} & 2(\Delta\rho_T - \Delta\rho_{CH2}) \frac{V_{CH3}D_{C,i}}{V_{CH2} + V_{CH3}} e^{-\frac{q^2\sigma_{CH3}^2}{2}} + \\ & 2\Delta\rho_{CH2} \frac{1}{q} e^{-\frac{q^2\sigma_{CH2}^2}{2}} \sin(qD_{C,i}) + \\ & 2(\Delta\rho_{CG} - \Delta\rho_{BW}) \frac{V_{CG}}{A} e^{-\frac{q^2\sigma_{CG}^2}{2}} \cos\left(q(D_{C,i} + d_{CG}/2)\right) + \\ & 2(\Delta\rho_{PCN} - \Delta\rho_{BW}) \frac{V_{PCN}}{A} e^{-\frac{q^2\sigma_{PCN}^2}{2}} \cos\left(q(D_{C,i} + d_{CG} + d_{PCN}/2)\right) + \\ & 2(\Delta\rho_{Chol} - \Delta\rho_{BW}) \frac{V_{Chol}}{A} e^{-\frac{q^2\sigma_{Chol}^2}{2}} \cos\left(q(D_{C,i} + d_{CG} + d_{PCN} + d_{Chol}/2)\right) + \\ & 4\Delta\rho_{BW} \frac{1}{q} e^{-\frac{q^2\sigma_{CH2}^2}{2}} \sin\left(q \frac{d_{CG} + d_{PCN} + d_{Chol} + d_{shell}}{2}\right) \cos\left(q(D_{C,i} + \frac{d_{CG} + d_{PCN} + d_{Chol} + d_{shell}}{2})\right) \end{aligned} \right]^2 + I_{inc}$$

To describe the contribution from the overall vesicle shape, we use the Schultz-distributed form factor of a sphere, as described in Kucerka et al. 2007 [56]:

$$F_{sphere} = \frac{8\pi^2(z+1)(z+2)}{s^2q^2} \left\{ 1 - \left(1 + \frac{4q^2}{s^2} \right)^{-(z+3)/2} \cos \left[(z+3) \arctan \left(\frac{2q}{s} \right) \right] \right\}$$

Mean vesicle radius R_m and polydispersity σ_R come in via the auxiliary quantities s and z :

$$s = \frac{R_m}{\sigma_R^2}, \quad z = \frac{R_m^2}{\sigma_R^2} - 1$$

Appendix B. SDP-Model Parameters

Tables A2 and A3 contain all information about the SDP-profiles for all studied lipids and references. Parameter notation was chosen to conform to former publications such as [3].

Table A2. Results from joint SAXS-SANS analysis of LUVs containing saturated lipids, in comparison to literature values and simulations. ϵ in the second column denotes relative error-estimates from our SAS-experiments. Quantities not marked with any symbol (*, †, ‡) were adjustable during the analysis.

	ϵ (%)	DPPC ^a	DPPC ^b	DPPC ^c	MSPC ^a	MSPC ^c	SMPC ^a	SMPC ^c	PMPC ^a	PMPC ^c
V_L^* (Å ³)		1232	1228.5	1209.2	1232	1210	1232	1211.1	1175.8	1155.7
V_H^* (Å ³)		328	331	314.4	328	314.6	328	315.4	328	314.7
r_{CG}^*		0.44	0.40	0.48	0.44	0.48	0.44	0.49	0.44	0.48
r_{PCN}^*		0.3	0.29	0.21	0.3	0.22	0.3	0.22	0.3	0.22

Table A2. Cont.

	ϵ (%)	DPPC ^a	DPPC ^b	DPPC ^c	MSPC ^a	MSPC ^c	SMPC ^a	SMPC ^c	PMPC ^a	PMPC ^c
r^*		2.09	1.95	2.06	2.09	2.06	2.09	2.06	2.09	2.05
D_B^\ddagger (Å)	5	40.3	38.9	39.3	40.3	39.1	40.3	38.2	38.4	36.6
D_{HH}^\ddagger (Å)	3	37.5	38.4	38.4	35.7	38.4	34.8	37.6	33.9	36
$2D_C^\ddagger$ (Å)	3	28.6	28.4	29.1	29.1	28.9	29.2	28.3	27.0	26.6
D_{H1}^\ddagger (Å)	20	4.5	4.97	4.7	3.3	4.8	2.8	4.7	3.5	4.7
A (Å ²)	2	63.1	63.1	61.6	62.2	62	62.0	63.4	62.9	63.2
z_{CG} (Å)	8	15.2	14.7	16.4	15.6	16.2	15.7	15.9	14.5	15
σ_{CG} (Å)	20	2.5	2.19	2.93	2.5	2.97	2.5	2.99	2.5	2.85
z_{PCN} (Å)	8	19.2	19.6	20.1	18.7	19.9	18.4	19.6	17.8	18.7
σ_{PCN} (Å)	20	2.3	2.35	2.99	3.1	3.04	3.1	3.06	3.0	2.92
z_{Chol} (Å)	3	21.1	20.2	21.39	22.3	21.2	23.1	20.89	21.5	20.1
σ_{Chol}^\ddagger (Å)		3	2.98	3.6	3	3.63	3	3.63	3	3.51
σ_{CH2}^\ddagger (Å)		2.5	2.47	2.83	2.5	2.88	2.5	2.88	2.5	2.73
σ_{CH3}^\ddagger (Å)	5	2.9	2.94	3.23	3.3	3.59	3.7	4.32	3.1	3.58
σ_{poly} (%)	6	3.6	0		2.9		5.3		3.5	
$V_{W,bound}^\ddagger$ (Å ³)	6	29.3			29.3		29.3		29.3	
n_W^\ddagger	10	9.7			11.3		12.8		12.1	
γ^\ddagger	7	0.43	0.46	0.52	0.55	0.63	0.65	0.88	0.54	0.71

^a SAS—analysis, this work; ^b Kučerka et al. [3]; ^c MD—simulations, this work, * fixed according to Nagle et al. [30], † fixed, ‡ calculated quantity.

Table A3. Results from joint SAXS-SANS analysis of LUVs containing unsaturated lipids and comparison to literature values. ϵ in the second column denotes relative error-estimates from our SAS experiments. Quantities not marked with any symbol (*, †, ‡) were adjustable during the analysis.

	ϵ (%)	POPC ^a	POPC ^b	SOPC ^a	SOPC ^b	MSM ^a	
V_L^* (Å ³)		Lipid volume	1276.9	1275.5	1333.1	1327.5	1336.3
V_H^* (Å ³)		Headgroup volume	320	331	328	331	274
r_{CG}^*		V_{CG}/V_H	0.45	0.41	0.44	0.43	0.32
r_{PCN}^*		V_{PCN}/V_H	0.29	0.3	0.3	0.3	0.32
r_{12}^*		V_{CH3}/V_{CH2}	2.09	1.93	2.09	1.94	2.09
r_{12}^*		V_{CH}/V_{CH2}	0.8	0.8	0.8	0.8	0.8
D_B^\ddagger (Å)	5	Luzzati bilayer thickness	38.4	37.9	39.4	39.0	42.1
D_{HH}^\ddagger (Å)	3	Head-head distance	37.5	35.9	35.7	37.0	43.0
$2D_C^\ddagger$ (Å)	3	Hydrophobic thickness	28.4	28.1	29.2	29.3	32.8
D_{H1}^\ddagger (Å)	20	$(D_{HH} - 2D_C)/2$	4.6	3.91	3.3	3.9	5.1
A (Å ²)	2	Area per lipid	67.5	67.3	68.8	68.1	64.8
z_{CG} (Å)	8	$D_C + d_{CG}/2$	15.0	14.8	15.9	15.5	18.4
σ_{CG} (Å)	20		2.5	2.48	2.5	2.5	2.5
z_{PCN} (Å)	8	$D_{C,i} + d_{CG} + d_{PCN}/2$	19.1	19.3	19.0	19.5	22.1
σ_{PCN} (Å)	20		2.5	2.81	3.0	2.7	2.4
z_{Chol} (Å)	3	$D_C + d_{CG} + d_{PCN} + d_{Chol}/2$	23.4	20.3	23.0	20.5	22.1
σ_{Chol}^\ddagger (Å)			3	2.98	3	2.98	3
σ_{CH2}^\ddagger (Å)			2.5	2.50	2.5	2.5	2.5
σ_{CH3}^\ddagger (Å)	5		3.4	2.69	3.3	3.1	4.3
σ_{poly} (%)	6	Thickness polydispersity	7.9	0	3.6	0	3.5
$V_{W,bound}^\ddagger$ (Å ³)	6	Volume per bound water molecule	29.9		29.7		29.8
n_W^\ddagger	10	Number of bound waters	16.6		15.1		9.6
γ^\ddagger	7	Relative methyl overlap	0.60	0.41	0.55	0.50	0.71

^a SAS—analysis, this work; ^b Kučerka et al. [3]; ^c MD—simulations, this work, * fixed according to Nagle et al. [30], † fixed, ‡ calculated quantity.

The volume of MSM was measured via the vibrating tube principle [57] using a DMA 4500 M density meter (Anton Paar). We measured the density ρ_s of 3 concentrations of MSM at 50 °C, prepared as described in Section 4.1 in H₂O without extruding (Table A4). The volume per MSM molecule was calculated by the following Equation [58], using the lipid molecular weight $M_L = 785.034$ g/mol, masses of water m_w and lipid m_L according to the concentrations given in Table A4, and a water density ρ_w of 0.98806 g/ml. The density measurements were performed with a nominal accuracy of 0.00005 g/ml:

$$V_L = \frac{M_L}{0.6022\rho_s} \left[1 + \frac{m_w}{m_L} \left(1 - \frac{\rho_s}{\rho_w} \right) \right], \quad (\text{A3})$$

Table A4. Volumetric measurements of MSM vesicles in H₂O. c ... concentration of lipid. ρ_s ... measured density. V_L ... volume per MSM molecule according to Equation (A3)

c (g/L)	ρ_s (g/mL)	V_L (Å ³)
10	0.98798	1330
5	0.98803	1327
2.5	0.98800	1351
0	0.98806	(pure H ₂ O)
average		1336 ± 15

Appendix C. Evaluation of σ_{CH_3} -data

Table A5. Chain lengths D_C at 50 °C in chain-symmetric phosphatidylcholines from previous scattering studies.

Chain	D_C	Reference
14:0	12.4	[3]
16:0	14.3	[3]
18:0	16.2	[3], extrapolated
22:0	20.1	[3], extrapolated
18:1	13.0	[59], extrapolated
PSM	13.3	[34], 45 °C

Appendix D. Supplementary Figures

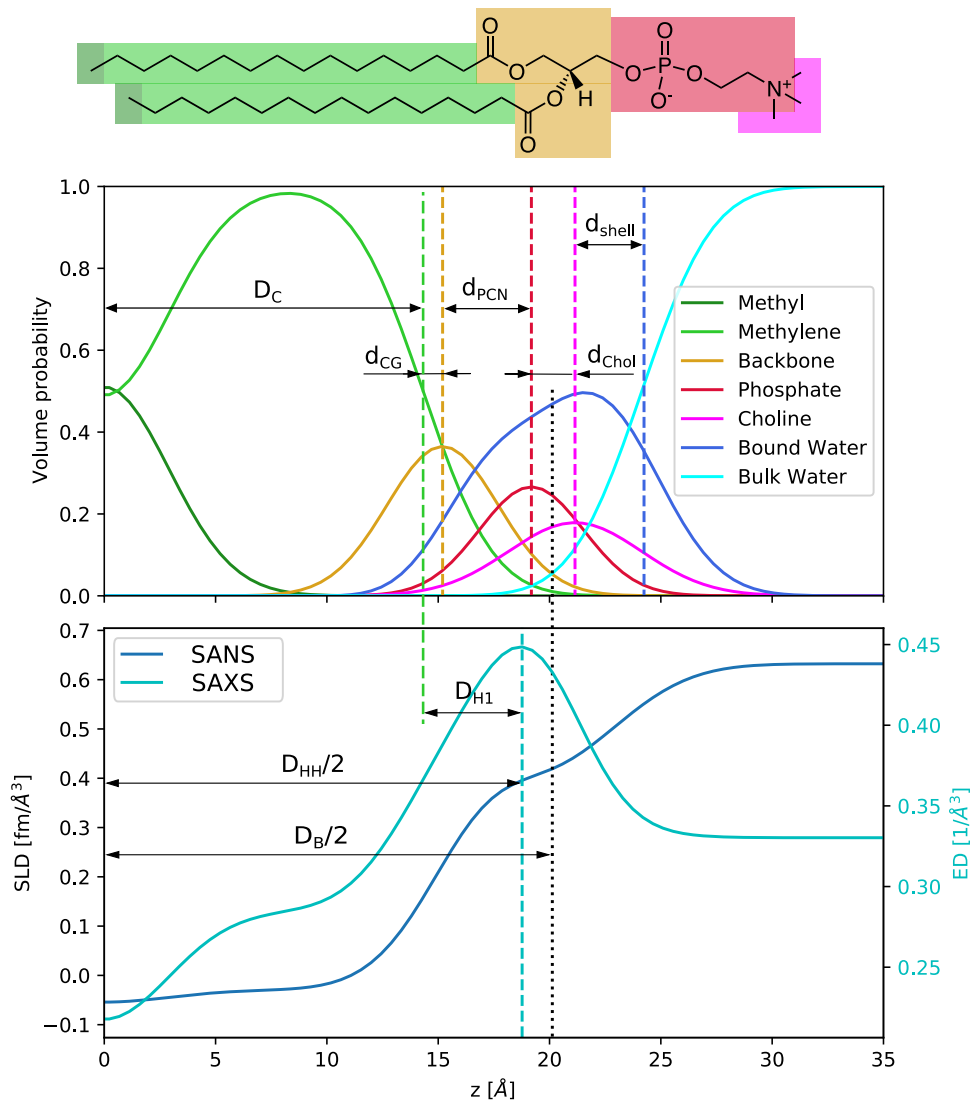


Figure A1. Exemplary profile of probability distribution functions (**top**) and scattering length density (SLD)/electron density (ED) profiles (**bottom**) with definitions of distances used in the SDP-model.

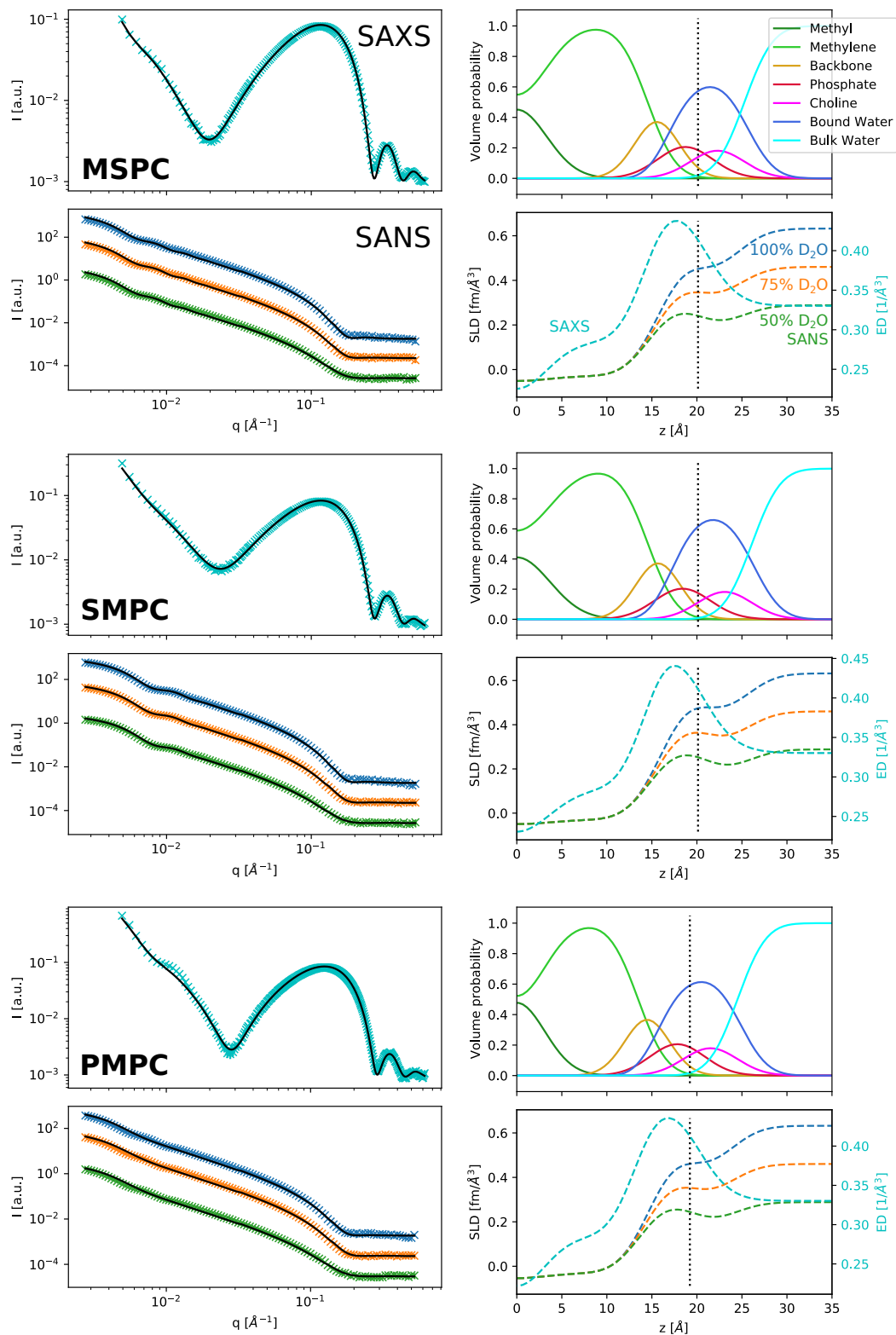


Figure A2. SAXS and SANS data with fits (black lines); SDP-volume probability, electron density and neutron scattering length density profiles for MSPC, SMPC and PMPC. Neutron intensities of different contrasts have been shifted for better visibility.

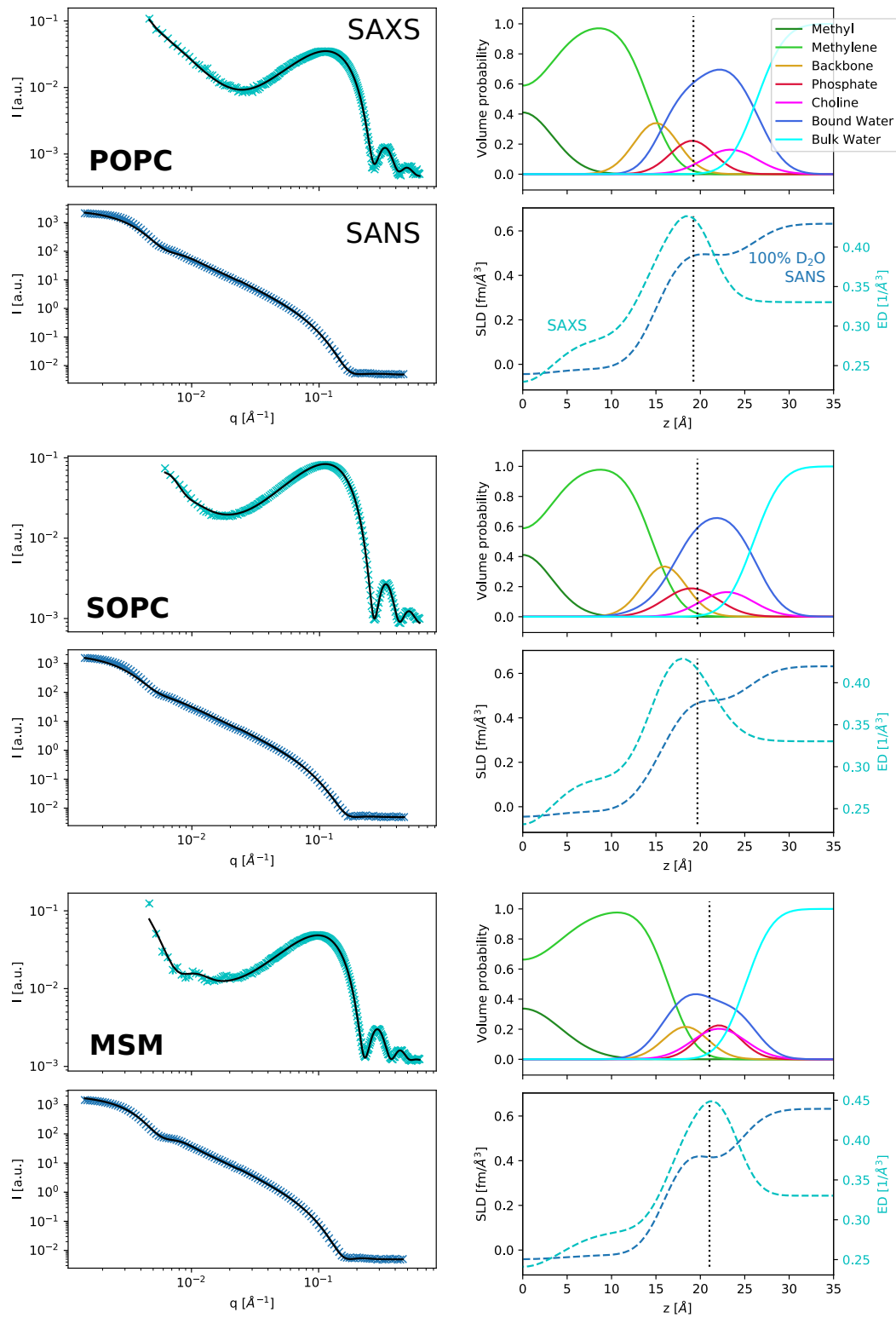


Figure A3. SAXS and SANS data with fits (black lines); SDP volume probability, electron density and neutron scattering length density profiles for POPC, SOPC and MSM.

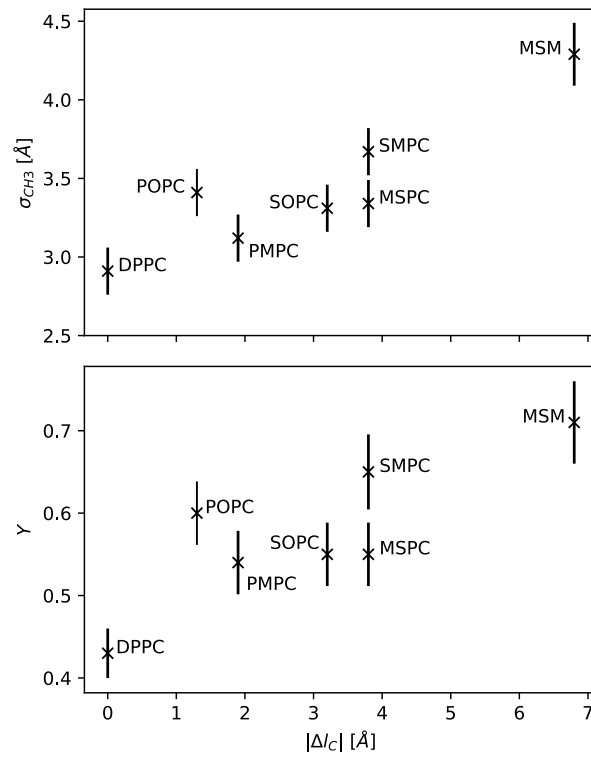


Figure A4. Standard deviations σ_{CH_3} of the Gaussian volume distributions of the terminal methyl groups (upper plot) and relative interdigitation parameters (lower plot), plotted over the chain length mismatch Δl_c of the respective lipids.

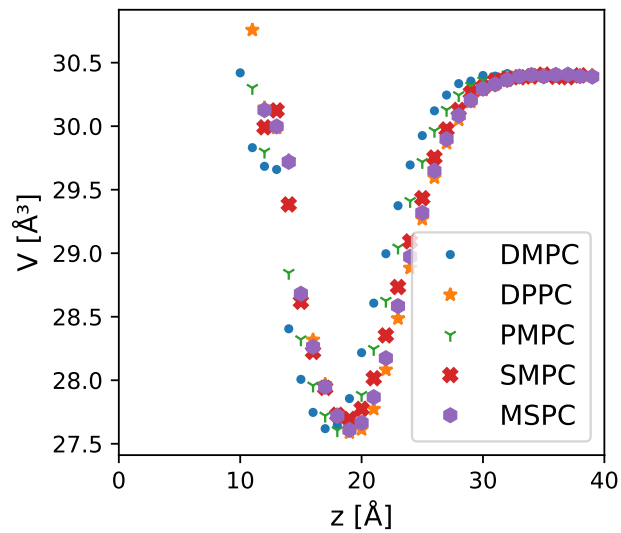


Figure A5. Volume per water molecule across the bilayer calculated from MD simulations. Regions without data points (notably for $z < 10$ Å) do not contain water molecules.

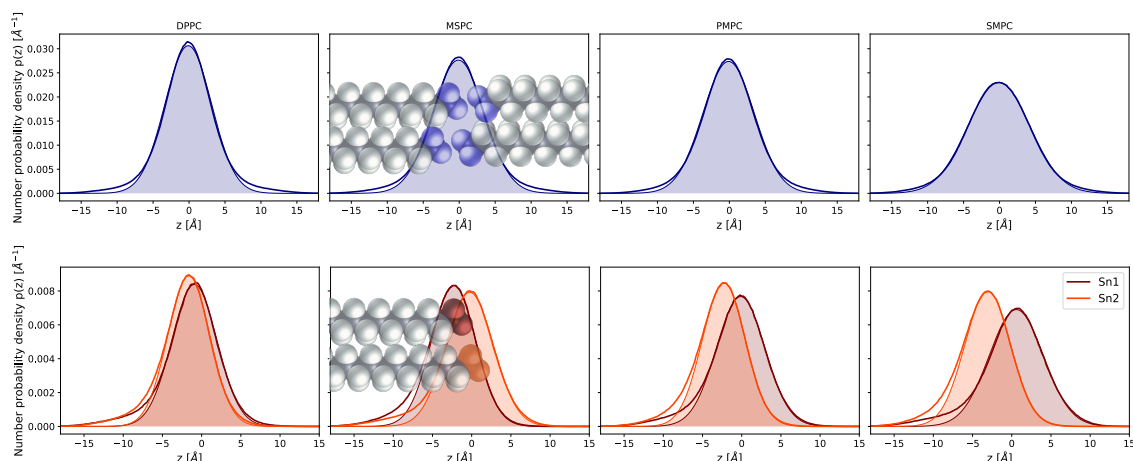


Figure A6. The upper panels show the total number probability density distributions of all CH₃ groups in the bilayer for DPPC and the chain-asymmetric saturated lipids MSPC, PMPC and SMPC. Shaded areas and lightly drawn lines correspond to Gaussian functions fitted to the distribution. In the lower panels, the distributions are divided into the CH₃ groups of sn1 and sn2 chains, showing just the lipids from the left side of the bilayer. Again, Gaussians are inserted in the form of shaded areas. They fit almost perfectly in all cases on the right side of the distributions, however, to the left, there is some mismatch, which also causes the mismatch of the overall distribution. This might be caused by chains bending back towards their headgroups.

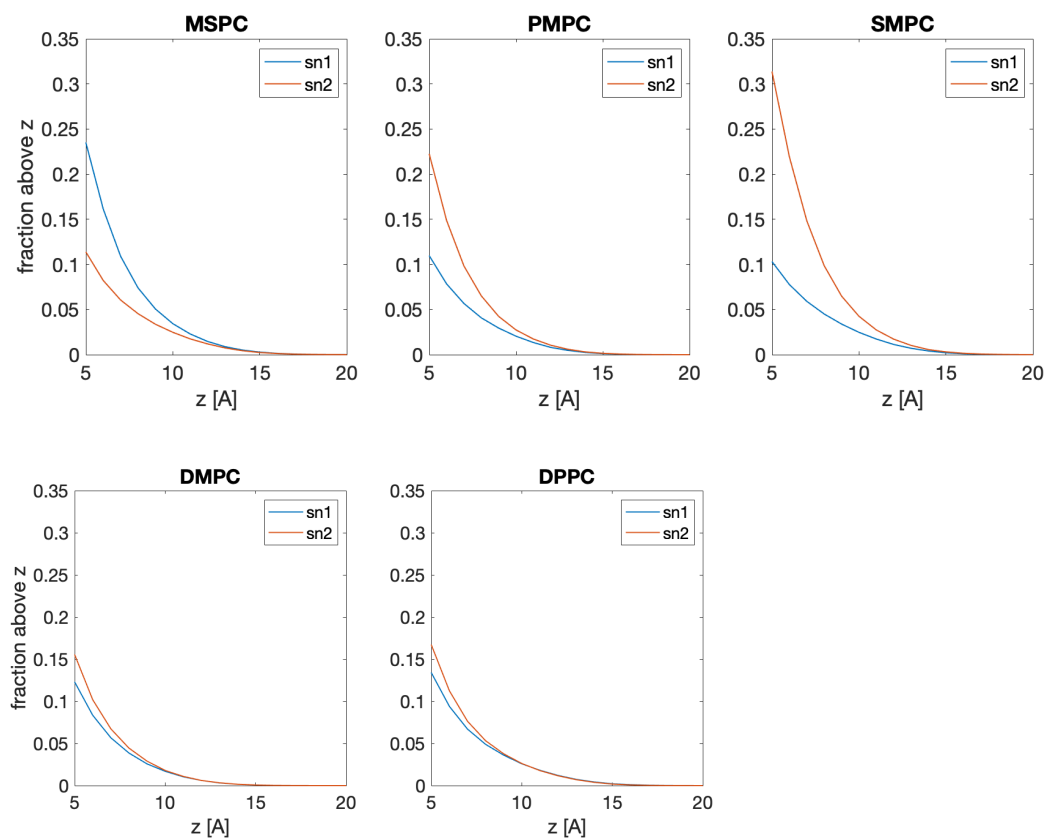


Figure A7. Fraction of lipids whose terminal methyl group is above a certain z position. The fraction was calculated at every point in time (i.e., in each frame of the simulation trajectory) and is averaged over all frames. The bilayer midplane in all bilayers is at z = 0. The data show that more lipids bend their 14:0 chains in the chain-asymmetric bilayers while both chains bend to a similar extent in the chain-symmetric bilayers.

References

1. Lorent, J.H.; Levental, K.R.; Ganesan, L.; Rivera-Longworth, G.; Sezgin, E.; Doktorova, M.; Lyman, E.; Levental, I. Plasma membranes are asymmetric in lipid unsaturation, packing and protein shape. *Nat. Chem. Biol.* **2020**, *16*, 644–652, doi:10.1038/s41589-020-0529-6.
2. Ejsing, C.S.; Sampaio, J.L.; Surendranath, V.; Duchoslav, E.; Ekroos, K.; Klemm, R.W.; Simons, K.; Shevchenko, A. Global analysis of the yeast lipidome by quantitative shotgun mass spectrometry. *Proc. Natl. Acad. Sci. USA* **2009**, *106*, 2136–2141, doi:10.1073/pnas.0811700106.
3. Kučerka, N.; Nieh, M.P.; Katsaras, J. Fluid phase lipid areas and bilayer thicknesses of commonly used phosphatidylcholines as a function of temperature. *Biochim. Biophys. Acta Biomembr.* **2011**, *1808*, 2761–2771, doi:10.1016/j.bbamem.2011.07.022.
4. Filippov, A.; Orädd, G.; Lindblom, G. Sphingomyelin structure influences the lateral diffusion and raft formation in lipid bilayers. *Biophys. J.* **2006**, *90*, 2086–2092, doi:10.1529/biophysj.105.075150.
5. Collins, M.D. Interleaflet coupling mechanisms in bilayers of lipids and cholesterol. *Biophys. J.* **2008**, *94*, 32–34, doi:10.1529/biophysj.107.124362.
6. May, S. Trans-monolayer coupling of fluid domains in lipid bilayers. *Soft Matter* **2009**, *5*, 3148–3156, doi:10.1039/b901647c.
7. Chiantia, S.; London, E. Acyl Chain length and saturation modulate interleaflet coupling in asymmetric bilayers: Effects on dynamics and structural order. *Biophys. J.* **2012**, *103*, 2311–2319, doi:10.1016/j.bpj.2012.10.033.
8. Marsh, D. Analysis of the bilayer phase transition temperatures of phosphatidylcholines with mixed chains. *Biophys. J.* **1992**, *61*, 1036–1040, doi:10.1016/S0006-3495(92)81911-2.
9. Pearson, R.H.; Pascher, I. The molecular structure of lecithin dihydrate. *Nature* **1979**, *281*, 499–501, doi:10.1038/281499a0.
10. Han, X.; Gross, R.W. Plasmenylcholine and Phosphatidylcholine Membrane Bilayers Possess Distinct Conformational Motifs. *Biochemistry* **1990**, *29*, 4992–4996, doi:10.1021/bi00472a032.
11. Nagle, J.F.; Cognet, P.; Dupuy, F.G.; Tristram-Nagle, S. Structure of gel phase DPPC determined by X-ray diffraction. *Chem. Phys. Lipids* **2019**, *218*, 168–177, doi:10.1016/j.chemphyslip.2018.12.011.
12. Veatch, S.L.; Soubias, O.; Keller, S.L.; Gawrisch, K. Critical fluctuations in domain-forming lipid mixtures. *Proc. Natl. Acad. Sci. USA* **2007**, *104*, 17650–17655.
13. Pabst, G.; Kučerka, N.; Nieh, M.P.; Rheinstädter, M.C.; Katsaras, J. Applications of neutron and X-ray scattering to the study of biologically relevant model membranes. *Chem. Phys. Lipids* **2010**, *163*, 460–479, doi:10.1016/j.chemphyslip.2010.03.010.
14. Kučerka, N.; Nagle, J.F.; Sachs, J.N.; Feller, S.E.; Pencer, J.; Jackson, A.; Katsaras, J. Lipid bilayer structure determined by the simultaneous analysis of neutron and X-ray scattering data. *Biophys. J.* **2008**, *95*, 2356–2367, doi:10.1529/biophysj.108.132662.
15. Pencer, J.; Krueger, S.; Adams, C.P.; Katsaras, J. Method of separated form factors for polydisperse vesicles. *J. Appl. Crystallogr.* **2006**, *39*, 293–303, doi:10.1107/S0021889806005255.
16. Wiener, M.C.; White, S.H. Fluid bilayer structure determination by the combined use of x-ray and neutron diffraction. II. “Composition-space” refinement method. *Biophys. J.* **1991**, *59*, 174–185, doi:10.1016/S0006-3495(91)82209-3.
17. Kučerka, N.; Gallová, J.; Uhríková, D.; Balgavý, P.; Bulacu, M.; Marrink, S.J.; Katsaras, J. Areas of monounsaturated diacylphosphatidylcholines. *Biophys. J.* **2009**, *97*, 1926–1932, doi:10.1016/j.bpj.2009.06.050.
18. Pan, J.; Heberle, F.A.; Tristram-Nagle, S.; Szymanski, M.; Koepfinger, M.; Katsaras, J.; Kučerka, N. Molecular structures of fluid phase phosphatidylglycerol bilayers as determined by small angle neutron and X-ray scattering. *Biochim. Biophys. Acta Biomembr.* **2012**, *1818*, 2135–2148, doi:10.1016/j.bbamem.2012.05.007.
19. Pan, J.; Cheng, X.; Monticelli, L.; Heberle, F.A.; Kučerka, N.; Tieleman, D.P.; Katsaras, J. The molecular structure of a phosphatidylserine bilayer determined by scattering and molecular dynamics simulations. *Soft Matter* **2014**, *10*, 3716–3725, doi:10.1039/c4sm00066h.
20. Kučerka, N.; Van Oosten, B.; Pan, J.; Heberle, F.A.; Harroun, T.A.; Katsaras, J. Molecular structures of fluid phosphatidylethanolamine bilayers obtained from simulation-to-experiment comparisons and experimental scattering density profiles. *J. Phys. Chem. B* **2015**, *119*, 1947–1956, doi:10.1021/jp511159q.
21. Doktorova, M.; Kučerka, N.; Kinnun, J.J.; Pan, J.; Marquardt, D.; Scott, H.L.; Venable, R.M.; Pastor, R.W.; Wassall, S.R.; Katsaras, J.; Heberle, F.A. Molecular Structure of Sphingomyelin in Fluid Phase Bilayers Determined by the Joint Analysis of Small-Angle Neutron and X-ray Scattering Data. *J. Phys. Chem. B* **2020**, *124*, 5186–5200, doi:10.1021/acs.jpcc.0c03389.
22. Marquardt, D.; Heberle, F.A.; Pan, J.; Cheng, X.; Pabst, G.; Harroun, T.A.; Kučerka, N.; Katsaras, J. The structures of polyunsaturated lipid bilayers by joint refinement of neutron and X-ray scattering data. *Chem. Phys. Lipids* **2020**, *229*, 104892, doi:10.1016/j.chemphyslip.2020.104892.
23. Brzustowicz, M.R.; Brunger, A.T. X-ray scattering from unilamellar lipid vesicles. *J. Appl. Crystallogr.* **2005**, *38*, 126–131, doi:10.1107/S0021889804029206.
24. Konarev, P.V.; Gruzinov, A.Y.; Mertens, H.D.T.; Svergun, D.I. Restoring structural parameters of lipid mixtures from small-angle X-ray scattering data. *J. Appl. Crystallogr.* **2021**, *54*, 169–179, doi:10.1107/s1600576720015368.
25. Heberle, F.A.; Doktorova, M.; Scott, H.L.; Skinkle, A.D.; Waxham, M.N.; Levental, I. Direct label-free imaging of nanodomains in biomimetic and biological membranes by cryogenic electron microscopy. *Proc. Natl. Acad. Sci. USA* **2020**, *117*, 19943–19952, doi:10.1073/pnas.2002200117.
26. Zaccai, G. Hydration shells with a pinch of salt. *Biopolymers* **2013**, *99*, 233–238, doi:10.1002/bip.22154.

27. Spinozzi, F.; Ferrero, C.; Ortore, M.G.; De Maria Antolinos, A.; Mariani, P. GENFIT: Software for the analysis of small-angle X-ray and neutron scattering data of macro-molecules in solution. *J. Appl. Crystallogr.* **2014**, *47*, 1132–1139, doi:10.1107/S1600576714005147.
28. Tan, L.; Elkins, J.G.; Davison, B.H.; Kelley, E.G.; Nickels, J. Implementation of a self-consistent slab model of bilayer structure in the SasView suite. *J. Appl. Crystallogr.* **2021**, *54*, 363–370, doi:10.1107/s1600576720015526.
29. Pabst, G.; Katsaras, J.; Raghunathan, V.A.; Rappolt, M. Structure and interactions in the anomalous swelling regime of phospholipid bilayers. *Langmuir* **2003**, *19*, 1716–1722, doi:10.1021/la026052e.
30. Nagle, J.F.; Venable, R.M.; Marocco-Kemmerling, E.; Tristram-Nagle, S.; Harper, P.E.; Pastor, R.W. Revisiting Volumes of Lipid Components in Bilayers. *J. Phys. Chem. B* **2019**, *123*, 2697–2709, doi:10.1021/acs.jpcc.8b12010.
31. Frewein, M.P.K.; Rumetshofer, M.; Pabst, G. Global small-angle scattering data analysis of inverted hexagonal phases. *J. Appl. Crystallogr.* **2019**, *52*, 403–414, doi:10.1107/S1600576719002760.
32. Tristram-Nagle, S. Use of X-Ray and Neutron Scattering Methods with Volume Measurements to Determine Lipid Bilayer Structure and Number of Water Molecules/Lipid. In *Membrane Hydration: The Role of Water in the Structure and Function of Biological Membranes*; Disalvo, E.A., Ed.; Springer International Publishing: Cham, Switzerland, 2015; pp. 17–43, doi:10.1007/978-3-319-19060-0_2.
33. Nickels, J.D.; Katsaras, J. Water and Lipid Bilayers. In *Membrane Hydration: The Role of Water in the Structure and Function of Biological Membranes*; Disalvo, E.A., Ed.; Springer International Publishing: Cham, Switzerland, 2015; pp. 45–67, doi:10.1007/978-3-319-19060-0_3.
34. Arsov, Z.; González-Ramírez, E.J.; Goñi, F.M.; Tristram-Nagle, S.; Nagle, J.F. Phase behavior of palmitoyl and egg sphingomyelin. *Chem. Phys. Lipids* **2018**, *213*, 102–110, doi:10.1016/j.chemphyslip.2018.03.003.
35. Cantor, R.S. Lipid composition and the lateral pressure profile in bilayers. *Biophys. J.* **1999**, *76*, 2625–2639, doi:10.1016/S0006-3495(99)77415-1.
36. Capponi, S.; Freitas, J.A.; Tobias, D.J.; White, S.H. Interleaflet mixing and coupling in liquid-disordered phospholipid bilayers. *Biochim. Biophys. Acta Biomembr.* **2016**, *1858*, 354–362, doi:10.1016/j.bbmem.2015.11.024.
37. Pabst, G.; Frewein, M.P.K.; Gerelli, Y.; Marx, L.; Porcar, L.; Scott, H.; Semeraro, E.F. *Hydrocarbon Chain-Mediated Transleaflet Coupling in Asymmetric Lipid Vesicles*; Institute Laue-Langevin: Grenoble, France, 2019. doi:10.5291/ILL-DATA.9-13-822.
38. Pernot, P.; Brennich, M.; Tully, M. The rise of BioSAXS at the ESRF: BM29 beamline for SAXS on proteins in solution. *Acta Crystallogr. Sect. A* **2018**, *74*, a7, doi:10.1107/S0108767318099920.
39. Wiener, M.C.; White, S.H. Structure of a fluid dioleoylphosphatidylcholine bilayer determined by joint refinement of x-ray and neutron diffraction data. III. Complete structure. *Biophys. J.* **1992**, *61*, 434–447, doi:10.1016/S0006-3495(92)81849-0.
40. Nagle, J.F.; Tristram-Nagle, S. Lipid bilayer structure. *Curr. Opin. Struct. Biol.* **2000**, *10*, 474–480, doi:10.1016/s0959-440x(00)00117-2.
41. Shekhar, P.; Nanda, H.; Lösche, M.; Heinrich, F. Continuous distribution model for the investigation of complex molecular architectures near interfaces with scattering techniques. *J. Appl. Phys.* **2011**, *110*, 102216, doi:10.1063/1.3661986.
42. Lindahl, E.; Edholm, O. Mesoscopic undulations and thickness fluctuations in lipid bilayers from molecular dynamics simulations. *Biophys. J.* **2000**, *79*, 426–433, doi:10.1016/S0006-3495(00)76304-1.
43. Virtanen, P.; Gommers, R.; Oliphant, T.E.; Haberland, M.; Reddy, T.; Cournapeau, D.; Burovski, E.; Peterson, P.; Weckesser, W.; Bright, J.; et al. SciPy 1.0: Fundamental algorithms for scientific computing in Python. *Nat. Methods* **2020**, *17*, 261–272, doi:10.1038/s41592-019-0686-2.
44. Hoffman, M.D.; Gelman, A. The no-U-turn sampler: Adaptively setting path lengths in Hamiltonian Monte Carlo. *J. Mach. Learn. Res.* **2014**, *15*, 1593–1623.
45. Salvatier, J.; Wiecki, T.V.; Fonnesbeck, C. Probabilistic programming in Python using PyMC3. *PeerJ Comput. Sci.* **2016**, *2016*, e55, doi:10.7717/peerj-cs.55.
46. Jo, S.; Kim, T.; Iyer, V.G.; Im, W. CHARMM-GUI: A web-based graphical user interface for CHARMM. *J. Comput. Chem.* **2008**, *29*, 1859–1865, doi:10.1002/jcc.20945.
47. Lee, J.; Cheng, X.; Swails, J.M.; Yeom, M.S.; Eastman, P.K.; Lemkul, J.A.; Wei, S.; Buckner, J.; Jeong, J.C.; Qi, Y.; et al. CHARMM-GUI Input Generator for NAMD, GROMACS, AMBER, OpenMM, and CHARMM/OpenMM Simulations Using the CHARMM36 Additive Force Field. *J. Chem. Theory Comput.* **2016**, *12*, 405–413, doi:10.1021/acs.jctc.5b00935.
48. Brooks, B.R.; Brooks, C.L.; Mackerell, A.D.; Nilsson, L.; Petrella, R.J.; Roux, B.; Won, Y.; Archontis, G.; Bartels, C.; Boresch, S.; et al. CHARMM: The biomolecular simulation program. *J. Comput. Chem.* **2009**, *30*, 1545–1614, doi:10.1002/jcc.21287.
49. Wu, E.L.; Cheng, X.; Jo, S.; Rui, H.; Song, K.C.; Dávila-Contreras, E.M.; Qi, Y.; Lee, J.; Monje-Galvan, V.; Venable, R.M.; et al. CHARMM-GUI Membrane Builder toward realistic biological membrane simulations. *J. Comput. Chem.* **2014**, *35*, 1997–2004.
50. Lee, J.; Patel, D.S.; Stähle, J.; Park, S.J.; Kern, N.R.; Kim, S.; Lee, J.; Cheng, X.; Valvano, M.A.; Holst, O.; et al. CHARMM-GUI Membrane Builder for Complex Biological Membrane Simulations with Glycolipids and Lipoglycans. *J. Chem. Theory Comput.* **2019**, *15*, 775–786, doi:10.1021/acs.jctc.8b01066.
51. Phillips, J.C.; Hardy, D.J.; Maia, J.D.C.; Stone, J.E.; Ribeiro, J.V.; Bernardi, R.C.; Buch, R.; Fiorin, G.; Hénin, J.; Jiang, W.; et al. Scalable molecular dynamics on CPU and GPU architectures with NAMD. *J. Chem. Phys.* **2020**, *153*, 044130, doi:10.1063/5.0014475.
52. Klauda, J.B.; Venable, R.M.; Freitas, J.A.; O'Connor, J.W.; Tobias, D.J.; Mondragon-Ramirez, C.; Vorobyov, I.; MacKerell, A.D.; Pastor, R.W. Update of the CHARMM All-Atom Additive Force Field for Lipids: Validation on Six Lipid Types. *J. Phys. Chem. B* **2010**, *114*, 7830–7843, doi:10.1021/jp101759q.

53. Klauda, J.B.; Monje, V.; Kim, T.; Im, W. Improving the CHARMM Force Field for Polyunsaturated Fatty Acid Chains. *J. Phys. Chem. B* **2012**, *116*, 9424–9431, doi:10.1021/jp304056p.
54. Humphrey, W.; Dalke, A.; Schulten, K. VMD: Visual molecular dynamics. *J. Mol. Graph.* **1996**, *14*, 33–38, doi:10.1016/0263-7855(96)00018-5.
55. Doktorova, M.; Harries, D.; Khelashvili, G. Determination of bending rigidity and tilt modulus of lipid membranes from real-space fluctuation analysis of molecular dynamics simulations. *Phys. Chem. Chem. Phys.* **2017**, *19*, 16806–16818, doi:10.1039/C7CP01921A.
56. Kučerka, N.; Pencer, J.; Sachs, J.N.; Nagle, J.F.; Katsaras, J. Curvature effect on the structure of phospholipid bilayers. *Langmuir* **2007**, *23*, 1292–1299, doi:10.1021/la062455t.
57. Kratky, O.; Leopold, H.; Stabinger, H. [5] The determination of the partial specific volume of proteins by the mechanical oscillator technique. *Methods Enzymol.* **1973**, *27*, 98–110, doi:10.1016/S0076-6879(73)27007-6.
58. Hallinen, K.M.; Tristram-Nagle, S.; Nagle, J.F. Volumetric stability of lipid bilayers. *Phys. Chem. Chem. Phys.* **2012**, *14*, 15452–15457, doi:10.1039/c2cp42595e.
59. Pan, J.; Tristram-Nagle, S.; Kučerka, N.; Nagle, J.F. Temperature dependence of structure, bending rigidity, and bilayer interactions of dioleoylphosphatidylcholine bilayers. *Biophys. J.* **2008**, *94*, 117–124, doi:10.1529/biophysj.107.115691.



Interdigitation-Induced Order and Disorder in Asymmetric Membranes

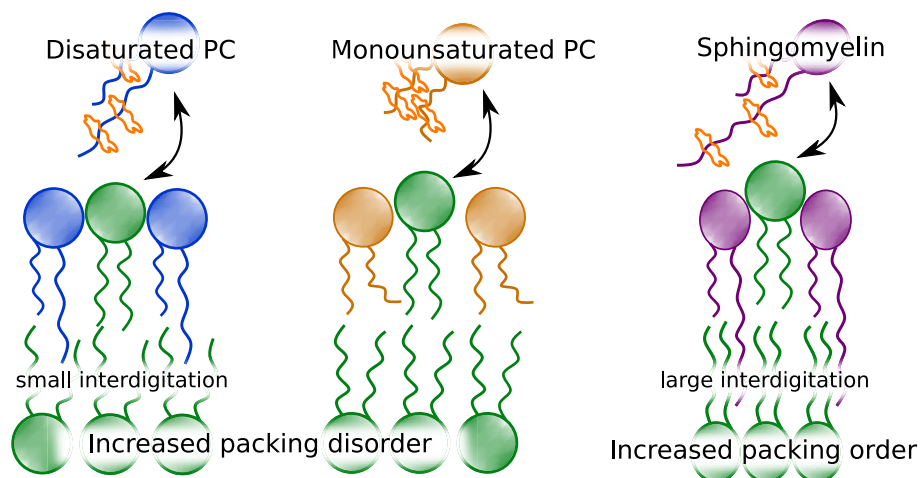
Moritz P. K. Frewein^{1,2,3,4} · Paulina Piller^{1,3,4} · Enrico F. Semeraro^{1,3,4} · Krishna C. Batchu² · Frederick A. Heberle⁵ · Haden L. Scott^{6,7} · Yuri Gerelli⁸ · Lionel Porcar² · Georg Pabst^{1,3,4} 

Received: 14 January 2022 / Accepted: 26 March 2022
© The Author(s) 2022

Abstract

We studied the transleaflet coupling of compositionally asymmetric liposomes in the fluid phase. The vesicles were produced by cyclodextrin-mediated lipid exchange and contained dipalmitoyl phosphatidylcholine (DPPC) in the inner leaflet and different mixed-chain phosphatidylcholines (PCs) as well as milk sphingomyelin (MSM) in the outer leaflet. In order to jointly analyze the obtained small-angle neutron and X-ray scattering data, we adapted existing models of trans-bilayer structures to measure the overlap of the hydrocarbon chain termini by exploiting the contrast of the terminal methyl ends in X-ray scattering. In all studied systems, the bilayer-asymmetry has large effects on the lipid packing density. Fully saturated mixed-chain PCs interdigitate into the DPPC-containing leaflet and evoke disorder in one or both leaflets. The long saturated acyl chains of MSM penetrate even deeper into the opposing leaflet, which in turn has an ordering effect on the whole bilayer. These results are qualitatively understood in terms of a balance of entropic repulsion of fluctuating hydrocarbon chain termini and van der Waals forces, which is modulated by the interdigitation depth. Monounsaturated PCs in the outer leaflet also induce disorder in DPPC despite vestigial or even absent interdigitation. Instead, the transleaflet coupling appears to emerge here from a matching of the inner leaflet lipids to the larger lateral lipid area of the outer leaflet lipids.

Graphical abstract



Keywords Asymmetric membranes · Transleaflet coupling · Cyclodextrin · Small-angle X-ray scattering · Small-angle neutron scattering

✉ Georg Pabst
georg.pabst@uni-graz.at

Extended author information available on the last page of the article

Introduction

Plasma membranes play pivotal roles in cell physiological processes by regulating and controlling diverse signaling, sensing and transport mechanisms. One of the outstanding features of plasma membranes on the molecular level is a pronounced asymmetric distribution of its lipids across the bilayer, which is generated and controlled by proteins known as flippases, floppases and scramblases (van Meer 2011). Historically, lipid asymmetry was proposed for erythrocytes already half a century ago (Bretscher 1972), i.e. the same year the famous fluid-mosaic model for membrane structure was coined by Singer and Nicolson (1972). Only 1 year later Verkleij et al. reported first experimental data for lipid asymmetry in erythrocytes using a clever combination of lipid degrading enzymes (Verkleij et al. 1973). Most recently these data were confirmed also for other eukaryotes and extended to details of hydrocarbon chain asymmetry (Lorent et al. 2020). The emerging picture is that eukaryotic plasma membranes have an outer leaflet enriched in choline lipids, such as phosphatidylcholines (PC) and sphingomyelins (SM), and an inner leaflet containing the amino lipids phosphatidylethanolamine and phosphatidylserine, as well as phosphatidylinositol.

There is yet another type of asymmetry. Most naturally occurring membrane lipids have mixed hydrocarbons. Phospholipids for example typically have a saturated hydrocarbon chain at the *sn*-1 position of the glycerol backbone and unsaturated hydrocarbon at *sn*-2. In eukaryotic plasma membranes the majority of these (poly)unsaturated hydrocarbons is located in the inner leaflet (Lorent et al. 2020). Mammalian sphingomyelin in turn has in general only few double bonds in its hydrocarbons, but significantly different chain lengths. Interestingly, lipidomics data on plasma membrane leaflet composition showed also small amounts (~ 1 mol %) of saturated chain asymmetric phosphatidylcholine, such as 14:0–16:0 PC, 14:0–18:0 PC and 16:0–18:0 PC (Lorent et al. 2020). While mixed saturated/unsaturated hydrocarbons have been related to a compromise between bilayer bending flexibility and permeability (Antonny et al. 2015), little is known about the role of mixed saturated phospholipids. Chiantia and London reported an effect of brain sphingomyelin and milk sphingomyelin (MSM) on the lateral diffusion of inner leaflet lipids using asymmetric lipid vesicles fabricated by cyclodextrin (CD)-mediated lipid exchange (Chiantia and London 2012). This type of coupling was found to depend on the extent of chain-length asymmetry, as well as the hydrocarbon chain composition of the inner leaflet lipids. That is, the lateral diffusion of dioleoyl PC was slowed down by MSM only, which was attributed to the longer interdigitating N-acyl chain of MSM. Surprisingly,

fluorescence lifetime measurements of the systems found no effect of hydrocarbon chain interdigitation on the overall order of the inner leaflet lipids, demonstrating that interleaflet coupling can be different for different membrane properties. Hydrocarbon chain interdigitation-mediated ordering of lipids in the opposing leaflet was observed in molecular dynamics (MD) simulations, however (Róg et al. 2016).

In general, hydrocarbon chain interdigitation is thought to be an important factor in a functional coupling of both membrane leaflets even in the absence of proteins, although other mechanisms have also been discussed (see e.g. Eicher et al. 2018 and references therein). Interdigitation is believed to increase the shear viscosity between membrane leaflets, which appears to be consistent with the observed reduction of lateral diffusion discussed above (Chiantia and London 2012). This is contrasted, however by experiments with short and long chain fluorescent lipid analogues penetrating to different amounts into the opposing lipid leaflet, which did not reveal different interleaflet viscosities (Horner et al. 2013). We have recently reported the structure of 14:0–18:0 PC (MSPC), 18:0–14:0 PC (SMPC), 16:0–14:0 PC (PMPC) and MSM symmetric bilayers combining small-angle X-ray and neutron scattering (SAXS, SANS) and MD-simulations (Frewein et al. 2021). Indeed, we observed an increase of the extent of interdigitation with increasing length difference between the two chains. Interestingly, however, we also found that a significant fraction of the longer chain is bending back and hence not penetrating into the opposing leaflet. This indicates that effects of hydrocarbon ordering in the opposing leaflet might at least to some extent not originate from interdigitation and the associated interleaflet viscosity.

In order to gain further insight, we performed SAXS/SANS experiments on asymmetric large vesicles (aLUVs) with an inner leaflet composed of mainly di16:0 PC (DPPC) and outer leaflets enriched in either MSPC, SMPC, PMPC or MSM. In the following, these systems are referred to as DPPCⁱⁿ/MSPC^{out}, DPPCⁱⁿ/SMPC^{out}, DPPCⁱⁿ/PMPC^{out} and DPPCⁱⁿ/MSM^{out}. This does not imply, however, complete lipid exchange. The advantage of SAXS/SANS experiments is the lack of bulky labels that might either perturb the delicate balance of intermolecular forces in bilayers or not sample all intramembraneous environments equally. This advantage is, however, frequently challenged by the need for extensive data modeling (Semeraro et al. 2021). We have previously reported models for analyzing scattering data of aLUVs (Heberle et al. 2016; Eicher et al. 2017). For the hitherto studied systems, containing 16:0–18:1 PC (POPC), 16:0–18:1 phosphatidylethanolamine, and DPPC, we observed a structural leaflet coupling only when at least one of the leaflets was in the gel phase, but not for all-fluid membranes, i.e. in the L_α phase (Heberle et al. 2016; Eicher et al. 2018). Here, we focus on fluid membranes using a

modified asymmetry model, which features in addition to the recently introduced headgroup hydration layer (Frewein et al. 2021) also the possibility that the center of mass of the terminal methyl groups does not coincide with the center of the lipid bilayer. Such scenarios might occur due to hydrocarbon chain interdigitation or back-bending and are expected for the currently studied systems.

We found that all aLUVs with saturated chain asymmetric PCs have an increased area per lipid in both leaflets, i.e. decreased molecular packing, as compared to the same lipids, but in symmetric bilayers. Apparently, this results from only a minor interdigitation of the longer hydrocarbon chain into the opposing DPPC leaflet that presumably leads to an increase of configurational entropy of all lipid chains. In contrast we observed for DPPCⁱⁿ/MSM^{out} an about three times deeper interdigitation of the long MSM acyl chains and a concomitant lateral condensation of both lipid leaflets, suggesting a loss of hydrocarbon configurational entropy due to increased van der Waals forces. We additionally, applied our analysis to aLUVs with an outer leaflet enriched in the monounsaturated lipids POPC and 18:0–18:1 PC (SOPC), i.e., DPPCⁱⁿ/POPC^{out}, and DPPCⁱⁿ/SOPC^{out}. In this case, we find an increased area per lipid in both cases, however the direction of the shift of the methyl-groups is opposite in the cases. While back-bending of the 18:1-chains prevails for POPC, the longer 18:0-chains in SOPC slightly interdigitate into the DPPC-leaflet.

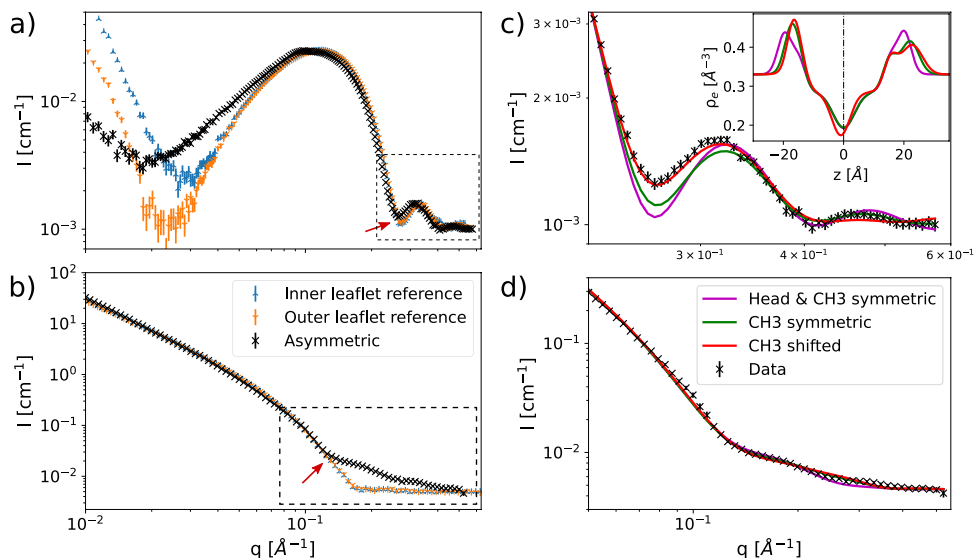
Results and Discussion

Modeling aLUVs with Chain Asymmetric Lipids

Figure 1a and b show SAXS/SANS data of DPPCⁱⁿ/SMPC^{out} aLUVs in comparison to scattering data from symmetric

LUVs composed of DPPC/SMPC mixtures representing either the inner or the outer leaflets of the aLUVs. Data have been obtained at 50°C, i.e. well-above the chain melting temperatures of both lipids (Marsh 2013). SAXS data most clearly deviate at low scattering vectors, q . This indicates a modification of the lipid's headgroup scattering contrast, e.g. due to differing hydration (Frewein et al. 2021). As discussed previously (Frewein et al. 2021), SANS is not sensitive to this effect because of the lower contrast in the headgroup regime. In the following, we focus specifically on the mid- q range, however, where SAXS and SANS data of aLUVs both show a pronounced 'lift-off' of the scattered intensity as compared to the compositionally symmetric LUVs (dashed boxes in Fig. 1a, b). The degree the asymmetric curves lift off from the incoherent baseline in SANS is a known measure for the difference in deuteration between inner and outer leaflet that creates a contrast in the neutron SLD-profile in the hydrocarbon regime, see e.g. Eicher et al. 2017). This effect can also be used to monitor the stability of the system with respect to lipid flip-flop (Nguyen et al. 2019; Marx et al. 2021) (for stability checks for the presently studied systems, see Appendix B). To accentuate this lift-off in SANS, we used chain deuterated DPPC (DPPCd62) as acceptor lipid. For our here studied aLUVs this matches the scattering contrast between the inner leaflet hydrocarbons and the solvent in case of 100 % D₂O. Also SAXS data show an intensity lift-off in this q -range, which can, however, not be uniquely attributed to the asymmetric composition of the aLUVs. For example, a similar effect has been observed before for small unilamellar vesicles and interpreted as head group asymmetry due to an increased membrane curvature (Brzustowicz and Brunger 2005; Kučerka et al. 2007). However, even compositionally symmetric LUVs may show such features, which can be accounted for by considering membrane thickness fluctuations (Frewein et al. 2021).

Fig. 1 Comparison of SAXS (a) and SANS (100 % D₂O, b) curves of reference-LUVs and aLUVs consisting of DPPC (DPPC-d62 for aLUVs) and SMPC. Data have been rescaled for clarity. c Shows SAXS model fits of the window indicated with a dashed line in (a), with the corresponding electron density trans-bilayer profiles in the inset. SANS (100 % D₂O, d) data of DPPCd62^{acc} SMPC^{don} asymmetric vesicles and model fits (solid lines) using 3 different models with increasing asymmetry



To jointly analyze SAXS/SANS data of asymmetric vesicles with both leaflets in the L_α phase, we adopted the following strategy. Firstly, we modified the scattering density profile (SDP)-model for flat asymmetric bilayers (Eicher et al. 2017) with a vesicle form factor and a headgroup hydration layer as detailed recently for symmetric LUVs (Frewein et al. 2021). Compared to previous SAXS/SANS reports on aLUV structure this allowed us to include also low- q data in the analysis (Eicher et al. 2017, 2018). The modified SDP-model for aLUVs also included the above mentioned membrane thickness fluctuations (Frewein et al. 2021). However, the obtained fits yielded unsatisfying results (Fig. 1c). Inspired by (Brzustowicz and Brunger 2005; Kučerka et al. 2007), we therefore considered, in a second attempt, the possibility of headgroup asymmetry. That is, the volume distribution functions describing inner and outer leaflet phosphate groups (PCN) and choline- CH_3 groups were allowed to differ in their relative positions to the backbones, and also in the widths of the phosphate groups $\sigma_{PCN}^{\text{in/out}}$. This improved the agreement between model and data only slightly, however (Fig. 1c). In the third step we finally took into account that the longer hydrocarbon of the outer leaflet SMPC can interdigitate into the inner leaflet. In

terms of our SDP-model this means that some of the terminal methyls will be off-centered from the interface between the lipid leaflets; for details see “SAS-Data Analysis” section and Appendix A. The obtained fits gave the overall best agreement with SAXS data (Fig. 1c). Note that differences between the three models are small in SANS (Fig. 1d). This supports the idea that the observed lift-off in SAXS is dominated by hydrocarbon interdigitation. We also tried to model data with interdigitated hydrocarbons, but symmetric heads. This decreased the agreement between model and data, however (data not shown). The final successful model therefore allows in addition to our previous model for aLUVs (Eicher et al. 2018) also for interdigitated hydrocarbons and asymmetric lipid heads. The origin of headgroup asymmetry for the here studied systems is unclear at present, but might be due to lipid crowding (mass imbalance) because of CD-mediated lipid exchange.

Figure 2a demonstrates the excellent agreement of our model for $\text{DPPC}^{\text{in}}/\text{SMPC}^{\text{out}}$ aLUVs over the complete studied q -range. These data also include SANS measurements performed at 37% D_2O . At this contrast the solvent roughly matches the outer leaflet of our vesicles, which mostly contains protiated lipids. A combination with other contrasts

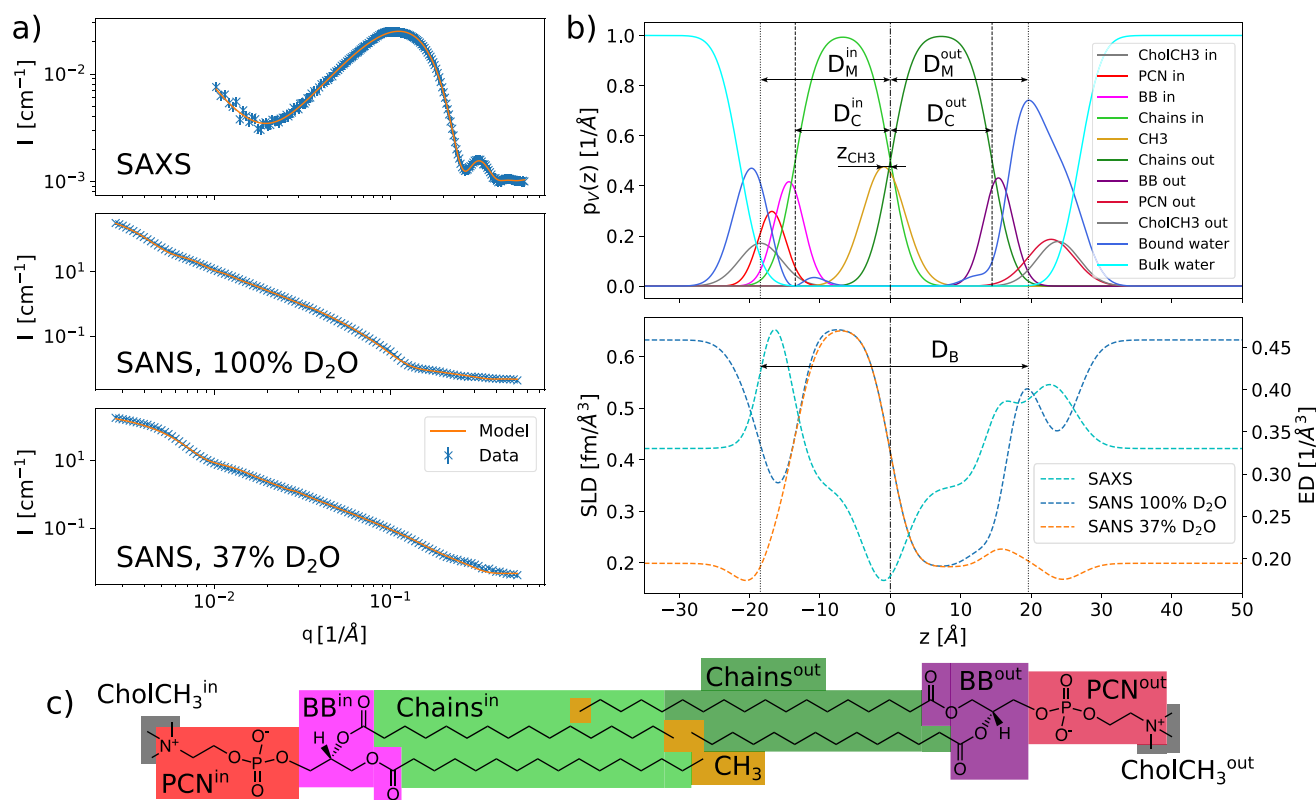


Fig. 2 Model fits to full q -range SAXS and SANS data (a), using the asymmetric SDP- and separated form factor model. b Shows the SDP-model volume probability functions of lipid moieties and surrounding water and the resulting neutron-SLD and electron den-

sity (ED) profiles. The neutron-SLD of inner and outer leaflet chain regions differ greatly due to the inner leaflet enriched in chain-deuterated DPPCd62 . The parsing scheme for PCs is shown in c, using the corresponding colors to the SDP model functions

gives therefore additional constraints for the adjustable parameters of our model. The applied parsing of membrane structure with volume distribution functions and resulting electron and neutron scattering density profiles are presented in Fig. 2b and c. Figure 2b also shows several parameters used to describe the transmembrane structure. These include the Luzzati bilayer thickness D_B , as the sum of the inner and outer monolayer thicknesses, D_M^{in} , D_M^{out} , the leaflet thicknesses of the hydrocarbons, D_C^{in} , D_C^{out} , as well as the position of the center of the terminal CH_3 distribution function, z_{CH_3} . Due to the ability of hydrocarbons to also bend back, z_{CH_3} measures interdigitation and back-bending at the same time. For details and all definitions see “SAS-Data Analysis” section and Appendix A. The results for the structure of DPPCⁱⁿ/SMPC^{out} aLUVs are listed in Table 1 and will be discussed in the next section; all adjustable parameters for the fits are reported in Supplementary Table S2.

Structure of aLUVs with Saturated Chain Asymmetric Lipids

Having established a structural model for the analysis of asymmetric vesicles containing chain asymmetric lipids we first applied it to aLUVs with outer leaflets enriched in MSPC, SMPC and PMPC, while maintaining DPPC based inner leaflets. Results listed in Table 1 report our best fit-results for the main compositional and structural parameters (full details are given in Tables S2 and S3; for

fits see Figs. 2, S2 and S3). $\chi_{\text{acc/don}}$ designate the acceptor/donor concentrations in the vesicles, which we constrained during the modeling by the results of the compositional analysis using gas chromatography (see “Compositional Analysis Using Gas Chromatography” section and Supplement). The distribution over both leaflets is given by $\chi_{\text{acc/don}}^{\text{in/out}}$ and results from the analysis of SANS-data, as discussed in “Modelling aLUVs with Chain Asymmetric Lipids” section. The lipid exchange efficiencies yielded an about 70% exchange of the outer leaflet and varied only slightly between the different samples. Only for MSPC this was reduced to 55%. Regarding structural parameters, the Luzzati thickness D_B is a well established measure for the width of a bilayer, taking into account its smeared out water/bilayer interface (Tristram-Nagle 2015). Our measure for the interdigitated state of the hydrocarbon chains is the position of the center of the volume probability distribution of the terminal methyl groups with respect to the bilayer center z_{CH_3} . Negative values imply a shift towards the inner leaflet and *vice versa*. We introduced the parameters V_{bw} and σ_{poly} in Frewein et al. (2021) to describe the volume per bound water molecule and the membrane thickness polydispersity. We do not discuss these results in further detail, as the exact nature of this polydispersity is still unclear and V_{bw} is strongly coupled to the total number of bound water molecules, n_w . The numbers we find here for V_{bw} and σ_{poly} agree quite well with the ones observed for symmetric vesicles (Frewein et al. 2021). We

Table 1 Fit results for saturated mixed-chain PCs and MSM as well as properties of inner/outer leaflet reference LUVs. ϵ is the error for all aLUV parameter values

Donor lipid	ϵ [%]	MSPC		SMPC		PMPC		MSM	
		aLUV	Ref	aLUV	Ref	aLUV	Ref	aLUV	Ref
$\chi_{\text{acc}} : \chi_{\text{don}} \%$	5	69:31		59:41		62:38		54:46	
$\chi_{\text{acc}}^{\text{in}} : \chi_{\text{don}}^{\text{in}} \%$	5	96:04		92:08		95:05		83:17	
$\chi_{\text{acc}}^{\text{out}} : \chi_{\text{don}}^{\text{out}} \%$	5	45:55		30:70		33:67		28:72	
D_B [Å]	3	37.0	39.6	38.1	39.5	36.1	38.6	40.9	40.0
z_{CH_3} [Å]	10	− 0.96		− 0.95		− 0.69		− 2.59	
V_{bw} [Å ³]	6	29.4		29.3		29.6		29.5	
σ_{poly} [%]	6	4.1		2.8		3.3		7.3	
D_M^{in} [Å]	6	18.0	19.8	18.5	19.8	18.0	19.3	20.0	19.4
D_M^{out} [Å]	6	18.9	19.8	19.6	19.7	18.1	19.3	21.0	20.6
D_C^{in} [Å]	5	13.2	14.5	13.5	14.6	13.2	14.1	14.8	14.3
D_C^{out} [Å]	5	14.0	14.5	14.5	14.4	13.2	14.0	16.4	16.1
A^{in} [Å ²]	5	67.4	62.4	65.8	62.1	67.5	63.7	60.9	64.2
A^{out} [Å ²]	5	65.8	62.2	63.5	62.7	66.5	61.7	63.9	63.2
A^{acc} [Å ²]	5	67.6	63.1 [†]	66.1	63.1 [†]	67.6	63.1 [†]	60.0	63.1 [†]
A^{don} [Å ²]	5	64.4	62.2 [†]	62.4	62.0 [†]	66.0	62.9 [†]	65.4	64.8 [†]
n_w^{in}	6	9.5	6.4	6.5	6.8	9.0	12.5	8.0	7.8
n_w^{out}	6	15.7	4.6	15.2	5.5	15.8	4.5	11.1	6.8

*Reference values from symmetric inner/outer leaflet references (Figs. S4–S6; Tables S3 and S4)

† From single lipid references (Table S1)

therefore expect no fundamental differences in these properties between symmetric and asymmetric vesicles. $D_M^{\text{in/out}}$ are the monolayer thicknesses and calculated equivalently to D_B , but separately for each leaflet. In case of the references, $D_M^{\text{in/out}}$ is $D_B/2$ of the respective vesicle and D_B is the sum of both half-bilayer thicknesses. The hydrophobic thicknesses $D_C^{\text{in/out}} = V_{\text{HC}}^{\text{in/out}}/A^{\text{in/out}}$ are connected to the area per lipid of the respective leaflet $A^{\text{in/out}}$ by the chain volumes $V_{\text{HC}}^{\text{in/out}}$, for which we used tabulated values depending on the number of hydrocarbons in the lipid (Nagle et al. 2019). To get a feeling how the structure compares to the one of its components, we also calculated the area for each lipid $A_{\text{acc/don}}$, by assuming linear additivity of the areas: $A^{\text{in/out}} = \chi_{\text{acc}}^{\text{in/out}} A_{\text{acc}} + \chi_{\text{don}}^{\text{in/out}} A_{\text{don}}$. The structure of the lipid headgroup is determined by several adjustable parameters, which are further discussed in section A. Here we give the number of water molecules per headgroup within the Luzzati thickness $n_W^{\text{in/out}}$, which reflects the extension of the headgroup into the aqueous phase. In symmetric LUVs of chain-asymmetric PCs values for n_W between 9 and 15 were found (Frewein et al. 2021).

The transbilayer structures of symmetric DPPC, MSPC, SMPC and PMPC bilayers in the L_α phase have been recently shown to be relatively similar, with the most striking difference being the localization of the CH_3 -groups, which exhibits a linear dependence on the chainlength-mismatch (Frewein et al. 2021). In particular, the lateral area per lipid of these lipids was between 62 and 63 \AA^2 , suggesting that there are no significant perturbations in the bilayer caused by chain-mismatch. Also symmetric mixtures of either of the chain-asymmetric lipids with DPPC, which were prepared as symmetric references mimicking either the inner or the outer leaflet of the aLUVs, showed no significant differences in structure; structural parameters for these reference samples are given in Table 1 (see also Tables S1 and S3; Figs. S4 and S5).

In the case of asymmetric vesicles, however, the presence of a chain-asymmetric lipid in the outer leaflet leads to a shift of the terminal methyl groups towards the DPPC-containing (inner) leaflet. We note the high experimental uncertainty of the absolute values of CH_3 location (Table 1), which impedes us from discussing differences between MSPC, SMPC, and PMPC. A common observation for all three lipids is that the area per lipid in the inner leaflet is increased, for MSPC and PMPC also in the outer leaflet. This suggests that hydrocarbon chains, which penetrate into an opposing leaflet of lipids with less chainlength-mismatch, evoke a state of higher disorder in the hydrocarbon chain region. Notably, there are also changes in the headgroup regions, which seem to emerge along with the CH_3 -asymmetry. Outer leaflet headgroups extend further into the water and therefore accommodate a higher number of water molecules than in the symmetric references. Overall compared

to membranes of symmetric inner and outer leaflet references these asymmetric bilayers are thinner, as a result of the increase of area per lipid in one or both leaflets.

Next we focused on the natural lipid mixture MSM, which comprises a much higher chain-asymmetry than the here studied PCs due to its prevalent long acyl chains (22:0, 23:0, 24:0, 24:1). In symmetric vesicles of MSM we found a wider spread of the CH_3 -region than for all studied PCs and a slightly higher area per lipid of 64.8 \AA^2 (Frewein et al. 2021). Inner and outer leaflet mixtures of MSM and DPPC have $A^{\text{in}} \sim 64 \text{ \AA}^2$ and $A^{\text{out}} \sim 63 \text{ \AA}^2$ in symmetric LUVs (Tables 1 and S4; Fig. S6). In asymmetric vesicles the area per lipid of the inner leaflet is $\sim 5\%$ smaller than in the reference, with about twice as much interdigitating hydrocarbons as compared to aLUVs with the donors MSPC and SMPC. The long chains of MSM seem to have an ordering effect on DPPC, which is neither present in symmetric vesicles, nor in asymmetric vesicles with less interdigitation. In contrast, outer leaflet MSM has a similar effect on the headgroup regions of the asymmetric vesicles compared to outer leaflet MSPC, SMPC, and PMPC, i.e., the outer leaflet of the asymmetric vesicle is more hydrated than the inner leaflet.

Given that for fluid phase asymmetric vesicles there is not yet any evidence that opposing monolayers would influence each others structures (Eicher et al. 2017, 2018) and that interdigitation has been shown to have little to no influence on lipid diffusion in symmetric bilayers (Schram and Thompson 1995; Horner et al. 2013), this is a surprising result in asymmetric bilayers. Our data suggest a delicate interplay between repulsive entropic/steric forces and attractive van der Waals interactions. In asymmetric bilayers with low interdigitation, the configurational entropy contribution of the hydrocarbon termini apparently dominate and the penetrating chain segments perturb the packing of the opposing DPPC. In contrast, the long chains of MSM share a larger surface of contact and their cohesion leads to an ordering of chains. Indeed, MD-simulations of asymmetric membranes containing 24:0-sphingomyelin reported an increase of order for the interdigitating moieties of its hydrocarbon chain (Róg et al. 2016).

Structure of aLUVs with Monounsaturated Lipids

Finally, we extended our study also to aLUVs with outer leaflets enriched in POPC or SOPC, i.e. lipids with mixed saturated and unsaturated hydrocarbons. Such mixed chain lipids are much more common in mammalian plasma membranes than those studied in the previous section (Lorent et al. 2020). Interestingly, these lipids share with PMPC, SMPC, and MSPC, a nearly equal overlap region of interdigitating and back-bending terminal methyl groups in symmetric bilayers (Frewein et al. 2021). In the case of asymmetric membranes the role of unsaturated hydrocarbons

at the bilayer center is even less clear. We have therefore employed the here developed analysis model also to DPPCⁱⁿ/POPC^{out} and DPPCⁱⁿ/SOPC^{out} aLUVs.

Table 2 gives the corresponding results for the main structural parameters (see also Table S4; Fig. S3). The overall lipid exchange was about equal for both lipids, although POPC flipped slightly more into the inner leaflet during aLUV preparation. The overall membrane thickness D_B of both aLUVs was about 2 Å thinner than the combined $D_B/2$ -values of symmetric inner and outer leaflet mimics. Within experimental uncertainty these thickness changes occurred almost equally in both leaflets, i.e. $\Delta D_M^{\text{in}} \sim \Delta D_M^{\text{out}}$, although the inner leaflets thickness appears to be somewhat more affected. This is particularly reflected in the changes of D_C^{in} and D_C^{out} , which were more pronounced for the DPPC-enriched inner leaflet. This leads to a large increase of A^{in} by about 8% as compared to symmetric DPPC bilayers, or a change of DPPC lateral area $\Delta A^{\text{acc}}/A^{\text{acc}} \sim 7\%$. The area per lipid values in the outer leaflet remained unchanged within experimental uncertainty. Moreover, the areas per lipid in the inner leaflet closely matched those of the outer leaflet.

Analysis for the position of the terminal CH₃ center of mass revealed interesting differences between POPC and SOPC containing aLUVs. In particular, we found that in

the case of a POPC-donor, the CH₃ function is located in the outer leaflet and resides for SOPC slightly within the inner leaflet. This could mean that, the 18:1-chains in the leaflet containing POPC bends back to match the length of 16:0. Another possibility is that the kink induced by the double bond of the 18:1-chains is responsible for the terminal methyls being located further in the outer leaflet. SOPC in turn, with its longer 18:0 chain seems to slightly interdigitate, thus shifting the CH₃ center of mass again into the DPPC-rich inner leaflet. The headgroups in both systems also exhibit a high degree of asymmetry. In the SOPC-rich leaflet they stretch to the outside, as it happens in the saturated systems, leading to a high number of water molecules per headgroup in the outer leaflet. For DPPCⁱⁿ/POPC^{out} this situation is reversed, showing a broader headgroup with more water in the inner leaflet. The symmetric reference vesicles qualitatively mirror this behavior, with the outer leaflet mimics having a higher number of hydration waters than the inner ones, however not to the extent of the asymmetric vesicles.

While understanding the subtle effects on headgroup hydration encourage additional experiments, the loosening of lipid packing in the inner leaflet of the presently studied aLUVs containing monounsaturated lipids emerges as a salient feature. Previous SANS experiments on POPCⁱⁿ/DPPC^{out} experiments also reported a softening of the DPPC-enriched leaflet below the melting temperature of DPPC, but no coupling effects when both leaflets were in the L_α phase (Heberle et al. 2016). Also in a later report, using joint SAXS/SANS experiments, we found no coupling for fluid POPCⁱⁿ/DPPC^{out} aLUVs (Eicher et al. 2017). We tested the parameters used in that study for our vesicles and indeed found another local minimum with the same areas per lipid. However, this drove the system to $z_{\text{CH}_3} = -2.5$ Å, which would imply a similar interdigitation into the inner leaflet as MSM. We therefore consider this solution less likely. We speculate that absence of interleaflet coupling in our previous studies is a combination of lower data quality, and improved modeling and optimization routines used for fitting present data. However, we cannot fully exclude sample specific properties or slight differences in sample preparation as a potential cause.

Conclusion

To the best of our knowledge the present study provides the first experimental evidence of structural coupling of all-fluid asymmetric bilayers. Previously, transbilayer coupling was only observed when at least one leaflet was in the gel phase (Heberle et al. 2016; Eicher et al. 2018), including also lateral diffusion studies of chain asymmetric sphingomyelin (Chiantia and London 2012). The observed coupling suggests a subtle balance of ordering and disordering

Table 2 Fit results for aLUVs with POPC and SOPC as donor lipids, as well as properties of inner/outer leaflet reference LUVs

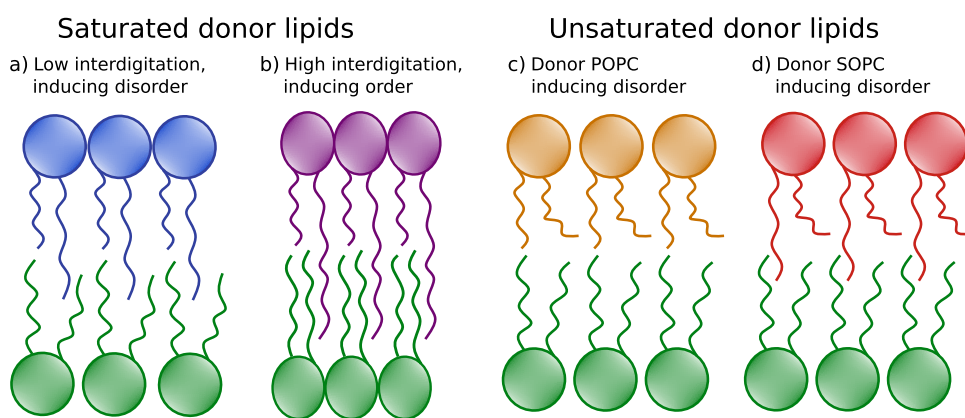
Donor lipid	ϵ [%]	POPC		SOPC	
		aLUV	Ref	aLUV	Ref
$\chi_{\text{acc}} : \chi_{\text{don}}$ %	5	64:36		61:39	
$\chi_{\text{acc}}^{\text{in}} : \chi_{\text{don}}^{\text{in}}$ %	5	85:15		93:07	
$\chi_{\text{acc}}^{\text{out}} : \chi_{\text{don}}^{\text{out}}$ %	5	45:55		33:67	
D_B [Å]	3	36.3	38.9*	37.3	39.3*
z_{CH_3} [Å]	10	1.00		-0.35	
V_{bw} [Å ³]	6	29.60		29.6	
σ_{poly} [%]	6	4.5		6.1	
D_M^{in} [Å]	6	17.8	19.7*	18.2	20.0*
D_M^{out} [Å]	6	18.6	19.2*	19.1	19.4*
D_C^{in} [Å]	5	13.0	14.5*	13.4	14.7*
D_C^{out} [Å]	5	13.8	14.2*	14.3	14.5*
A^{in} [Å ²]	5	68.9	62.8*	67.7	62.3*
A^{out} [Å ²]	5	68.3	65.9*	68.5	67.3*
A^{acc} [Å ²]	5	67.4	63.1 [†]	67.6	63.1 [†]
A^{don} [Å ²]	5	68.9	67.5 [†]	69.0	68.8 [†]
n_W^{in}	6	17.9	11.0*	9.0	7.2*
n_W^{out}	6	9.0	4.9*	20.4	14.6*

ϵ is the error for all aLUV parameter values

* Reference values from symmetric inner/outer leaflet references (Figs. S6 and S7; Table S4)

[†] From single lipid references (Table S1)

Fig. 3 Schematic of possible lipid arrangements of interdigitated systems with saturated lipids of low (a) (DPPCⁱⁿ/MSPC^{out}, DPPCⁱⁿ/SMPC^{out}, DPPCⁱⁿ/PMPC^{out}) and high (b) chainlength-mismatch (DPPCⁱⁿ/MSM^{out}), as well as DPPCⁱⁿ/POPC^{out} (c) and DPPCⁱⁿ/SOPC^{out} (d)



effects at the hydrophobic interface between the two leaflets as schematically shown in Fig. 3. For MSPC, SMPC, PMPC we found a minor interdigitation, which led to a loosening of the packing of inner leaflet DPPC. MSM, whose long acyl chains penetrates significantly into the opposing monolayer instead caused an overall lateral condensation of the bilayer. We propose that the configurational entropy of the hydrocarbons, which increases with chain length is able to disorder by fluctuation-mediated steric repulsion the inner lipid leaflets only upon minor chain overlap. On the contrary, energetic optimization of hydrocarbon cohesive forces outweighs this effect in the case of large interdigitation. Such a scenario indeed was suggested from MD simulations (Róg et al. 2016).

The decrease of inner leaflet DPPC packing in the case of outer leaflets enriched in POPC and SOPC suggest an additional scenario. Here, the larger lateral area required by the unsaturated hydrocarbon seems to generate a packing mismatch, which is alleviated by increasing the area per lipid of DPPC residing in the inner leaflet. Both scenarios are likely to affect differential stress between the two leaflets (Hossein and Deserno 2020). As most chain-asymmetric saturated lipids are long-chain sphingomyelins such as the ones used in this study or phospholipids with one mono or polyunsaturated hydrocarbon chain, such transleaflet coupling schemes might indeed be present also in natural membranes. We note, however, that cholesterol, which is the most abundant lipid in mammalian plasma membranes has been shown to modulate interdigitation-based ordering of inner leaflet lipids (Róg et al. 2016). In order to keep our analysis tractable, we had to exclude cholesterol in the present study. With ongoing efforts in fabricating and analyzing more realistic models of mammalian plasma membranes such goals seem within reach.

Methods

Lipids, Chemicals and Sample Preparation

Lipids were purchased from Avanti Polar Lipids (Alabaster, AL, USA) and used without further purification. Chloroform, methanol (pro analysis grade), sucrose and methyl- β -cyclodextrin (m β CD) were obtained from Merck KGaA, Darmstadt, Germany. We prepared asymmetric unilamellar vesicles following the heavy donor cyclodextrin exchange protocol (Doktorova et al. 2018). Acceptor and donor lipids were weighed (ratio 1:2 mol/mol), dispersed separately in a chloroform/methanol mixture (2:1, vol/vol) and dried under a soft argon beam in a glass vial. Acceptor vesicles were prepared from a mixture (19:1 mol/mol) of chain deuterated DPPC (DPPCd62) and dipalmitoyl phosphatidylglycerol (DPPGd62); donor vesicle consisted of the single species indicated. The resulting films were kept over night in vacuum to ensure the evaporation of all solvent and hydrated with ultrapure H₂O containing 25 mM NaCl (acceptors, 10 mg/ml lipid) or 20% (wt/wt) sucrose (donors, 20 mg/ml) followed by 1 h incubation at 50 °C (room temperature for POPC and SOPC) and 5 freeze/thaw cycles. Acceptor vesicles were extruded at 50 °C using a handheld mini extruder (Avanti Polar Lipids, AL, USA) with a 100 nm pore diameter polycarbonate filter 31 times or until reaching a polydispersity index < 10% (measured by dynamic light scattering (DLS) using a Zetasizer NANO ZS90, MalvernPanalytical, Malvern, UK).

Donor vesicles were diluted 20-fold with water and centrifuged at 20,000 g for 30 min. The supernatant was discarded, the resulting pellet suspended in a 35 mM m β CD solution (lipid:m β CD 1:8 mol/mol) and incubated for 2 h at 50 °C, while being shaken at a frequency of 600 min⁻¹. Acceptor vesicles were added and incubated for another 15 min. The exchange was stopped by diluting the mixture 8-fold with water and centrifuging again at 20,000 g for 30 min. The supernatant containing the asymmetric vesicles

was then concentrated to $< 500 \mu\text{l}$ using 15 ml-Amicon centrifuge filters (Merck, 100 kDa cut-off) at $5000 \times g$. To remove residual CD and sucrose, the filters were filled with the desired solvent (H_2O for SAXS and 37% and 100% D_2O for SANS) and re-concentrated in 3 cycles. The final vesicle-sizes were again measured by DLS to ensure the absence of donor MLVs.

Symmetric reference vesicles were prepared using only protiated lipids and extruded as the acceptor vesicles, but using pure H_2O or D_2O . Inner leaflet mimics contained 90 mol% acceptor lipid (DPPC/DPPG 19:1 mol/mol), 10 mol% donor lipid; the outer leaflet samples were mixtures of 30 mol% acceptor and 70 mol% donor lipid.

Small-Angle Scattering (SAS) Experiments

SANS measurements were performed at D22, Institut Laue-Langevin, Grenoble, France, equipped with either 1 (DOI: 10.5291/ILL-DATA.9-13-822, DOI: ILL-DATA.TEST-3063) or 2 (DOI: 10.5291/ILL-DATA.9-13-938) ^3H multidetectors. Sample-to-detector distances were 1.6, 5.6 and 17.8 m with corresponding collimations of 2.8, 5.6 and 17.8 m for the single detector setup; or 5.6 and 17.8 m with the second detector out of center at 1.3 m, with 5.6 and 17.8 m collimations. The neutron wavelength was 6 Å ($\Delta\lambda/\lambda = 10\%$). Samples were filled in Hellma 120-QS cuvettes of 1 mm pathway and heated to 50 °C using a bath circulator. Lipid concentrations were about 5 mg/ml in 100% D_2O and 15 mg/ml in 37% D_2O . Data were reduced using GRASP (www.ill.eu/users/support-labs-infrastructure/software-scientific-tools/grasp/ accessed on 25 June 2019), performing flat field, solid angle, dead time and transmission correction, normalizing by incident flux and subtracting contributions from empty cell and solvent.

SAXS data were recorded at BM29, ESRF, Grenoble, France (DOI: <https://doi.org/10.1515/ESRF-ES-514136943>), equipped with a Pilatus3 2 M detector, using a photon energy of 15 keV at a sample-to-detector distance of 2.867 m (Pernot et al. 2018). Samples were measured at a concentration of 10 mg/ml, at 50 °C and exposed for 20 times 2 s in a flow-through quartz capillary of 1 mm light path length. Data reduction and normalization were done by the automated ExiSAXS system; for subtraction of solvent and capillary contributions SAXSutilities 2 (www.saxsutilities.eu accessed on 29 October 2020) was used.

SAS-Data Analysis

To analyze SAS-data we model our lipid bilayer using volume probability distribution functions describing the localization and extent of different parts of the lipids within the membrane. This approach has been previously introduced for SAS data evaluation as the SDP-model (Kučerka et al.

2008) and later extended to asymmetric bilayers (Eicher et al. 2017). For symmetric vesicles we use a previously introduced (Frewein et al. 2021) modified version of the SDP-model, which includes the vesicle form factor via the separated form factor-method (Pencer et al. 2006), membrane polydispersity and a headgroup-hydration shell. We also extend the asymmetric SDP-model by the same aspects, as well as modifying the distribution function of the terminal methyl to better allow for examining hydrocarbon chain interdigitation. The full model is presented in Appendix section A. To take into account the presence of lipid mixtures, we average all volumes and scattering lengths for each part of the lipid. To give an example, for a 1:1 mixture of DPPC and PMPC we assume an average lipid with 31 hydrocarbons. This includes the assumption that the lipids mix homogeneously within their leaflet. We note that the disagreement between model and low- q SAXS data for symmetric vesicles (Figs. S4–S7) is due to technical issues that occurred during the experiments, not to inadequacies of the model. Previously reported SAXS data of symmetric LUVs were fully accounted for in this q -range by including a hydration shell (Frewein et al. 2021). Moreover, we also showed that the hydration shell does not contribute to higher scattering vectors. Consequently, reported structural data for symmetric reference LUVs are not affected by difficulties in fitting low- q SAXS data.

Fitting was done as described in Frewein et al. (2021), including the same SAXS/SANS-weighting, negative water-penalty and Trust Region Reflective optimization algorithms (Virtanen et al. 2020). Errors were estimated from the covariance matrix, considering also possible systematic errors (e.g. from aLUV compositional uncertainties). For derived quantities we used Gaussian error propagation. For asymmetric vesicles we constrained the areas per lipid A_{acc} and A_{don} by Gaussian priors with mean and standard deviations of the results in Frewein et al. (2021). Also the total lipid concentrations $\chi_{\text{acc}}/\chi_{\text{don}}$ were constrained by Gaussian priors, using the results from gas chromatography (GC) compositional analysis. As the number of parameters describing the transmembrane structure is doubled, compared to symmetric vesicles, we fixed the distance between the hydrophobic interfaces and the backbones d_{BB} to 0.9 Å and the backbone width σ_{BB} to 2.1 Å. Like for symmetric vesicles, we fixed the volumes of the individual moieties of the lipids according to Nagle et al. (2019) and the smearing parameters were set to $\sigma_{\text{CH}_2} = 2.5 \text{ \AA}$ and $\sigma_{\text{Chol}} = 3 \text{ \AA}$.

Compositional Analysis Using Gas Chromatography

Fatty acid methyl esters (FAMES) were prepared upon incubation with a Methanolic- H_2SO_4 solvent mixture and performed GC measurements using a GC 2010 Plus (Shimadzu), equipped with a split/splitless injector and a

SGE BPX70-Cyanopropyl Polysilphenylene-siloxane column (25 m by 0.22 mm ID and 0.25 m film thickness) as described in Marx et al. (2021). For the calibration curves of 14:0, 18:0 and 18:1 hydrocarbon chains, we performed the same protocol with a concentration series with 1,2-dimyristoyl[1]sn-glycero-3-phosphocholine, 1,2-distearoyl-sn-glycero-3-phosphocholine and 1,2-dioleoyl-sn-glycero-3-phosphocholine, purchased from Avanti Polar Lipids (Alabaster, AL, USA). Calibration curves and measurements can be found in the Supplementary Information Tables S5 and S6; Fig. S8.

Appendix A

Asymmetric SAS-Model

Models for asymmetric flat bilayers distinguish themselves from symmetric models mainly by the necessity to include the imaginary part of the form factor. We adopted the SDP model for asymmetric bilayers introduced in Eicher et al. (2017), with the following modifications: We included the vesicle form factor by the separated form factor method (Pencer et al. 2006) to describe low- q SANS data. We introduced some flexibility in the headgroup contrast using a higher-density hydration layer as described in Frewein et al. (2021). Finally, we described the terminal methyl groups of all lipids by a single error-function which is not necessarily centered around the bilayer center.

The necessary Fourier-transforms for the used distributions are given in the following. The error-function slab is centered around μ , has a width of d , a smearing parameter of σ and its area normalized to 1.

$$p_{\text{erf}}(z) = \frac{1}{2d} \int_{-\infty}^{\infty} \left[\text{erf}\left(\frac{z - \mu + d/2}{\sqrt{2}\sigma}\right) - \text{erf}\left(\frac{z - \mu - d/2}{\sqrt{2}\sigma}\right) \right] e^{iqz} dz$$

$$= \frac{\sin(qd/2)}{qd/2} e^{-\frac{\sigma^2 q^2}{2}} [\cos(\mu q) + i \sin(\mu q)] \quad (1)$$

For the Gaussian distribution centered at μ and standard deviation σ we use:

$$p_{\text{Gauss}}(z) = \int_{-\infty}^{\infty} \frac{1}{\sqrt{2\pi}\sigma} e^{-\frac{(x-\mu)^2}{2\sigma^2}} e^{iqz} dz = e^{-\frac{q^2\sigma^2}{2}} [\cos(\mu q) + i \sin(\mu q)] \quad (2)$$

Table 3 Molecular groups described by individual functions

Abbr.	Content	Function
<i>CH3</i>	Terminal methyl group	Error-function
<i>CH2</i>	Methylene chains	Error-function
<i>BB</i>	Backbone*	Gaussian
<i>PCN</i>	Phosphate + CN	Gaussian
<i>Chol</i>	Choline-CH3 group	Gaussian
<i>BW</i>	Hydration layer	Error-function

*Carbonyl-glycerol or sphingosine

We calculate the form factor by summing over the parts given in Table 3 for inner and outer leaflet, using the functions reported in Eqs. (1) and (2), multiplied by the respective weighting and contrast. Weighting factors for the headgroup contributions (*BB*, *PCN*, *Chol*) are $\frac{V_k}{A}$, A denoting the area per lipid and V_k the volume of the respective moiety. All terminal methyl groups are condensed into one error function, whose center can deviate from the membrane center. This allows the description of interdigitated or back-bent states without increasing the number of parameters. Finally, *CH2* and *BW* are weighted by the respective chain widths $D_C^{\text{in/out}}$, to fill the whole unit cell area, followed by subtraction of the quasi molecular groups they contain. In the case of an asymmetric *CH3*-distribution, however, the contribution of the methyl groups are not necessarily contained in the respective *CH2*-distributions. In this case, one of the leaflets loses some material with the volume V_s , which has to be respected in the model.

The connection between chain widths, volumes and area per lipid is then given by the following relations:

$$D_C^{\text{in}} = \frac{(V_{\text{CH2}}^{\text{in}} + V_{\text{CH3}}^{\text{in}} + V_s)}{A^{\text{in}}} \quad (3)$$

$$D_C^{\text{out}} = \frac{(V_{\text{CH2}}^{\text{out}} + V_{\text{CH3}}^{\text{out}} - V_s)}{A^{\text{out}}}$$

We define V_s as half the integral over the terminal methyl group distribution function from its center μ_{CH3} to the center of the bilayer (the area indicated in Fig. 5), multiplied by the area per lipid of the leaflet towards which the distribution shifts:

$$V_s = \frac{A^{\text{in/out}}}{2 \int_{\mu_{\text{CH3}}}^0 p_{\text{CH3}}(z) dz} \quad (4)$$

Fig. 4 SDP-model and parameters used in the membrane form factor. Inner leaflet parameters are defined analogously

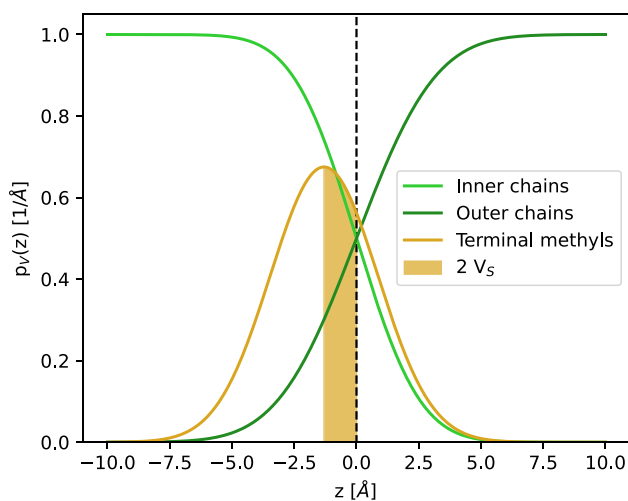
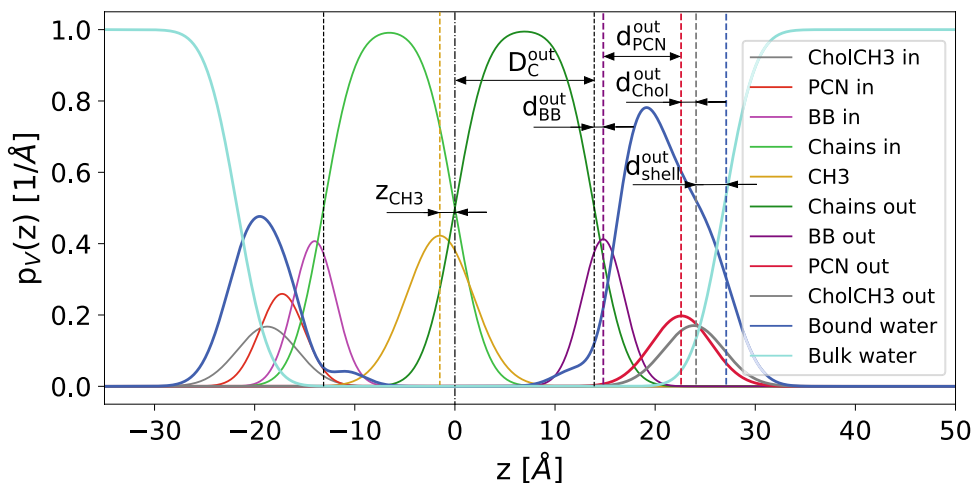


Fig. 5 Arrangement of the hydrocarbon chain volume probability distributions in the membrane center. The distribution of CH3-groups (yellow) is assumed to shift to the left (inner leaflet), causing a transfer of volume V_s from the outer to the inner leaflet. As the yellow curve comprises the methyl groups of both inner and outer leaflet, the shaded area corresponds to twice this volume

Note that the sign of V_s changes according to the direction of the shift, being positive in case of a shift towards the inner leaflet and *vice versa*.

The membrane thickness polydispersity is implemented as described in Frewein et al. (2021), applying the same relative Gaussian distribution on inner and outer chain-width. Contrasts of the individual moieties k are defined by $\Delta\rho_k = \frac{b_k}{V_k} - \rho_{solvent}$, b and ρ denoting scattering length and scattering length density for either radiation (X-rays or neutrons). A graphical representation of all distances between moieties and thicknesses is given in Fig. 4.

The full model includes the vesicle form factor F_{sphere} , the weighted average of bilayer form factors F_{bil} , which we split into real and imaginary part, and the incoherent background I_{inc} :

$$I(q) \propto F_{sphere}(R_m, \sigma_R) \sum_k \mathcal{N}(D_{C,k} | \overline{D_C}, \sigma_{poly}) \left\{ |F_{bil,k}^{real}|^2 + |F_{bil,k}^{imag}|^2 \right\} + I_{inc} \quad (5)$$

with

$$\begin{aligned}
 F_{bil,k}^{real} = & 4\Delta\rho_{bw} \frac{1}{q} e^{-\frac{q^2\sigma_{CH2}^2}{2}} \sin\left(q \frac{d_{BB}^{in} + d_{PC}^{in} + d_{shell}^{in}}{2}\right) \\
 & \cos\left(q \left(-D_{C,k}^{in} - \frac{d_{BB}^{in} + d_{PC}^{in} d_{shell}^{in}}{2}\right)\right) \\
 & + 2(\Delta\rho_{PC}^{in} - \Delta\rho_{bw}) \frac{V_{PC}}{A} e^{-\frac{q^2\sigma_{PC}^2}{2}} \\
 & \cos\left(q \left(\frac{-D_{C,k}^{in} - d_{BB}^{in} - d_{PC}^{in}}{2}\right)\right) \\
 & + 2(\Delta\rho_{BB}^{in} - \Delta\rho_{bw}) \frac{V_{BB}^{in}}{A} e^{-\frac{q^2\sigma_{BB}^2}{2}} \\
 & \cos\left(q \left(\frac{-D_{C,k}^{in} - d_{BB}^{in}}{2}\right)\right) \\
 & + 2\Delta\rho_{CH2}^{in} \frac{1}{q} e^{-\frac{q^2\sigma_{CH2}^2}{2}} \sin\left(\frac{qD_{C,k}^{in}}{2}\right) \\
 & \cos\left(q \left(\frac{-D_{C,k}^{in}}{2}\right)\right) \\
 & + f_{CH3,k} e^{-\frac{q^2\sigma_{CH3}^2}{2}} \sin\left(\frac{qz_{CH3}}{2}\right) \\
 & \cos\left(\frac{qz_{CH3}}{2}\right) \\
 & + 2\Delta\rho_{CH2} \frac{1}{q} e^{-\frac{q^2\sigma_{CH2}^2}{2}} \sin\left(\frac{qD_{C,k}^{out}}{2}\right) \\
 & \cos\left(\frac{qD_{C,k}^{out}}{2}\right) \\
 & + 2(\Delta\rho_{BB}^{out} - \Delta\rho_{bw}) \frac{V_{BB}^{out}}{A} e^{-\frac{q^2\sigma_{BB}^2}{2}} \\
 & \cos\left(q \left(\frac{D_{C,k}^{out} + d_{BB}^{out}}{2}\right)\right) \\
 & + 2(\Delta\rho_{PC}^{out} - \Delta\rho_{bw}) \frac{V_{PC}^{out}}{A} e^{-\frac{q^2\sigma_{PC}^2}{2}} \\
 & \cos\left(q \left(\frac{D_{C,k}^{out} + d_{BB}^{out} + d_{PC}^{out}}{2}\right)\right) \\
 & + 4\Delta\rho_{bw} \frac{1}{q} e^{-\frac{q^2\sigma_{CH2}^2}{2}} \sin\left(q \frac{d_{BB}^{out} + d_{PC}^{out} + d_{shell}^{out}}{2}\right) \\
 & \cos\left(q \left(D_{C,k}^{out} + \frac{d_{BB}^{out} + d_{PC}^{out} + d_{shell}^{out}}{2}\right)\right)
 \end{aligned} \tag{6}$$

and

$$\begin{aligned}
 F_{bil,k}^{imag} = & 4\Delta\rho_{bw} \frac{1}{q} e^{-\frac{q^2\sigma_{CH2}^2}{2}} \sin\left(q \frac{d_{BB}^{in} + d_{PC}^{in} + d_{shell}^{in}}{2}\right) \\
 & \sin\left(q \left(-D_{C,k}^{in} - \frac{d_{BB}^{in} + d_{PC}^{in} d_{shell}^{in}}{2}\right)\right) \\
 & + 2(\Delta\rho_{PC}^{in} - \Delta\rho_{bw}) \frac{V_{PC}}{A} e^{-\frac{q^2\sigma_{PC}^2}{2}} \\
 & \sin\left(q \left(\frac{-D_{C,k}^{in} - d_{BB}^{in} - d_{PC}^{in}}{2}\right)\right) \\
 & + 2(\Delta\rho_{BB}^{in} - \Delta\rho_{bw}) \frac{V_{BB}^{in}}{A} e^{-\frac{q^2\sigma_{BB}^2}{2}} \\
 & \sin\left(q \left(\frac{-D_{C,k}^{in} - d_{BB}^{in}}{2}\right)\right) \\
 & + 2\Delta\rho_{CH2}^{in} \frac{1}{q} e^{-\frac{q^2\sigma_{CH2}^2}{2}} \sin\left(\frac{qD_{C,k}^{in}}{2}\right) \\
 & \sin\left(\frac{q(-D_{C,k}^{in})}{2}\right) \\
 & + f_{CH3,k} e^{-\frac{q^2\sigma_{CH3}^2}{2}} \sin\left(\frac{qz_{CH3}}{2}\right) \\
 & \sin\left(\frac{qz_{CH3}}{2}\right) \\
 & + 2\Delta\rho_{CH2} \frac{1}{q} e^{-\frac{q^2\sigma_{CH2}^2}{2}} \sin\left(\frac{qD_{C,k}^{out}}{2}\right) \\
 & \sin\left(\frac{qD_{C,k}^{out}}{2}\right) \\
 & + 2(\Delta\rho_{BB}^{out} - \Delta\rho_{bw}) \frac{V_{BB}^{out}}{A} e^{-\frac{q^2\sigma_{BB}^2}{2}} \\
 & \sin\left(q \left(\frac{D_{C,k}^{out} + d_{BB}^{out}}{2}\right)\right) \\
 & + 2(\Delta\rho_{PC}^{out} - \Delta\rho_{bw}) \frac{V_{PC}^{out}}{A} e^{-\frac{q^2\sigma_{PC}^2}{2}} \\
 & \sin\left(q \left(\frac{D_{C,k}^{out} + d_{BB}^{out} + d_{PC}^{out}}{2}\right)\right) \\
 & + 4\Delta\rho_{bw} \frac{1}{q} e^{-\frac{q^2\sigma_{CH2}^2}{2}} \sin\left(q \frac{d_{BB}^{out} + d_{PC}^{out} + d_{shell}^{out}}{2}\right) \\
 & \sin\left(q \left(D_{C,k}^{out} + \frac{d_{BB}^{out} + d_{PC}^{out} + d_{shell}^{out}}{2}\right)\right)
 \end{aligned} \tag{7}$$

The prefactor for the methyl group error functions $f_{CH3,k}$ is given by:

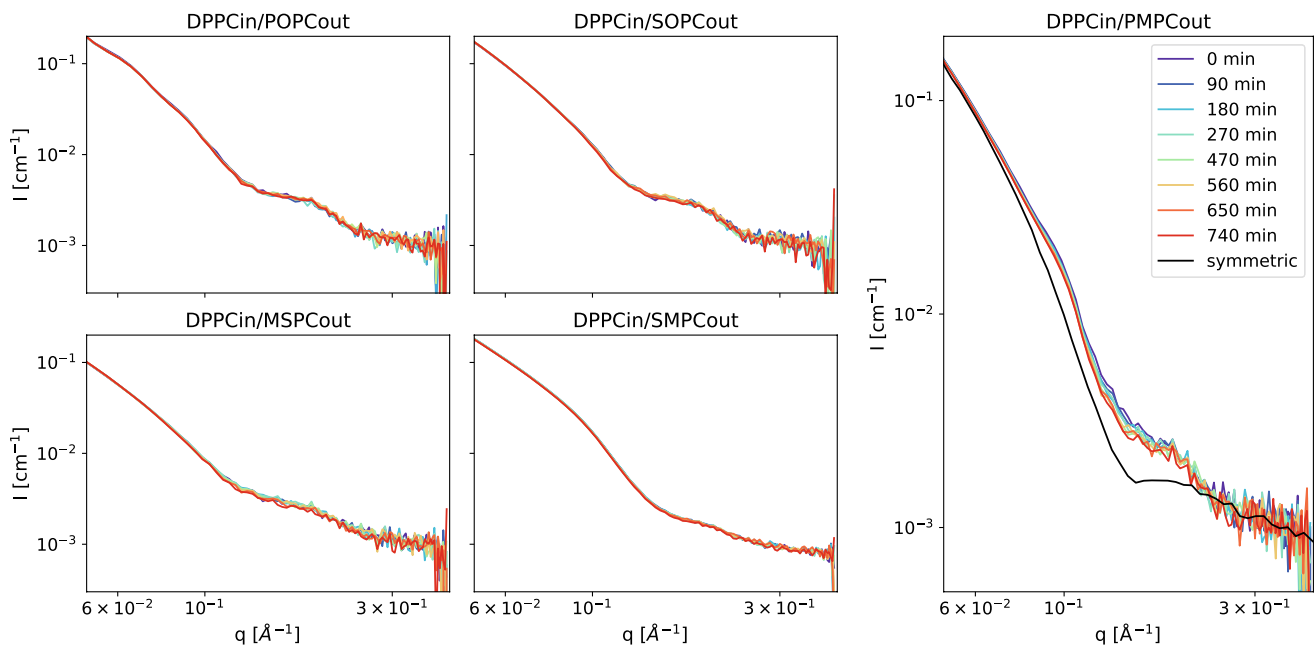


Fig. 6 SANS-data of asymmetric vesicles monitored over 12 h at 50 °C. For DPPCⁱⁿ/PMPC^{out} the inner leaflet mimic is given as a reference

$$f_{\text{CH3},k} = \left[\frac{\Delta\rho_{\text{CH3}}^{\text{in}} + \Delta\rho_{\text{CH3}}^{\text{out}}}{2} - \frac{\left(1 + \frac{V_s}{V_{\text{CH3}}^{\text{in}}}\right)}{2\Delta\rho_{\text{CH2}}^{\text{in}}} - \frac{\left(1 - \frac{V_s}{V_{\text{CH3}}^{\text{out}}}\right)}{2\Delta\rho_{\text{CH2}}^{\text{out}}} \right] \frac{2(V_{\text{CH3}}^{\text{in}} + V_{\text{CH3}}^{\text{out}})}{\left(1 + \frac{V_s}{V_{\text{CH3}}^{\text{out}}}\right) \frac{V_{\text{CH3}}^{\text{in}} + V_{\text{CH2}}^{\text{in}} + V_s}{D_{C,k}^{\text{in}}} + \left(1 - \frac{V_s}{V_{\text{CH3}}^{\text{in}}}\right) \frac{V_{\text{CH3}}^{\text{out}} + V_{\text{CH2}}^{\text{out}} - V_s}{D_{C,k}^{\text{out}}} } \quad (8)$$

To describe the contribution from the overall vesicle shape we use the Schultz-distributed form factor of a sphere, as described in Kučerka et al. (2007):

$$F_{\text{sphere}} = \frac{8\pi^2(z+1)(z+2)}{s^2q^2} \left\{ 1 - \left(1 + \frac{4q^2}{s^2}\right)^{-(z+3)/2} \cos \left[(z+3) \arctan \left(\frac{2q}{s} \right) \right] \right\} \quad (9)$$

Mean vesicle radius R_m and polydispersity σ_R enter via the auxiliary quantities $s = \frac{R_m}{\sigma_R}$ and $z = \frac{R_m^2}{\sigma_R^2} - 1$.

Appendix B

Stability of Membrane Asymmetry

To check the stability of our asymmetric vesicles, we monitored their SANS signal over one night while keeping them at 50 °C. The systems DPPCⁱⁿ/POPC^{out}, DPPCⁱⁿ/SOPC^{out}, DPPCⁱⁿ/MSPC^{out} and DPPCⁱⁿ/SMPC^{out} were completely

stable both in their overall vesicle structure (low- q) and in their transmembrane structure (high- q). For DPPCⁱⁿ/PMPC^{out} the low- q region also remained unchanged. How-

ever, in the high- q , the sample slowly equilibrated towards a less asymmetric state (Fig. 6). We hypothesize that the reason we could only observe this flip-flop for the PMPC-donor is due to its lower hydrophobic volume and thus a lower energy barrier for the head-groups when traversing through the membrane. Compared to the timescale of our other SAS-experiments, the flip-flop was slow and is therefore assumed not to interfere with the results.

Supplementary Information The online version of this article (<https://doi.org/10.1007/s00232-022-00234-0>) contains supplementary material, which is available to authorized users.

Acknowledgements This research was supported by the ILL graduate school, Ph.D. No. 181-19. PP and EFS are supported by the Austrian Science Fund (FWF), grant no. P32514 to GP. We thank the ILL for

neutron beamtime, the PSCM for access to support laboratories, and Petra Pernot, Mark Tully, Dihia Moussaoui and Anton Popov for their assistance with SAXS-experiments at BM29.

Author Contributions Conceptualization, MPKF, YG, LP and GP; formal analysis, MPKF and GP; investigation, MPKF, PP, EFS, KB, HLS and LP; methodology, MPKF and EFS; software, MPKF; supervision, LP and GP; visualization, MPKF; writing—original draft, MPKF and GP; writing-review and editing, MPKF, PP, EFS, KB, FAH, HLS, YG, LP and GP All authors have read and agreed to the published version of the manuscript.

Funding Open access funding provided by University of Graz. PP and EFS are supported by the Austrian Science Fund (FWF), Grant No. P32514 to GP. This research was supported by the ILL graduate school, Ph.D. No. 181-19.

Data Availability SANS data (DOI: 10.5291/ILL-DATA.9-13-822, DOI: ILL-DATA.TEST-3063, DOI: 10.5291/ILL-DATA.9-13-938); SAXS data (DOI: 10.1515/ESRF-ES-51413694)

Code Availability Upon request (M.P.K.F. and G.P.)

Declarations

Conflict of interest All authors have no financial or non-financial interest declare.

Open Access This article is licensed under a Creative Commons Attribution 4.0 International License, which permits use, sharing, adaptation, distribution and reproduction in any medium or format, as long as you give appropriate credit to the original author(s) and the source, provide a link to the Creative Commons licence, and indicate if changes were made. The images or other third party material in this article are included in the article's Creative Commons licence, unless indicated otherwise in a credit line to the material. If material is not included in the article's Creative Commons licence and your intended use is not permitted by statutory regulation or exceeds the permitted use, you will need to obtain permission directly from the copyright holder. To view a copy of this licence, visit <http://creativecommons.org/licenses/by/4.0/>


References

- Antony B, Vanni S, Shindou H, Ferreira T (2015) From zero to six double bonds: phospholipid unsaturation and organelle function. *Trends Cell Biol* 25(7):427–436. <https://doi.org/10.1016/j.tcb.2015.03.004>
- Bretscher MS (1972) Asymmetrical lipid bilayer structure for biological membranes. *Nat New Biol* 236(61):11–12. <https://doi.org/10.1038/newbio236011a0>
- Brzustowicz MR, Brunger AT (2005) X-ray scattering from unilamellar lipid vesicles. *J Appl Crystallogr* 38(1):126–131. <https://doi.org/10.1107/S0021889804029206>
- Chiantia S, London E (2012) Acyl chain length and saturation modulate interleaflet coupling in asymmetric bilayers: effects on dynamics and structural order. *Biophys J* 103(11):2311–2319. <https://doi.org/10.1016/j.bpj.2012.10.033>
- Doktorova M, Heberle FA, Eicher B, Standaert RF, Katsaras J, London E, Pabst G, Marquardt D (2018) Preparation of asymmetric phospholipid vesicles for use as cell membrane models. *Nat Protoc* 13(9):2086–2101. <https://doi.org/10.1038/s41596-018-0033-6>
- Eicher B, Heberle FA, Marquardt D, Rechberger GN, Katsaras J, Pabst G (2017) Joint small-angle X-ray and neutron scattering data analysis of asymmetric lipid vesicles. *J Appl Crystallogr* 50:419–429. <https://doi.org/10.1107/S1600576717000656>
- Eicher B, Marquardt D, Heberle FA, Letofsky-Papst I, Rechberger GN, Appavou MS, Katsaras J, Pabst G (2018) Intrinsic curvature-mediated transbilayer coupling in asymmetric lipid vesicles. *Biophys J* 114(1):146–157. <https://doi.org/10.1016/j.bpj.2017.11.009>
- Frewein MPK, Doktorova M, Heberle FA, Scott HL, Semeraro EF, Porcar L, Pabst G (2021) Structure and interdigitation of chain-asymmetric phosphatidylcholines and milk sphingomyelin in the fluid phase. *Symmetry* 13(8):1441. <https://doi.org/10.3390/sym13081441>
- Heberle FA, Marquardt D, Doktorova M, Geier B, Standaert RF, Heftberger P, Kollmitzer B, Nickels JD, Dick RA, Feigenson GW, Katsaras J, London E, Pabst G (2016) Subnanometer structure of an asymmetric model membrane: interleaflet coupling influences domain properties. *Langmuir* 32(20):5195–5200. <https://doi.org/10.1021/acs.langmuir.5b04562>
- Horner A, Akimov SA, Pohl P (2013) Long and short lipid molecules experience the same interleaflet drag in lipid bilayers. *Phys Rev Lett* 110:268101. <https://doi.org/10.1103/PhysRevLett.110.268101>
- Hossein A, Deserno M (2020) Spontaneous curvature, differential stress, and bending modulus of asymmetric lipid membranes. *Biophys J* 118(3):624–642. <https://doi.org/10.1016/j.bpj.2019.11.3398>
- Kučerka N, Pencer J, Sachs JN, Nagle JF, Katsaras J (2007) Curvature effect on the structure of phospholipid bilayers. *Langmuir* 23(3):1292–1299. <https://doi.org/10.1021/la062455t>
- Kučerka N, Nagle JF, Sachs JN, Feller SE, Pencer J, Jackson A, Katsaras J (2008) Lipid bilayer structure determined by the simultaneous analysis of neutron and X-ray scattering data. *Biophys J* 95(5):2356–2367. <https://doi.org/10.1529/biophysj.108.132662>
- Lorent JH, Levental KR, Ganesan L, Rivera-Longworth G, Sezgin E, Doktorova M, Lyman E, Levental I (2020) Plasma membranes are asymmetric in lipid unsaturation, packing and protein shape. *Nat Chem Biol* 16(6):644–652. <https://doi.org/10.1038/s41589-020-0529-6>
- Marsh D (2013) Handbook of lipid bilayers. CRC Press, Boca Raton. <https://doi.org/10.1201/b11712>
- Marx L, Frewein MPK, Semeraro EF, Rechberger GN, Lohner K, Porcar L, Pabst G (2021) Antimicrobial peptide activity in asymmetric bacterial membrane mimics. *Faraday Discuss* 34(4):240–241. <https://doi.org/10.1039/D1FD00039J>
- Nagle JF, Venable RM, Marocco-Kemmerling E, Tristram-Nagle S, Harper PE, Pastor RW (2019) Revisiting volumes of lipid components in bilayers. *J Phys Chem B* 123(12):2697–2709. <https://doi.org/10.1021/acs.jpcc.8b12010>
- Nguyen MHL, DiPasquale M, Rikeard BW, Doktorova M, Heberle FA, Scott HL, Barrera FN, Taylor G, Collier CP, Stanley CB, Katsaras J, Marquardt D (2019) Peptide-induced lipid flip-flop in asymmetric liposomes measured by small angle neutron scattering. *Langmuir* 35(36):11735–11744. <https://doi.org/10.1021/acs.langmuir.9b01625>
- Pencer J, Krueger S, Adams CP, Katsaras J (2006) Method of separated form factors for polydisperse vesicles. *J Appl Crystallogr* 39(3):293–303. <https://doi.org/10.1107/S0021889806005255>
- Pernot P, Brennich M, Tully M (2018) The rise of BioSAXS at the ESRF: BM29 beamline for SAXS on proteins in solution. *Acta Crystallogr Sect A* 74(a1):7. <https://doi.org/10.1107/S0108767318099920>
- Róg T, Orłowski A, Llorente A, Skotland T, Sylvänne T, Kauhanen D, Ekroos K, Sandvig K, Vattulainen I (2016) Interdigitation of long-chain sphingomyelin induces coupling of membrane leaflets in a

- cholesterol dependent manner. *Biochim Biophys Acta Biomembr* 1858(2):281–288. <https://doi.org/10.1016/j.bbamem.2015.12.003>
- Schram V, Thompson TE (1995) Interdigitation does not affect translational diffusion of lipids in liquid crystalline bilayers. *Biophys J* 69(6):2517–2520. [https://doi.org/10.1016/S0006-3495\(95\)80122-0](https://doi.org/10.1016/S0006-3495(95)80122-0)
- Semeraro EF, Marx L, Frewein MP, Pabst G (2021) Increasing complexity in small-angle x-ray and neutron scattering experiments: from biological membrane mimics to live cells. *Soft Matter* 17(2):222–232. <https://doi.org/10.1039/C9SM02352F>
- Singer SJ, Nicolson GL (1972) The fluid mosaic model of the structure of cell membranes. *Science* 175(4023):720–731. <https://doi.org/10.1126/science.175.4023.720>
- Tristram-Nagle S (2015) Use of X-ray and neutron scattering methods with volume measurements to determine lipid bilayer structure and number of water molecules/lipid. In: Disalvo EA (ed) *Membrane hydration*. Springer, Cham, pp 17–43. https://doi.org/10.1007/978-3-319-19060-0_2
- van Meer G (2011) Dynamic transbilayer lipid asymmetry. *Cold Spring Harbor Perspect Biol* 3(5):004671. <https://doi.org/10.1101/cshperspect.a004671>
- Verkleij AJ, Zwaal RFA, Roelofsen B, Comfurius P, Kastelijn D, van Deenen LLM (1973) The asymmetric distribution of phospholipids in the human red cell membrane. A combined study using phospholipases and freeze-etch electron microscopy. *BBA Biomembranes* 323(2):178–193. [https://doi.org/10.1016/0005-2736\(73\)90143-0](https://doi.org/10.1016/0005-2736(73)90143-0)
- Virtanen P, Gommers R, Oliphant T.E., Haberland M, Reddy T, Cournapeau D, Burovski E, Peterson P, Weckesser W, Bright J, van der Walt S.J., Brett M, Wilson J, Millman K.J., Mayorov N, Nelson A.R.J., Jones E, Kern R, Larson E, Carey C.J., Polat, Feng Y, Moore E.W., VanderPlas J, Laxalde D, Perktold J, Cimrman R, Henriksen I, Quintero E.A., Harris C.R., Archibald A.M., Ribeiro A.H., Pedregosa F, van Mulbregt P, Vijaykumar A, Bardelli A.P, Rothberg A, Hilboll A, Kloeckner A, Scopatz A, Lee A, Rokem A, Woods C.N., Fulton C, Masson C, Häggström C, Fitzgerald C, Nicholson D.A., Hagen D.R., Pasechnik D.V., Olivetti E, Martin E, Wieser E, Silva F, Lenders F, Wilhelm F, Young G, Price G.A., Ingold G.L., Allen G.E., Lee G.R., Audren H, Probst I, Dietrich J.P, Silterra J., Webber J.T., Slavič J, Nothman J, Buchner J, Kulick J, Schönberger J.L, de Miranda Cardoso J.V, Reimer J, Harrington J, Rodríguez J.L.C, Nunez-Iglesias J, Kuczynski J, Tritz K, Thoma M, Newville M, Kümmerer M, Bolingbroke M, Tartre M, Pak M, Smith N.J., Nowaczyk N, Shebanov N, Pavlyk O, Brodtkorb P.A., Lee P, McGibbon R.T, Feldbauer R, Lewis S, Oshyia T, Pingel T.J., Robitaille T.P., Spura T, Jones T.R., Cera T, Leslie T, Zito T, Krauss T, Upadhyay U, Halchenko Y.O., Vázquez-Baeza Y (2020) *SciPy 1.0: fundamental algorithms for scientific computing in Python*. *Nat Methods* 17(3):261–272. <https://doi.org/10.1038/s41592-019-0686-2>

Publisher's Note Springer Nature remains neutral with regard to jurisdictional claims in published maps and institutional affiliations.

Authors and Affiliations

Moritz P. K. Frewein^{1,2,3,4} · Paulina Piller^{1,3,4} · Enrico F. Semeraro^{1,3,4} · Krishna C. Batchu² · Frederick A. Heberle⁵ · Haden L. Scott^{6,7} · Yuri Gerelli⁸ · Lionel Porcar² · Georg Pabst^{1,3,4} 

Moritz P. K. Frewein
moritz.frewein@uni-graz.at; frewein@ill.fr

Paulina Piller
paulina.piller@uni-graz.at

Enrico F. Semeraro
enrico.semeraro@uni-graz.at

Krishna C. Batchu
batchu@ill.fr

Frederick A. Heberle
fheberle@utk.edu

Haden L. Scott
hscott3@vols.utk.edu

Yuri Gerelli
y.gerelli@staff.univpm.it

Lionel Porcar
porcar@ill.fr

¹ Institute of Molecular Biosciences, University of Graz, NAWI Graz, 8010 Graz, Austria

² Institut Laue-Langevin, 38042 Grenoble, France

³ BioTechMed Graz, 8010 Graz, Austria

⁴ Field of Excellence BioHealth, 8010 Graz, Austria

⁵ Department of Chemistry, University of Tennessee, Knoxville, TN 37996, USA

⁶ Center for Environmental Biotechnology, University of Tennessee, Knoxville, TN 37996, USA

⁷ Shull Wollan Center, Oak Ridge National Laboratory, Oak Ridge, TN 37831, USA

⁸ Department of Life and Environmental Sciences, Università Politecnica delle Marche, 60131 Ancona, Italy

Interdigitation-induced Order and Disorder in Asymmetric Membranes - Supplementary Information

Moritz PK Frewein, Paulina Piller, Enrico F Semeraro, Krishna C Batchu,
Frederick A Heberle, Haden L Scott, Yuri Gerelli, Lionel Porcar and Georg Pabst

1 SAS-model parameters of pure lipids

Table S1: Properties of pure lipid bilayers as published in [1]. Bilayer thicknesses have been updated. The lower part of the table contains parameters used in fitting aLUV SAS data. These were taken from [2] and fixed during the analysis.

	DPPC	MSPC	SMPC	PMPC	MSM	POPC	SOPC
D_B [Å]	39.0	39.6	39.7	37.4	41.3	37.83	38.73
$D_{B/2}$ [Å]	19.5	19.8	19.9	18.7	20.6	18.9	19.4
D_C [Å]	14.3	14.5	14.6	13.5	16.4	14.18	15.9
A [Å ²]	63.1	62.2	62.0	62.9	64.8	67.5	68.8
σ_{poly} %	3.6	2.9	5.3	3.5	3.5	7.9	3.6
V_W [Å ³]	29.3	29.3	29.3	29.3	29.8	29.9	29.7
n_W	9.7	11.3	12.8	12.1	9.6	16.64	15.1
V_L [Å ³]	1232	1232	1232	1175.8	1336.3	1276.9	1333.1
V_H [Å ³]	328	328	328	328	274	320	328
r_{BB}	0.44	0.44	0.44	0.44	0.32	0.45	0.44
r_{PCN}	0.3	0.3	0.3	0.3	0.32	0.29	0.3
r	2.09	2.09	2.09	2.09	2.09	2.09	2.09
r_{12}					0.8	0.8	0.8

$V_L...$ Total lipid volume

$V_H...$ Headgroup volume

$r_{BB}...$ Backbone volume fraction relative to the headgroup (V_{BB}/V_H)

$r_{PCN}...$ Phosphate group volume fraction relative to the headgroup (V_{PCN}/V_H)

$r...$ Volume of a CH₃-segment relative to CH₂ (V_{CH3}/V_{CH2})

$r_{12}...$ Volume of a CH-segment relative to CH₂ (V_{CH}/V_{CH2})

2 SAS-model parameters of asymmetric vesicles

Table S2: SAS-fitting parameters of aLUVs containing DPPCd62 as acceptor lipid and MSPC, SMPC, PMPC, MSM, POPC and SOPC donor lipids.

	ϵ [%]	MSPC	SMPC	PMPC	MSM	POPC	SOPC
Total acc/don %	5	69:31	59:41	62:38	54:46	64:36	61:39
In acc/don %	5	96:4	92:8	95:5	83:17	84:16	93:7
Out acc/don %	5	45:55	30:70	33:67	28:72	46:54	33:67
D_B [Å]	3	37.0	38.1	36.1	40.9	36.7	37.3
D_{HH} [Å]	3	37.9	39.1	36.9	35.8	37.8	37.9
D_M^{in} [Å]	6	18.0	18.5	18.0	20.0	18.1	18.2
D_M^{out} [Å]	6	18.9	19.6	18.1	21.0	18.6	19.1
D_C^{in} [Å]	5	13.2	13.5	13.2	14.8	13.3	13.4
D_C^{out} [Å]	5	14.0	14.5	13.2	16.4	13.8	14.3
D_{H1}^{in} [Å]	20	2.6	2.9	2.5	2.7	8.3	2.5
D_{H1}^{out} [Å]	20	8.1	8.2	8.0	1.9	2.5	7.8
A^{in} [Å ²]	5	67.4	65.8	67.5	60.9	67.6	67.7
A^{out} [Å ²]	5	65.8	63.5	66.5	63.9	68.2	68.5
z_{BB}^{in} [Å]	6	-14.1	-14.4	-14.1	-15.7	-14.2	-14.3
z_{BB}^{out} [Å]	6	14.9	15.4	14.1	17.3	14.7	15.2
$\sigma_{BB}^{in/out}$ [Å]		2.1	2.1	2.1	2.1	2.1	2.1
z_{PCN}^{in} [Å]	10	-16.3	-16.8	-16.1	-18.0	-21.6	-16.2
z_{PCN}^{out} [Å]	10	22.2	22.9	21.3	20.2	16.6	22.1
σ_{PCN}^{in} [Å]	10	2.2	2.0	2.0	2.0	2.5	2.0
σ_{PCN}^{out} [Å]	10	3.1	3.3	2.8	3.6	2.0	2.0
$z_{CholCH3}^{in}$ [Å]	10	-19.3	-18.5	-19.1	-21.0	-22.6	-19.2
$z_{CholCH3}^{out}$ [Å]	10	23.2	23.9	22.3	23.2	19.6	25.1
$\sigma_{CholCH3}^{in/out}$ [Å]		3.0	3.0	3.0	3.0	3.0	3.0
$\sigma_{HC}^{in/out}$ [Å]		2.5	2.5	2.5	2.5	2.5	2.5
z_{CH3} [Å]	10	-1.0	-1.0	-0.7	-2.6	1.0	-0.4
σ_{CH3} [Å]	20	3.0	3.0	3.0	3.0	3.3	2.7
σ_{poly} [%]	6	4.1	2.8	3.3	7.3	4.4	6.1
$V_{W,bound}$ [Å ³]	6	29.4	29.3	29.6	29.5	29.6	29.6
n_W^{in}	6	9.5	6.5	9.0	8.0	16.8	9.0
n_W^{out}	6	15.7	15.2	15.8	11.1	9.0	20.4
R_m [Å]	10	400	340	360	360	390	390
σ_R [Å]	10	110	90	90	120	100	100

D_{H1} ... distance between head group (phosphate) and hydrophobic/hydrophilic interface

$z_x^{in/out}$... position of moiety x relative to the membrane center

$\sigma_x^{in/out}$... Gaussian standard deviation of moiety x

R_m ... mean vesicle radius

σ_R ... vesicle radius polydispersity

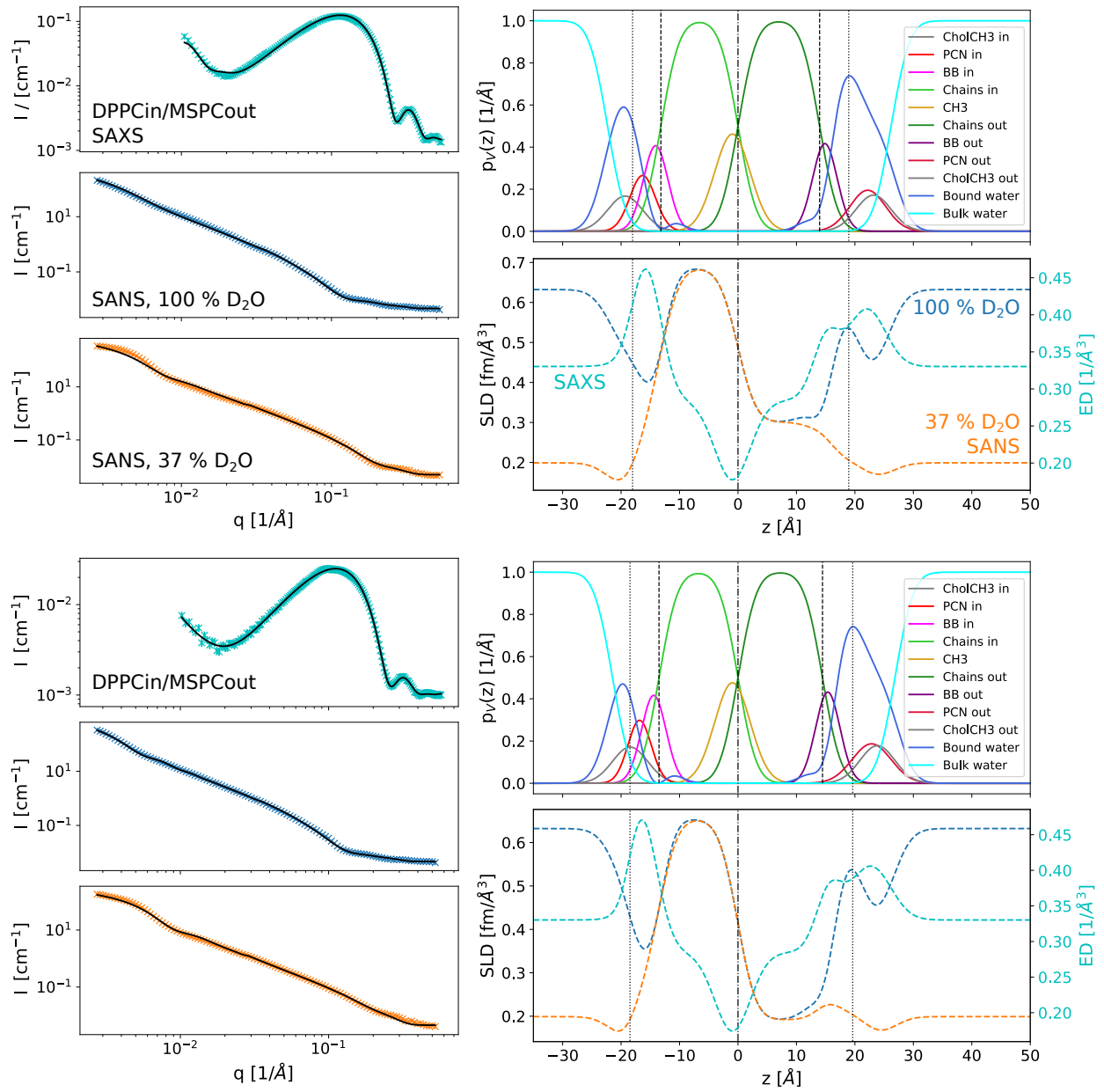


Figure S1: SAXS and SANS data with fits (black lines); SDP volume probability, electron density and neutron scattering length density profiles for the systems DPPCⁱⁿ/MSPC^{out} and DPPCⁱⁿ/SMPC^{out}.

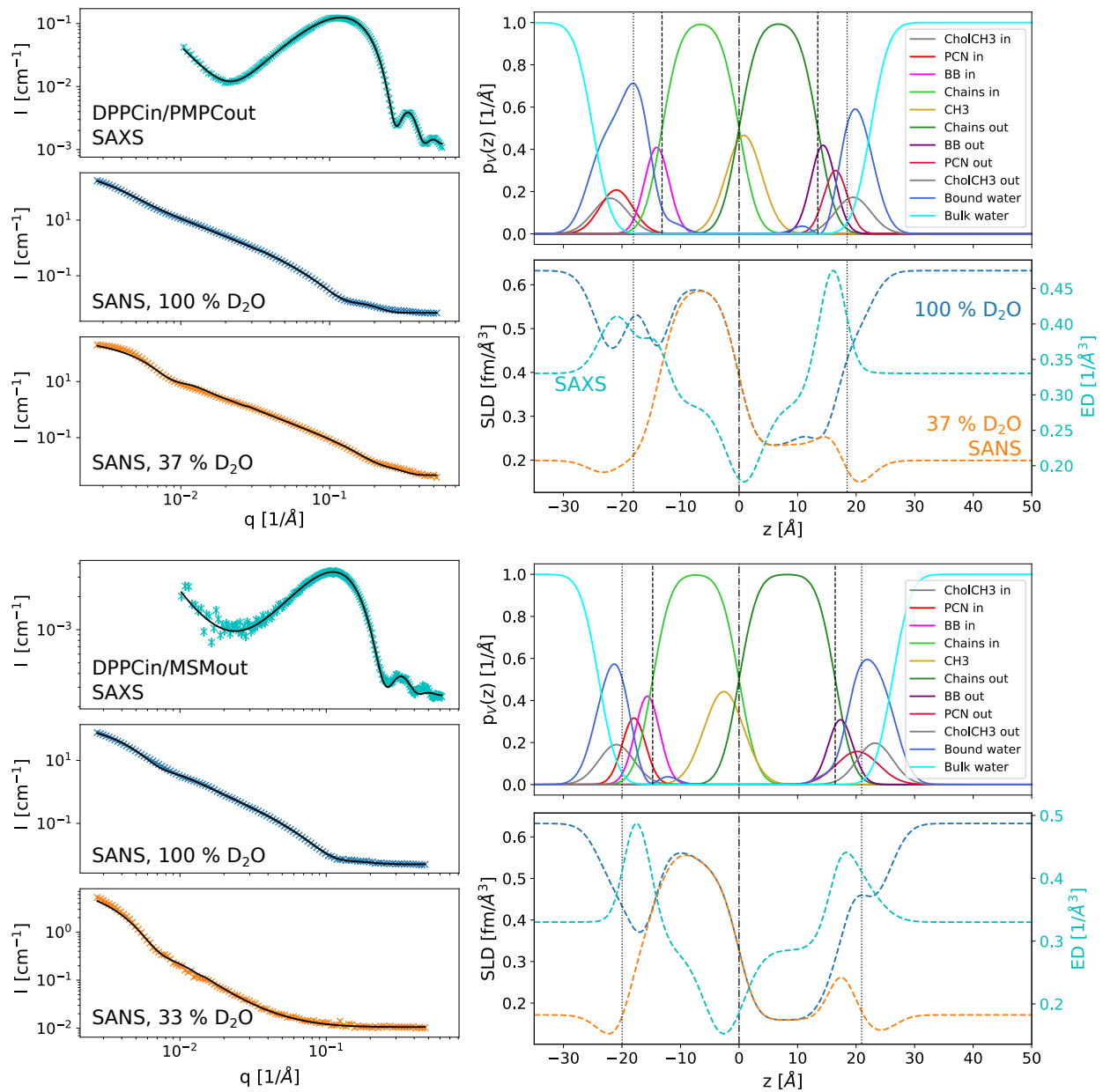


Figure S2: SAXS and SANS data with fits (black lines); SDP volume probability, electron density and neutron scattering length density profiles for the systems $\text{DPPC}^{\text{in}}/\text{PMPC}^{\text{out}}$ and $\text{DPPC}^{\text{in}}/\text{MSMout}$.

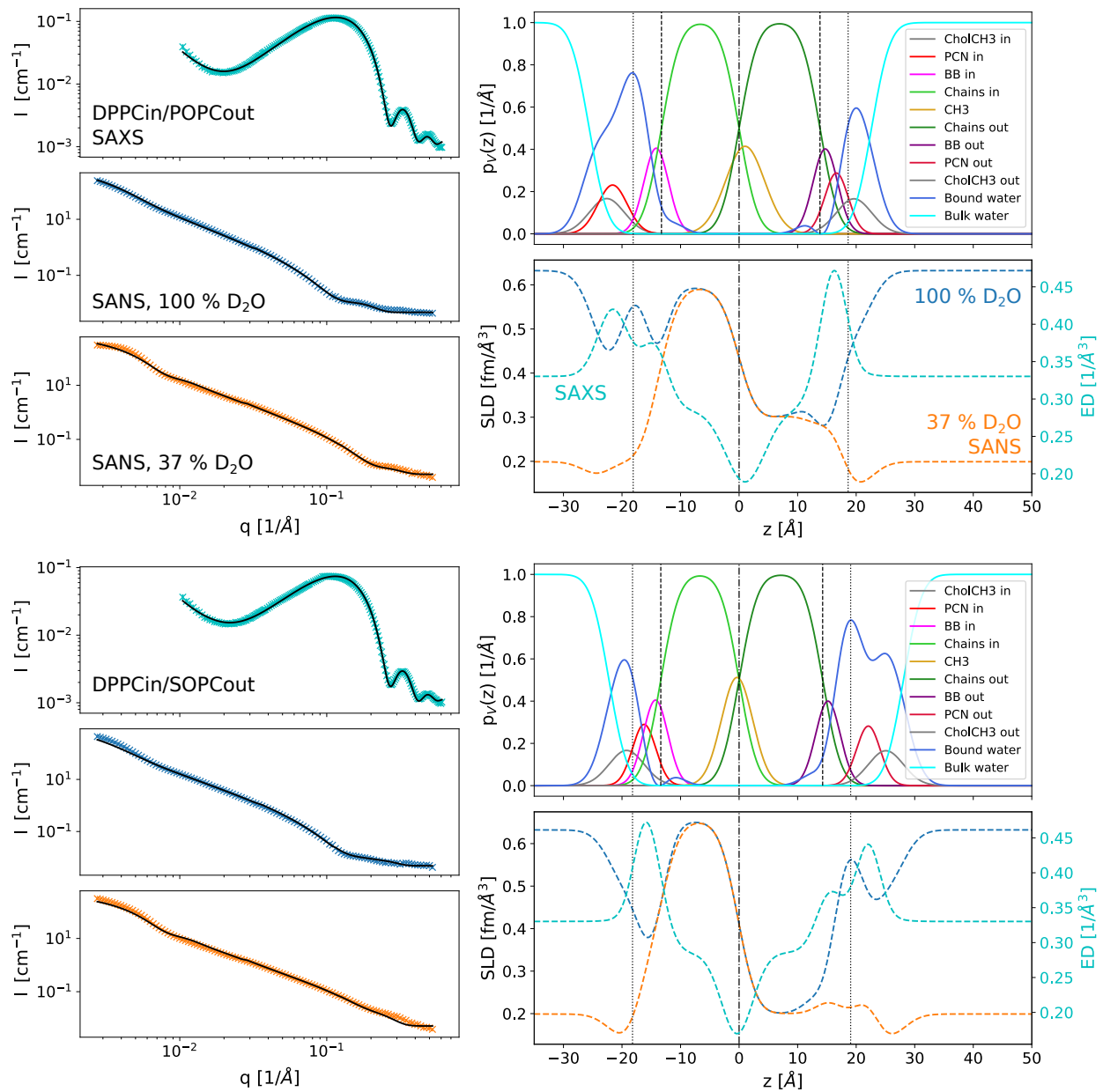


Figure S3: SAXS and SANS data with fits (black lines); SDP volume probability, electron density and neutron scattering length density profiles for the systems $\text{DPPC}^{\text{in}}/\text{POPC}^{\text{out}}$ and $\text{DPPC}^{\text{in}}/\text{SOPC}^{\text{out}}$.

3 SAS-model parameters of reference LUVs

Table S3: SAS-fitting parameters of symmetric reference LUVs containing 90% (in) or 30% (out) DPPC, complemented by MSPC, SMPC, or PMPC.

	ϵ [%]	MSPC		SMPC		PMPC	
		in	out	in	out	in*	out
D_B [Å]	3	39.9	39.6	39.7	39.30	38.53	38.66
D_{HH} [Å]	3	35.3	35.1	35.1	34.78	34.77	33.92
$2D_C$ [Å]	3	29.3	29.1	29.1	28.84	28.22	28.03
D_{H1} [Å]	20	3.0	3.0	3.0	3.0	3.3	2.9
A [Å ²]	2	61.7	62.2	62.1	62.7	63.7	61.7
z_{BB} [Å]	8	16.3	15.9	16.0	15.8	17.1	15.7
σ_{BB} [Å]	20	2.5	2.5	2.5	2.5	2.5	2.5
z_{PCN} [Å]	8	18.3	18.3	18.2	18.2	17.2	17.5
σ_{PCN} [Å]	20	3.5	3.3	3.5	3.5	2.2	3.5
$z_{CholCH3}$ [Å]	3	18.8	19.0	20.1	19.3	22.2	18.6
$\sigma_{CholCH3}^\dagger$ [Å]		3.0	3.0	3.0	3.0	3.0	3.0
σ_{HC} [Å]		2.5	2.5	2.5	2.5	2.5	2.5
σ_{CH3} [Å]	5	2.7	3.2	3.6	3.5	2.4	3.0
σ_{poly} [%]	6	4.0	4.0	8.4	4.7	0.0	3.7
$V_{W,bound}$ [Å ³]	6	27.3	27.4	27.3	27.5	27.3	27.5
n_W	6	3.7	4.6	6.8	5.5	12.5	4.5
R_m [Å]	10	480	340	350	440	420	470
σ_R [Å]	10	130	200	130	140	170	160

Table S4: SAS-fitting parameters of symmetric reference LUVs containing 90% (in) or 30% (out) DPPC, complemented by MSM, POPC, or SOPC.

	ϵ [%]	MSM		POPC		SOPC	
		in	out	in	out	in	out
D_B [Å]	3	38.7	41.29	39.4	38.4	39.9	38.7
D_{HH} [Å]	3	38.4	40.79	34.8	34.6	35.1	35.5
$2D_C$ [Å]	3	28.7	32.1	29.0	28.4	29.4	29.0
D_{H1} [Å]	20	4.87	4.35	2.9	3.1	2.87	3.26
A [Å ²]	2	64.19	63.22	62.8	65.9	62.25	67.32
z_{BB} [Å]	8	15.21	17.28	15.7	16.1	16.27	16.68
σ_{BB} [Å]	20	2.5	2.5	2.5	2.5	2.5	2.5
z_{PCN} [Å]	8	20.04	20.9	18.3	17.7	18.2	18.27
σ_{PCN} [Å]	20	2.97	2.72	3.4	3.4	3.5	3.25
$z_{CholCH3}$ [Å]	3	20.04	20.9	22.0	18.4	20.46	22.9
$\sigma_{CholCH3}^\dagger$ [Å]		3	3	3.0	3.0	3	3
σ_{HC} [Å]		2.5	2.5	2.5	2.5	2.5	2.5
σ_{CH3} [Å]	5	4	4	3.1	3.5	3.09	3.14
σ_{poly} [%]	6	3.91	6.19	3.6	6.9	4.75	4.21
$V_{W,bound}$ [Å ³]	6	28.28	28.68	29.0	27.3	28.21	29.28
n_W	6	7.83	6.81	11.0	4.9	7.22	14.58
R_m [Å]	10	430	500	470	480	520	540
σ_R [Å]	10	120	150	190	170	190	170

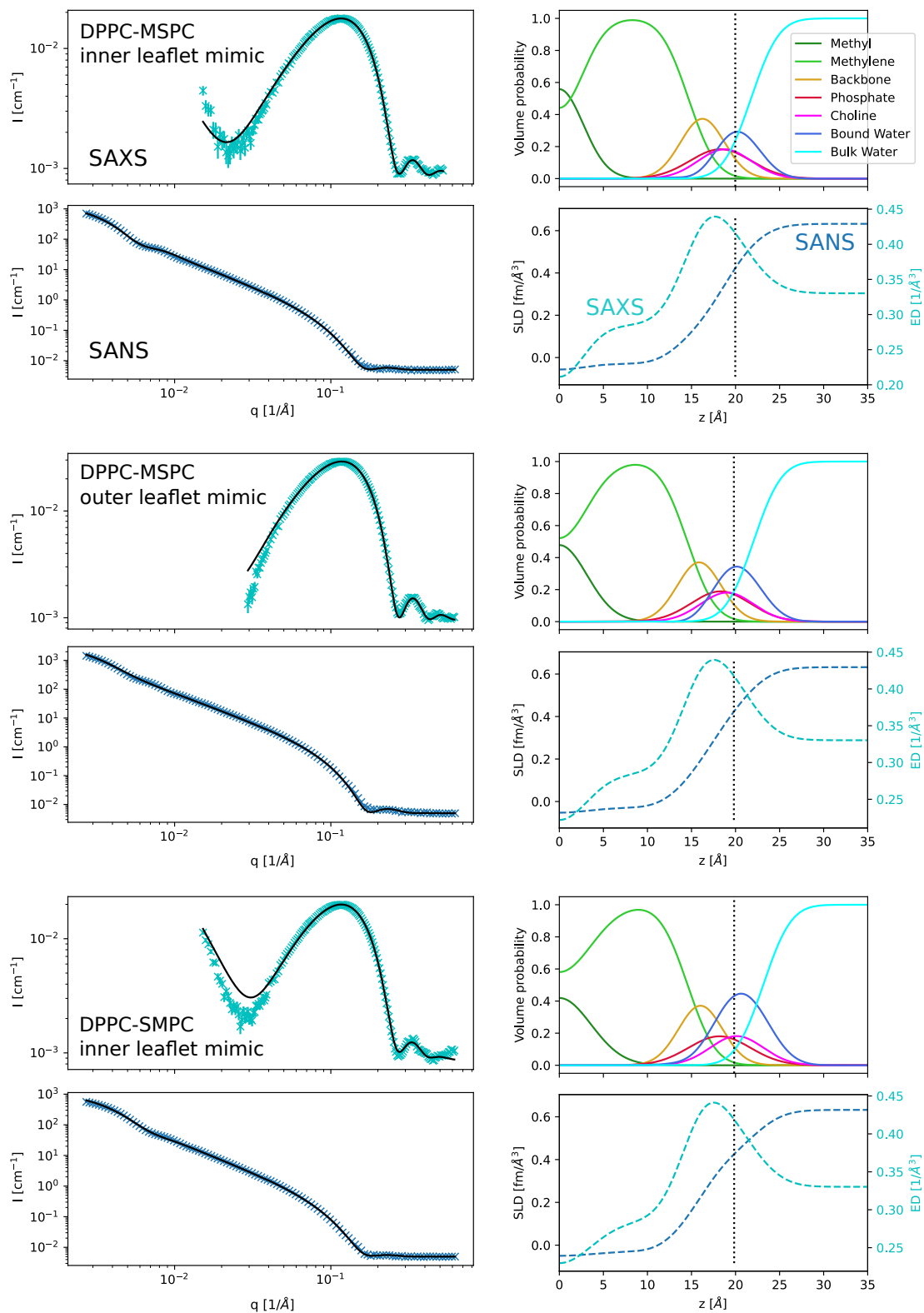


Figure S4: SAXS and SANS data with fits (black lines); SDP volume probability, electron density and neutron scattering length density profiles for DPPC-MSPC inner/outer leaflet symmetric mimics, as well as DPPC-SMPC inner leaflet mimics.

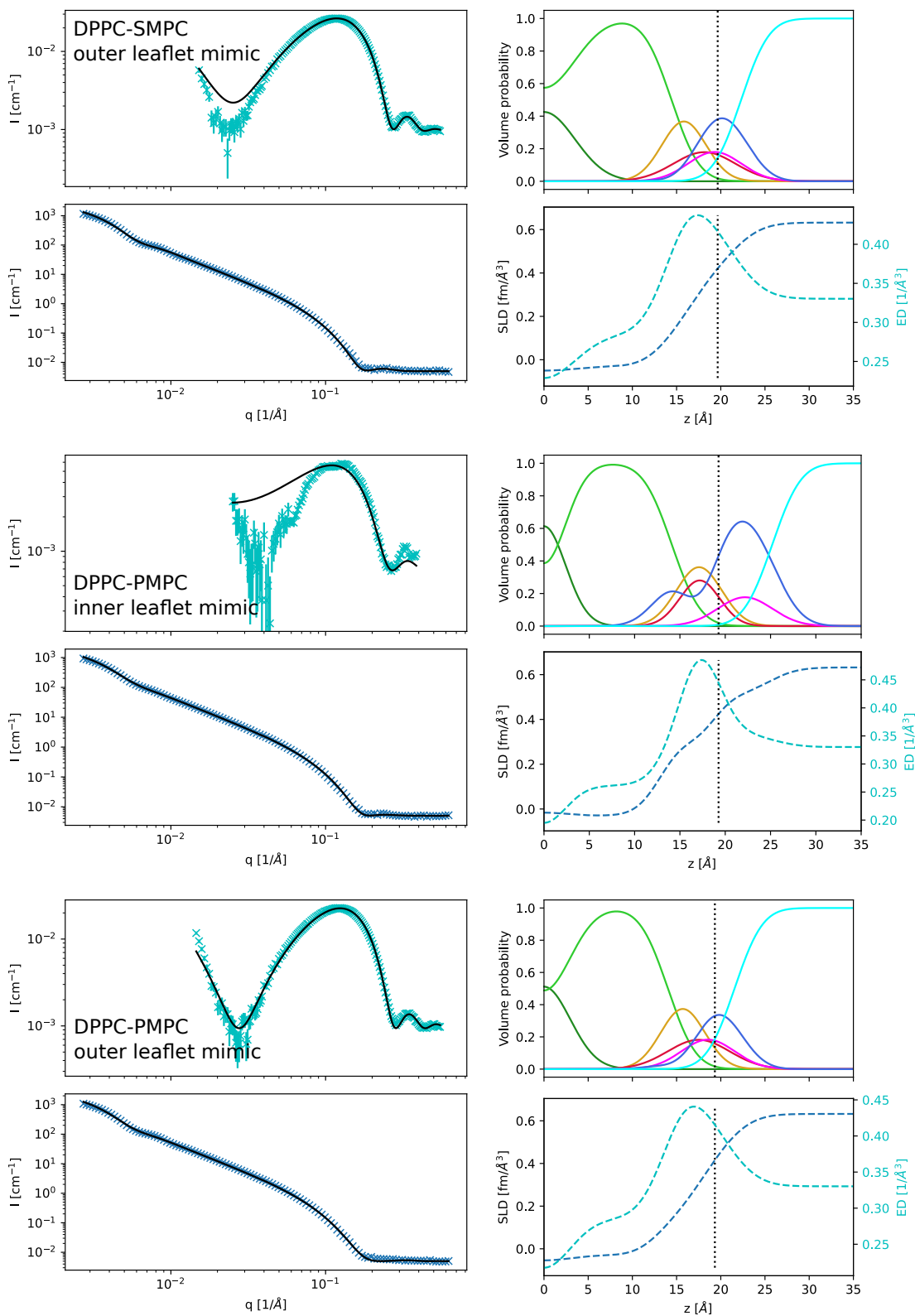


Figure S5: SAXS and SANS data with fits (black lines); SDP volume probability, electron density and neutron scattering length density profiles for DPPC-SMPC outer leaflet mimics and DPPC-PMPC inner/outer leaflet symmetric mimics.

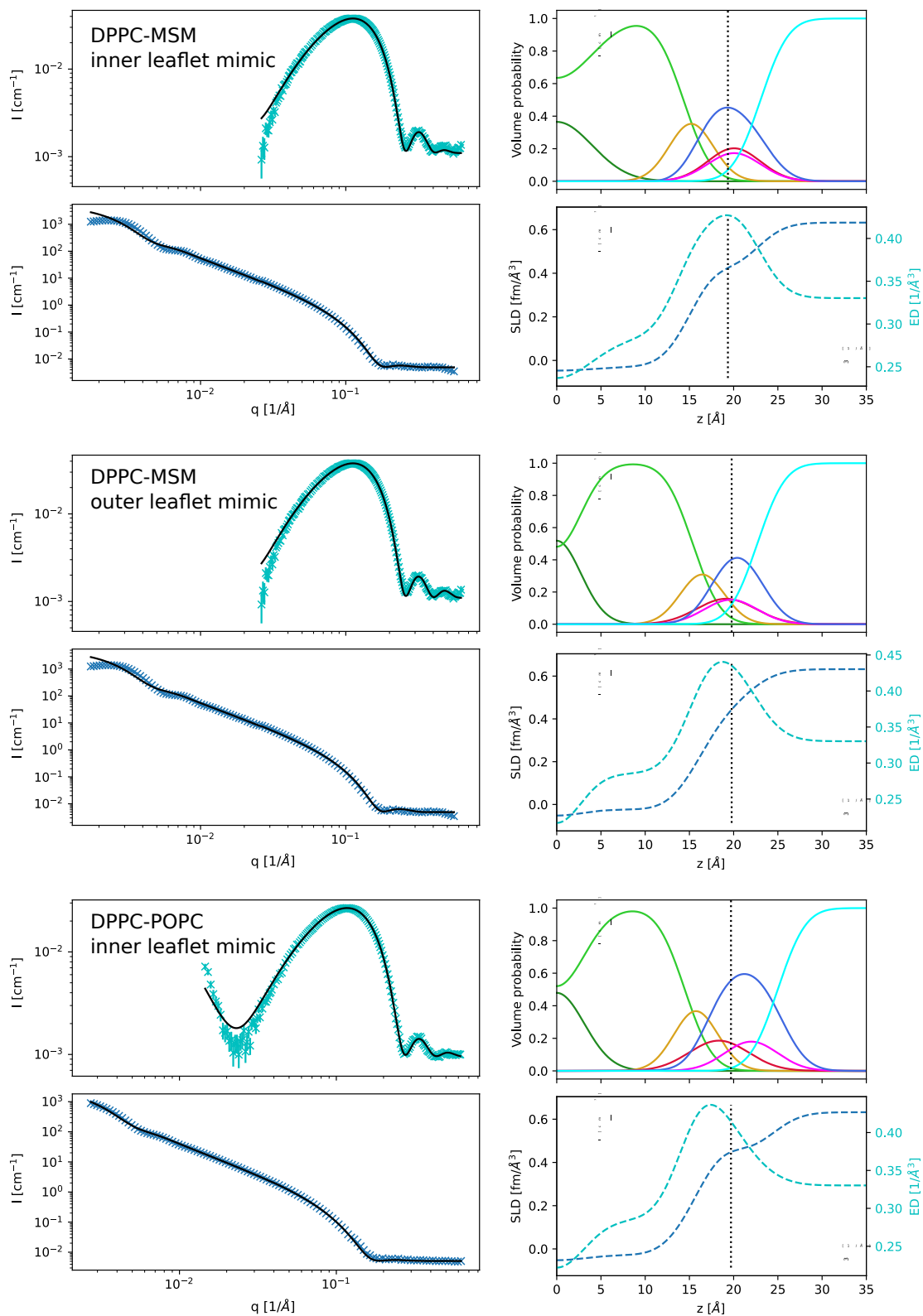


Figure S6: SAXS and SANS data with fits (black lines); SDP volume probability, electron density and neutron scattering length density profiles for DPPC-MSM inner/outer leaflet symmetric mimics, as well as DPPC-POPC inner leaflet mimics.

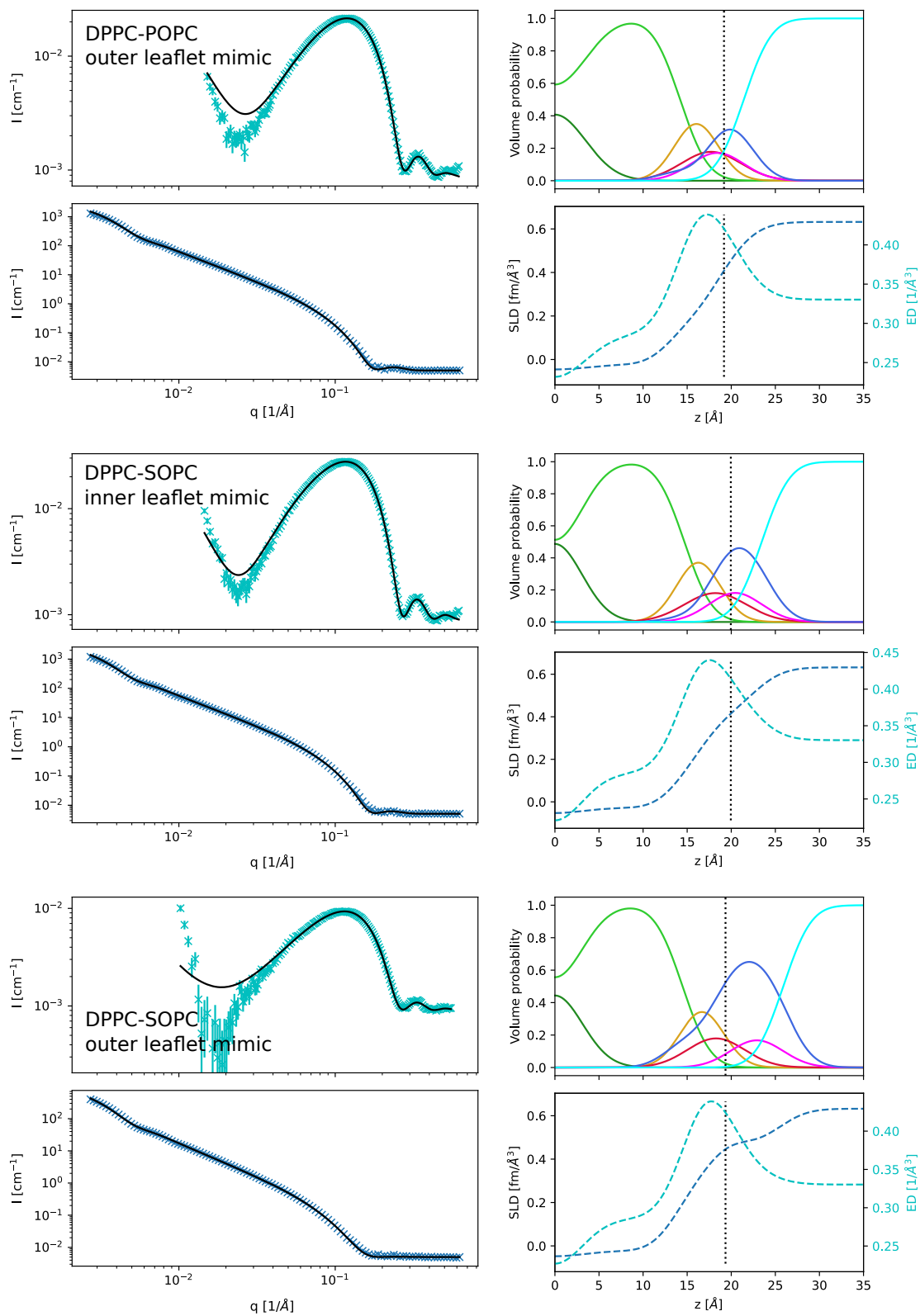


Figure S7: SAXS and SANS data with fits (black lines); SDP volume probability, electron density and neutron scattering length density profiles for DPPC-POPC outer leaflet mimics and DPPC-SOPC inner/outer leaflet symmetric mimics.

4 Gas Chromatography

Table S5: Calibration curves of all hydrocarbon chains occurring in the used lipids and the 3 most abundant chains in MSM. In the last line the slope k of the linear fit is given.

μmol	C14:0	μmol	C16:0d	μmol	C16:0	μmol	C18:0
0.002	19747	0.002	16043	0.002	17697	0.002	15594
0.004	36066	0.004	36370	0.004	31270	0.004	33143
0.015	110938	0.013	87194	0.014	114122	0.013	106044
0.030	276664	0.025	238040	0.027	266841	0.025	241047
0.059	596070	0.050	528481	0.055	558479	0.051	567215
0.118	994664	0.101	1064457	0.109	1064457	0.101	1079925
0.236	2046908	0.201	2768564	0.218	2423189	0.203	1877413
0.472	3768187	0.402	3779355	0.436	3600379	0.405	4021069
k [mol/count]	1.14E-07		9.31E-08		1.03E-07		9.99E-08

μmol	C18:1	μmol	MSM C22:0	C23:0	C24:0
0.002	20803				
0.004	42162				
0.012	97706	0.013	5917	7228	6132
0.025	257572	0.025	13873	19961	13672
0.049	557266	0.051	30440	45868	30504
0.099	1064919	0.102	45564	69095	46701
0.198	2824137	0.204	115858	176708	116561
0.395	3773470	0.408	126005	181364	123150
k [mol/count]	8.94E-08		2.28E-06	1.49E-06	2.28E-06

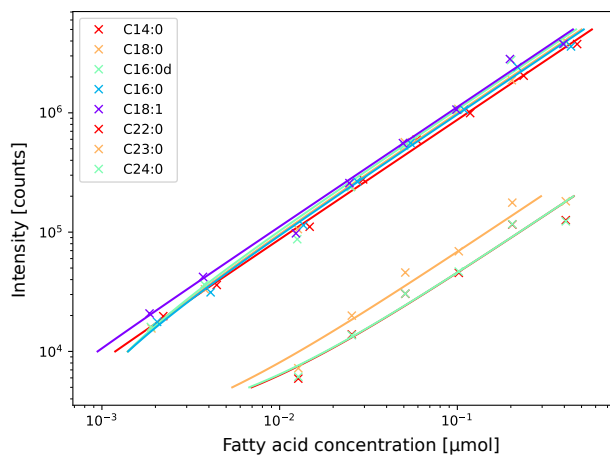


Figure S8: Calibration curves as given in tab. S5 and linear fits.

Table S6: Results from GC-analysis of asymmetric vesicles.

DPPC ⁱⁿ /MSPC ^{out}						
	C16:0d	C14:0	C18:0	χ_{acc}	χ_{don}	
Sample 1	205104	58523	41678			
	0.020	0.007	0.005	0.63	0.38	
Sample 2	215107	61004	43908			
	0.021	0.007	0.005	0.64	0.36	
DPPC ⁱⁿ /SMPC ^{out}						
	C16:0d	C14:0	C18:0	χ_{acc}	χ_{don}	
Sample 1	409420	158486	125415			
	0.039	0.016	0.014	0.57	0.43	
Sample 2	457413	177140	139695			
	0.043	0.018	0.016	0.56	0.44	
DPPC ⁱⁿ /PMPC ^{out}						
	C16:0d	C16:0	C14:0	χ_{acc}	χ_{don}	
Sample 1	1590184	768008	643108			
	0.149	0.079	0.074	0.49	0.51	
Sample 2	1616790	780218	654394			
	0.151	0.081	0.075	0.49	0.51	
DPPC ⁱⁿ /POPC ^{out}						
	C16:0d	C16:0	C18:1	χ_{acc}	χ_{don}	
Sample 1	409420	158486	125415			
	0.029	0.011	0.009	0.59	0.41	
Sample 2	457413	177140	139695			
	0.032	0.013	0.010	0.58	0.42	
DPPC ⁱⁿ /SOPC ^{out}						
	C16:0d	C18:0	C18:1	χ_{acc}	χ_{don}	
Sample 1	213421	46984	67409			
	0.020	0.005	0.006	0.65	0.35	
Sample 2	234851	50921	72924			
	0.022	0.005	0.007	0.65	0.35	
DPPC ⁱⁿ /MSMout						
	C16:0d	C22:0	C23:0	C24:0	χ_{acc}	χ_{don}
Sample 1	213421	17259	26170	18423		
	0.049	0.035	0.037	0.037	0.57	0.43

References

- [1] Frewein, M.P.K., Doktorova, M., Heberle, F.A., Scott, H.L., Semeraro, E.F., Porcar, L., Pabst, G.: Structure and Interdigitation of Chain-Asymmetric Phosphatidylcholines and Milk Sphingomyelin in the Fluid Phase. *Symmetry* **13**(8), 1441 (2021). <https://doi.org/10.3390/sym13081441>
- [2] Nagle, J.F., Venable, R.M., Maroclo-Kemmerling, E., Tristram-Nagle, S., Harper, P.E., Pastor, R.W.: Revisiting Volumes of Lipid Components in Bilayers. *Journal of Physical Chemistry B* **123**(12), 2697–2709 (2019). <https://doi.org/10.1021/acs.jpcc.8b12010>

Supplement: SAS analysis results of Asymmetric Vesicles for NSE

1 SAS-model parameters of donor/acceptor lipids

Table S1: Properties of pure lipid bilayers from SAXS/SANS analysis.

	ϵ [%]	POPE	PEPS	ESM
V_L^* [\AA^3]		1193.8	1199.3	1218.5
V_H^* [\AA^3]		249.6	254.9	274.9
r_{CG}^*		0.51	0.50	0.33
r_{PCN}^*		0.14	0.18	0.31
r^*		2.09	2.09	2.09
r_{12}^*		0.8	0.8	0.8
D_B [\AA]	3	39.5	36.8	43.4
D_{HH} [\AA]	3	36.0	37.1	41.5
$2D_C$ [\AA]	3	31.2	28.9	33.6
D_{H1} [\AA]	20	2.4	4.1	4.0
A [\AA^2]	2	60.5	65.3	56.2
z_{BB} [\AA]	8	17.0	17.0	19.8
σ_{BB} [\AA]	20	2.5	2.5	3.2
z_{PCN} [\AA]	8	18.8	20.0	21.1
σ_{PCN} [\AA]	20	3.5	3.0	2.9
$z_{CholCH3}$ [\AA]	3	23.8	20.0	21
$\sigma_{CholCH3}^\dagger$ [\AA]		2.8	3	3.0
σ_{HC} [\AA]		2.5	2.5	2.5
σ_{CH3} [\AA]	5	3.0	3.0	4.1
σ_{poly} [%]	6	4.0	8.1	3.5
$V_{W,bound}$ [\AA^3]	6	29.6	29.4	27.3
n_W	6	13.8	10.0	4.4
Y	9	0.40	0.45	0.62

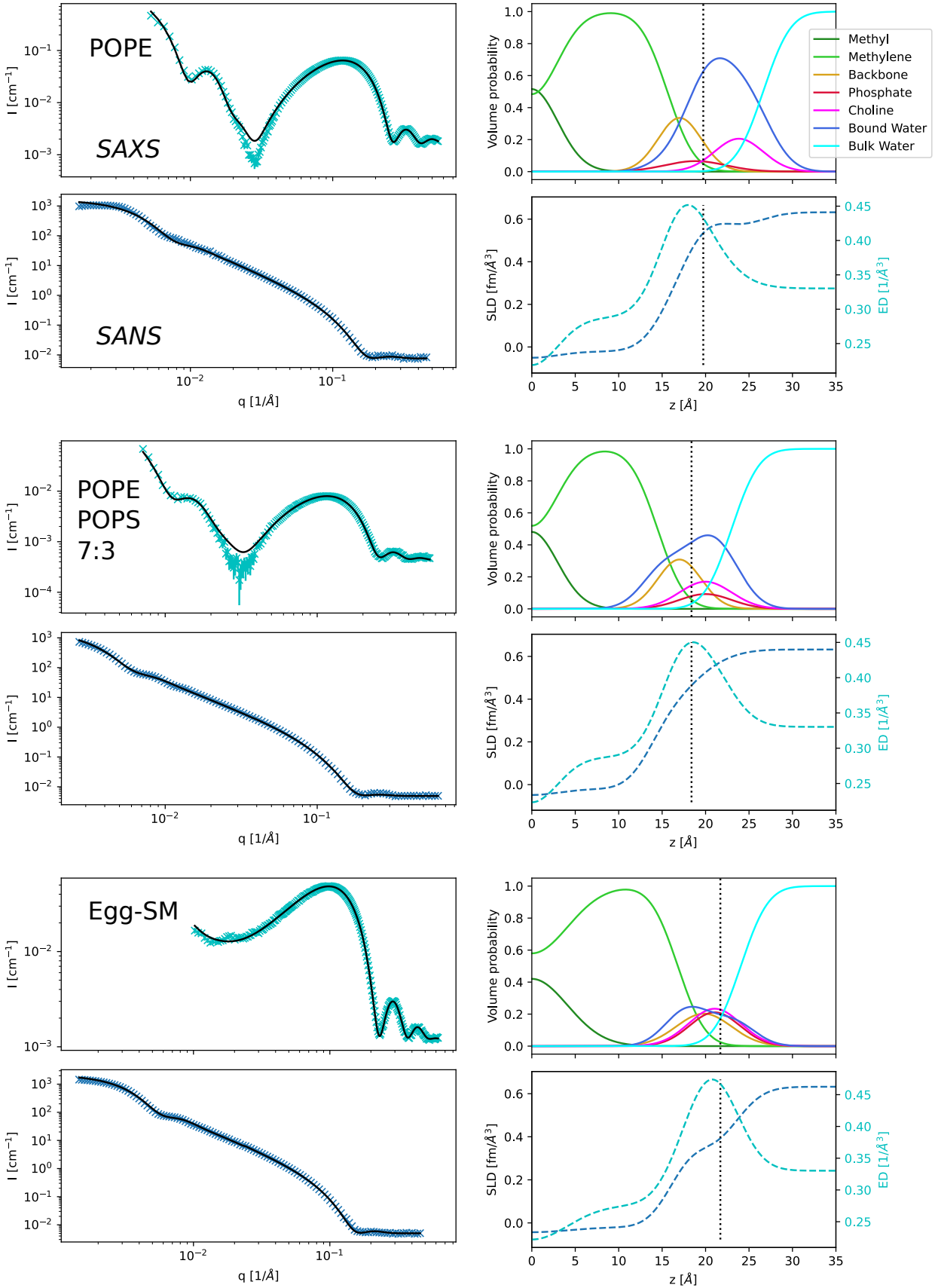


Figure S1: SAXS and SANS data with fits (black lines); SDP volume probability, electron density and neutron scattering length density profiles for the systems POPE, PEPS and ESM.

2 SAS-model parameters of asymmetric vesicles

Table S2: SAS-fitting parameters of aLUVs containing DPPCd62 as acceptor lipid and MSPC, SMPC, MSM, POPC and SOPC donor lipids.

	ϵ [%]	POPE ESM	POPE POPC	POPE MSM	POPE Mix	PEPS POPC	PEPS MSM	PEPS Mix
Total acc/don %	5	61:39	77:23	67:33	52:48	71:29	59:41	62:38
In acc/don %	5	98:2	90:10	82:18	65:35	97:3	97:3	77:23
Out acc/don %	5	28:72	65:35	54:46	40:60	48:52	25:75	49:51
D_B [Å]	3	37.6	39.0	40.3	39.6	37.1	40.0	39.1
D_{HH} [Å]	3	37.3	36.6	37.8	37.8	34.3	37.4	38.5
$2D_C$ [Å]	3	29.5	30.4	31.9	30.9	28.8	31.6	30.5
D_C^{in} [Å]	5	14.3	15.2	15.4	15.7	13.5	16.3	15.1
D_C^{out} [Å]	5	15.2	15.2	16.5	15.2	15.3	15.3	15.5
D_{H1}^{in} [Å]	20	4.6	2.8	3.3	3.8	2.3	3.4	3.9
D_{H1}^{out} [Å]	20	3.2	3.4	2.6	3.2	3.2	2.4	4.1
A^{av} [Å ²]	5	64.0	62.0	61.4	62.9	66.0	62.8	63.4
z_{BB}^{in} [Å]	6	-16.4	-16.0	-16.2	-16.5	-14.3	-17.1	-15.9
z_{BB}^{out} [Å]	6	17.4	16.0	17.3	16.0	16.1	16.1	16.3
$\sigma_{BB}^{in/out}$ [Å]		2.5	2.5	2.5	2.5	2.5	2.5	2.5
z_{PCN}^{in} [Å]	10	-19.4	-21.0	-19.2	-21.2	-17.3	-20.1	-19.3
z_{PCN}^{out} [Å]	10	22.4	19.0	21.5	19.0	19.7	19.9	20
σ_{PCN}^{in} [Å]	10	2.0	3.5	2	3.0	4.0	2.0	2
σ_{PCN}^{out} [Å]	10	4.0	2.0	3.5	2.3	3.0	3.8	2
$z_{CholCH3}^{in}$ [Å]	10	-21.7	-24.0	-22.2	-24.2	-20.3	-23.1	-22.3
$z_{CholCH3}^{out}$ [Å]	10	24.6	22.0	24.5	22.0	22.7	22.9	23
$\sigma_{CholCH3}^{in/out}$ [Å]		3.0	3.0	3	3.0	3.0	3.0	3
$\sigma_{HC}^{in/out}$ [Å]		2.5	2.5	2.5	2.5	2.5	2.5	2.5
σ_{CH3} [Å]	20	3.7	3.0	3.4	3.7	5.0	3.6	3.1
σ_{poly} [%]	6	0.0	3.9	4.3	5.0	10.0	7.0	7
$V_{W,bound}$ [Å ³]	6	30.3	30.3	30.2	30.0	29.4	29.6	29.3
n_W^{in}	6	14.4	15.4	11.8	14.6	14.2	10.3	12.8
n_W^{out}	6	16.7	11.0	13.4	11.5	11.6	14.8	12.7
R_m [Å]	10	361	361	345.3	373.4	369	361.2	381.9
σ_R [Å]	10	133	133	101.4	111.7	116.1	133	134.7

$D_{H1}...$ distance between head group (phosphate) and hydrophobic/hydrophilic interface

$z_x^{in/out}$... position of moiety x relative to the membrane center

$\sigma_x^{in/out}$... Gaussian standard deviation of moiety x

$R_m...$ mean vesicle radius

$\sigma_R...$ vesicle radius polydispersity

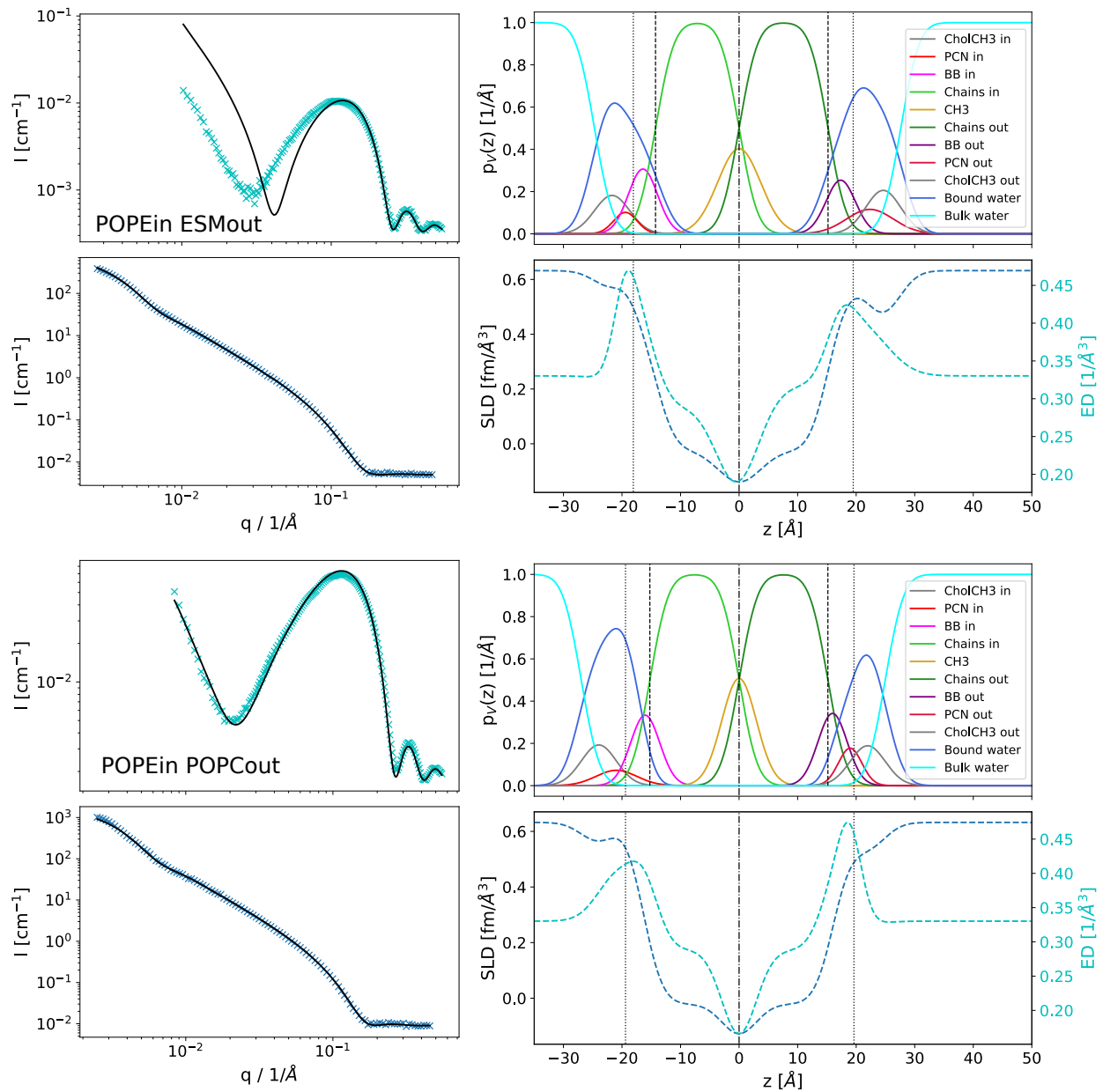


Figure S2: SAXS and SANS data with fits (black lines); SDP volume probability, electron density and neutron scattering length density profiles for the systems DPPCⁱⁿ/MSPC^{out} and DPPCⁱⁿ/SMPC^{out}.

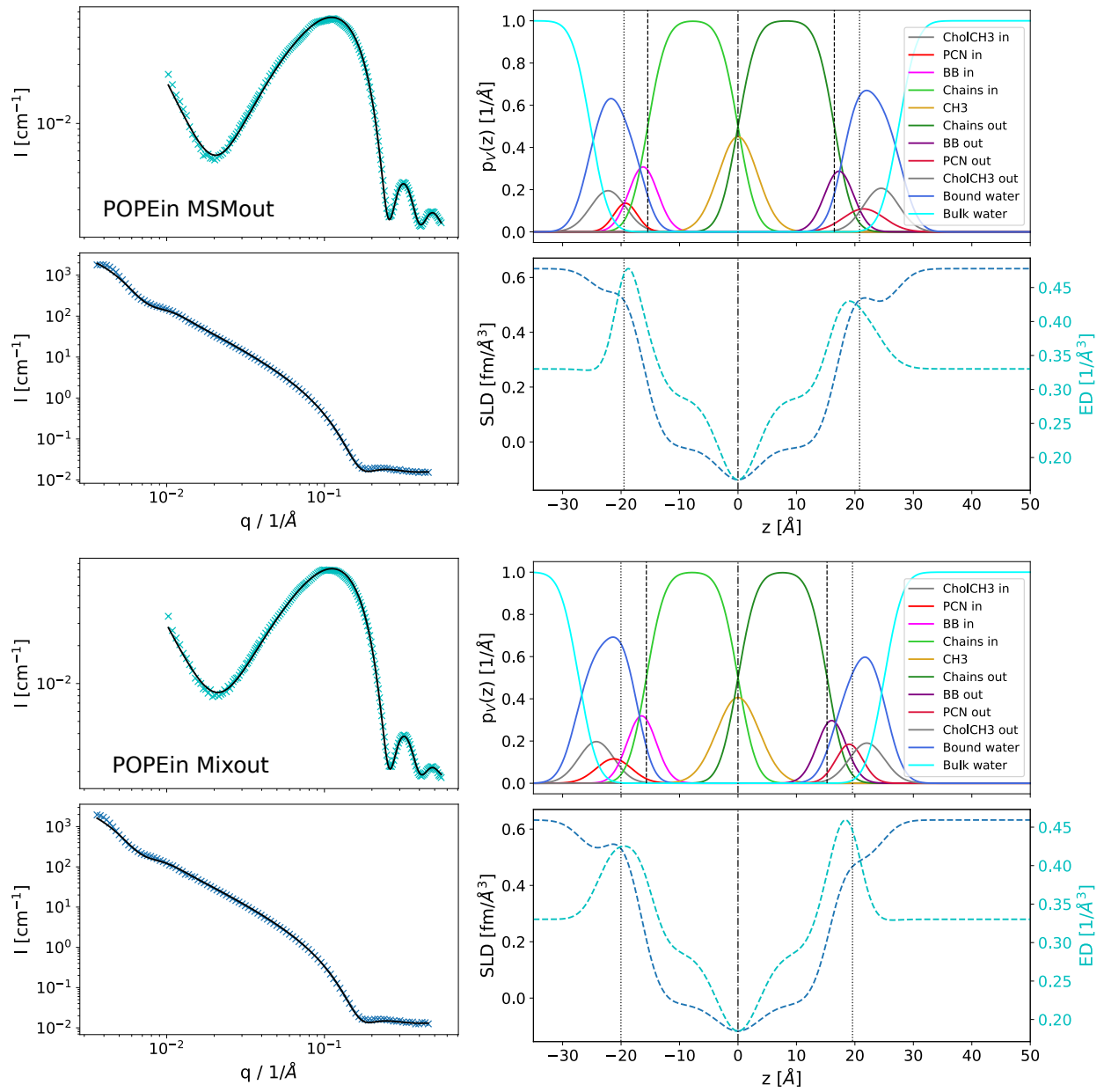


Figure S3: SAXS and SANS data with fits (black lines); SDP volume probability, electron density and neutron scattering length density profiles for the systems DPPCⁱⁿ/PMPC^{out} and DPPCⁱⁿ/MSMout.

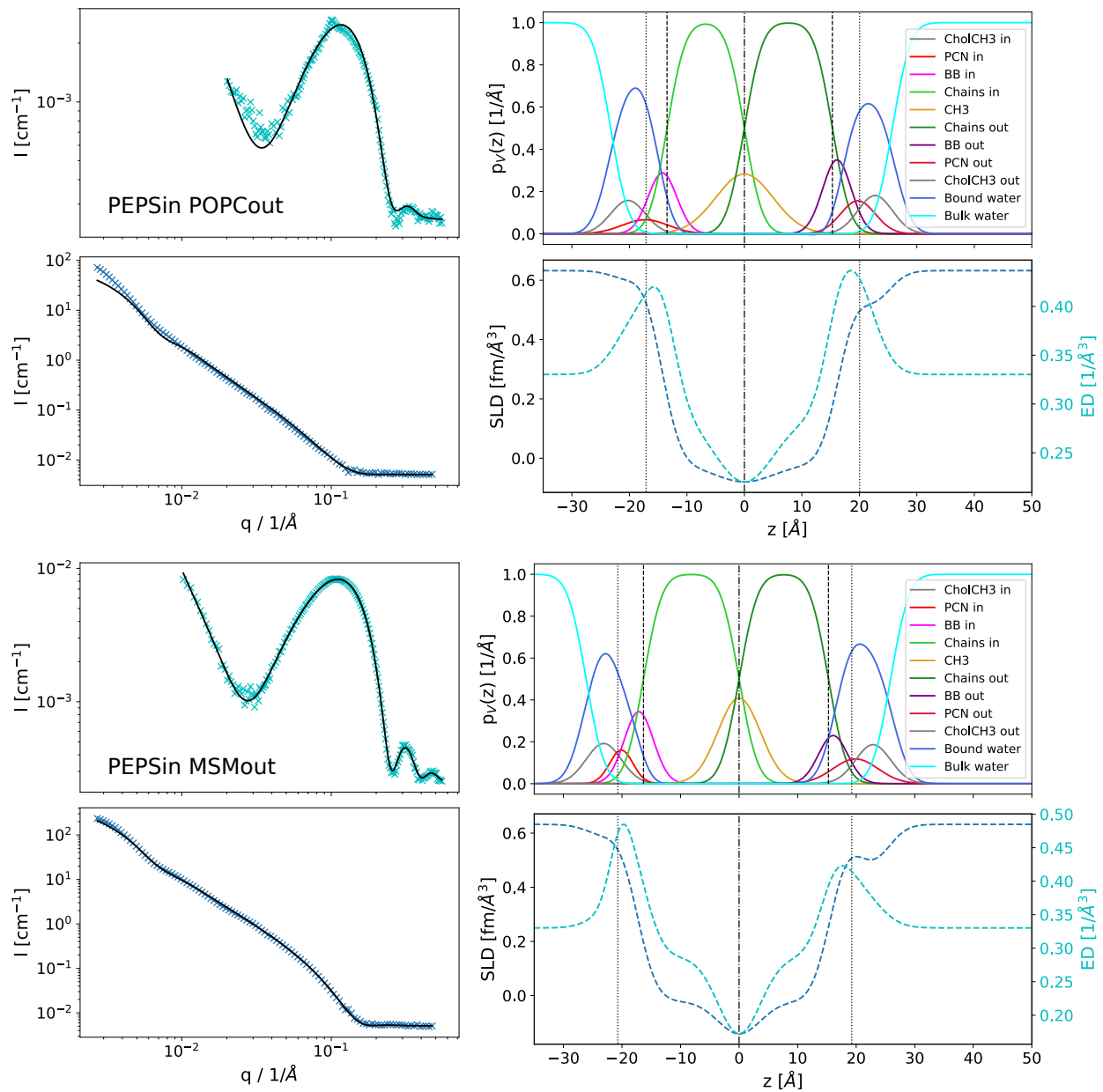


Figure S4: SAXS and SANS data with fits (black lines); SDP volume probability, electron density and neutron scattering length density profiles for the systems DPPCⁱⁿ/POPC^{out} and DPPCⁱⁿ/SOPC^{out}.

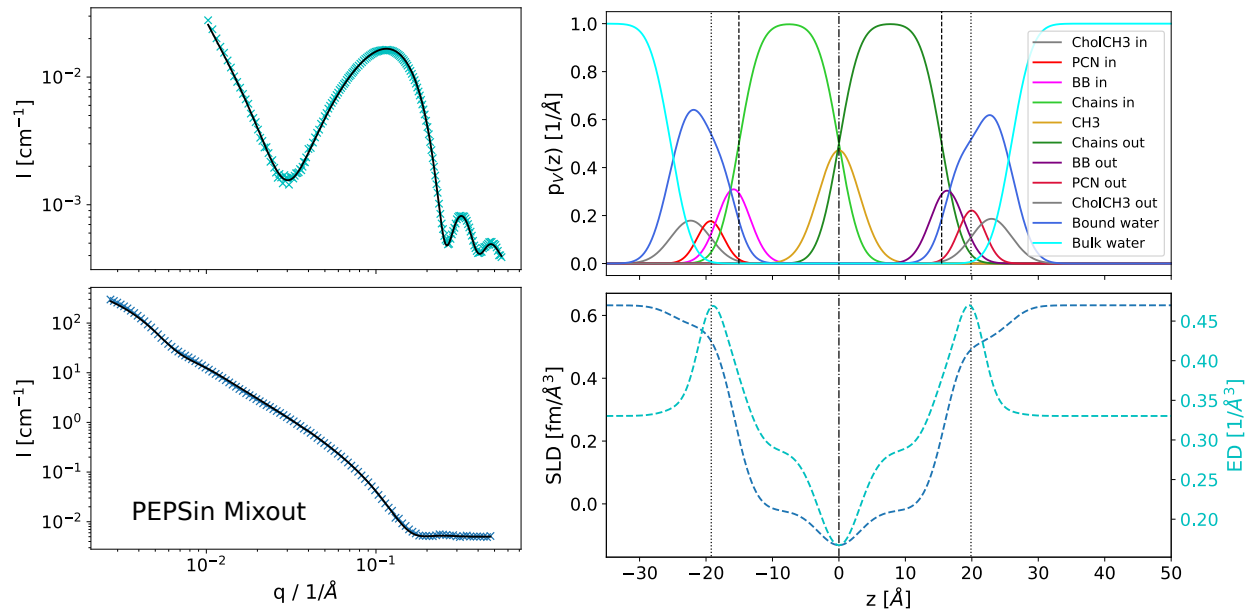


Figure S5: SAXS and SANS data with fits (black lines); SDP volume probability, electron density and neutron scattering length density profiles for the systems DPPCⁱⁿ/POPC^{out} and DPPCⁱⁿ/SOPC^{out}.

3 SAS-model parameters of reference LUVs

Table S3: SAS-fitting parameters of symmetric reference LUVs containing 90% (in) or 30% (out) POPE/POPG (9:1), complemented by POPC, MSM or a 1:1 mixture POPC/MSM.

	ϵ [%]	POPC			MSM			Mix		
		in	out	scram	in	out	scram	in	out	scram
V_L^* [\AA^3]		1202.1	1252.0	1212.94	1208.1	1293.56	1240.85	1205.11	1272.77	1247.96
V_H^* [\AA^3]		257.4	304.48	267.63	252.0	266.68	257.65	254.74	285.58	274.27
r_{CG}^*		0.50	0.46	0.49	0.49	0.38	0.45	0.5	0.42	0.45
r_{PCN}^*		0.16	0.25	0.18	0.16	0.27	0.2	0.16	0.26	0.22
r^*		2.09	2.09	2.09	2.09	2	2.09	2.09	2.09	2.09
r_{12}^*		0.8	0.8	0.8	0.8	1	0.8	0.8	0.8	0.8
D_B [\AA]	3	39.6	38.9	37.37	40.6	43.13	38.87	39.92	41.28	38.36
D_{HH} [\AA]	3	37.2	35.6	33.84	37.0	39.44	35.59	36.3	37.53	35.31
$2D_C$ [\AA]	3	31.1	29.4	29.12	32.2	34.23	30.79	31.47	32.01	29.92
D_{H1} [\AA]	20	3.1	3.1	2.36	2.4	2.61	2.4	2.41	2.76	2.7
A [\AA^2]	2	60.8	64.5	64.93	59.5	60	63.86	60.39	61.68	65.08
z_{BB} [\AA]	8	17.9	17.1	15.65	17.7	18.24	16.53	17.13	18.04	16.63
σ_{BB} [\AA]	20	2.5	2.5	2.5	2.5	2.5	2.5	2.5	2.5	2.5
z_{PCN} [\AA]	8	19.1	18.2	17.66	18.9	20.83	18.81	19.15	19.21	18.21
σ_{PCN} [\AA]	20	3.0	3.2	3.2	3.0	3	3.3	3.5	3.01	3.05
$z_{CholCH3}$ [\AA]	3	22.0	21.5	19.95	23	23.72	21.37	23.06	21.1	20.02
$\sigma_{CholCH3}^\dagger$ [\AA]		2.8	2.8	2.8	2.8	2.8	2.8	2.8	2.8	2.8
σ_{HC} [\AA]		2.5	2.5	2.5	2.5	2.5	2.5	2.5	2.5	2.5
σ_{CH3} [\AA]	5	2.4	2.4	2.79	2.4	4	3.76	3.51	2.7	4
σ_{poly} [%]	6	4.8	3.22	5.96	5.4	6.34	4.82	4.31	3.66	7.5
$V_{W,bound}$ [\AA^3]	6	29.8	29.9	28.83	29.5	29.8	29.01	29.75	29.87	28.47
n_W	6	10.0	10.3	8.73	10.8	9.83	10	11.77	6.66	7.84
R_m [\AA]	10	370.1	370.2	430.7	372.5	470.2	408.6	356.2	391.4	390.6
σ_R [\AA]	10	103.9	123.7	171.7	102.3	127.7	182.9	91.67	106.7	188.3

Table S4: SAS-fitting parameters of symmetric reference LUVs containing 90% (in) or 30% (out) POPE/POPS (7:3), complemented by POPC, MSM or a 1:1 mixture POPC/MSM.

	ϵ [%]	POPC			MSM			Mix		
		in	out	scram	in	out	scram	in	out	scram
V_L^* [\AA^3]		1207.1	1253.6	1221.8	1213.03	1295.21	1255.49	1210.06	1274.42	1240.09
V_H^* [\AA^3]		262.2	306.07	276.1	256.81	268.27	262.73	259.51	287.17	272.42
r_{CG}^*		0.49	0.46	0.48	0.48	0.37	0.42	0.48	0.41	0.45
r_{PCN}^*		0.19	0.26	0.21	0.19	0.28	0.24	0.19	0.27	0.23
r^*		2.09	2.09	2.09	2.09	2	2.09	2.09	2.09	2.09
r_{12}^*		0.8	0.8	0.8	0.8	1	0.8	0.8	0.8	0.8
D_B [\AA]	3	37.8	38.2	37.2	38.22	42.65	39.08	38.06	40.22	37.09
D_{HH} [\AA]	3	37.0	35.3	32.7	36.85	38.99	38.93	36.28	37.2	36.53
$2D_C$ [\AA]	3	29.6	28.8	28.8	30.12	33.81	30.89	29.89	31.15	28.93
D_{H1} [\AA]	20	3.7	3.2	2.0	3.37	2.59	4.02	3.19	3.03	3.8
A [\AA^2]	2	63.8	65.7	65.8	63.49	60.75	64.27	63.61	63.39	66.89
z_{BB} [\AA]	8	16.3	16.1	16.0	17.22	18.53	19.39	16.8	17.84	17.31
σ_{BB} [\AA]	20	2.5	2.5	2.5	2.5	2.5	2.86	2.5	2.5	2.5
z_{PCN} [\AA]	8	19.1	18.3	16.0	19.92	20.34	19.39	19.59	19.1	19.42
σ_{PCN} [\AA]	20	2.2	2.8	2.9	3.5	3.29	2.2	3.5	3.27	3.5
$z_{CholCH3}$ [\AA]	3	24.1	23.3	21	19.92	21.77	24.39	19.59	19.47	19.42
$\sigma_{CholCH3}^\dagger$ [\AA]		2.8	2.8	2.8	2.8	2.8	2.8	2.8	2.8	2.8
σ_{HC} [\AA]		2.5	2.5	2.5	2.5	2.5	2.5	2.5	2.5	2.5
σ_{CH3} [\AA]	5	3.5	3.1	4.0	3.32	3.89	2.4	3.26	3.19	4
σ_{poly} [%]	6	7.3	6.63	10.0	5.26	4.81	9.46	6.08	5.58	6.92
$V_{W,bound}$ [\AA^3]	6	30.0	29.7	30.3	30.03	29.78	30.01	28.97	29.26	29.41
n_W	6	16.9	15.2	11.4	7.58	6.53	16.25	7.07	4.54	8.14
R_m [\AA]	10	381	392.6	469.1	409.5	495.7	607.7	430.9	451.9	500.7
σ_R [\AA]	10	109.2	133.5	154.4	131.7	167.1	151.9	140.6	133.1	128.7

Table S5: SAS-fitting parameters of symmetric reference LUVs containing 90% (in) or 30% (out) POPE/POPG (9:1), complemented by ESM.

	ϵ [%]	ESM		
		in	out	scram
V_L^* [\AA^3]		1196.5	1212.2	1181.0
V_H^* [\AA^3]		252.0	266.68	259.1
r_{CG}^*		0.49	0.38	0.44
r_{PCN}^*		0.16	0.27	0.21
r^*		2.09	2.09	2.09
r_{12}^*		0.8	0.8	0.8
D_B [\AA]	3	38.0	41.1	38.2
D_{HH} [\AA]	3	36.9	37.0	34.9
$2D_C$ [\AA]	3	30.0	32.0	29.8
D_{H1} [\AA]	20	3.4	2.5	2.6
A [\AA^2]	2	63.0	59.1	61.8
z_{BB} [\AA]	8	17.6	17.6	15.7
σ_{BB} [\AA]	20	2.5	2.5	2.5
z_{PCN} [\AA]	8	19.4	18.7	20.2
σ_{PCN} [\AA]	20	3.5	2.7	3.5
$z_{CholCH3}$ [\AA]	3	19.4	22.9	21
$\sigma_{CholCH3}^\dagger$ [\AA]		2.8	2.8	2.8
σ_{HC} [\AA]		2.5	2.5	2.5
σ_{CH3} [\AA]	5	3.1	2.4	4.0
σ_{poly} [%]	6	5.3	4.95	8.5
$V_{W,bound}$ [\AA^3]	6	27.7	27.6	30.3
n_W	6	6.7	10.0	8.8
R_m [\AA]	10	393.1	455	531.6
σ_R [\AA]	10	114.1	132.9	138.9

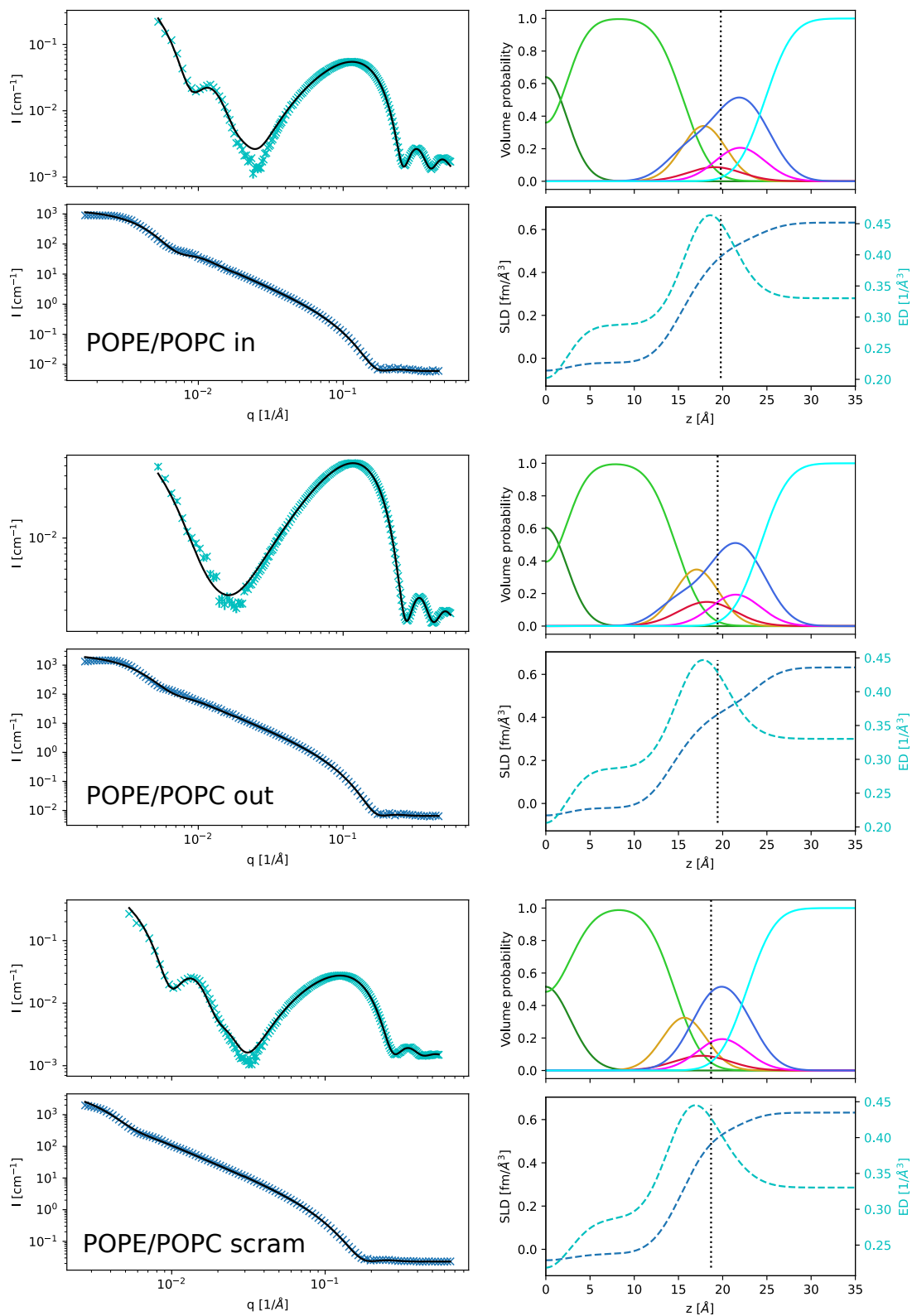


Figure S6: SAXS and SANS data with fits (black lines); SDP volume probability, electron density and neutron scattering length density profiles for DPPC-MSPC inner/outer leaflet symmetric mimics, as well as DPPC-SMPC inner leaflet mimics.

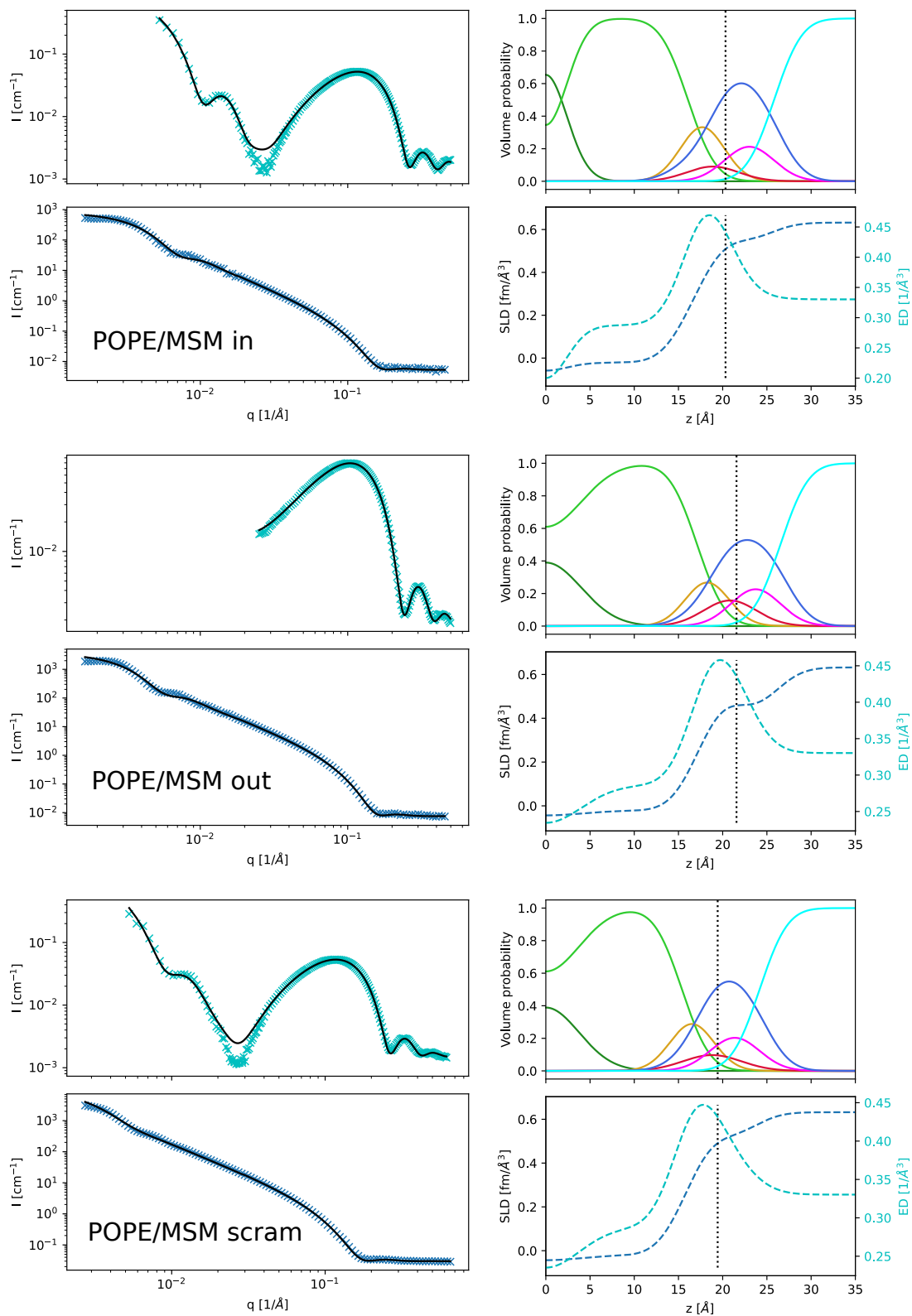


Figure S7: SAXS and SANS data with fits (black lines); SDP volume probability, electron density and neutron scattering length density profiles for DPPC-MSPC inner/outer leaflet symmetric mimics, as well as DPPC-SMPC inner leaflet mimics.

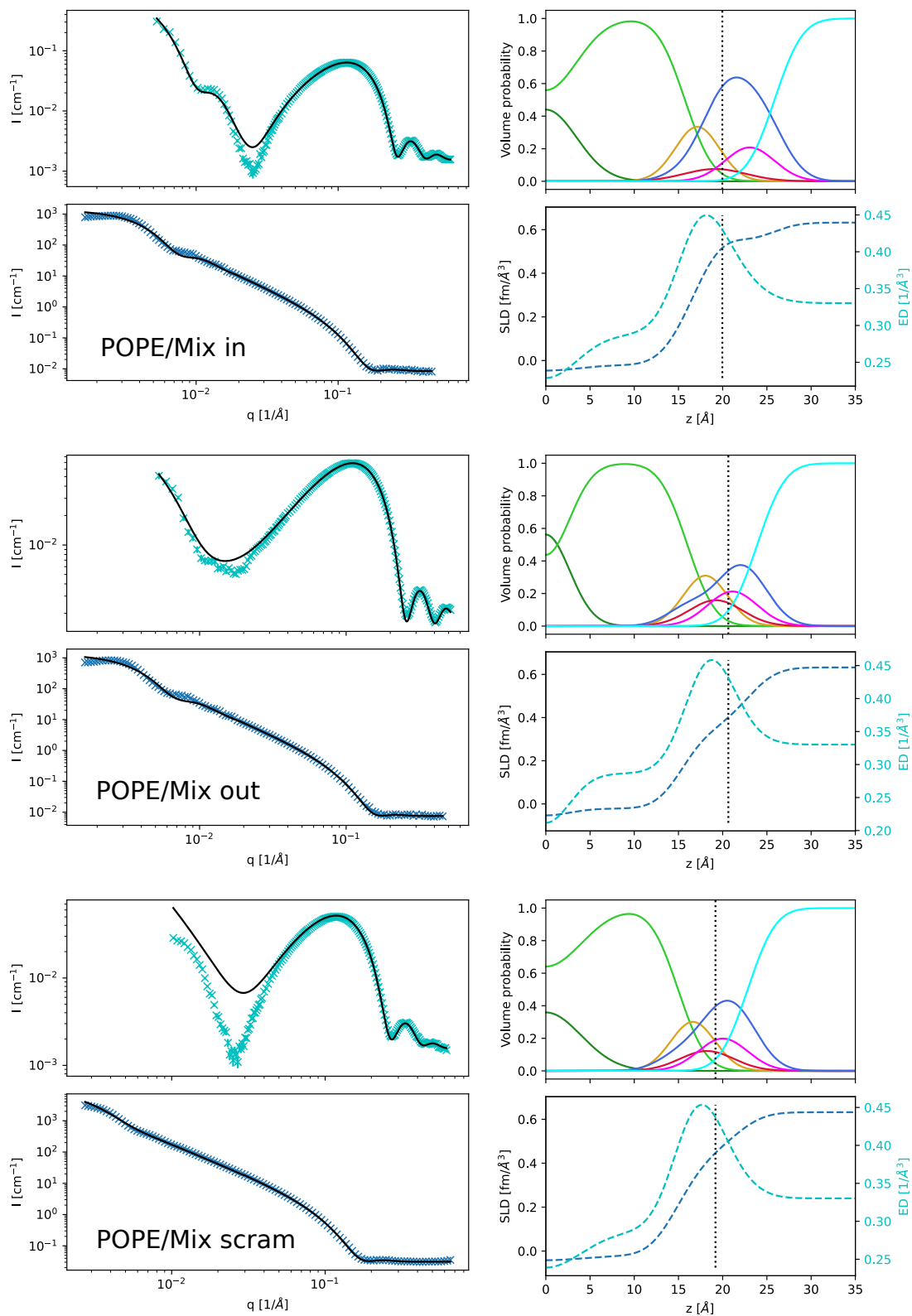


Figure S8: SAXS and SANS data with fits (black lines); SDP volume probability, electron density and neutron scattering length density profiles for DPPC-MSPC inner/outer leaflet symmetric mimics, as well as DPPC-SMPC inner leaflet mimics.

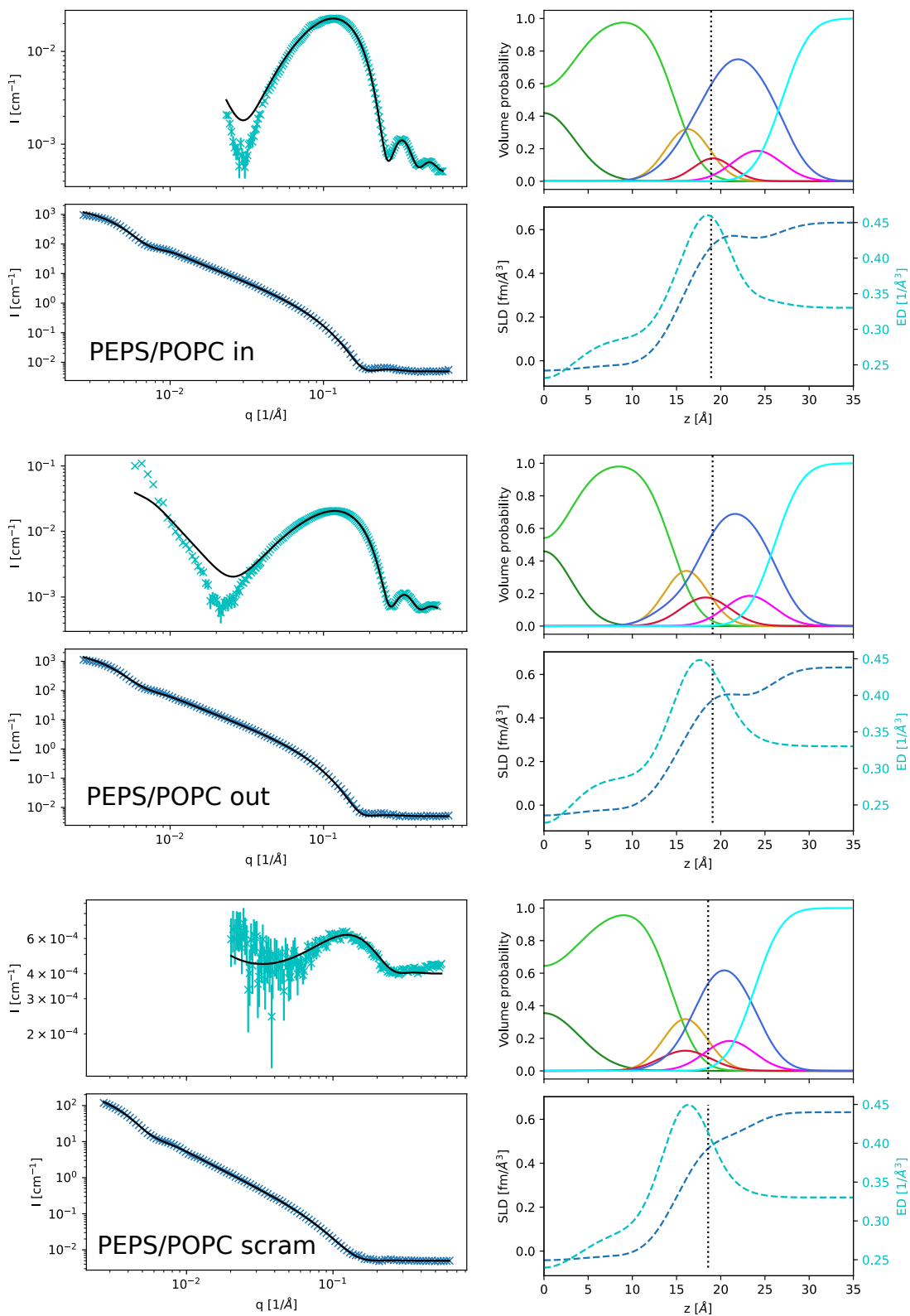


Figure S9: SAXS and SANS data with fits (black lines); SDP volume probability, electron density and neutron scattering length density profiles for DPPC-MSPC inner/outer leaflet symmetric mimics, as well as DPPC-SMPC inner leaflet mimics.

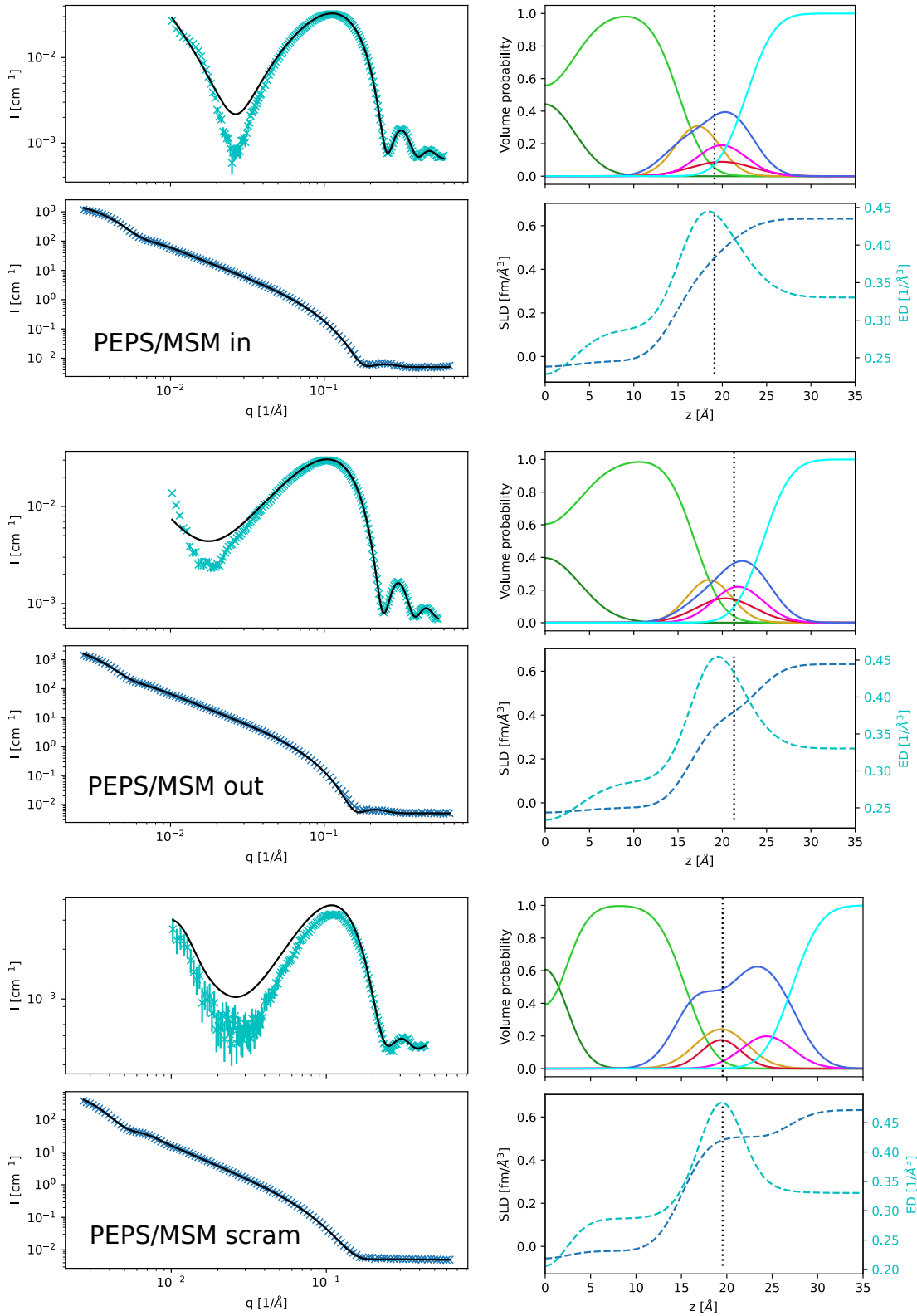


Figure S10: SAXS and SANS data with fits (black lines); SDP volume probability, electron density and neutron scattering length density profiles for DPPC-MSM inner/outer leaflet symmetric mimics, as well as DPPC-SMPC inner leaflet mimics.

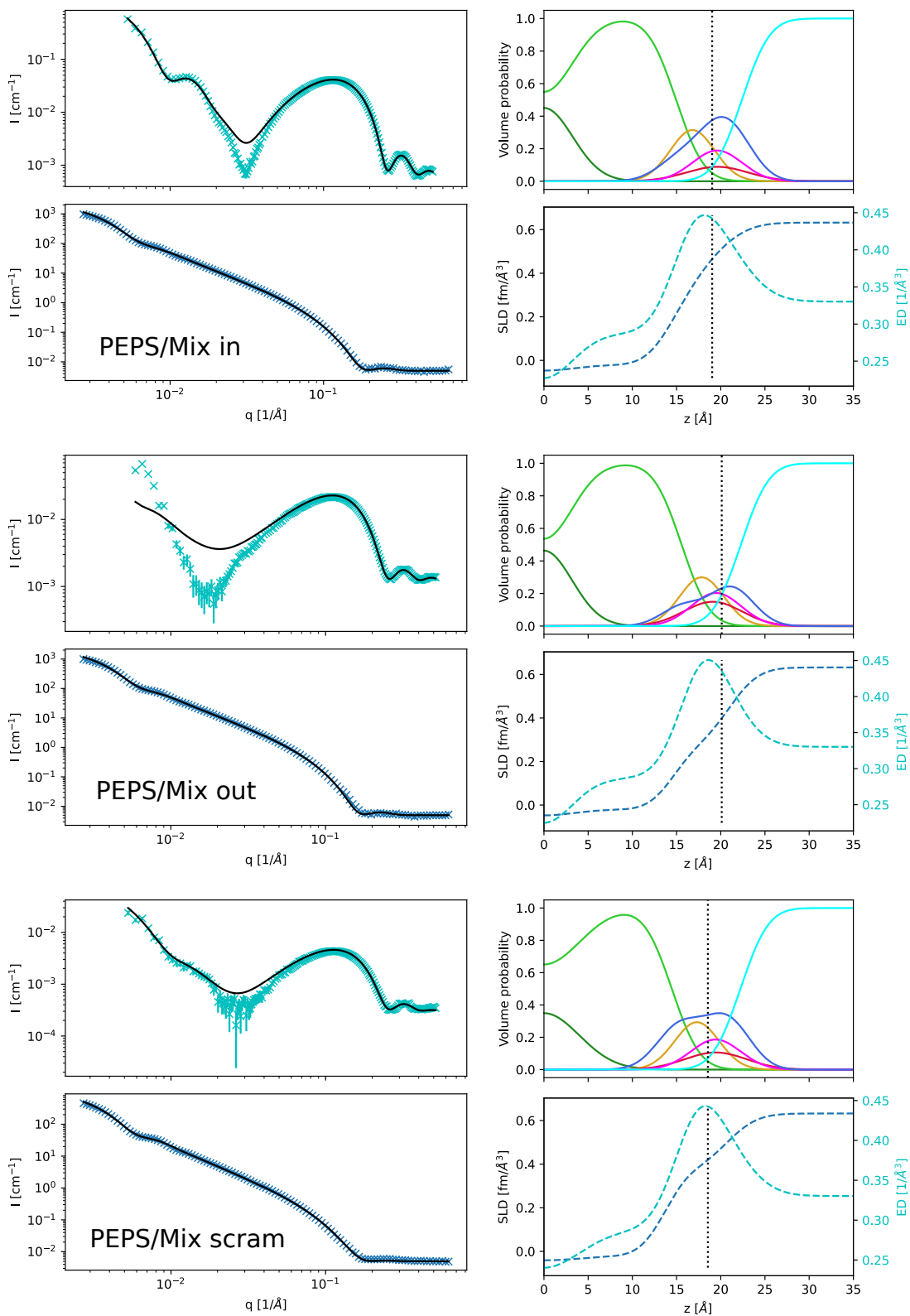


Figure S11: SAXS and SANS data with fits (black lines); SDP volume probability, electron density and neutron scattering length density profiles for DPPC-MSPC inner/outer leaflet symmetric mimics, as well as DPPC-SMPC inner leaflet mimics.

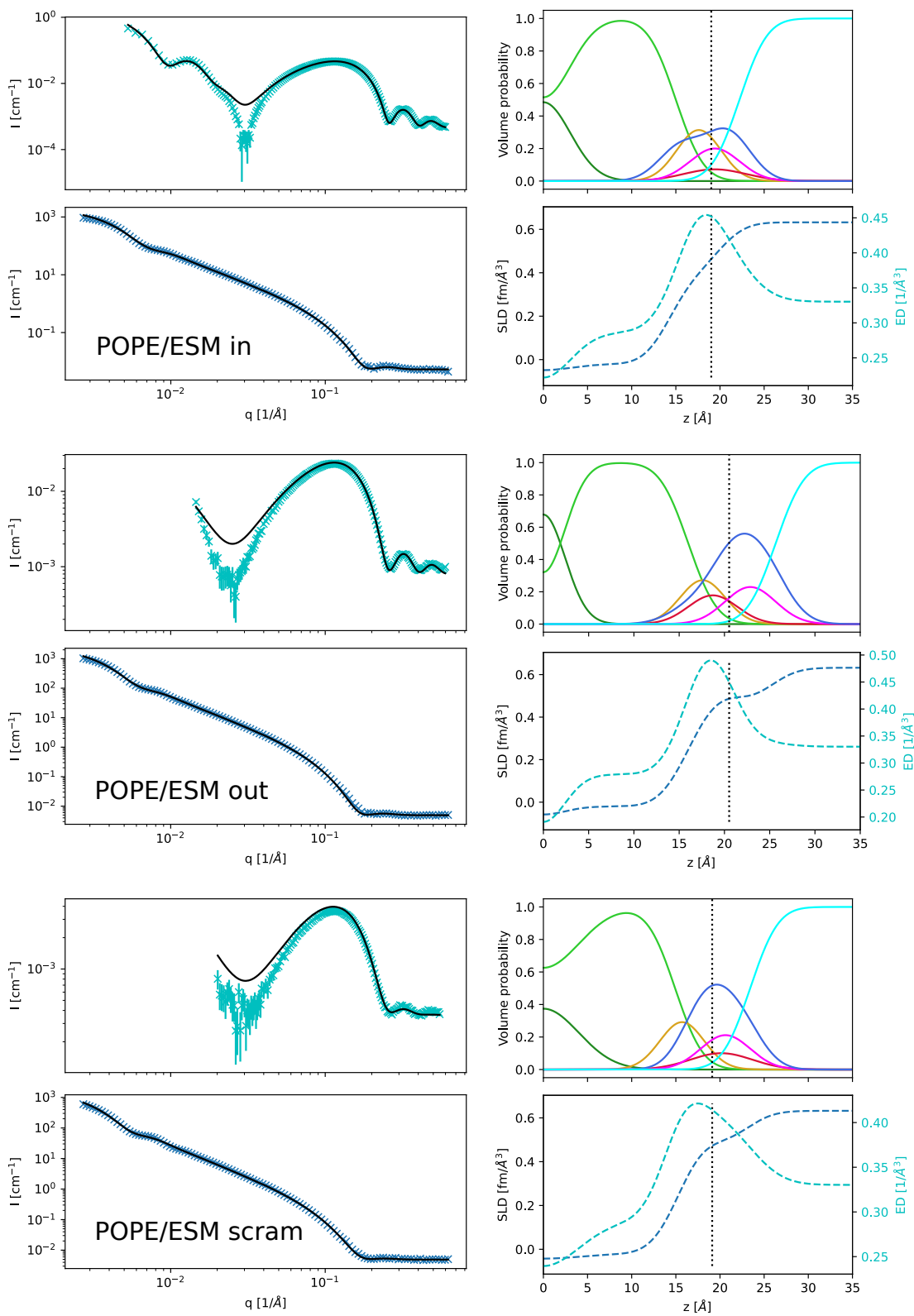


Figure S12: SAXS and SANS data with fits (black lines); SDP volume probability, electron density and neutron scattering length density profiles for DPPC-MSPC inner/outer leaflet symmetric mimics, as well as DPPC-SMPC inner leaflet mimics.